Stochastic modelling of large cavities : random and coherent field applications

Andrea Cozza

UNIVERSITÉ PARIS-SUD

École Doctorale STITS

HABILITATION À DIRIGER DES RECHERCHES

présentée par

Andrea COZZA

Spécialité : Physique

Stochastic modelling of large cavities

Random and coherent field applications

Soutenue le 28 septembre 2012, devant le jury constitué de :

Rapporteurs :	Philippe BESNIER	Chargé de Recherche, IETR (Rennes)
	Paolo CORONA	Professeur, Università Parthenope (Naples)
	Françoise PALADIAN	Professeur, Université Blaise Pascal (Clermont-Ferrand)
Examinateurs :	Hans-Georg KRAUTHÄUSER	Professeur, Technische Universität Dresden
	Marc LAMBERT	Chargé de Recherche, L2S (Gif sur Yvette)
	Christian PICHOT DU MEZERAY	Directeur de Recherche, LEAT, (Nice)

Andrea Cozza

Stochastic modelling of large cavities

Random and coherent field applications

May 2012

To Eleonora, for her unwavering love and patience

Contents

Preface

This memoir was written in partial fulfillment of the requirements of the "Habilitation à Diriger des Recherches" degree, as defined by the French law. It is therefore intended as a summary of my research activity and vision developed during the last 4 years, since I have started working on reverberation chambers.

Because of the specific nature of this document, it should not be regarded as a sort of monograph about large cavities: in no possible way it could be considered as complete enough for such a purpose; discussions are often on an informal level and mostly the main results from my work are presented. It should be regarded as more of an overview of my work than a self-contained presentation on the physics of large cavities.

This memoir is organized into four chapters. The first chapter introduces the main ideas and concepts that allow modelling large cavities in a harmonic steady-state, where the field distribution can often be modelled as a random process: the two main theoretical approaches currently employed are then introduced, with the aim of showing why most of the current activities surrounding reverberation chambers in the electromagnetic compatibility (EMC) community is wanting; original contributions are then presented, showing how getting back to simple first-principle approaches can shed some light on misunderstandings mainly affecting the EMC community.

The second chapter is a direct continuation of the first one, focused on the use of simple statistical models in order to understand why real-life cavities naturally behave in a manner that can be very different from the ideal case of a diffusive medium.

The third chapter introduces the idea of merging the statistical properties of large cavities with those of time-reversed waves, in order to make a coherent propagation out of a random medium. The theoretical and practical feasibility of emulating propagation environments from free-space propagation to multipath ones is discussed, together with ideas of future developments and applications based on these concepts.

The fourth and final chapter discusses how these contributions point to a coherent approach that let foresee a number of future contributions directly motivated and supported by my current research activities. The appendices present a short curriculum vitæ, together with selected papers and a complete list of my publications.

Acknowledgements

The ideas and work discussed in this dissertation have benefited from the implication of undergraduate and graduate students during the last 4 years. I wish to thank those who have been involved in the process of developing and testing these ideas; their questions have often served the important role of requiring an assessment of my own understanding.

I am deeply indebted towards Prof. Jean-Charles Bolomey, former Director of the Département Électromagnétisme in Supélec, for having given me the opportunity to work on several transversal projects during my post-doctorate years; Dr. Marc Lesturgie, also a former Director of our department, for having been the unexpected source of my even more unexpected interest in reverberation chambers; Dr. Dominique Lecointe, our current Director, for his support and the total freedom of research of which my work has strongly benefited.

I also wish to thank my colleagues, particularly Dr. Marc Lambert, Senior Researcher at CNRS, for our discussions and Dr. Florian Monsef, Lecturer at Paris Sud University and close collaborator. Florian has often contributed to the settling of my ideas and has lent his ears to my most unlikely ideas for future research topics. If they will be proved right one day, his role shall not be regarded as a passive one. I am sure our research partnership will provide new and exciting results in the next few years.

I cannot forget to acknowledge the contribution of distant colleagues, particularly Prof. Paolo Corona, Full Professor at Università Parthenopea, Italy, Dr. Niklas Wellander, Senior Researcher at FOI, Sweden, Dr. Koh Wee jin, Laboratory Head at DSO, Singapore and Dr. Philippe Besnier, Senior Researcher at CNRS. All of them have in some way at a certain time led me to question my understanding. A special thank goes to Dr. Gabriele Gradoni, Junior Researcher at the Maryland University, USA, who has acted (and still does so) as a rare bridge between the ideas of wave-chaos theory and the electrical engineering education we share.

The importance of the excellent forum provided by the several discussion groups of the GDR Ondes, a researchers' network in France, has also played a fundamental role in my getting in touch with ideas and concepts from fields whose existence I was not even aware of until a few years ago. The time and efforts spent by the organizers of workshops, seminaries and summer schools should be applauded.

Chapter 1

Large cavities in a harmonic steady state

The method of science depends on our attempts to describe the world with simple theories: theories that are complex may become untestable, even if they happen to be true. Science may be described as the art of systematic over-simplification – the art of discerning what we may with advantage omit.

Karl Raimund Popper

CAVITIES could appear as a peculiar choice for research. They basically consist of a contiguous (eventually multiply-connected) region of space surrounded by impenetrable and weakly absorbing boundary conditions. Propagation of waves through this type media is seldom treated in graduate courses, giving a large preference for free-space propagation while introducing diffraction from medium discontinuities often as local-perturbation phenomena.

In fact, free-space-like propagation based on the idea of line-of-sight propagation is hardly found in practice. The feeling that line-of-sight propagation should be taken as the obvious reference in radio-wave propagation is probably due to the fact that radio-links are often designed (or at least presented) in such a way as to provide a point-to-point link from a transmitter A to a receiver B. More complex propagation scenarios are found in radio-wave applications, e.g., in indoor and urban environments, but are often presented as special cases at the end of an electrical-engineer degree cursus.

At the antipodes of line-of-sight propagation lies wave diffusion. Wave diffusion can be stated as a peculiar configuration where an observer experiences a large number of

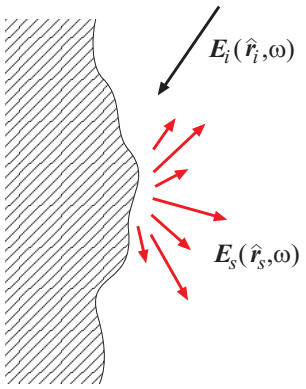

Figure 1.1 – Non-specular scattering from a generic surface.

waves directed at him, covering with the same frequency of occurrence all directions of arrival. As a result, no preferential direction of arrival can be identified, nor their common origin. This kind of phenomenon basically occurs in two configurations: 1) wave scattering over a rough surface and 2) multiple-scattering events. In the framework of this dissertation, we will not discuss about the first case, since it is of limited interest for microwave cavities, though some attempts at introducing rough surfaces within such cavities has been made in the past within the electromagnetic compatibility (EMC) community [R63, R62], as inspired by previous work in acoustics [R76, R44, R14].

When thinking about our daily experience it is self-evident that most wave-propagation events occur more often within at least partially bounded structures than in a free-space-like scenario. For microwaves, most radio-links typically involve waves interacting with the interior or exterior of buildings or geological structures, and in a similar manner acoustic waves and visible light. Wave diffusion should therefore be regarded as a common phenomenon occurring in a number of practical situations. For instance, scattering of light from most of natural surfaces has strongly diffusive characteristics, as well known to scientists working in computer graphics, where the efforts to render realistic scenes passes through the use of physical models representing wave diffusion by rough surfaces.

Wave diffusion should not be expected exclusively for wave propagating *through* open media prone to wave scattering, such as the case of Rayleigh scattering of Solar visible radiation through the atmosphere [R88], but is similarly found in practice when waves are excited *within* a bounded medium with sufficiently reflective boundaries, i.e., a cavity with boundaries such that an incident local plane wave $\boldsymbol{E}_i(\hat{\boldsymbol{r}},\omega)$ propagating along the direction $\hat{\boldsymbol{r}}_i$ is scattered along a set of directions $\hat{\boldsymbol{r}}_s$ into a field $\boldsymbol{E}_s(\hat{\boldsymbol{r}}_s,\omega)$ with negligible loss of power, i.e.,

$$\int \|\boldsymbol{E}_s(\hat{\boldsymbol{r}}_s,\omega)\|^2 \mathrm{d}\hat{\boldsymbol{r}}_s \simeq \|\boldsymbol{E}_i(\hat{\boldsymbol{r}}_i,\omega)\|^2, \tag{1.1}$$

where the integral is computed over all directions pointing away from the region of impact of the impinging wave and towards the inside of the cavity; this situation is depicted in Fig. 1.1. The present dissertation will be limited to this special case of diffusive media. Weak dissipation is not the only assumption that will be taken for granted; cavities will also be assumed to be much larger than the wavelength imposed

by the medium inside the cavity, i.e., electrically large cavities. The rationale for this condition will be discussed in §§ 1.3.1 and 2.2.

Under these conditions, the field generated and propagating within a cavity can often be approximated as a diffuse field, as introduced earlier in this section. Here is to be found one of the two major themes of this dissertation: as every approximation, even the most effective holds only within given bounds imposed by the context of its application. Wave-diffusion models *can* be used for large weakly dissipative cavities, but their accuracy depends on what we need to compute in our investigations.

Some reflections pertaining to this question are presented in § 2, showing how diffuse-field models can be misleading when forgetting under what conditions this approximation is valid. To this end, we present a simplified discussion in this chapter showing how wave-diffusion models can be expected to work, and what other models can be applied in order to understand their limitations.

1.1 Large cavities as test facilities

A large variety of practical configurations can be approximated by large cavities: urban setting, rooms, the interior of airplanes and any system equipped with a metallic shield, lasers, quantum wells, cavity interferometers, etc. Although the scale and dimensionality change, the phenomena are fundamentally the same, with the appearance of natural resonances as soon as the boundary conditions of the cavity are highly reflective.

While the physical phenomena are shared by all of the previous examples, the ability of cavities to generate resonances can be regarded as a nuisance or an advantage. For example, wireless communications within indoor media typically require some clever signal processing and coding, due to their strongly frequency-selective response, which would otherwise make wide-band communications through indoor media an unlikely idea. On the contrary, resonances have been exploited within the framework of two generic groups of applications: 1) to design very selective filters; 2) to design diffusive media. The first one can be accessed when at least one of the cavity's dimensions is comparable to the working wavelength; in this case, the resonances are typically not overlapping and cavity filters (e.g., in microwaves but also surface acoustic-wave filters) can provide very narrow pass-band/stop-band responses. As soon as the frequency increases, a larger number of resonances are allowed, leading to increasingly more likely overlapping of their frequency responses. An example of these two trends is given in Fig. 1.2.

If the interest of the single-resonance regime is obvious, it could be less clear why a complex frequency selective system should be of any use. In order to have an intuitive understanding, we should rather switch to a wave-propagation point of view. Fig. 1.3(a) shows, in a very simplified way, how a single source within a large cavity (i.e., with respect to the working wavelength) generates a large number of waves propagating along very diverse trajectories. Intuitively, if the structure of the cavity were

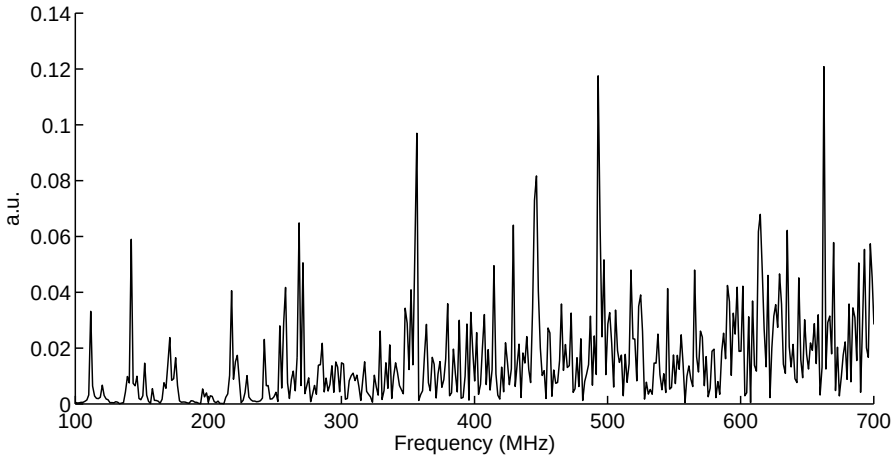

Figure 1.2 – An example of frequency response measured in Supélec's reverberation chamber, over its low to intermediate region before the establishment of a diffuse-field condition.

complex enough, it could be expected that each point of the cavity would be crossed by waves propagating along every direction. This idea becomes even more natural if we think about what makes a room having a good "acoustics": it is typically the fact of ensuring an experience, as a listener, that is practically independent from our position *and* orientation, as well as a frequency response that is flat (no distortion); distinguishable echoes should not exist. In fact, this is exactly what happens within a reverberating cavity, where echoes are so close to each other to be indistinguishable, while the multipath propagation of waves practically annihilates any difference related to frequency, direction and orientation. The result is a *diffuse field*, identical *on average* everywhere. It is therefore not surprising that the field of acoustics, and in particular room acoustics, has been the first to thoroughly investigate the physics of large cavities [R69, R73, R44].

Large cavities are not only important to ensure a good experience to concert-goers; the same ideas and requirements are at the base of their use as test facilities. Reverberating cavities capable of supporting a diffuse-field regime, are fundamental tools in a large number of fields, from microwaves to acoustics passing through optics. Their main use is given by a simple observation: if a source radiates a scalar field $F(\hat{\boldsymbol{k}})$ along the directions $\hat{\boldsymbol{k}}$, then the signal V_o received by an isotropic transducer would be (Fig. 1.3)

$$V_o = \sum_{n=1}^{N} \alpha_n F(\hat{\boldsymbol{k}}_n), \tag{1.2}$$

where N is the total number of echoes or propagation paths between the source and the transducer. Each contribution arriving along different directions $\hat{\boldsymbol{k}}_n$ will be weighted by

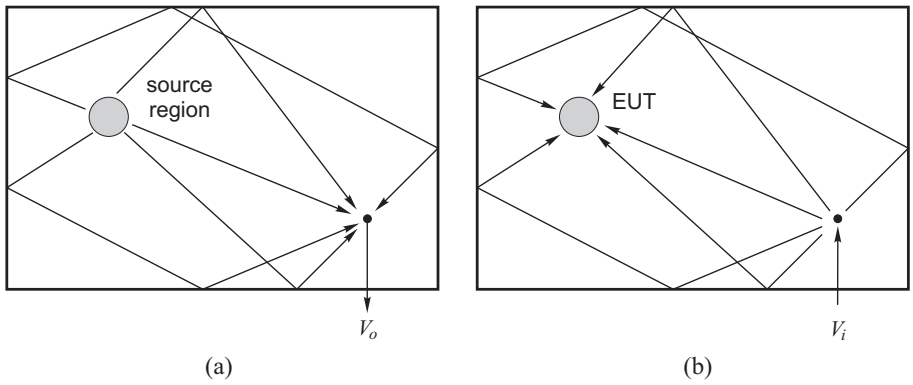

Figure 1.3 – Wave diffusion in a cavity, exploited to : (a) collect data about the radiation of a source along all possible directions; (b) simultaneously excite an EUT along a large number of directions.

a random coefficient α_n, as in the case of a listener in a concert hall. By taking the squared modulus of V_o and repeating this operation a number of times in different configurations (moving the source, the transducer, etc.), yields

$$\left\langle |V_o|^2 \right\rangle = \sum_{n=1}^{N} \left\langle |\alpha_n|^2 \right\rangle |F(\hat{\boldsymbol{k}}_n)|^2 \tag{1.3}$$

where $\langle \cdot \rangle$ is the result of averaging over all the different test configurations. If the cavity generates a diffuse field, then $\left\langle |\alpha|^2 \right\rangle = \alpha_{\text{rms}}^2$ and

$$\left\langle |V_o|^2 \right\rangle = \alpha_{\text{rms}}^2 \sum_{n=1}^{N} |F(\hat{\boldsymbol{k}}_n)|^2 \propto \int_{4\pi} |F(\hat{\boldsymbol{k}})|^2 \mathrm{d}\hat{\boldsymbol{k}}, \tag{1.4}$$

since the number N of random directions $\{\hat{\boldsymbol{k}}_n\}$ would be ideally infinite, implying that (1.4) is nothing else than an excellent Monte Carlo approximation of the total radiated power integral. The averaging therefore appears to allow passing from an integral over angles to one over random realizations, a property related to the *ergodicity* of the field in diffusive cavities. Realizations involving different sets of $\{\alpha_n\}$ can be generated with a number of techniques, but they are all intended to lead to an *ensemble* of cavities. The integrating property of large cavities is exploited in the characterization of sources of propagating waves, in a very general way. In the case of optics, integrating spheres are also equipped with diffusive boundaries which allow a further averaging mechanism. For longer wavelengths, e.g., in acoustics and microwaves, scatterers are routinely inserted within the cavity for the same reason.

Reciprocity implies Fig 1.3(b): now the transducer is the source of radiation, and an equipment under test (EUT) is submitted to a large number of waves with random

amplitude, direction of arrival and (eventually) polarizations. The average power impinging over the EUT is known: it is therefore possible, from simple computations based on power conservation, to assess the power absorbed by the EUT. This further application is important in acoustics (e.g., assessing the performance of absorbers for phonic insulation, but also the amount of power lost in comfortable seats), as well as in the characterization of any material.

In all of these examples, reverberation chambers allow reducing the overall duration of tests, since if the same operations were carried out within anechoic environments, it would be necessary to scan an EUT along all possible directions, in order to collect enough data: in this case, a source could only generate line-of-sight excitations.

These ideas are given a twist in the case of EMC [R33, R45, R42], where the EUT is now an electronic system, in which impinging waves can disrupt its nominal behaviour. A well-known example of this problem is the requirement to turn off radiating devices on airplanes. Another important specificity of EMC tests is that in order to ensure a good safety margin, reverberation chambers are not only used to reduce the test duration, but also as an effective way of generating very strong fields from relatively low-power sources. Resonances take on their full importance in EMC tests, since field levels as high as 10 kV/m can be required in aeronautics, in order to simulate the conditions experienced when passing close to radars.

It is important to understand that the diffuse-field condition is not only invoked as a simple ideal approximation. The most important point is that when a field is diffuse, its *statistical* properties does not depend any longer on the fine details of the cavity, by definition. The direct consequence is that the results of a test can be expected to be independent from the cavity, i.e., they can be reproduced in other test facilities. It is this simplification that is important, since it ensures that reverberating cavities can be regarded as fit for metrology tasks. The rich literature dealing with the study of the behaviour of reverberating cavities is largely justified by this need of assessing their accuracy.

It is worth mentioning that cavities, in particular microwave cavities, are also the backbone of another field of investigation, that of wave-chaos theory [R81]. In this case, the motivation is by far less practical: the problem is to find a simple way of experimentally verifying the theoretical predictions of quantum-chaos theory, as well as of the mathematical theory of billiards [R11].

In short, cavities are a rather familiar component in many experimental fields of investigation. Perhaps less familiar are the modelling tools used in order to understand their peculiarities. The rest of this dissertation is concerned with this topic, together with the introduction of even more peculiar features enabled by time-reversed excitations.

1.2 Wave-propagation modelling in large cavities

When thinking about models capable of representing the propagation of waves within cavities, and in general bounded media, their nature strongly depends on the context of application. While in wireless communications the most important issue is to predict figures of merit such as the power-delay spread and the number of degrees of freedom, in wave-chaos theory one would rather look for the statistical behaviour of the frequencies of resonance and the field distribution, whereas in radiated tests the spatial invariance of statistical moments would be more important.

As a result, a number of methods have been proposed independently in each field of application, with scant cross-fertilization, leading to a collection of techniques that are tuned to each specific need. The peculiarity of this situation, far from being the only such case in physics, is that imporrtant results are scattered over a number of domains where it is not always possible to browse through them easily. This problem will be apparent in § 2, where notions that have been available in acoustics and wave-chaos theory for some decades have been practically unknown to the electromagnetic community; tools and concepts routinely applied in statistical optics are scantly used, too.

This section will not try to sort out these models, though such operation would be badly needed. We would rather limit our discussions to two antipodal approaches available for the goals we have set ourselves for §§ 2 and 3, namely understanding the physical phenomena at the basis of harmonic and time-reversal excitation of large cavities. Our discussions will be the starting point for the introduction of surprisingly simple models based on random spectral representations; passing from a rigid deterministic point of view to a statistical one, we will argue in § 1.4 that there is room for misunderstandings about the interpretation and use of these methods. This same discussion will constitute the foundation for the analyses introduced in § 2.

1.2.1 Green's functions

In the context of linear systems studied under a harmonic steady state, the most general technique employed to deal with their spatiotemporal evolution is that of Green's functions [R56, R21], which generalizes the concept of impulse response. In the context of this dissertation we will just need to recall the main ideas needed to introduce the spectral representation of Green's functions, as applied in § 1.3 and § 2.

Green's functions can be introduced for a linear system of which we want to observe the evolution of a given quantity, here referred to as $u(\boldsymbol{r})$. This quantity depends, in a general way, on the value taken by a parameter; for our discussion, we will consider the position $\boldsymbol{r}$ in a multidimensional space where $u(\boldsymbol{r})$ is sampled (measured). The region of space Ω where the phenomena of interest occur will be considered finite in our discussions, and with a simple topology (e.g., Fig 1.4). The choice of the variable $\boldsymbol{r}$ should not mislead into regarding it as merely representing space, but can more

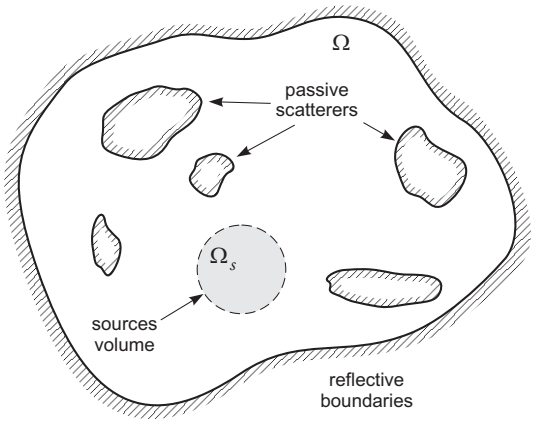

Figure 1.4 – A typical configuration for a reverberating cavity, delimited by reflective boundaries (external boundaries), including reflective scatterers (internal boundaries) and at least a source region. The space Ω delimited by the external and internal boundaries is filled by a homogeneous medium, assumed to be air, for simplicity.

generally include time as well. Typically, for a practical configuration, the quantities of interest are state variables used to define the phase-space of a system; being dependent on $\boldsymbol{r}$, they are by definition fields and we will assume a scalar field in this section for the sake of simplicity.

When the problem at hand is the propagation of waves through a medium, the field of interest is causally excited by a physical event $f(\boldsymbol{r})$, such as a variation in pressure or electric current; knowledge of the physical laws underpinning the phenomena of interest allow writing a formal relationship between cause and effect

$$L(\boldsymbol{r})u(\boldsymbol{r}) = f(\boldsymbol{r}) \quad \boldsymbol{r} \in \Omega, \quad (1.5)$$

where $L(\boldsymbol{r})$ is a linear operator. In a general way, it is also necessary to specify a set of auxiliary equations describing boundary or initial conditions over, e.g., the border $\partial\Omega$ of the region of existence of $u(\boldsymbol{r})$

$$B(\boldsymbol{r})u(\boldsymbol{r}) = g(\boldsymbol{r}) \quad \boldsymbol{r} \in \partial\Omega. \quad (1.6)$$

Observation of (1.5) shows that it cannot be directly used in practical settings: as a matter of fact, we are typically more interested in predicting the outcome $u(\boldsymbol{r})$ due to a cause $f(\boldsymbol{r})$, so that the following equation would be of more direct help

$$L^{-1}(\boldsymbol{r})f(\boldsymbol{r}) = u(\boldsymbol{r}), \quad (1.7)$$

where the exponent in $L^{-1}(\boldsymbol{r})$ should clearly be interpreted as a symbolic convention indicating the inverse operator. Green's functions actually provide a way of computing this inverse operator, by solving (1.5) for a special case, where

$$u(\boldsymbol{r}) = G(\boldsymbol{r}, \boldsymbol{r}') \quad (1.8)$$
$$f(\boldsymbol{r}) = \delta(\boldsymbol{r} - \boldsymbol{r}'), \quad (1.9)$$

with $\boldsymbol{r}, \boldsymbol{r}' \in \Omega$. Clearly, the above problem is still submitted to the constraints imposed by (1.6).

Once the Green's function $G(\boldsymbol{r},\boldsymbol{r}')$ is available, it is possible to show that any solution of (1.7) is readily accessible for a given excitation [R56]

$$u(\boldsymbol{r}) = \int_{\Omega} G(\boldsymbol{r},\boldsymbol{r}')f(\boldsymbol{r})\mathrm{d}\boldsymbol{r}'. \tag{1.10}$$

An example of interest involving vector fields is the operator linking electric currents $\boldsymbol{J}_e(\boldsymbol{r})$ to the electric field $\boldsymbol{E}(\boldsymbol{r})$ they generate; it can be directly derived from Maxwell's equations and put in operator form as

$$\underline{\boldsymbol{L}}(\boldsymbol{r})\cdot\boldsymbol{E}(\boldsymbol{r}) = \boldsymbol{J}_e(\boldsymbol{r}), \tag{1.11}$$

where $\underline{\boldsymbol{L}}(\boldsymbol{r})$ is now a dyadic operator (second-rank tensor). This last case is the one of interest in this dissertation, where (1.10) can now be written as [R56]

$$\boldsymbol{E}(\boldsymbol{r}) = \int_{\Omega} \underline{\boldsymbol{G}}_{\mathrm{ee}}(\boldsymbol{r},\boldsymbol{r}')\cdot\boldsymbol{J}_e(\boldsymbol{r})\mathrm{d}\boldsymbol{r}', \tag{1.12}$$

with $\cdot$ the inner vector product. The dyadic Green's function $\underline{\boldsymbol{G}}_{\mathrm{ee}}(\boldsymbol{r},\boldsymbol{r}')$ used in this case is intended to link the electric field to electric currents, hence the subscript "ee". Other Green's functions can therefore be considered, linking electric/magnetic fields to electric/magnetic currents.

In practice, the problem of finding a solution $G(\boldsymbol{r},\boldsymbol{r}')$ is far from trivial, and only for very simple canonical geometries it is possible to express it in closed form [R87]. Numerical techniques are most often needed, but as they do not allow the derivation of predictive models, they will not be considered in the context of this dissertation.

This is where spectral approaches come in handy, by allowing to break down the problem of Green's functions into simpler problems, particularly when dealing with cavities. As we will discuss in the rest of this section, the spectral approach in itself does not provide any simpler solution to the above problem, but rather a short-cut to (and an informal justification for) the use of simple, but very effective, approximations based on statistical considerations.

Moreover, spectral representations provide a direct insight into the physical mechanisms responsible for certain properties of a system. This last claim is particularly true for resonant cavities, as we will show in § 2 when discussing the importance of available degrees of freedom.

1.2.2 Spectral representations

The problem of modelling wave propagation through the use of Green's functions can be simplified by the use of spectral expansions. This standard procedure [R56, R81] consists of expressing the Green's functions as a linear combination of the eigensolutions $\{\boldsymbol{\psi}_n(\boldsymbol{r})\}$ of Helmholtz equation, defined as

$$\nabla^2 \boldsymbol{\psi}_n(\boldsymbol{r}) + k_n^2 \boldsymbol{\psi}_n(\boldsymbol{r}) = 0, \tag{1.13}$$

submitted to the boundary conditions (1.6), where $\boldsymbol{\psi}_n(\boldsymbol{r})$ takes the place of the generic solution $u(\boldsymbol{r})$ in the special case of a sourceless configuration. The set $\{\boldsymbol{\psi}_n(\boldsymbol{r})\}$ of eigenfunctions can be shown to form a complete basis of orthogonal functions, thus capable of representing any field distribution satisfying the boundary conditions imposed by the configuration of the cavity.

The set $\{\boldsymbol{\psi}_n(\boldsymbol{r})\}$ can be normalized in such a way as to ensure their orthonormality, i.e.,

$$\left[\boldsymbol{\psi}_m \middle| \boldsymbol{\psi}_n\right] = \int_\Omega \boldsymbol{\psi}_m^\dagger(\boldsymbol{r}) \cdot \boldsymbol{\psi}_m(\boldsymbol{r}) \mathrm{d}\boldsymbol{r} = \delta_{mn}, \tag{1.14}$$

where † stands for the Hermitian transpose and δ_{mn} is Kronecker's delta.

When considering the $\underline{\boldsymbol{G}}_{\mathrm{ee}}(\boldsymbol{r}, \boldsymbol{r}')$ dyadic Green's function the eigenfunctions could be of two natures: solenoidal or irrotational field distributions. Being interested in the behaviour of electromagnetic reverberation chambers, we will just focus our attention on the former group of eigenfucntions and note them as $\{\boldsymbol{e}_n(\boldsymbol{r})\}$; as a matter of fact, irrotational solutions are related to TEM modes that are not of practical interest in the use of reverberating chambers, since they are not associated to resonant phenomena [R87]. As a result, the electric field within a cavity can be expressed as[R56, R87]

$$\boldsymbol{E}(\boldsymbol{r}, \omega) = \sum_{n=1}^{\infty} \gamma_n \boldsymbol{e}_n(\boldsymbol{r}) \phi_n(\omega) \tag{1.15}$$

with

$$\gamma_n = \left[\boldsymbol{J}_e \middle| \boldsymbol{e}_n\right] \tag{1.16}$$

the modal coefficients and

$$\phi_n(\omega) = \frac{1}{k^2 - k_n^2} \tag{1.17}$$

the modal responses, with k_n the square root of the eigenvalue associated to the eigenfucntion $\boldsymbol{e}_n(\boldsymbol{r})$ and $k = k(\omega)$ the wave number.

What should be the advantage of using (1.15) rather than (1.10)? There are several reasons for choosing the former, such as a more efficient model with reduced complexity, but in the context of resonating media (here cavities) we will mainly stick to the physical insight brought in by the presence of the modal responses $\{\phi_n(\omega)\}$ in (1.15).

In order to understand their role, we should start by observing that their modulus essentially correspond to a Lorentzian function, and are related to the response of a damped harmonic resonator. In the ideal case of undamped resonances, the generic k_n is purely real and corresponds to a resonance frequency

$$f_n = \frac{k_n c_0}{2\pi}, \tag{1.18}$$

with c_0 the average speed of light in the medium filling the cavity.

In practice, dissipation mechanisms lead to the appearance of an imaginary part in k_n, whose amplitude is typically much smaller than the real part. This scenario of weakly damped resonances implies that the dissipation mechanisms can be treated as weak perturbations, by having the singularities of $\phi_n(\omega)$ not laying on the real axis any longer, requiring [R87]

$$k_n \rightsquigarrow k_n(1 - \mathrm{j}/Q_n), \tag{1.19}$$

where Q_n is the quality factor of the resonance associated to the n-th eigenfunction, or normal mode. The quality factors involved in electromagnetic reverberation chambers are very easily higher that several thousand units, so that the frequency of resonance can be regarded as unaffected by the introduction of losses, which thus behave as a weak perturbation.

The frequency evolution of a generic $\phi_n(\omega)$ is represented in Fig. 1.5, for several values of Q_n. While for an increasing Q_n the peak-value of $\phi_n(\omega)$ increases, the function becomes more tightly concentrated around its resonance frequency. The width of the modal response can be assessed by introducing the half-power modal bandwidth $B_{M,n}$

$$\frac{B_{M,n}}{f_n} \simeq \frac{1}{Q_n} \quad , \quad Q_n \gg 1. \tag{1.20}$$

which implies that the $\{\phi_n(\omega)\}$ essentially act as very effective narrow-band filters. A different way of looking at this result is to observe that each mode brings a non-negligible contribution limited to frequencies very close to the resonance frequency. It is therefore possible to associate a notion of locality to the spectral expansion; as it will be discussed in § 1.3, this interpretation has important consequences on the statistical modelling of the fields generated within large cavities, with direct impact on practical applications, as shown in §2.

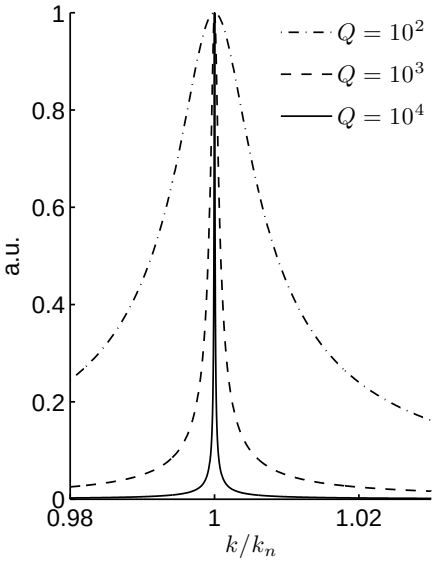

Figure 1.5 – Some examples of peak-normalized modal response $\phi_n(\omega)$, plotted against the normalized frequency k/k_n for a varying quality factor Q.

In a similar way, the electric energy $U(\omega)$ stored in a cavity at a single frequency can be expressed as

$$U(\omega) = \epsilon_0 \int_\Omega \|\boldsymbol{E}(\boldsymbol{r},\omega)\|^2 \mathrm{d}\boldsymbol{r} = \epsilon_0 \sum_{n=1}^{\infty} |\gamma_n|^2 |\phi_n(\omega)|^2, \tag{1.21}$$

having exploited the orthonormality of the eigenfunctions $\boldsymbol{e}_n(\boldsymbol{r})$. As a result of being a spectral expansion, the energy can be easily computed as a discrete sum rather than as an integral. The real-valued nature of (1.21) allows a simple graphical illustration, as proposed in Fig. 1.6: each mode contributes with a degree of freedom only for a narrow bandwidth around its frequency of resonance, thus implying that for a given working frequency only the few modes within this bandwidth will actively contribute to the overall field distribution. This maximum bandwidth, here referred to as B_e, allows estimating the number of degrees of freedom underpinning the field distribution within a cavity, as discussed in §§ 1.3.1 and 2.2. As demonstrated in [J4], B_e corresponds to the average modal bandwidth.

Hence, it is possible to approximate the infinite sum (1.21) by a finite one, limited to the set of M modes $\mathscr{M} = \{m : |f_m - f| < B_e/2\}$, i.e.,

$$U(\omega) = \epsilon_0 \sum_{m \in \mathscr{M}} |\gamma_m|^2 |\phi_m(\omega)|^2. \tag{1.22}$$

Clearly, the same line of reasoning can be applied to the overall electric field.

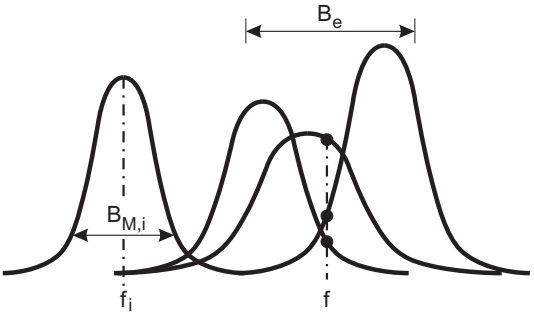

Figure 1.6 – A schematic illustration of the local contributions provided to the electric energy by each resonant mode within a cavity. Only the modes with a frequency of resonance within a distance $B_e/2$ from the working frequency actively contribute.

The idea of limiting the infinite summation (1.15) to a finite number of terms can be regarded as a fundamental advantage of the spectral expansion, allowing a reduced-order modelling of reverberating structures. But we deem that the main interest of this approach is the clear and natural appearance of the concept of degrees of freedom in a cavity: it is this concept that subtend all the results we have introduced during the last 4 years. In the rest of this chapter, these ideas will be largely invoked as a powerful yet simple way of drawing general conclusions about the behaviour of a cavity.

1.2.3 Black-box (empirical) statistical modelling

Before passing to the core of this dissertation, we need to introduce several ideas that constitute the foundation of the statistical modelling of wave propagation in complex media. It was already noted at the beginning of § 1.2.1 that Green's functions in analytical form are hardly available but for canonical configurations. Numerical approaches can be applied to compute Green's functions, but this implies a clear assumption : that the details of the system/medium in which we are interested are available. As strange as it could appear to a first reading, this is seldom the case. Examples abound, but we will stick to the case of cavity-like media: the case of indoor and urban propagation media is perhaps the first example that comes to mind to an electrical engineer, because of its omnipresence in wireless communication settings. Numerical approaches would be put in jeopardy by three very practical difficulties :

1. the geometrical details of the propagation medium are typically unknown : let just think of the position of furniture, walls, buildings, their geometrical dimensions, etc. ;
2. the electrical characteristics of the material making up the elements of the medium are also typically unknown;
3. even if these details were known, the Green's functions associated to the medium could be accessed only by means of numerical simulations. Since in practice indoor/urban setups span regions of space well larger than a wavelength, numerical models would involve a quickly untractable number of unknowns.

Clearly, these limitations do not mean that it is impossible to predict any trend in complex media, but that we should rather change our perspective in propagation modelling. We should ask ourselves what kind of information we really need in order to satisfyingly engineer a system based on the propagation of waves in complex media. As an example, in wireless communications the main issue is ensuring a given level of received power, i.e., a good coverage, with a given probability, rather than a perfect knowledge of the actual level at the receiver. In other words, a probabilistic approach is often sufficient.

As a result an alternative, and more importantly *viable*, approach is that of describing wave propagation in statistical terms. A number of statistical quantities can be defined to this effect; we will just introduce the most basic ones, as they will also be needed in the rest of this dissertation. Statistical descriptions often correspond to phenomenological approaches, where one can only assess the effects of the medium structure on wave propagation rather than the causes of specific behaviours. Data needed to the extraction of statistical models can be obtained from extensive measurement campaigns or parametric numerical simulations.

From the receiver point of view, the amplitude of the received signal is of paramount importance. Therefore it makes sense to study the probability density function $p_H(x, \omega)$

of the value x taken by the complex transfer function $H(\omega)$ between a transmitter and a receiver ports. In many practical configurations, this probability density function can be set beforehand, as soon as certain conditions are satisfied; an example is given by the family of media displaying Rice/Rayleigh statistics, requiring a diffusive propagation [R66]. More details about these ideas will be presented in § 1.4.

It is therefore possible to predict the probability of observing a given level at the receiver, even though hardly any detail of the propagation medium are known. The price to pay for this simplification is the difficulty of establishing/identifying any causal relationship between the physical parameters of the medium and the statistical properties of waves propagating through it: as a result, we are somewhat stuck with a functional approach that only allows blind design procedures. Other quantities of physical and practical interest can be modelled in this way, providing a large scope for this type of approaches: angles of arrival of waves and time-delay spread profiles are but two examples of interest in wireless communications [R84, R70].

Once probability density functions are introduced, any statistical moment can be computed for a quantity modelled as a random variable; for a random scalar variable $X \in \mathbb{R}$, the moment of order n is defined as

$$\langle X^n \rangle = \int X^n p_X(x) \mathrm{d}x, \tag{1.23}$$

where the integral is taken over all the possible random realizations of X, while $p_X(x)$ is its probability density function. The brackets notation will be used in the rest of this dissertation as a compact notation for averages computed over all the possible values taken by X. The first-order moment (average value) is instrumental to the definition of centered moments, where the zero mean-valued random variable $X - \langle X \rangle$ is now considered in (1.23) instead of X. The most widely used centered moment is certainly the variance, $\sigma_X^2 = \left\langle (X - \langle X \rangle)^2 \right\rangle$ and the associated standard deviation σ_X.

In the case of $X \in \mathbb{C}$, complex-valued moments can be considered, but in order to be assimilable to a distance, the Euclidean norm is typically used, i.e., $\sigma_X^2 = \left\langle |X|^2 \right\rangle$. A further generalization is needed when dealing with random vector quantities, e.g., noted as $\boldsymbol{X}$; the main modification is in moments greater than one, where they take the shape of n-rank tensors, where n is also the order of the statistical moment. We will just consider the case of the covariance matrix $\boldsymbol{C_X}$, defined as

$$\boldsymbol{C_X} = \left\langle (\boldsymbol{X} - \langle \boldsymbol{X} \rangle)(\boldsymbol{X} - \langle \boldsymbol{X} \rangle)^\dagger \right\rangle. \tag{1.24}$$

In practice, the random vector could be any vector transfer function, for instance the one relating the excitation signal applied to a transduced to the electric field it generates at a given position $\boldsymbol{r}$, i.e., $\boldsymbol{X} = \boldsymbol{H}(\boldsymbol{r}, \omega)$.

While $\boldsymbol{C_X}$ assesses the statistical dependence between the single scalar elements of vector $\boldsymbol{X}$, a similar idea can be introduced to study the global statistical dependence

of, e.g., the vector transfer functions observed at two different positions $\boldsymbol{r}_1$ and $\boldsymbol{r}_2$, introducing the spatial correlation

$$C(\boldsymbol{r}_1, \boldsymbol{r}_2) = \left\langle \boldsymbol{H}(\boldsymbol{r}_1, \omega)^\dagger \cdot \boldsymbol{H}(\boldsymbol{r}_2, \omega) \right\rangle, \tag{1.25}$$

often expressed as a function of the variances by introducing the spatial-correlation function

$$\rho(\boldsymbol{r}_1, \boldsymbol{r}_2, \omega) = \frac{\left\langle \boldsymbol{H}(\boldsymbol{r}_1, \omega)^\dagger \cdot \boldsymbol{H}(\boldsymbol{r}_2, \omega) \right\rangle}{\sqrt{\left\langle \|\boldsymbol{H}(\boldsymbol{r}_1, \omega)\|^2 \right\rangle \left\langle \|\boldsymbol{H}(\boldsymbol{r}_2, \omega)\|^2 \right\rangle}}, \tag{1.26}$$

with $|\rho(\boldsymbol{r}_1, \boldsymbol{r}_2, \omega)| \in [0, 1]$; in (1.26), $\boldsymbol{H}(\boldsymbol{r}, \omega)$ was assumed to have a zero average value. A spatial correlation close to one implies that though the field observed at two positions can still be modelled as two random variables, they essentially present a non-fully stochastic nature, with a partially deterministic relationship linking them. The simplest such representation is provided by a first-order regression model

$$\boldsymbol{H}(\boldsymbol{r}_2, \omega) \simeq \underline{\boldsymbol{T}}(\boldsymbol{r}_1, \boldsymbol{r}_2)\boldsymbol{H}(\boldsymbol{r}_1, \omega) + \delta\boldsymbol{H}(\omega), \tag{1.27}$$

where $\underline{\boldsymbol{T}}(\boldsymbol{r}_1, \boldsymbol{r}_2) \in \mathbb{C}^{3\times 3}$ (e.g., for a three-component vector field) is a dyadic operator, in general anisotropic, while $\delta\boldsymbol{H}(\omega)$ is a fully random process, independent from $\boldsymbol{H}(\boldsymbol{r}_1, \omega)$. In practice, the relative contributions of the deterministic and random parts in (1.27) are functions of the offset vector $\boldsymbol{d} = \boldsymbol{r}_2 - \boldsymbol{r}_1$, but this point is out of the scope of this dissertation.

Typically $\rho(\boldsymbol{r}_1, \boldsymbol{r}_2, \omega)$ depends only on the offset vector $\boldsymbol{d}$, while the absolute positions $\boldsymbol{r}_i$ affects only the scaling of the covariance through the field variances in (1.26). In this case, spatial correlation is virtually independent of the absolute position and will be expressed as $\rho(\boldsymbol{d}, \omega)$. The same ideas can be applied to other parameters on which $\boldsymbol{H}(\boldsymbol{r}, \omega)$ depends, most notably the frequency.

Spatial correlation and covariance are important since the use of probability density functions could suggest the modelling of wave propagation as a random process $\boldsymbol{H}(\boldsymbol{r}, \omega)$, where $\boldsymbol{r}$ and ω just act as parameters leading to independent random processes, i.e.,

$$\left\langle \boldsymbol{H}(\boldsymbol{r}_1, \omega) \cdot \boldsymbol{H}^\dagger(\boldsymbol{r}_2, \omega) \right\rangle \propto \delta(\boldsymbol{r}_2 - \boldsymbol{r}_1) \tag{1.28}$$

$$\left\langle \boldsymbol{H}(\boldsymbol{r}, \omega_1) \cdot \boldsymbol{H}^\dagger(\boldsymbol{r}, \omega_2) \right\rangle \propto \delta(\omega_2 - \omega_1). \tag{1.29}$$

Even in the case of very complex media, e.g., diffusive ones, correlations are typically present. These express physical mechanisms of varying nature: e.g., spatial correlation are always limited by the wavelength of propagating waves, effectively setting a minimum spatial resolution that is of fundamental importance when dealing with time-reversed signals (§ 3).

In practice, $\rho(\boldsymbol{d},\omega)$ is a smooth function of the distance $d = \|\boldsymbol{d}\|$ between the two observation points and typically characterized by an infinite support, i.e., it is never identically equal to zero beyond a given minimum distance (§ 1.4.1). It is nonetheless possible to define a minimum distance D_c, called the coherence distance [R93], beyond which the spatial correlation is always smaller than a given maximum value

$$D_c(\omega) = \min\left\{\boldsymbol{d} : |\rho(\boldsymbol{d},\omega)| < \rho_{\max}\right\}, \tag{1.30}$$

or, alternatively, as the distance at which the spatial correlation crosses the zero value for the first time when incrementing $\|\boldsymbol{d}\|$ from zero to infinity. The minimum in (1.30) is taken over the Euclidean norm of the offset vectors $\boldsymbol{d}$. Since the spatial correlation is typically anisotropic (§ 1.4.1), D_c should rather be expressed as a function of the direction $\hat{\boldsymbol{d}}$ linking $\boldsymbol{r}_1$ and $\boldsymbol{r}_2$; the maximum of all observed correlation distances can therefore be taken as

$$D_c(\omega) = \max_{\hat{\boldsymbol{d}}} D_c(\hat{\boldsymbol{d}},\omega), \tag{1.31}$$

and provides a simple manner of assessing the distance beyond which two samples of the field can always be approximated as statistically uncorrelated.

The correlation distance is at the basis of the definition of the coherence cell of a random field distribution, defined as the region of space

$$\mathscr{C} = \{\boldsymbol{d} : \|\boldsymbol{d}\| \leqslant D_c(\hat{\boldsymbol{d}},\omega)\}. \tag{1.32}$$

It bears important insight in statistical modelling, especially for phase-space representations [R93, R81], e.g., in the prediction of the number of spatial degrees of freedom of the field generated within a cavity [R50, R93]. Moreover, the presence of statistical correlation also has a major impact on any averaging method, as discussed in §§ 1.4 and 2.1. Spatial correlation appears in a number of configurations, of which the memory effect [R24] highlighted in wave-propagation through multiple-scattering media is just an example.

The fact that correlations involve two quantities leads to their being referred to as second-order statistics. We will neglect even higher order statistics, although they play a fundamental role in statistical field theories [R81].

These ideas can be directly transposed to the analysis of the correlation between field samples observed at two different frequencies, but over the same position in space. A coherence bandwidth can therefore be defined, which will play an important role in § 3.

1.3 Random spectral models

The modelling tools introduced in the two previous sections are somewhat extreme approaches, switching from the rigid framework of a perfectly detailed deterministic

representation to a black-box statistical description based on phenomenological observations, without any physical insight. In between them, there exists a class of statistical models based on the physical representation offered by the spectral models introduced in § 1.2.2.

Their rationale is very pragmatic. Spectral models are capable of capturing some important features, such as the existence of a discrete set of degrees of freedom, under the shape of resonant modes actively excited at the working frequency. While the precise value of the modal quantities introduced in (1.15) is typically not accessible, it is actually not always important to know the details of the field distribution, or of the frequency response of a complex medium. The main reason for this point of view is that it is simply not possible most of the time.

But there are more sensible reasons involving the fact that the geometry of the medium may change from one *random realization* to another, with these realizations still sharing some common features. A simple example is the case of cavities with exactly the same volume and nature of the boundaries, while presenting an infinite number of random realizations for their detailed shape. Similarly, families of cavities can be identified by the amount of average overall dissipation losses experienced by waves propagating through them, or a given geometry can be excited in an infinite number of ways by changing the position and orientation of a given group of sources. All of these examples share the idea of at least a common *macroscopic* feature which can be at the same time found in a large (ideally infinite) number of random and independent sub-configurations. In this case, it makes sense to wonder what would be the *average* behaviour of field-related quantities, as a function of the macroscopic parameters. For instance, it is of practical importance to understand how the behaviour of a cavity changes when its volume is increased. This kind of problem cannot be easily answered in either of the two extreme modelling approaches introduced so far; conversely, the approach presented in this section will be shown to be capable of providing insight even without knowing anything about the details of a single realization.

The origin of this idea of modelling the average behaviour of a complex system can be traced back to the work of J.C. Maxwell and L.E. Boltzmann about the statistical-mechanical explanation of the thermodynamical laws of gases [R83]. The problem they faced was very similar to ours: the dynamics of gases was studied by introducing the idea of an infinite number of collections of particles each one provided of a random position and velocity. The deterministic solution of such a system was and still is practically impossible, but for the sake of thermodynamical laws it was not a matter of importance. The *microscopic* details of the state of each particle is not the focus in this context, whereas the *average* state of the system is fundamental, particularly if related to *macroscopic* quantities such as the temperature, volume or pressure of the system. The idea of an *ensemble* was therefore introduced as a clever way of bypassing a complex problem, allowing to extract still useful information from first-principle laws coupled to a statistical analysis. A more recent and complex example of interest in our discussion is that of wave chaos (see § 1.3.2), where the focus is set on the properties

of eigenvalues, rather than of field-related quantities [R81].

In a similar manner, the microscopic degrees of freedom in a spectral representation are the modes, or energy levels in quantum mechanics, of the system. Their state is now modelled by their modal coefficients, while the equivalent of the macroscopic features are the overall electric field observed at a given position. The analogy could be thought as complete, but there is a fundamental difference that still generates much confusion and misunderstanding: the number of degrees of freedom in the case of gases is simply huge, with orders of magnitude set by Avogadro's number; comparing this number to the few modes typically excited within a cavity (as discussed in § 1.3.1) under a harmonic steady state should appear as a formidable obstacle to the application of the ideas of statistical physics to the case of cavities. Unfortunately, because of the lack of simpler alternative approaches, this problem is often not acknowledged, leading to expectations that are simply not realized in practice; examples will be presented from the field of electromagnetic compatibility in the next chapter.

This mismatch was the motivation of some of the analyses that we have carried out, where the focus was on a specific macroscopic parameter, namely the number of degrees of freedom actually available in a cavity. As discussed in the next chapter, things get even more confused by the fact that it is not even the availability of a large number of modes that enables diffuse-field approximation (see § 1.4.1) but rather the overlapping of their frequency responses. This type of questions can be very effectively answered by means of a statistical analysis of (1.15).

In order to enable these results, the modal quantities in (1.15) are modelled as random variables, hence the idea of random spectral models. Randomness can originate on a number of levels

- frequencies of resonance $\{f_n\}$: their number, position and interdistance;
- modal topographies $\{\boldsymbol{e}_n(\boldsymbol{r})\}$: changing boundary conditions, through material and/or geometry modifications or displacements (e.g., of scatterers);
- modal coefficients $\{\gamma_n\}$: a direct consequence of randomness in the sources $\boldsymbol{J}_e(\boldsymbol{r})$ and/or the modal topographies, as implied by (1.16).

Modelling any of these parameters as random variables requires the definition of suitable probability density functions capable of capturing the variations observed in practice due to randomness. In certain cases, it is possible to justify these choices on the basis of physical models, such as in the case of elementary excitations of the kind

$$\boldsymbol{J}_e(\boldsymbol{r},\omega) = \boldsymbol{J}_0(\omega)\delta(\boldsymbol{r}-\boldsymbol{r}_0), \tag{1.33}$$

where $\boldsymbol{r}_0$ is the randomly chosen position of the current; the modal coefficients defined in (1.16) are therefore given by

$$\gamma_n = \boldsymbol{J}_0(\omega_n)\cdot\boldsymbol{e}_n(\boldsymbol{r}_0), \tag{1.34}$$

corresponding to a random sampling of the modal topographies. In the case of canonical geometries for the cavity boundaries, these functions are known, so that setting the probability density function of the random position $\boldsymbol{r}_0$ can be readily translated into the probability density function of the random modal coefficients.

In most cases, though, this physically-based procedure is not feasible, forcing to choose axiomatic distributions. An example is given by the assumption of Gaussian-distributed modal coefficients, which is typically regarded as reasonable when assuming an ensemble of cavities: randomness is here justified on the impossibility to know the exact modal topographies.

Without going into the details of this issue, recalling the statistical convergence ensured by the central limit theorem in presence of a *large* number of independent and identically distributed (iid) random contributions implies that whatever choice made for the individual (microscopic) contributions would inevitably lead to the same kind of overall probability distribution. The actual difference in the choice of the probability distributions of the modal coefficients (and similarly for other parameters) has an impact only on the dispersion of the overall field, not on its statistical nature. For this reason we do not attach a great importance on the choice of the microscopic-level probability density functions, as long as this choice is not motivated on physical grounds, but rather presented as axiomatic.

A counterexample is discussed in § 1.3.2, where random-matrix theory results provide physical-based, though asymptotic, probability laws for the spacing that should be expected between two consecutive frequencies of resonance.

It is fundamental to take into account the actual conditions of operation of a cavity before applying any assumptions on the probability laws underpinning the modal parameters. An example is given by the case of a cavity with a fixed geometry, where the observer position can be regarded as random; if we were interested in studying the average field intensity observed, while treating the modal parameters as random variables, only a single random realization should be considered to represent the electromagnetic behaviour of the entire cavity. In this case there is no ensemble of cavities, since the problem is centered around the statistics of the field for a given cavity geometry, rather than the average behaviour expected for a group of cavities sharing the same macroscopic quantities. We should therefore consider two levels of randomness:

1. a single realization for the random modal coefficients;

2. a random ensemble for the position of observation of the field.

The second point will therefore be at the basis of the computation of the average field intensity, being the only random variable that could be expected to change. Ensemble averages should be applied only when dealing with a different problem, e.g., when computing the average field intensity observed within *any* cavity with a given volume.

In this case, an ensemble average should also be computed across all the possible realizations of the modal coefficients, as dictated by the random boundaries underpinning the concept of an ensemble of random cavities.

This apparently superfluous difference has important consequences when dealing with the estimation of the number of degrees of freedom available within a cavity and will be at the center of § 1.4.2, when considering the asymptotic validity of the diffuse-field approximation.

In the following sections we present further information about the use of this kind of approach, particularly for what concerns the use of random-matrix theory as a tool for predicting modal statistics. The notions here discussed are then applied to the question of modal-coefficient independence and to the fundamental problem of how to assess the degrees of freedom in a cavity, in view of the application of the diffuse-field approximation (see § 1.4.1).

1.3.1 Modal density and overlapping

When thinking about the modal density, one intuitively associates it to a certain number of modes resonating around the working frequency. The modal density can therefore be defined as the average number M_B of modes found in a bandwidth B,

$$m_B(f) = \frac{M_B(f)}{B}, \tag{1.35}$$

and is therefore dependent on B itself. As long as B is large enough to encompass several modes, then (1.35) is an average value that can be expected to converge to a single value, for B large enough, predicted by Weyl's approximation [R86]

$$m_{\mathrm{W}}(f) = \frac{8\pi V}{c_0^3} f^2 + o(f) = \frac{8\pi V_\lambda}{f} + o(f), \tag{1.36}$$

with V the volume of the cavity, c_0 the speed of light in the filling medium and V_λ the volume measured in cubic wavelengths.

The definition (1.35) provides a more general framework than (1.36), since the modal density is considered in a local setting: for this reason, it will be referred to as the local modal density, associated to a specific bandwidth.

It is often practical to associate a specific value to the modal density $m(f)$, e.g., by taking the limit for $B \to 0$: the discrete nature of the set of frequencies $\{f_i\}$ at which a cavity resonates implies that in practice $m(f)$ can only take two values, i.e., zero if no mode resonates at the working frequency f or infinity otherwise [R81], i.e.,

$$m(f) = \lim_{B\to 0} m_B(f) = \sum_{i=1}^{\infty} \delta(f - f_i). \tag{1.37}$$

This outcome is inevitable as the distribution of the normal modes cannot approach the completeness of real numbers, thus leaving inevitable "gaps" between them.

The estimate $m_{\mathrm{W}}(f)$ is in general different from $m_B(f)$ because it is not derived as in (1.37), but in a less direct manner, by first introducing the function $N(f)$ describing the overall number of modes of a cavity up to the frequency f

$$N(f) = \#\{f_i : f_i \leqslant f\}, \tag{1.38}$$

with # the cardinality of a set. This function can be represented as the sum of a smooth approximation $N_{\mathrm{W}}(f)$ and a fluctuating function $N_{\mathrm{f}}(f)$ with zero average value

$$N(f) = N_{\mathrm{W}}(f) + N_{\mathrm{f}}(f). \tag{1.39}$$

This smooth approximation was first derived by Weyl and was intended to provide an approximate solution asymptotically exact at infinite frequency [R86]. The fact that the intensity of the residual fluctuations grows less quickly than $N_{\mathrm{W}}(f)$ as $f \to \infty$, thus ensuring

$$\lim_{f\to\infty} \left| \frac{N_{\mathrm{f}}(f)}{N_{\mathrm{W}}(f)} \right| = 0, \tag{1.40}$$

should not be mistaken for an indication that modal density can be defined as often done, by taking the derivative of $N_{\mathrm{W}}(f)$ at the working frequency f, leading to the approximation

$$m(f) = \lim_{B\to 0} \frac{M_B}{B} \cong \frac{\mathrm{d}N_{\mathrm{W}}(f)}{\mathrm{d}f} = m_{\mathrm{W}}(f). \tag{1.41}$$

As a matter of fact, the residual $R_m(f) = |m_{\mathrm{W}}(f) - M_B/B|$ does not converge to zero, since $N_{\mathrm{f}}(f)$ takes on the discrete nature of $N(f)$, thus preserving the results in (1.37). It could be expected that the accuracy of the approximation (1.41) improves as the frequency, and thus $N(f)$, increases, hence leading to modes getting close enough to provide a sort of approximate continuity; unfortunately, this is not the case and these fluctuations should not be dismissed as minor approximation errors, particularly when the average number of overlapped modes is not high enough, as happens to be the case even at frequencies well above the lowest usable frequency (or LUF) as usually defined by thumb rules proposed in practice within the framework of EMC tests [R2].

The differences between $m(f)$ and $m_{\mathrm{W}}(f)$ play a central role when studying the average local modal overlapping $M_{\mathrm{loc}}(f)$. This quantity represents the average number of modes found within a bandwidth B_M equal to the average -3 dB width of a mode, i.e., $B_M = f/\bar{Q}$, hence

$$M_{\mathrm{loc}}(f) = m_{B_M}(f) \frac{f}{\bar{Q}(f)}, \tag{1.42}$$

with $\bar{Q}(f)$ the ensemble-average composite quality factor of a MSRC.

As proven in [J4], a high modal density in itself is not a guarantee of a diffuse field, ensuring Gaussian-distributed scalar field components; the dominant parameter is rather $M_{\mathrm{loc}}(f)$, which is required to be $M_{\mathrm{loc}}(f) \gg 1$ in order to support a diffuse field. Therefore, it makes more sense to directly count the number of modes overlapping over B_M, rather than passing through (1.42), since it requires an estimate of the local modal density $m_{B_M}(f)$, as defined in (1.35). This apparently subtle distinction makes all the difference and should not be underestimated: it could seem more natural to assume $m_{B_M}(f) \simeq m_W(f)$ and derive $M_{\mathrm{loc}}(f)$ from (1.42), i.e.,

$$M_W(f) = \frac{8\pi V_\lambda}{\bar{Q}(f)} + o(1), \tag{1.43}$$

assuming

$$M_{\mathrm{loc}}(f) \simeq M_W(f), \tag{1.44}$$

but in this way we would implicitly accept the notion of a deterministic and smoothly increasing modal density, with no random fluctuations, with an $m_W(f)$ not depending on B_M, thus neglecting the discrete nature of the distribution of the frequencies of resonance. On the other hand, it is tempting to just consider the average modal density (and overlapping), since in practice the ensemble-average of $m_{B_M}(f)$ can be quite close to $m_W(f)$; as discussed in § 2.3, such an approximation directly leads to a fundamental misunderstanding about the origin of statistical anomalies, or outliers, originated by strong random fluctuations in the modal density expected for single realizations of the cavity.

When directly considering the number of modes overlapping over B_M, the corresponding modal density should rather be defined as in (1.35), with an implicit local definition depending on B_M. In practice, (1.35) is an average modal density, but in this context the average is not over the realizations (ensemble average), but rather over the bandwidth B_M for a single realization. In other words, it represents a sort of locally homogenized modal density, spread equally over the entire modal bandwidth B_M rather than as a set of singularities as in (1.37). For this reason, we will refer to it as a *local* average, in contrast with the *ensemble* average. It will be shown in § 2.3 that this apparently redundant distinction makes a big difference.

We can already consider a representative example shown in Fig. 1.7, where the modal density predicted by (1.36) is compared to a direct count of the number of modes within a 1 % and 0.1 % relative bandwidths for a cuboid cavity. As stated at the beginning of this section, the local modal density is well approximated by (1.36) when dealing with relatively large local bandwidths; but when recalling that the modal bandwidth is typically very narrow, large fluctuations naturally appear. In order to have access to the probability density function of the local modal density, results from random-matrix theory are needed, as presented in § 1.3.2; the consequences of these results will be discussed in § 2.3.

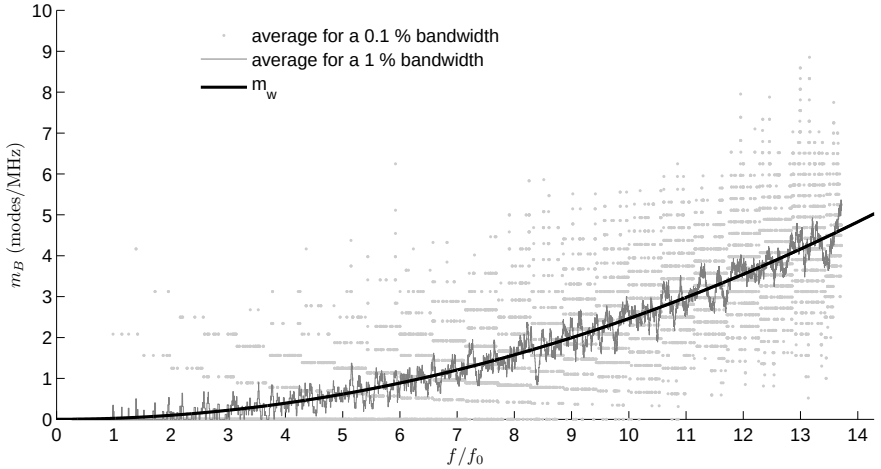

Figure 1.7 – Local modal density for a cuboid cavity characterized by a fundamental resonance at f_0, averaged over 0.1 % and 1 % relative bandwidths. The thick black curve is the result predicted by deriving Weyl's approximation (1.36). The relative bandwidth over which the average modal density should be computed is rather $1/\bar{Q}$, which is usually much smaller than the 0.1 % value here considered. Much stronger fluctuations should be expected in this case, making their graphical representation by far less clear.

1.3.2 Some elements of random-matrix theory

This short summary is certainly not intended to serve as an introduction to random-matrix theory (RMT) and the interested Reader should refer to the first three chapters in Stöckmann's seminal book [R81]. Nonetheless, we will give a brief overview of the reasons why we can apply in practice the results derived in the context of quantum chaos to our problem of field statistics in mode-stirred reverberation chambers.

RMT was developed to deal with structures where a direct solution of Schrödinger equation is regarded as complex or simply ill-defined, e.g., when the Hamiltonian operator is unknown. This is the case for complex quantum structures, such as large nuclear compounds or mesoscopic structures (e.g., quantum dots). A solution to this type of problems was found by approximating the unknown Hamiltonian operator by means of a matrix, eventually of asymptotic infinite dimensions, whose entries are assumed to follow specific probability distributions [R92]. This idea is directly related to a previous and very successful approach, namely statistical mechanics, where in a similar manner the problem of studying the (thermo)dynamics of a large collection of interacting particles was solved by considering a random description of the state variables of the particles. The drive in these approaches is not having a fine-level information of the system at the scale of the individual elements it is composed of: the focus is rather on its macroscopic behavior, described by means of statistical quantities related to the sta-

tistical moments of physical quantities of interest and in general by means of probability distribution functions.

RMT has been widely successful in this respect, and at least in its basic idea surprisingly simple; the same cannot be said for the mathematical details. The structural similarity existing between Helmholtz and Schrödinger equations has motivated studies comparing the results predicted by RMT to those observed in microwave experiments [R82]. It is important to notice that a major difference between these two equations is the absence of an Hamiltonian operator in Helmholtz equation: the structure is the same, but the lack of an Hamiltonian hinders the drawing of a direct parallel between the two equations. It is for this reason that the application of RMT to cavities where classical waves (of any nature) propagate had virtually to wait for a fundamental piece of work, namely the Bohigas-Giannoni-Schmidt conjecture [R6], where it was postulated that the results of RMT should apply to any complex system. A number of experimental validations have confirmed this conjecture, which is today widely accepted as a physical fact. Of particular interest for the EMC community are the works dealing with microwave cavities, i.e., unstirred reverberation chambers, where the accuracy of the prediction of RMT was proven beyond any doubt (e.g., [R82]).

The rationale behind recalling these points is that the nomenclature used in RMT is somewhat cryptic, with definitions that make sense in the context of quantum chaos without having any correspondence in classical wave theory. The apparent validity of the Bohigas conjecture allowed a direct transfer of the RMT ideas from the former to the latter, hence the potentially confusing terminology.

In this framework, we need to recall that RMT is based on universality classes allowing to define fundamental symmetry properties of the random matrix approximation of the Hamiltonian, according to fundamental physical properties of the system under consideration, e.g., energy conservation, reciprocity, etc., independently from the fine details of the system. In this respect, we will consider two configurations of practical interest, the case of integrable systems, also referred to (improperly) as the Poissonian ensemble [R5], and that of the Gaussian Orthogonal Ensemble (GOE) [R81], characterized by time-reversal invariance, i.e., energy conservation. A precise definition of the first class is apparently not yet available outside the context of quantum chaos, but the analogy with microwave structures is still maintained. The important point to consider is that under the category of integrable systems is considered any system that do not present any trace of the features of wave-chaotic systems, in particular level repulsion and of course exponential sensitivity to initial conditions. In practice, the fact that frequencies of resonance can cross each other's path when a dynamical perturbation (stirring) is operating, is a direct measure of absence of a fully chaotic behavior. Integrable systems are actually regarded as an extreme case of non-chaotic systems, whereas in practice a certain amount of chaos is often observed [R29]. In practice, completely empty rectangular cuboid cavities are a good example of integrable systems, while the inclusion of a scatterer spurs partially chaotic responses as soon as its dimensions are comparable to the wavelength. The GOE provides the other extreme representation for

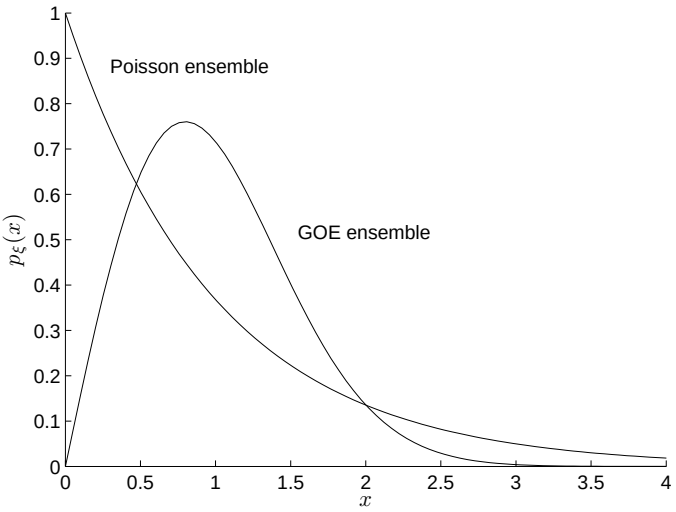

Figure 1.8 – Nearest-neighbor spacing probability density functions for an integrable and a GOE system, normalized to the ensemble-average spacing.

the ideal case of a fully chaotic system. It should be clear that the notion of integrable system is by no means related to the idea of degeneracy in the frequencies of resonance of a cavity, as in the case of an empty rectangular cavity with widths in rational proportion. Even in the case of irrational ratios, such a system will present the same behavior than any other integrable system.

We will limit our analysis to the modal spacing, defined as

$$s_i = f_{i+1} - f_i, \tag{1.45}$$

where s_i can be regarded, according to RMT, as the i-th realization of a random variable s, the probability density functions of the normalized nearest-neighbor spacing $\xi = s/\bar{s}$, with $\bar{s} = 1/m_\mathrm{W}$ the average nearest-neighbor spacing between adjacent modes, are [R81]

$$p_\xi(x) = \mathrm{e}^{-x}, \tag{1.46}$$

for a Poisson ensemble and

$$p_\xi(x) = \frac{\pi}{2} x \mathrm{e}^{-\pi x^2/4}, \tag{1.47}$$

for the GOE case. We are thus confronted to either an exponential distribution or a Rayleigh one with a parameter $\sigma^2 = 2/\pi$. These two functions are plotted in Fig. 1.8 where it is clear that the nil probability of superposed modes in chaotic systems is a direct consequence of level repulsion.

Two major differences can be noticed in these functions and will have a major impact on the statistics of the local modal density (see § 1.3.1): 1) for chaotic systems, the modal spacing is decidedly less dispersed than for an integrable system, with a probability distribution presenting a mode (peak) close to the average spacing $\xi = 1$; 2) for

an integrable system, it is clear that modes can come in clusters due to a high probability of superposition [R5], so that in order to maintain a fixed average spacing, the clusters must be relatively isolated one from the other, as justified by the longer exponential tail. We can refer to this phenomenon as modal depletion, i.e., the local lack of resonant modes, and it can be conjectured that the probability of incurring into what are often regarded as outliers [R42] can be explained by this phenomenon. In other words, it is a natural and inevitable phenomenon in an integrable system, whereas it should be expected to be less likely in chaotic systems.

According to the type of system we are dealing with, a higher probability of observing a wider nearest-neighbor spacing has a direct impact on the number of modes that can be observed in a fixed bandwidth, as will be recalled in § 2.3.

As already recalled, practical systems are often in between these two extreme configurations, although a Poisson ensemble behavior should be expected in the lower frequency range when dealing with rectangular cavities: this result holds as long as eventual scatterers in the cavity are electrically small, after which the system moves gradually towards a chaotic one, as shown experimentally in [R82]. Several methods have been devised to assess the degree of chaoticity of a cavity: in the context of this work, we will restrict our discussions and computations to the two extreme classes already introduced.

RMT is an asymptotical theory capable of accurately predicting the statistical properties of the spectrum of a system (here the frequencies of resonance of a cavity) as long as it permits a sufficiently large number of stable states. It should be clear that RMT cannot pretend to be exact when the electrical dimensions of a cavity become small, i.e., in its lower frequency range where it mainly behaves as a high quality factor resonator, allowing only a very limited number of resonances. Hence, RMT can be applied successfully even at frequencies below the LUF, since the modal density is typically high enough to justify a statistical description.

1.3.3 Correlation of the modal coefficients

Random spectral models are typically based on axiomatic assumptions on the probability density functions of the modal parameters. A further difficulty is deciding whether these parameters should be regarded as independent random variables or correlated ones. This issue has been the focus of theoretical investigations for the frequencies of resonance, as discussed in the previous section; conversely, modal coefficients are typically assumed to be independent without any proof: e.g., see [R90].

The random nature of the modal coefficients can appear due to a number of random processes, of which the random positioning and orientation of a source is of practical interest. This problem has recently been considered in [J8], where the source was assumed to have no impact on the modal topographies of the cavity under analysis; this assumption allows separating the randomization effects of changing boundary conditions due to moving sources, from those of the modification of the modal coefficients

for a changing set of equivalent current distributions. In practice, these two phenomena are intertwined and cannot be separated. The question asked here is whether a random positioning of the current distributions is sufficient to assume uncorrelated modal coefficients.

The analysis presented in [J8] is based on the statistical analysis of the projection (1.16), and more specifically on the computation of its covariance matrix elements

$$\sigma_{ij}^2 = \langle \gamma_i \bar{\gamma}_j \rangle, \tag{1.48}$$

where the independence assumption implies $\sigma_{ij}^2 = \sigma_\gamma^2 \delta_{ij}$. The use of a common variance σ_γ^2 translate the assumption of a uniformly sharing of the total energy over all of the available modes, which is reasonable in the case of an ensemble of sources, as it is the case here, since the changing nature of the source can be expected to sweep all of the positions/orientations that will lead to an effective excitation of all the modes with the same intensity.

In practice, recalling (1.16)

$$\sigma_{ij}^2 = \int_\Omega \mathrm{d}\boldsymbol{r}\ \boldsymbol{e}_i^\dagger(\boldsymbol{r}) \cdot \int_\Omega \mathrm{d}\boldsymbol{r}'\ \underline{\boldsymbol{C}}(\boldsymbol{r},\boldsymbol{r}') \cdot \boldsymbol{e}_j(\boldsymbol{r}), \tag{1.49}$$

where $\underline{\boldsymbol{C}}(\boldsymbol{r},\boldsymbol{r}')$ can be referred to as the coupling dyad, defined as

$$\underline{\boldsymbol{C}}(\boldsymbol{r},\boldsymbol{r}') = \left\langle \boldsymbol{J}_e(\boldsymbol{r}) \boldsymbol{J}_e^\dagger(\boldsymbol{r}') \right\rangle. \tag{1.50}$$

The coupling dyad is basically the covariance matrix of the scalar components of the current distribution of the sources, submitted to random orientation and positioning. Since the coupling dyad operates in (1.50) as a kernel weighting in the orthonormality relation (1.14), the condition (1.48) would be valid as soon as the inner integral in (1.49) did not alter the modal topographies $\boldsymbol{e}_j(\boldsymbol{r})$.

In [J8], it was shown that this requirement is satisfied for a coupling dyad with spherical symmetry (isotropy), unpolarized, i.e., diagonal, and invariant with respect to the space variables. These conditions are satisfied only when the position and orientation of the sources have no preferential value over the entire set of possible positions and orientations.

Since these conditions are typically valid in practice, particularly in EMC reverberation chambers, equipped with complex-shaped stirrers acting as source randomizers, the modal coefficients can be assumed to be uncorrelated. The extension to independence is less trivial but can be simplified by recalling that if the modal coefficients could be modelled as Gaussian-distributed random variables, then uncorrelation would rhyme with independence. It happens that this assumption is systematically taken for granted [R90], but without any formal proof, to the best of our knpowledge. In fact, this assumption is formally correct only in the case of chaotic ensembles [R81]. We will not go further on this topic, but it is clear that the actual statistics of the modal coefficients are far from a closed subject of investigation.

1.4 Random plane-wave spectra

A close observation of (1.15) shows that the main limitation of random spectral models is the absence of information about the behaviour of the modal field topographies $\{\boldsymbol{e}_n(\boldsymbol{r})\}$; while this is not a fundamental problem when modelling the field behaviour at one single position, it hinders any attempt at extrapolating its spatial evolution. Spatial-related quantities are of interest in a number of applications, but for the special case of EMC, spatial uniformity is the main quantity of interest.

The main approach used to cope with this issue consists in extending the random spectral approach to modal topographies. The eigenfunctions $\{\boldsymbol{e}_n(\boldsymbol{r})\}$ are now regarded as random processes, by treating them as random functions of the spatial coordinate $\boldsymbol{r}$; more generally, a space-frequency approach can be applied, modelling the eigenfunctions as random functions of the 4-dimensional coordinate $(\boldsymbol{r},\omega)$. This type of description is reminiscent of the statistical modelling discussed in § 1.2.3, where physical phenomena are no more directly accessible but behave as a hidden-variable model where only a few observables allow to probe the underlying physics of the system by observing its behaviour.

How to proceed with this further approximation? The simplest approach consists in expanding the modal topographies $\{\boldsymbol{e}_n(\boldsymbol{r})\}$ into a suitable basis of functions, i.e., a further spectral expansion. The main difference with respect to what we did in § 1.2.2 is that this new basis need not present any specific physical significance as it was the case when using the eigensolutions of Helmholtz equation. In that case the modal expansion bore physical significance and naturally yielded the concept of degrees of freedom associated to the number of resonant modes.

This further expansion is rather a mathematical technique to simplify the description of random processes depending on a multidimensional variable, the modal topographies. In this respect, any choice of basis functions is equivalent, as long as they are capable of effectively representing realistic modal topographies. Among the several potential candidates that are up to this task, the Fourier basis is perhaps the simplest option. First of all, it is likely the most widely studied basis, with a number of specific properties relating spatial and spectral representations [R59, R61]. Second, the spatial and spectral representations of a vector function, respectively $\boldsymbol{g}(\boldsymbol{r})$ and $\tilde{\boldsymbol{g}}(\boldsymbol{k})$ are linked through a Fourier-transform pair,

$$\boldsymbol{g}(\boldsymbol{r},\omega) = \mathscr{F}^{-1}\{\tilde{\boldsymbol{g}}\}(\boldsymbol{r},\omega) = \int_{\mathbb{C}^d} \tilde{\boldsymbol{g}}(\boldsymbol{k},\omega)\mathrm{e}^{-\mathrm{j}\boldsymbol{k}\cdot\boldsymbol{r}}\mathrm{d}\boldsymbol{k} \tag{1.51}$$

$$\tilde{\boldsymbol{g}}(\boldsymbol{k},\omega) = \mathscr{F}\{\boldsymbol{g}\}(\boldsymbol{k},\omega) = \int_{\mathbb{C}^d} \boldsymbol{g}(\boldsymbol{r},\omega)\mathrm{e}^{+\mathrm{j}\boldsymbol{k}\cdot\boldsymbol{r}}\mathrm{d}\boldsymbol{r}, \tag{1.52}$$

with d the dimensionality of the space in which the cavity is defined. The availability of numerical codes based on fast Fourier transforms implies that this choice is numerically efficient.

Third, the Fourier kernel does have a direct physical meaning of interest : it represents a plane wave propagating along the direction $\boldsymbol{k}$ corresponding to the a propagation constant $\|\boldsymbol{k}\|$. This fact is one of the main reasons for its large use in the modelling of wave-propagation phenomena, from Fourier optics [R57] to X-ray diffraction from crystals [R28]. This property is of fundamental importance for the understanding of the phenomena occurring within a cavity, as discussed in the next chapter: multiple-incidence scenarios become apparent through the use of Fourier basis. Fourier spectra applied to functions of the spatial variable are therefore typically referred to as plane-wave spectra (PWS), where the original function is represented as a superposition of plane waves propagating along a set of directions [R12].

Finally, plane-wave spectra allow a direct access to the physical phenomena underpinning the appearance of resonant patterns, i.e., the modal topographies as discussed in § 1.4.2.

Getting back to the idea of using the Fourier kernel as a complete basis, we need to acknowledge that this is a complete basis capable of representing any field distribution only if the entire domain of the spectrum if accessible, i.e., any value of the variable $\boldsymbol{k}$. In practice, the value taken by $\boldsymbol{k}$ provides important physical information about the nature of the plane wave associated: the spherical surface defined by $\|\boldsymbol{k}\| = k_0$ identifies a subregion of the reciprocal space representing plane waves propagating at the speed of light set by the medium filling the cavity. Other values cannot be associated to propagating waves, but are rather related to the reactive components of the spectrum [R12], thus localized to a region of space attached to sources, primary or secondary (scatterers). It is therefore reasonable to assume a plane-wave spectrum mainly composed of propagating contributions, i.e.,

$$\tilde{\boldsymbol{e}}_n(\boldsymbol{k}) = \mathring{\boldsymbol{e}}_n(\hat{\boldsymbol{k}})\delta(k - k_0), \tag{1.53}$$

where it is sufficient to specify the direction of propagation of the plane waves, since they all share the same wavenumber k_0. The function $\mathring{\boldsymbol{e}}_n(\hat{\boldsymbol{k}})$ therefore contains the entire information needed to reproduce the original spatial distributions, as

$$\boldsymbol{e}_n(\boldsymbol{r}) = \int_{4\pi} \mathring{\boldsymbol{e}}_n(\hat{\boldsymbol{k}}) \mathrm{e}^{-\mathrm{j}k_0\hat{\boldsymbol{k}}\cdot\boldsymbol{r}} \,\mathrm{d}\hat{\boldsymbol{k}}. \tag{1.54}$$

Being solely dependent on the angular direction $\hat{\boldsymbol{k}}$, $\mathring{\boldsymbol{e}}_n(\hat{\boldsymbol{k}})$ is sensibly referred to as the angular spectrum in some texts.

Although (1.51) seems to suggest that the plane-wave spectrum of the overall field distribution can be directly accessed from the original spatial distribution, it should be clear that there is a mismatch: Fourier-transform pairs are defined for an infinite support, whereas field distributions can only be defined within the cavity itself. Direct application of a spatial Fourier transform as done in (1.51) would require a continuation of the spatial distribution to the outside of the cavity. The choice of setting the

outside field to zero would imply an extended discontinuity over the frontier of the cavity, which would be translated in the plane-wave spectrum through the appearance of reactive components, required to represent local discontinuities, thus leading to fictive contributions to the spectrum. While the passage from the plane-wave spectrum to the spatial distribution can be carried out by means of a Fourier transform, the opposed passage is much more critical and requires estimation methods not relying on the orthonormality of the Fourier kernel, such as those at the base of MUSIC and ESPRIT algorithms [R71, R68].

We have introduced these tools and ideas in the first place to cope with our inability to predict the eigenfunctions $\{\boldsymbol{e}_n(\boldsymbol{r})\}$. Defining a plane-wave spectrum representation can be a simpler task, since the entire spatial distribution is now captured by a set of coefficients, potentially finite (see § 2.1). The question is how to choose a plane-wave spectrum in such a way as to represent a realistic field distribution in a complex medium? Two answers will be considered in § 1.4.1 and § 1.4.2, both relying on wave propagation in media complex enough as to make the idea of a random ensemble acceptable.

1.4.1 Diffuse-field approximation

The first solution to the problem of modelling the field distribution in a complex media is based on a very pragmatic observation. Let us consider a medium structured in such a way as to force any incoming wave to undergo a very large number of scattering phenomena. Reverberating cavities are an example of such media, but it is more intuitive to consider the example given in Fig. 1.9, where scatterers of lateral dimensions well smaller than a wavelength are distributed in a random manner. Randomness is here required in order to avoid the appearance of a discrete set of eigensolutions, or propagation modes, that would be possible in the case of periodic structures [R8].

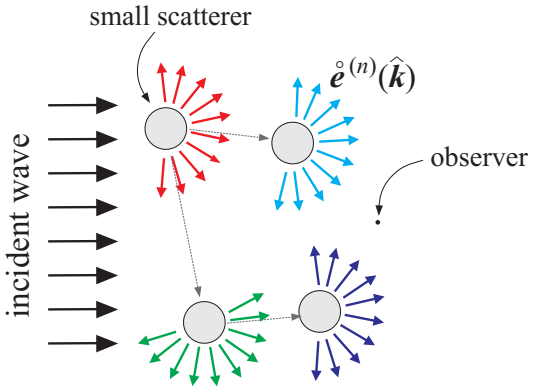

Figure 1.9 – A multiple-scattering propagation scenario, due to the presence of a large number of small scatterers interacting with each other, excited by a single incident wave. Each scatterer contributes to the overall non-coherent field with an elementary plane-wave spectrum.

When dealing with this kind of media, as an incoming plane wave interacts with the first scatterers the portion of the wave directly affected by each scatterer will be dis-

tributed over a continuous set of directions through Rayleigh scattering [R38]. Each scattering interaction can effectively be represented through plane-wave expansions, as schematically depicted in Fig. 1.9, making each scatterer a secondary source of plane waves propagating along a larger number of directions than the original one, with each event yielding a contribution $\mathring{\boldsymbol{e}}^{(n)}(\hat{\boldsymbol{k}})$ to the overall plane-wave spectrum.

This scenario is reiterated for all of the scatterers, intuitively leading to a pragmatic conclusion: in a medium presenting a number of scattering events large enough, with potentially multiple-interaction events (see Fig. 1.9), an observer deep enough within the medium would be unable to identify the direction of arrival of the original wave, since exposed to a very large number of waves providing each one a fraction of the original energy, propagating along any possible direction of arrival. This concept is usually referred to as diffuse-field approximation and it has a prominent role in wave propagation through complex media, from stellar nebulae to ultrasound imaging [R38].

Modelling the complex amplitudes of the overall plane-wave spectrum as a collection of iid random variables, this state of propagation can be defined by the observation that the Poynting vectors $\boldsymbol{S}_i$ of each wave satisfy the following conditions, similarly as to what is done in the analysis of percolation [R56]

$$\| \langle \boldsymbol{S}(\omega) \rangle \| \ll \sqrt{\langle \| \boldsymbol{S}_i(\omega) \|^2 \rangle} \tag{1.55}$$

with

$$\boldsymbol{S}(\omega) = \sum_i \boldsymbol{S}_i(\omega), \tag{1.56}$$

implying that the net flux of power across any surface is negligible with respect the root-mean-square flux contributed by each wave.

The passage from a relatively unperturbed free-space-like propagation to a diffuse-field one implies some sort of spatial transient; this problem is at the core of the radiative-transfer theory, first introduced to understand how light propagating through stellar nebulae is affected [R10]. In the context of this dissertation, our interest will be limited to the properties of diffuse-field propagation under a spatial steady-state condition, i.e., when the field has lost any trace of the original coherence of the incoming wave.

This approximation allows a strong simplification of the problem that has led us to use plane-wave spectra in order to represent modal topographies. To understand them, let recall that under a diffuse-field approximation the overall field is expressed as a superposition of the contributions generated by an infinite number of scattering events (see Fig. 1.9)

$$\boldsymbol{E}(\boldsymbol{r}, \omega) = \sum_{n=1}^{\infty} \int_{4\pi} \mathring{\boldsymbol{e}}^{(n)}(\hat{\boldsymbol{k}}, \omega) \mathrm{e}^{-\mathrm{j}k_0 \hat{\boldsymbol{k}} \cdot \boldsymbol{r}} \mathrm{d}\hat{\boldsymbol{k}}, \tag{1.57}$$

where each such event contributes with a plane-wave spectrum $\mathring{\boldsymbol{e}}^{(n)}(\hat{\boldsymbol{k}},\omega)$, i.e., an overall plane-wave spectrum

$$\mathring{\boldsymbol{E}}(\hat{\boldsymbol{k}},\omega)=\sum_{n=1}^{\infty}\mathring{\boldsymbol{e}}^{(n)}(\hat{\boldsymbol{k}},\omega). \tag{1.58}$$

This last consideration allows a direct derivation of the statistical properties of diffuse-field scenarios. If we assume that each contribution $\mathring{\boldsymbol{e}}^{(n)}(\hat{\boldsymbol{k}},\omega)$ is statistically independent from the others, and of similar intensity, then the central-limit theorem allows stating that $\mathring{\boldsymbol{E}}(\hat{\boldsymbol{k}},\omega)$ will behave as a Gaussian process, by virtue of the infinite superposition of iid contributions propagating along a direction $\hat{\boldsymbol{k}}$, as coming from all of the scattering events [R38].

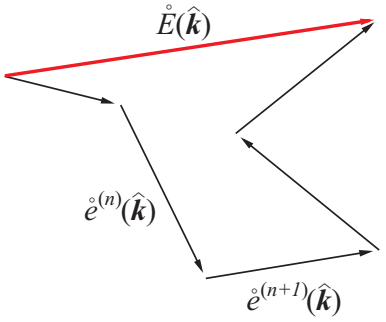

Figure 1.10 – Random-walk interpretation of the complex amplitude of the plane-wave spectrum along the direction $\hat{\boldsymbol{k}}$. The field is here a scalar complex quantity, for the sake of simplicity.

In order to invoke this result, it is necessary to have at least an heuristic explanation of why the elementary contributions $\mathring{\boldsymbol{e}}^{(n)}(\hat{\boldsymbol{k}},\omega)$ can be regarded as iid and independent of the direction $\hat{\boldsymbol{k}}$. To this end, we can make reference to Fig. 1.9: it is clear that after a relatively large number of interactions, the field measured in proximity of the observer will be dominated by contributions from scattering events occurring at close range. These events will be very likely excited by incoming contributions generated by previous scattering events and so on. Since each event is capable of scattering an incoming wave over a large fan of output directions, multiple-scattering events can be reasonably expected to provide a plane-wave spectrum statistically independent of the direction of observation, i.e., stationary in $\hat{\boldsymbol{k}}$, or isotropic. Counter-examples of plane-wave spectra with anisotropic statistics can be expected for structures where a dominant direction of propagation can be identified, such as periodic media, where the periodicity of their structure implies a quantization of their plane-wave spectrum, thus leading to a reduced number of permitted directions of propagation, or propagation modes [R8].

The Gaussian nature of a diffuse field can be explained by invoking the central-limit theorem, but having oriented our whole discussion under a harmonic steady-state condition, complex fields are to be expected. The phase shift of the plane-wave spectrum can also be shown to be uniformly distributed over $[0,2\pi]$, by virtue of the central-limit theorem [R26].

Propagation through multiple-scattering random media can be effectively treated by means of random-walk models, where the overall plane-wave spectrum for a given

direction can be visualized as a random path over the complex plane, as shown in Fig. 1.10: each elementary contribution to the overall plane-wave spectrum is represented as a random phase shift and amplitude. The statistics of this kind of processes has been studied for a long time, first to explain Brownian motion [R20] and more recently in fields such as optics, to model light propagation through diffusive media [R26].

The last property usually associated to diffusive media is that of depolarization: the plane-wave spectrum of the overall field will be effectively non-polarized, presenting a polarization matrix [R93], i.e., the covariance matrix of the scalar components of the plane-wave spectrum,

$$\underline{\boldsymbol{P}}(\hat{\boldsymbol{k}},\omega) = \left\langle \mathring{\boldsymbol{E}}(\hat{\boldsymbol{k}},\omega)\mathring{\boldsymbol{E}}^{\dagger}(\hat{\boldsymbol{k}},\omega)\right\rangle \tag{1.59}$$

proportional to the identity matrix, hence iid scalar components. Again, the reasons for this outcome are quite intuitive when looking at Fig. 1.9 and recalling that actively propagating waves must present a polarization normal to their direction of propagation. Since the directions of propagation are uniformly distributed over 4π steradian, the polarization vectors are also bound to behave in the same manner.

A diffuse-field approximation therefore implies the following properties:

1. Depolarization

$$\underline{\boldsymbol{P}}(\hat{\boldsymbol{k}},\omega) = \frac{S_{\mathring{\boldsymbol{E}}}(\omega)}{3}\mathbf{1}, \tag{1.60}$$

   with $S_{\mathring{\boldsymbol{E}}}(\omega)$ the spatial spectral power density of the plane-wave spectrum, independent of the direction $\hat{\boldsymbol{k}}$.

2. Circular Gaussian probability distribution for any scalar component along a direction $\hat{\boldsymbol{u}}_n$, with zero average and a variance equal to the spatial spectral power density $S_{\mathring{\boldsymbol{E}}}(\omega)/3$

$$\mathring{\boldsymbol{E}}(\hat{\boldsymbol{k}},\omega)\cdot\hat{\boldsymbol{u}}_n \in \mathcal{N}(0, S_{\mathring{\boldsymbol{E}}}(\omega)/3). \tag{1.61}$$

3. Angular invariance of the probability distributions (isotropy) .

The overall field is therefore described as an incoherent process, analogous to thermal radiation [R93]. This representation of the field directly implies field uniformity in space, i.e., a spectral intensity independent of the position of the observer. Indeed, the spectral intensity $S_{\boldsymbol{E}}$ of the electric field

$$S_{\boldsymbol{E}}(\boldsymbol{r},\omega) = \left\langle \|\boldsymbol{E}(\boldsymbol{r},\omega)\|^2\right\rangle = \int_{4\pi}\int_{4\pi}\left\langle \mathring{\boldsymbol{E}}^{\dagger}(\hat{\boldsymbol{k}}_1,\omega)\mathring{\boldsymbol{E}}(\hat{\boldsymbol{k}}_2,\omega)\right\rangle \mathrm{e}^{+\mathrm{j}k_0(\hat{\boldsymbol{k}}_1-\hat{\boldsymbol{k}}_2)\cdot\boldsymbol{r}}\,\mathrm{d}\hat{\boldsymbol{k}}_1\mathrm{d}\hat{\boldsymbol{k}}_2, \tag{1.62}$$

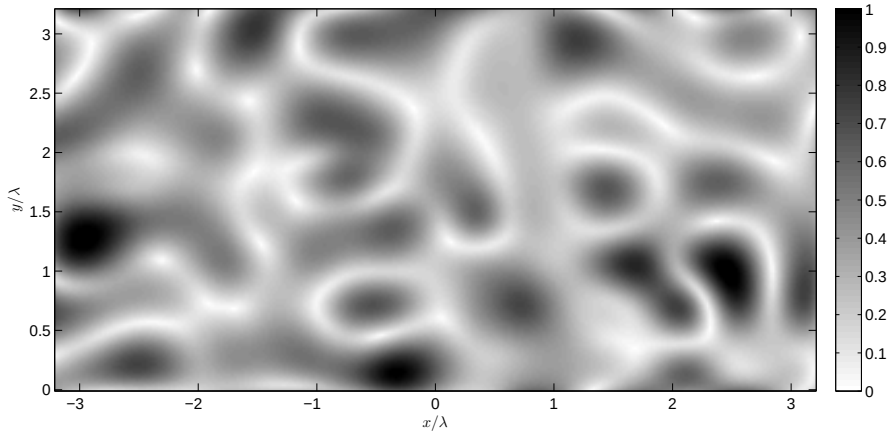

Figure 1.11 – An example of a speckled field distribution (amplitude shown). The coherence distance is close to a wavelength and clearly related to the average dimension of the field spots.

for which the hypothesis of iid plane-wave contributions implies

$$\left\langle \mathring{\boldsymbol{E}}^{\dagger}(\hat{\boldsymbol{k}}_1,\omega)\mathring{\boldsymbol{E}}(\hat{\boldsymbol{k}}_2,\omega)\right\rangle = S_{\mathring{\boldsymbol{E}}}(\omega)\delta(\hat{\boldsymbol{k}}_2-\hat{\boldsymbol{k}}_1), \tag{1.63}$$

where

$$S_{\mathring{\boldsymbol{E}}}(\omega) = \left\langle \|\mathring{\boldsymbol{E}}(\hat{\boldsymbol{k}},\omega)\|^2\right\rangle \tag{1.64}$$

is the spatial spectral power density, i.e., the average power density of the plane-wave spectrum. Hence

$$S_{\boldsymbol{E}}(\omega) = 4\pi S_{\mathring{\boldsymbol{E}}}(\omega) \quad \forall \boldsymbol{r}\in\Omega, \tag{1.65}$$

i.e., a statistically uniform intensity of the electric field over space. In a similar manner, it can be shown that the scalar components of the electric field have the same average intensity,

$$S_E(\omega) = \left\langle |\boldsymbol{E}(\boldsymbol{r},\omega)\cdot\hat{\boldsymbol{p}}|^2\right\rangle \quad \hat{\boldsymbol{p}}\in 4\pi \tag{1.66}$$

yielding

$$S_{\boldsymbol{E}}(\omega) = \left\langle \|\boldsymbol{E}(\boldsymbol{r},\omega)\|^2\right\rangle = 3S_E(\omega). \tag{1.67}$$

The most visual product of a diffusive medium is a field distribution known under the name of speckle distribution, of which an example is given in Fig. 1.11. It results

from the superposition of a large number of plane waves propagating along random directions, with random complex amplitude governed by a circular normal distribution [R26]. This kind of field distribution can be a nuisance in imaging techniques based on coherent illumination, while its generation is the goal of any reverberation chamber used for EMC [R34] as well as acoustic tests [R44]. The existence of media for which the diffuse-field approximation is valid is also at the base of the ideas discussed in § 3.

The explanations introduced so far to justify the properties and use of the diffuse-field approximation have been based on the case of a plane wave propagating through a collection of small scatterers. Its extension to a cavity passes through the acknowledgement that the phenomena occurring in the former case are very similar to those in a reverberating cavity. As a matter of fact, the presence of highly reflective boundaries ensures that any locally plane wave would be reflected a large number of times before seeing its intensity becoming negligible; therefore, for a given original direction of propagation, the set of plane waves generated by the subsequent reflection/scattering events will yield a much larger number of inter-dependent plane waves, oriented along a potentially very large number of directions and polarizations. Similarly to the case of multiple-scattering events in collections of scatterers, the superposition of a large number of independent contributions can be expected to lead to a plane-wave spectrum behaving as for a diffuse-field configuration, thanks to the central-limit theorem [R44].

This qualitative picture of a large cavity as a multiple-scattering rich environment is often invoked to justify the use of the diffuse-field approximation; though very effective and simple, it is all too often forgotten that it is indeed an approximation that is only asymptotically valid for an increasingly large number of *independent* degrees of freedom. A number of properties expected for diffusive reverberation chambers are therefore based on a model which is admittedly never fully satisfied and for which very qualitative arguments are made to justify its use. Quantitative estimations of the errors involved in the use of this approximation for not fully diffusive media are usually not considered, to put it mildly. The extent to which the diffuse-field approximation can be reasonably invoked is discussed in § 2.1.

The diffuse-field approximation has been widely used in acoustics to model the properties of the field generated within a reverberation chamber, especially for the prediction of the accuracy of spatial-averaging techniques [R51, R52, R74]. This application is revisited in § 2.1, where the diffuse-field approximation is modified to take into account the concept of a finite number of degrees of freedom.

Independently from its limitations, the diffuse-field model provides important insights in the asymptotic properties of complex media, which can be used to establish reference results that are independent from the fine details of implementation of a diffusive medium. Apart from the plane-wave spectrum and spatial field distributions already discussed, universal spatial correlation functions can also be derived, as defined in § 1.3. For the case of the electromagnetic field, these functions have been studied in details in [R32, R35] and will be briefly recalled in the following.

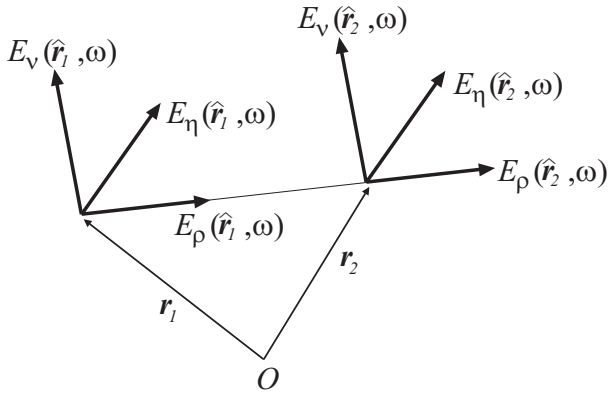

Figure 1.12 – Expansion of two vector fields into longitudinal, $E_\rho(\boldsymbol{r},\omega)$ and transversal components, $E_\nu(\boldsymbol{r},\omega)$ and$E_\eta(\boldsymbol{r},\omega)$, for the computation of their spatial-correlation functions.

With reference to Fig. 1.12, non-trivial spatial-correlation functions for the electromagnetic field can be shown to be limited to just four cases

1. Between vector electric fields

$$S_{\boldsymbol{E}}(\omega)\rho_{\boldsymbol{E}}(\boldsymbol{r}_1,\boldsymbol{r}_2,\omega)=\left\langle \boldsymbol{E}^\dagger(\boldsymbol{r}_1,\omega)\cdot\boldsymbol{E}(\boldsymbol{r}_2,\omega)\right\rangle. \tag{1.68}$$

2. Between the transversal scalar components of the electric field

$$S_E(\omega)\rho_t(\boldsymbol{r}_1,\boldsymbol{r}_2,\omega)=\left\langle E_\nu^*(\boldsymbol{r}_1,\omega)E_\nu(\boldsymbol{r}_2,\omega)\right\rangle, \tag{1.69}$$

   as well as along the η components.

3. Between the longitudinal scalar components of the electric field

$$S_E(\omega)\rho_l(\boldsymbol{r}_1,\boldsymbol{r}_2,\omega)=\left\langle E_\rho^*(\boldsymbol{r}_1,\omega)E_\rho(\boldsymbol{r}_2,\omega)\right\rangle. \tag{1.70}$$

4. Between orthogonal transversal scalar components of the electric and magnetic field

$$\frac{S_E(\omega)}{\zeta_0}\rho_m(\boldsymbol{r}_1,\boldsymbol{r}_2,\omega)=\left\langle E_\nu^*(\boldsymbol{r}_1,\omega)H_\eta(\boldsymbol{r}_2,\omega)\right\rangle, \tag{1.71}$$

   with ζ_0 the wave impedance of the filling medium in the cavity.

The above results are based upon the properties of spatial uniformity and depolarization valid under a diffuse-field approximation. Dual expressions can be derived by considering the magnetic field instead of the electric field. Any other type of spatial correlation of field components is identically equal to zero.

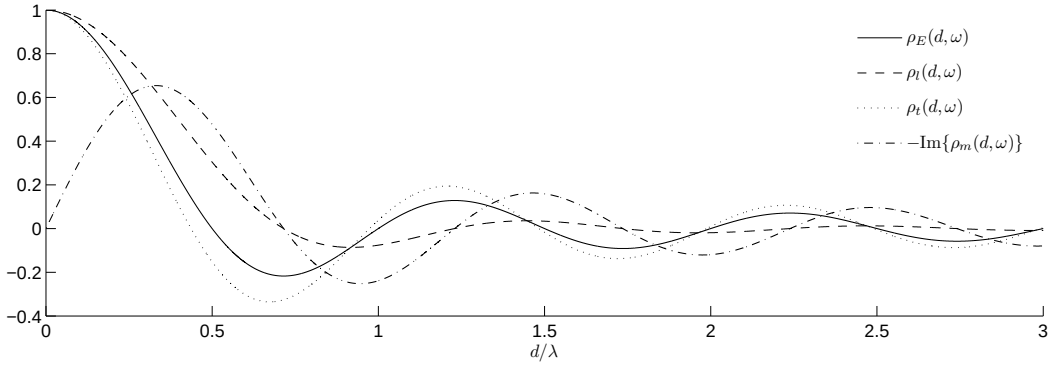

Figure 1.13 – The four spatial correlation functions introduced in (1.72)-(1.75), as functions of the electrical distance d/λ.

All these spatial correlation functions can be readily computed by applying the statistical properties associated with the diffuse-field approximation, as expressed at page 33, yielding [R32, R35]

$$\rho_{\boldsymbol{E}}(d,\omega) = \mathrm{sinc}(k_0 d) \tag{1.72}$$

$$\rho_l(d,\omega) = \frac{3}{(k_0 d)^2}\left[\mathrm{sinc}(k_0 d) - \cos(k_0 d)\right] \tag{1.73}$$

$$\rho_t(d,\omega) = \frac{1}{2}\left[3\rho_{\boldsymbol{E}}(d,\omega) - \rho_l(d,\omega)\right] \tag{1.74}$$

$$\rho_m(d,\omega) = -\frac{3}{2\mathrm{j}k_0 d}\left[\mathrm{sinc}(k_0 d) - \cos(k_0 d)\right], \tag{1.75}$$

with $d = \|\boldsymbol{r}_2 - \boldsymbol{r}_1\|$.

The four spatial-correlation functions are shown in Fig. 1.13 against the electrical distance d/λ. The electric-magnetic correlation $\rho_m(d,\omega)$ being purely imaginary, its imaginary part is plotted. Spatial-correlation functions play a fundamental role in harmonic-driven cavities since they allow estimating the number of independent samples that can be extracted from measurements taken at different positions (e.g., spatial averaging), or the statistical coupling between two devices (e.g., mutual influence). These functions will also be shown to be at the basis of the generation of deterministic wavefronts within large cavities, as discussed in § 3. In all of these cases, spatial-correlation functions quantify the idea that having only access to the propagative components of the plane-wave spectrum the smallest concentration of energy that can be generated within a cavity (and in free space, too) is limited to a spot of about half a wavelength in width, when measuring the spot between two consecutive zero crossings. This limitation goes under the name of diffraction limit (in free space) and is at

the origin of the impossibility of generating separate adjacent spots of energy without having them merged into a single contiguous region, if these spots are closer than half a wavelength.

1.4.2 A hybrid approach

The diffuse-field approximation is an effective response to the need of predicting in a simple manner the behaviour of fields generated within a large cavity. Unfortunately, results based on its use are bound to predict an ideal behaviour that is never fully met in practical configurations (see § 2). The most disturbing implication of a diffuse-field configuration is that it assumes the existence of an infinite number of degrees of freedom within a system of finite energy and extent.

The actual limitations of the diffuse-field approximation can be better grasped by means of an alternative approach which is halfway between a modal expansion and the diffusive approximation. Basically, it consists in expanding each modal topography into a plane-wave spectrum

$$\boldsymbol{e}_n(\boldsymbol{r}) = \sum_{p=1}^{N_n} \boldsymbol{\beta}_{np} \mathrm{e}^{-\mathrm{j}k_0 \hat{\boldsymbol{k}}_{np} \cdot \boldsymbol{r}}, \tag{1.76}$$

where N_n is the number of plane waves needed to reproduce $\boldsymbol{e}_n(\boldsymbol{r})$ and $\boldsymbol{\beta}_{np}$ are the vector coefficients associated with this expansion. The modal spectra in (1.76) are assumed to be discrete. There are good reasons for this choice, and we will try to make our point clearer in the rest of this section. Although the same approach can be straightforwardly extended to the case of continuous plane-wave spectra, we will stick to the idea of discrete spectra for the sake of simplicity.

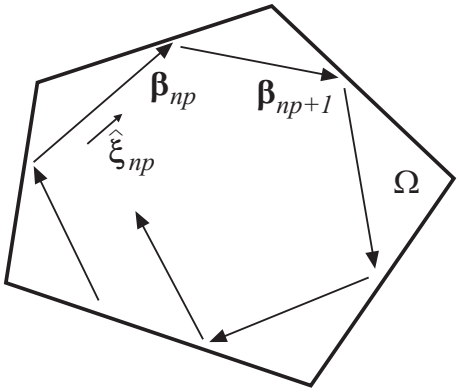

Figure 1.14 – A schematic illustration of the how the plane-wave spectrum of a modal topography $\boldsymbol{e}_n(\boldsymbol{r})$ is determined by the boundary conditions of a cavity.

First of all, we need to recall that for a given field distribution to self-sustain itself (resonance condition), its plane-wave spectrum must be defined in such a way to have its individual plane waves interfere constructively [R44]; this is the same idea at the base of any electronic oscillator, and is sometimes referred to as phase congruence. Constructive interference, leading to resonance, does not necessarily require periodic paths, nor a discrete plane-wave spectrum. But in the case of simple geometries for the cavity bound-

aries, especially if approximated by planar surfaces, this condition holds true. In all other case, even though no periodicity can be observed (chaotic cavities), constructive interference stays a fundamental condition for the appearance of resonances. For the sake of simplicity, we will limit our discussion to regular cavities, where plane waves generating a resonant pattern periodically travel along the same close path or orbit. These concepts are schematically illustrated in Fig. 1.14 and allow stating that the amplitude of each plane wave must be ideally identical in the case of a lossless cavity. A more general description will be considered at the end of this section.

Second, recalling that only the modes excited around their frequency of resonance contribute to the overall field distribution, and assuming that the total energy stored in the cavity is evenly shared, we can write

$$\psi_n(\omega)\boldsymbol{e}_n(\boldsymbol{r}) \simeq \beta_n \sum_{p=1}^{N_n} \hat{\boldsymbol{\xi}}_{np} \mathrm{e}^{-\mathrm{j}k_0 \hat{\boldsymbol{k}}_{np}\cdot\boldsymbol{r}}, \tag{1.77}$$

for the M dominant modes, while $\hat{\boldsymbol{\xi}}_{np}$ are now complex unit vectors modelling the polarization of each plane wave, characterized by a uniformly distributed random phase and a unpolarized state. Coherently with the above discussions about the need, for a resonant mode, of $\|\boldsymbol{\beta}_{np}\| \simeq \beta_n, \forall p \in [1, N_n]$, the intensity of the plane waves is controlled by a single parameter.

Substituting (1.77) into (1.15), the plane-wave spectrum of the overall field distribution is derived as

$$\boldsymbol{E}(\boldsymbol{r}) = \sum_{n=1}^{M} \gamma_n \beta_n \sum_{p=1}^{N_n} \hat{\boldsymbol{\xi}}_{np} \mathrm{e}^{-\mathrm{j}k_0 \hat{\boldsymbol{k}}_{np}\cdot\boldsymbol{r}}, \tag{1.78}$$

i.e., a plane-wave spectrum composed of groups of contributions associated to several modes. Our qualitative discussion about the inevitable causal links existing between plane waves belonging to the same mode imply that they should be treated as correlated random variables. More precisely, they should not be treated as random variables at all, since a priori knowledge of the geometry and boundary conditions of the cavity allow a perfect prediction of the entire causal chain of plane waves generated by any one of them. This idea is illustrated in Fig. 1.14, where the coefficients of two consecutive plane waves are directly related to the reflection coefficient of the cavity boundary. For the sake of simplicity, we will consider planar boundaries, thus neglecting the possibility of a more complex and general scattering scenario. In any case, it would also be possible to use a similar approach, establishing an iterative relationship

$$\boldsymbol{\beta}_{np+1} = \underline{\boldsymbol{R}}_{\mathrm{p}}(\hat{\boldsymbol{\xi}}_{np})\boldsymbol{\beta}_{np}, \tag{1.79}$$

with $\underline{\boldsymbol{R}}_{\mathrm{p}}(\hat{\boldsymbol{\xi}}_{np})$ a dyadic operator modelling the reflection experienced by the np-th plane wave interacting with the cavity boundary, plus the additional phase-shift cumulated

through propagation before the next scattering interaction. Due to the highly-reflective nature of boundaries used in reverberation chambers, it is reasonable to expect

$$\|\beta_{np}\| \simeq \beta_n, \forall n \in [1, N_n], \tag{1.80}$$

as long as $\|\underline{\boldsymbol{R}}_{\mathrm{p}}(\hat{\boldsymbol{\xi}})\| \simeq 1, \forall \hat{\boldsymbol{\xi}}, p$, as found in practice in reverberation chambers.

When considering regular cavities, a single plane wave propagates along a closed path a number of times until its energy is dissipated. It is useful to introduce partial plane wave coefficients $\boldsymbol{\beta}_{np}^{(k)}$, where (k) is an integer indicating the number of time the plane wave has completed a close orbit; the steady-state coefficients of the plane-wave spectrum can be computed as

$$\boldsymbol{\beta}_{np} = \sum_{k=1}^{\infty} \boldsymbol{\beta}_{np}^{(k)}. \tag{1.81}$$

This representation is useful when assessing the effective attenuation experienced by a plane wave propagating along a resonant path. This can be done by relating the quality factor of a mode to an effective attenuation coefficient α_n and a residual phase-shift angle $\Delta\varphi$ resulting from an imperfect synchronization (imperfect resonance) among each periodic orbit, thus yielding the following relationship between the phasor of a plane wave at the $k+1$-th and the k-th propagation cycle of an orbit of length L_n

$$\beta_{np}^{(k+1)} = \beta_{np}^{(k)} \mathrm{e}^{-\alpha L_n + \mathrm{j}\Delta\varphi_n}, \tag{1.82}$$

i.e.,

$$\beta_{np}^{(k)} = \beta_{np}^{(0)} \left(\mathrm{e}^{-\alpha_n L + \mathrm{j}\Delta\varphi_n}\right)^k. \tag{1.83}$$

The attenuation α_n is a homogenized coefficient taking into account the local dissipation events occurring during the interaction of a wave with imperfectly conductive boundary conditions and distributed dissipation caused by propagation losses through the media filling the cavity. The infinite superposition of contributions from each orbit potentially leads to a resonant build-up if $\alpha_n \simeq 0$ and $\varphi_n \simeq 0$, thanks to the coherent summing up of each contribution under a harmonic excitation, resulting into steady-state coefficients

$$\beta_{np} = \sum_{k=0}^{\infty} \beta_{np}^{(k)} = \frac{\beta_{np}^{(0)}}{1 - \mathrm{e}^{-\alpha_n L_n + \mathrm{j}\Delta\varphi_n}}, \tag{1.84}$$

where the denominator of the resulting fraction shows the resonant nature/origin of the steady-state coefficients. For a perfectly constructive interference $\Delta\varphi_n = 2m\pi$, corresponding to $m = L_n/\lambda_n \in \mathbb{N}$, where λ_n is one of the wavelengths at which this

condition is satisfied (respectively, occurring at the frequency f_n). In all other conditions where the plane-wave coefficients are computed for a slightly different frequency

$$\Delta\varphi = 2\frac{L_n}{\lambda_n}\left(1+\frac{\Delta f}{f_n}\right), \tag{1.85}$$

where $\Delta f = f - f_n$. Approximating the resonant part of (1.84) for $\Delta f \to 0$

$$\frac{1}{1-\mathrm{e}^{-\alpha_n L_n + \mathrm{j}\Delta\varphi_n}} \simeq \frac{1}{\mathrm{j}2\pi\dfrac{L_n}{\lambda_n}}\frac{1}{\dfrac{\Delta f}{f_n}+\mathrm{j}\dfrac{\alpha_n\lambda_n}{2\pi}}, \tag{1.86}$$

and comparing it with the asymptotic expansion of the functions $\psi_n(f)$

$$\frac{1}{f^2-f_n^2} \simeq \frac{1}{2f_n^2}\frac{1}{\dfrac{\Delta f}{f_n}+\mathrm{j}\dfrac{1}{Q_n}}, \tag{1.87}$$

leads to

$$\alpha_n = \frac{2\pi}{\lambda_n Q_n}, \tag{1.88}$$

which links the effective attenuation coefficient to the quality factor of the mode. If the main dissipation mechanism is in boundary interactions, then

$$\mathrm{e}^{-\alpha_n L_n} = \Gamma_e^{N_n}, \tag{1.89}$$

where N_n is the number of boundary interactions undergoing during a full orbit of length L_n, defining the number of plane waves making up the modal topography $\boldsymbol{e}_n(\boldsymbol{r})$. The parameter

$$\Gamma_e = \left\langle \|\underline{\boldsymbol{R}}(\hat{\boldsymbol{\xi}})\| \right\rangle \tag{1.90}$$

is the average intensity of the reflection coefficient along a random direction of incidence $\hat{\boldsymbol{\xi}}$ over all the boundaries. Noting $\Gamma_e \simeq 1-\delta_\Gamma$

$$N_n = \frac{2\pi}{\delta_\Gamma Q_n}\frac{L_n}{\lambda_n}. \tag{1.91}$$

This last result is of interest, since it provides a direct estimate of the order of magnitude of the number of boundary reflections occurring within a lossy cavity, and thus allows assessing the number of plane waves maintaining a similar intensity associated to each resonant mode.

We have seen thus far how a modal representation of the field can be recast into a plane-wave spectrum with elementary contributions within each mode of almost similar amplitude, as expected for overlapping modes (see § 1.3.1). In order to push further our

analysis of the validity of the diffuse-field approximation, it is necessary to demonstrate that these plane waves are indeed statistically independent, as required in § 1.4.1. We have already seen in § 1.3.3 that the modal coefficients can be reasonably regarded as independent. Computing the covariance of the plane-wave scalar coefficients

$$\left\langle \beta_{np}\beta_{ms}^{*}\right\rangle = \delta_{mn}\left\langle |\beta_{np}|^{2}\right\rangle \prod_{i=p}^{s} \mathrm{e}^{-\mathrm{j}\varphi_i} = \delta_{mn}\left\langle |\beta_{np}|^{2}\right\rangle \exp\left(-\mathrm{j}\sum_{i=p}^{s}\varphi_i\right) \quad s>p, \tag{1.92}$$

implying uncorrelated plane-wave coefficients when dealing with plane wave associated to different modes. Restricting our analysis to the case of plane waves associated to the same mode n, their correlation coefficient becomes

$$\rho_{ps}^{(n)} = \frac{\left\langle \beta_{np}\beta_{ns}^{*}\right\rangle}{\sqrt{\left\langle |\beta_{np}|^{2}\right\rangle \left\langle |\beta_{ns}|^{2}\right\rangle}} = \exp\left(-\mathrm{j}\sum_{i=p}^{s}\varphi_i\right) \quad s>p. \tag{1.93}$$

The direct consequence of (1.93) is that $|\rho_{ps}^{(n)}| = 1, \forall p,s,n$, i.e., the assumption of statistically independent plane waves is not realistic.

This outcome is in contrast with the assumption that each mode can contribute with a minimum number of independent plane waves [R44], e.g., assuming 8 plane waves per mode, as would be expected for an empty rectangular cavity. This apparent incongruence is due to the reasons already recalled in § 1.3: when considering a given cavity, the field distribution can be treated as a random process only by considering random sources, if the cavity is static. Under this condition, the only terms in the modal expansion (1.15) that can be regarded as random variables are those related to the sources, i.e., the modal weights. Therefore, for plane waves related to a same mode, their coefficients are inevitably correlated in a deterministic manner.

In many cases, the statistical properties of random media are regarded through the lens of ensemble theory, of interest in the case one wanted to know the *average* properties of a set of random realizations of cavities of different geometrical/electrical properties, but sharing the same macroscopic parameters, as discussed in § 1.3. If we applied this idea to the case of the correlation matrix made up by the correlation coefficients $\rho_{ps}^{(n)}$ in (1.93), we should compute their ensemble average

$$\left\langle \rho_{ps}^{(n)}\right\rangle = \left\langle \exp\left(-\mathrm{j}\sum_{i=p}^{s}\varphi_i\right)\right\rangle. \tag{1.94}$$

The argument of the ensemble average is now a random walk process involving steps with fixed length (equal to one) and random orientations within the complex plane. This type of processes have been studied in a number of fields, but perhaps the most relevant one is optical speckle [R26]. This type of random process has very simple

moments as soon as the phase shifts have no preferential direction, i.e., are uniformly distributed over the interval $[0, 2\pi]$. This condition is reasonable when considering an ensemble made up of random cavities all maintaining dimensions much larger than a wavelength. Under these conditions

$$\left\langle \exp\left(-\mathrm{j}\sum_{i=p}^{s} \varphi_i \right) \right\rangle = \delta_{ps}, \tag{1.95}$$

ultimately yielding

$$\left\langle \boldsymbol{\rho}^{(n)} \right\rangle = \mathbf{1}, \tag{1.96}$$

i.e., uncorrelated plane-wave coefficients. In our opinion, the origin of the misinterpretation of the statistics of plane-wave spectra generated by cavities is to be found in this result, which does not hold for a single static configuration.

Taking into account the true nature of the statistics of the plane-wave spectrum, the correlation matrix of the overall plane-wave spectrum in (1.78) must take a block-diagonal shape

$$\begin{pmatrix} \boldsymbol{\rho}^{(1)} & & \mathbf{0} \\ & \ddots & \\ \mathbf{0} & & \boldsymbol{\rho}^{(M)} \end{pmatrix} \tag{1.97}$$

This outcome appears as a natural consequence of the observation of the physics of resonant field topographies, and is fundamentally independent from the simplifying assumptions we have used to make our reasoning simpler and, hopefully, clearer. When comparing (1.97) with the perfectly diagonal covariance matrix expected in the case of a diffusive approximation, the resulting differences cannot be neglected. The first observation is that the actual number of degrees of freedom available in practice can no longer be thought to coincide with the number of plane waves propagating within the medium

$$N_{\mathrm{PW}} = \sum_{n=1}^{M} N_n, \tag{1.98}$$

but rather the number of modes, M. In other words, the rank of the correlation matrix of the PWS coefficients is much smaller then its dimension, thus implying a redundant representation. This conclusion seems to be implied in the fact that a modal expansion based on Helmholtz equation's eigenfunctions is efficient, so that any equivalent expansion over a different basis is bound to require a larger number of spectral coefficients. Hence, the latter will have to be substantially redundant, i.e., not statistically independent.

Clearly, this reduction in the number of available degrees of freedom has no major effect when a very large number of modes are available in the first place. Very large structures studied in their asymptotic regime at high frequencies will behave as predicted by the diffusion approximation. But as discussed in § 1.3.1 and demonstrated in § 2.2, field diffusion should not be taken for granted even though a very high modal density were potentially available. This mismatch has led (and still leads) to a number of wrong concepts and assumptions, particularly when cavities are employed as test facilities, as discussed in the next chapter.

These conclusions are apparently in contradiction with Berry's conjecture [R81], which states that for a fully chaotic cavity a single mode implies a continuous PWS, composed of an infinite number of iid contributions (1.3.2). His conjecture makes sense from a propagation point of view for what are the directions of arrival of the plane waves of a mode: the absence of periodic orbits in a chaotic cavity implies indeed that the boundary conditions will lead to a large number of scattering interactions likely distributed over a large number of directions of arrival. Now, the problem with this assumption is that it cannot be verified, since it would imply generating an ensemble of modes sharing the same macroscopic properties. In our opinion, this is an ill-defined concept; although resonant modes can share the same frequency of resonance, quality factor, etc, there is no way of linking two modal topographies in a causal manner, even for dynamical systems or in the case of the inclusion of small perturbations. An example should help here: if a single dot of perfect conductor where inserted in an electromagnetic cavity, at a position where the cavity presents a maximum of field for a given modal topography, the conductive dot would force the tangential component of the field to be identically equal to zero for any polarization, because of its infinitesimal dimensions. What would be the rational in comparing the PWS of the original modal distribution with the one including the dot?

Chapter 2

Understanding real-life cavities

To kill an error is as good a service as, and sometimes even better than, the establishing of a new truth or fact

Charles Darwin

THE aim of the previous chapter was to highlight the relationship existing between the widely used diffuse-field approximation and non-asymptotic models of wave propagation within reverberating cavities. The underlying idea was to instill doubts about the wisdom of applying asymptotic approximate models to physical systems operated at frequencies where they cannot in any manner provide a sufficiently large number of degrees of freedom. As it will be argued in this chapter, the faith of most reverberation chamber users in the validity of the diffuse-field approximation has led to rather imaginative explanations of the non-idealities observed when operating these tools.

It is therefore natural to ask the following question: is there a way of predicting under what conditions the field measured within a cavity is well *approximated* by the diffuse-field paradigm? Recalling that the diffuse-field hypothesis requires a large number of degrees of freedom and that this number increases *on average* with the electrical dimensions of the cavity, the previous question is typically translated in practical terms as : is there a minimum frequency starting from which the diffuse-field hypothesis works well? If yes, how to predict it?

The existence of such a minimum frequency is currently taken for granted, as an evidence, despite the fact that no precise definition or proof is available, to our knowledge. Referred to as lowest usable frequency (LUF) in EMC or Schröder's frequency in acoustics, theoretical or experimental knowledge of this minimum frequency is of

paramount importance to make any application of large cavities feasible. Hence the physical and practical interest in its study, as considered in this chapter.

The alternative idea of using random models mimicking a diffusive condition while enforcing a limited number of degrees of freedom will be applied in this chapter to several problems. All of them share the necessity of understanding why large cavities may sometimes behave in a manner that is not accounted for by diffuse-field models, e.g., presenting statistical anomalies. The simple models introduced in the previous chapter will be herein developed into theories showing inherent errors of interpretation, providing explanations for the non-ideal behaviour of large cavities with respect to the predictions of diffuse-field models. It should be clear from our approach that our motivation is not the use of complex mathematical tools; we are rather guided by the need of understanding the physical reasons for the actual behaviour of these peculiar systems. The results of these analyses will appear to be surprisingly simple in shape, bearing clear physical insights in the physical limitations of large cavities.

2.1 Spatial ergodicity

The conclusions from § 1.4.2 suggest the idea of considering an alternative random PWS model, where rather than struggling with correlated plane waves, an equivalent PWS composed of independent terms could be used. This straightforwardly implies using a finite number of independent plane waves, equal to the number of modes accessible at the working frequency. In the case of a pressure field $p(\boldsymbol{r},\omega)$ observed under harmonic excitation, the above ideas can be expressed as

$$p(\boldsymbol{r},\omega)=\sum_{p=1}^{N_d}\gamma_p \mathrm{e}^{-\mathrm{j}k_0\hat{\boldsymbol{k}}_p\cdot\boldsymbol{r}}. \tag{2.1}$$

The single plane waves of the finite PWS in (2.1) are assumed to follow exactly the same statistics of the infinite PWS associated to a diffuse-field approximation (§ 1.4.1), but the number of plane waves is regarded as finite and equal to N_d. A finite number of degrees of freedom is a condition more consistent with the physics of a finite-energy bounded medium.

A word of caution is necessary : the field distribution (2.1) should not be expected to be equivalent in a deterministic sense to that associated to random PWS with block-diagonal correlation matrices. The equivalence operates on two levels: 1) the number of degrees of freedom is the same as well as 2) all the statistical momenta of the PWS terms, including the spatial-correlation functions of the overall pressure field as defined in § 1.4. In this way, a statistical equivalence makes sense and can be defined without ambiguity. These ideas were introduced in [J14] in the case of acoustic reverberating rooms for the purpose of studying how far the equivalence between spatial and ensemble averages of the mean-square pressure can be stretched.

This model can be applied to enforce the availability of only a finite number of degrees of freedom, while maintaining most of the properties of the diffuse-field approximation. It is therefore possible to study how the statistics of field-related quantities can be expected to appear in a more realistic description; such an approach is of interest not only in the lower-frequency range of operation of reverberation chambers, where a limited number of resonant modes exist, but also higher frequencies where the probability of observing a lower number of modes *than expected on average* is far from negligible. This last issue is discussed in § 2.3, and can be regarded as a first step towards a better understanding of the physical reasons of statistical anomalies (outliers) observed even at high frequencies where the diffuse-field approximation is taken for granted.

Spatial averaging is widely used as an approximate technique for assessing the average mean-square pressure [R74, R51, R52, R53]

$$\mu_{p^2}(\omega) = \left\langle |p_\omega(\boldsymbol{r},\omega)|^2 \right\rangle \tag{2.2}$$

within a cavity, a quantity that was shown to be independent of the observer's position in (1.65). This quantity is fundamental when estimating the total acoustical power generated by a source, of practical importance in noise and absorption measurements [R44]. Average mean-square pressure should be assessed by means of ensemble averaging, e.g., by means of randomization techniques such as random source positioning, random geometry modifications of the cavity boundaries, etc [R44].

An alternative is to approximate the ensemble average by considering a single realization of the pressure field distribution, while collecting a set of samples over different positions within the cavity, i.e., averaging on spatial samples over a region $\Omega' \subseteq \Omega$, rather than on random realizations

$$\hat{\mu}_{p^2}(\omega) = \left\langle |p(\boldsymbol{r},\omega)|^2 \right\rangle_{\Omega'} = \frac{1}{N_s}\sum_{i=1}^{N_s} |p(\boldsymbol{r}_i,\omega)|^2, \quad \boldsymbol{r}_i \in \Omega' \quad \forall\ i \tag{2.3}$$

postulating

$$\hat{\mu}_{p^2}(\omega) \simeq \mu_{p^2}(\omega). \tag{2.4}$$

The reason for this assumed equivalence is that for a reverberating cavity, field-related quantities are usually expected to be ergodic in space and time: the set of random realizations of the pressure that would be observed at a single position are expected to sweep the same range of values (with the same probability distribution) than the samples collected over space within a single realization.

A simple analogy is to compare the results of the casting of one thousand dices at the same time with those of a single dice cast one thousand times; intuitively, for fair dices, one expects the same results, somehow putting on the same level ensemble averages (the set of dices) with time averages (recasting the dice).

In fact, ergodicity has been demonstrated only for some classes of geometry, of which a fundamental example is Sinai's billiard, a chaotic cavity [R11]. In simple words, ergodicity requires that a particle launched along any direction will pass through all points of the entire space of the cavity, crossing them along all possible directions, if one waited long enough. Without entering this complex topic, it is clear that the very notion of losses puts this property in jeopardy, limiting the trajectory of the particle before the end of its infinite journey.

Ergodicity is therefore postulated because of the large number of scattering interactions any wave experiences, redirecting their energy along different directions that should ensure a complete sweeping of the cavity. From an experimental point of view, this property cannot be verified easily, due to the fact that the true value of the ensemble and spatial averages are not know; only estimates are accessible, thus affected by residual uncertainties. They should be regarded, at their turn, as random variables. Since residual uncertainties of these estimators are typically far from negligible [R39], the accuracy of the spatial average estimator cannot be identified against a clear reference.

Our proposal for a finite PWS goes in this same direction, since the direct consequence of limiting the number of degrees of freedom is that the mean-square pressure will no longer follow a chi-square probability law, presenting an increased statistical dispersion, as demonstrated in [J4]. As a consequence, the accuracy of the spatial average estimator will be reduced.

First of all, the spatial-average estimator can be shown to be an unbiased estimator, i.e.,

$$\left\langle \hat{\mu}_{p^2}(\omega) \right\rangle = \mu_{p^2}(\omega), \tag{2.5}$$

whereas its variance is intuitively expected to decrease for an increasingly large number of *independent* samples entering the spatial average. Once again, the central limit theorem is the main reason for this expectation, hence predicting that the estimation relative error

$$\varepsilon_\mu = \frac{\hat{\mu}_{p^2}(\omega)}{\mu_{p^2}(\omega)} - 1 \tag{2.6}$$

should asymptotically behave as

$$\left\langle \varepsilon_\mu^2 \right\rangle \sim \mathcal{O}(N_s^\alpha), \tag{2.7}$$

with $\alpha = -1$; i.e., when repeating the same measurements in a large number of cavities all slightly different one from the other (i.e., an ensemble), the residual error of the estimator, while on average equal to zero, will present a residual statistical dispersion. As recalled in § 1.2.3, samples collected in space though behaving as random quantities cannot be assumed to be independent; residual spatial correlation implies that the asymptotic convergence predicted by (2.7) is a best-case that cannot be met

in practice, a fact well-known by users of reverberating rooms [R74, R89]. The samples are typically arranged over a Cartesian grid with a uniform distance $\lambda/2$, in order to minimize the spatial correlation between closest neighbours, while inevitably leading to residual long-range correlation with the rest of the samples. As demonstrated in [J14], the resulting convergence rates for (2.7) can now be as low as $\alpha = -2/3$ for a three-dimensional grid of measurement points, a significative reduction.

The analysis carried out in [J14] was meant to go a step further, showing that even the increase in the residual uncertainty due to spatial correlation is still only part of the whole picture. Having taken into account the finite number N_d of degrees of freedom underpinning the pressure field, (2.7) becomes

$$\left\langle \varepsilon_\mu^2 \right\rangle \sim A_1 N_s^\alpha + A_2 N_d^{-1}, \tag{2.8}$$

where $A_1, A_2 \in \mathbb{R}^+$. This result implies that even if the number N_s of spatial samples increased, the second term could set a lower bound depending exclusively on the number N_d of degrees of freedom. Clearly, in the case of an ideally diffuse pressure (2.8) would converge back to (2.7), as $N_d \to \infty$. Previously published experimental results [R39] presented hints of an increased variability of the spatial-average estimator. No explanation was available within the framework of validity of the diffuse-field model. Unpublished results from our analysis confirms that assuming one single degree of freedom per mode, (2.8) is capable of correctly predicting the deterioration of the accuracy of the spatial estimator. So far, this is the only example of application of this hybrid model. A similar idea, based on a random spectral model is presented in the next section.

2.2 Imperfect diffusion

As recalled in § 1.1, all test facilities based on the use of reverberating cavities are firmly founded on the assumption of a perfectly diffuse field distribution. This approximation is regarded as reasonably accurate as soon as a sufficiently high number of degrees of freedom are available, by virtue of the central limit theorem [R42, R45].

It is known that the actual number of degrees of freedom is the number of modes that can be *simultaneously* accessed at the working frequency [R75, R3], as measured by the modal overlapping introduced in § 1.3.1 and estimated, e.g., by means of Weyl's approximation (1.43). In the light of it, we need to be aware of two issues: 1) within the context of the EMC community, the vast majority of the users of reverberation chambers are still convinced that a high modal density is sufficient to enable a perfect diffusion [R33, R42, R2]; 2) in either case, no mention is given about the link between modal density/overlapping and the accuracy of the diffuse-field approximation. The first point is unfortunately endemic to the EMC community, for reasons not very clear; anterior research within the acoustics community was much more conclusive, leading mostly to empirical criteria based on the requirement of a high modal overlapping, as

the most significant figure of merit to invoke the diffuse-field approximation. Schröder's contributions were instrumental in this respect, though he also made large use of the assumption of a perfectly diffuse field even at relatively low frequencies.

Whatever the field of application, the second issue is still open: how many modes should overlap on average in order to accept that the diffuse-field approximation is accurate enough? Without going through the surprisingly arbitrary criteria invoked within the EMC community (see, e.g., [R2, R33]), it can be recalled that acoustic reverberation rooms are assumed to work properly as soon as at least 3 modes are overlapped on average [R77], a criterium due to Schröder. An alternative criterium, previously proposed by Schröder, rather required 10 overlapping modes [R72]. The existence of two criteria points, in our opinion, to the lack of a formal analysis of the physics of resonant cavities: 3 or 10 modes, these figures were derived on empirical appreciations that the accuracy of the diffuse-field approximation gets better for higher modal overlapping and the need for a working compromise. A quantitative assessment of the level of field diffusion can be obtained by means of the procedure presented in [J4] (reproduced at page 107) for the case of an electromagnetic cavity, briefly presented in § 2.2.1.

Acknowledging that the diffuse-field model is just an approximation, it is also important to know how good the predictions based on it are. This issue is particularly important within the EMC community, since a recent trend has the quality of a reverberation chamber assessed by comparing its field statistics against the ideal case of a diffuse-field. The implications of this approach are discussed in § 2.2.2.

2.2.1 Assessing the accuracy of the diffuse-field approximation

First of all, we need a mean of assessing the quality of the diffuse-field approximation; this can be done by taking the electric-energy density $W(\omega)$, herein assumed to be independent from the position $\boldsymbol{r}$ for the sake of simplicity,

$$W(\omega) = \epsilon_0 \|\boldsymbol{E}(\omega)\|^2, \tag{2.9}$$

where ϵ_0 is the dielectric permittivity of the homogeneous medium filling the cavity, and computing its relative variability

$$\varsigma_W^2(\omega) = \frac{\left\langle W^2(\omega)\right\rangle}{\langle W(\omega)\rangle^2} - 1, \tag{2.10}$$

defined as the ratio of its variance over the square of its average value. Under perfect diffusion, $\varsigma_W^2(\omega) = 1/3$, since in that case $W(\omega)$ would behave as a chi-square-distributed random variable with 6 degrees of freedom, due to the iid contributions of the real and imaginary parts of each of the three scalar field components. If the field did not behave as expected, the variability would allow defining an error

$$\epsilon_{\varsigma^2}(\omega) = \frac{\varsigma_W^2(\omega) - 1/3}{1/3} \tag{2.11}$$

that could be expected to assess the accuracy of the diffuse-field approximation.

Why picking the electric-energy density? There are several reasons; first of all, it is related to a quadratic form, hence it has nice mathematical properties for the computation of norms, simplifying the derivation. Second, it is a combination of the three scalar components of the field, so that it provides a global appreciation of the behaviour of the electric field. And third, it is more suitable for experimental tests, since estimators of a chi-square-distributed random variable with six degrees of freedom are more accurate (lower relative variance) than those of chi-square-distributed random variables with only two degrees of freedom, as is the case for any scalar field component under a diffuse-field approximation.

The spectral representation introduced in § 1.2.2 allows expressing in a closed-form $W(\omega)$ as a function of the modal parameters. In particular, adopting a random description as proposed in § 1.3, it can be shown that

$$\epsilon_{\varsigma^2}(\omega) = \frac{3(\kappa+1)}{2\pi}\frac{1}{M_M(\omega)}, \tag{2.12}$$

where κ is the kurtosis of the real (and imaginary) part of the modal coefficients. The above result was derived in [J4] by assuming the existence of an ensemble of cavities generated by a perfect stirring technique: by this term we consider any randomization technique capable of ensuring iid random realizations for the modal quantities introduced in § 1.3. These are the same assumption required for a perfectly diffuse-field configuration: the only difference is that we are now acknowledging and taking fully into account the fact that the Lorentzian shape of the modal responses implies that only a limited number of modes will be effectively excited at the working frequency.

It is remarkable to see how the modal overlapping $M_M(\omega)$ naturally appears to depend on the average number of modes found within the half-power bandwidth (-3 dB) of the modal responses $\psi_n(\omega)$; this value was not arbitrarily chosen, but neatly results from the computations. Another interesting point is that $\epsilon_{\varsigma^2}(\omega)$ is strictly positive, indicating that any deviation from the ideal diffuse-field configuration translates into an increased variability: this result is unsurprisingly close to the increased inaccuracy of the ensemble-average estimator studied in § 2.1.

Assuming Gaussian-distributed modal coefficients, (2.12) simplifies into

$$\epsilon_{\varsigma^2}(\omega) = \frac{6}{\pi}\frac{1}{M_M(\omega)}, \tag{2.13}$$

a remarkably simple expression relating the average number of overlapping modes (as defined in § 1.3.1) to the excess variability of the electric-energy density.

Equation (2.13) has a direct practical interest since it could be used to predict the accuracy of the diffuse-field approximation. As opposed to the qualitative criterium requiring a given number of modes to invoke field diffusion [R75, R44], (2.13) provides a quantitative criterium, by allowing the user of the cavity to decide how many overlapping modes should be available on average in order to limit discrepancies between

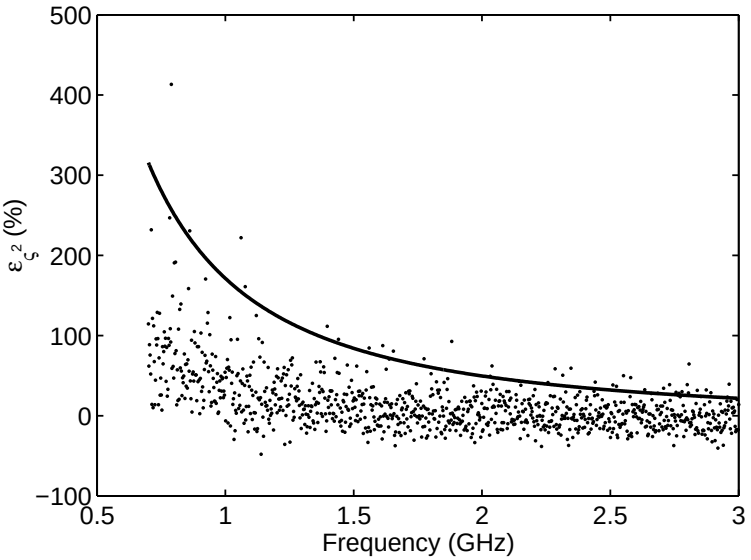

(a)

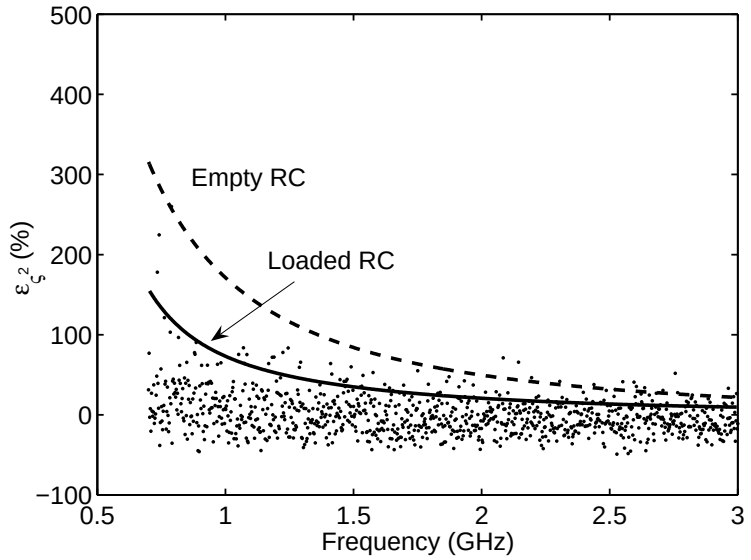

(b)

Figure 2.1 – Estimates of the standardized variance of the energy density W, as assessed from experimental results obtained for : (a) an empty cavity (apart for the excitation antenna) and (b) one loaded with a set of 4 pyramidal absorbers (about 30 cm high).

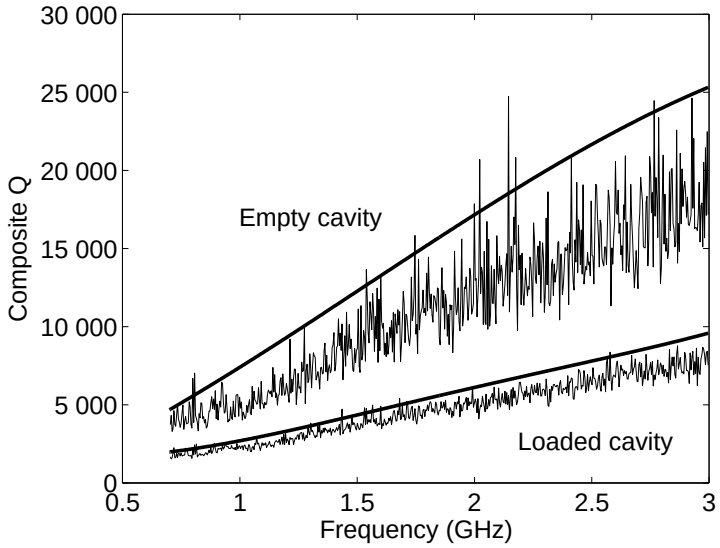

Figure 2.2 – Quality factors for the empty and loaded chambers. The smooth curves represent the loose majorants used for deriving the maximum-error results in Fig. 2.1.

theoretical (diffuse-field models) and experimental results. Such thought should be pushed a little step further by letting in statistical considerations about the estimators used during experimental work; the details of these discussions are out of the scope of this dissertation, but it suffices to recall that since the relative accuracy ϵ_m of the measurements/estimations are a priori known, there is no reason to try to enforce an average number of overlapping modes so high as to ensure $\epsilon_{\varsigma^2}(\omega) \leqslant \epsilon_m$; it seems therefore reasonable to propose a minimum M_M such that $\epsilon_{\varsigma^2}(\omega) = \epsilon_m$, corresponding to the best approximation of a diffuse-field configuration, in this case limited by experimental/statistical uncertainties [J4].

More generally, (2.13) proves that there is no universal definition of the minimum number of modes required to observe a good agreement with the predictions of diffuse-field models, as it all depends on the requirements of the user/experimenter. An example is provided in Fig. 2.1, where the excess variability error was estimated from experimental data. Being just an estimator, its accuracy is finite, as demonstrated in [J4, App. B], hence the random fluctuations around the unknown true value, as clearly apparent in the higher frequency range, where $\epsilon_{\varsigma^2}(\omega) \to 0$.

Experimental results are compared against theoretical predictions using (2.13) in conjunction with (1.43), using Weyl's approximation to predict the average number of overlapping modes, where the average composite quality factor was again estimated from experimental data and approximated by a third-degree polynomial curve. This last operation was defined in such a way as to be a loose upper bound of the experimental data, as shown in Fig. 2.2; the rationale for this choice was to capture the trend of the upper bound of $\epsilon_{\varsigma^2}(\omega)$, but without taking too large a margin. The results in Fig. 2.1 are quite conclusive, showing a good prediction of the trend of $\epsilon_{\varsigma^2}(\omega)$ against frequency.

Increasing losses in the shape of small absorbers lead to the improvement predicted by (2.13), because of the increased modal overlapping involved in a lower average composite quality factor. Still, this fact should not be regarded as a potential solution to the problem of extending the diffuse-field condition towards the lower frequency range. Increasing losses can improve the operation of a cavity if small enough to be treated as perturbations, without modifying the validity of the assumption of iid modal parameters. In any other case, as demonstrated in [R36], things get worse.

A final observation related to Fig. 2.1 is in order: while the global trend of the highest errors is correctly identified, it appears that (2.13) is far from begin a monotonous function. The intuitive understanding requires that as the frequency increases the average number of modes increases (see § 1.3.1) as well as the overall losses. How is it possible to observe *on a local scale* very strong fluctuations between very large errors and very small ones? Part of the answer is the random nature of the estimator of $\epsilon_{\varsigma^2}(\omega)$: this is inherent to its being an estimator of a statistical moment. But while this explanation can be readily accepted when observing the results in the higher frequency range of Fig. 2.1, the fluctuations are surprisingly strong at the opposite extreme. The question that should come to mind is: what is the accuracy of Weyl's approximation? Do we really have a clue about the actual number of modes being excited at a given frequency? The inevitable answer is no, there is no way of knowing it, unless for unrealistic canonical geometries. An explanation for the origin of these wild fluctuations is proposed in § 2.3, where the random nature of the modal density is fully taken into account.

It could be tempting, as it is the case for a number of people within the EMC community, to invoke much simpler explanations for local anomalies: 1) experimental errors; 2) inaccurate experimental setups; 3) statistical outliers. A detailed rebuttal of these oversimplified explanations is out of the scope of this dissertation; we can still suggest some ideas as to understand how to judge of their scientific pertinence. Although experimental errors do occur, the first point is one of the oldest techniques to discredit results that could, if proven right, put in jeopardy well-established, but perhaps not very accurate, models and explanations. The second point mostly refers to the idea of the presence of a deterministic residual contribution to the overall field; it can be observed as soon as a line-of-sight propagation path is possible between the sources exciting the cavity and the observer. While this scenario, usually referred to as partially developed speckle in optics [R26], results in a distortion of the field statistics, it has been proven theoretically and experimentally that what are often automatically regarded as unstirred components are in fact mathematical artifacts due to an incomplete statistical analysis; a detailed explanation was presented in [C7]. The third point does not deserve much attention in our opinion, as it is clearly a gross expedient to hide one's inability to explain physical phenomena. As it will be shown in § 2.3, statistical anomalies (outliers) can be explained on a physical ground.

2.2.2 Impact on confidence intervals

Despite the fact that (2.13) does not give any hint about the probability density functions of the electric (or magnetic) field, it can be used in order to predict another intriguing phenomenon, namely the increased rate of rejection of statistical tests aimed at assessing how close experimental data are to the probability density functions predicted by diffuse-field models.

The most widely used technique to measure how close an empirical probability distribution is to a theoretical one is that of goodness-of-fit tests [R15]. Perhaps the best known is Pearson's chi-squared test; within the EMC community, more stringent statistical tests have been adopted over the last 10 years, leading to a stronger preference for Kilmogorov-Smirnov and Anderson-Darling tests [R46]. A discussion of the rationale for applying this kind of tests to EMC-related tests is out of the scope of this dissertation, but some reflections have been presented in [C22].

Accepting the use of such tests as meaningful, it has been noticed that their is a non-negligible probability of rejecting the diffuse-field hypothesis even at relatively high frequencies, where a reverberation chamber is typically expected to work in an ideal state of diffusion [R46, R65]. Rather than resorting to the expedient of invoking rather unclear explanations [R54, R65, R42], an alternative approach can be devised thanks to (2.13).

Let us consider a real-life cavity, where the field statistics does not exactly correspond to the asymptotic laws predicted by the diffuse-field approximation. In practical configurations, quantities of interest are typically averaged over the random realizations generated by means of stirring techniques, in order to obtain a more accurate estimate of the true value of the quantity. An example is given by the average power received by a probe, or the average field intensity observed at a position.

We can exploit this use of averages by recalling that the central-limit theorem states that the asymptotic probability density function of these arithmetical averages is a Gaussian function. It is therefore sufficient to know the average and variance of each of the single realizations of the quantity of interest, in order to have a fair approximation of its probability density function. To this effect, (2.13) already provides the ratio of the first two moments of the electric-energy density, while it can be very easily modified to account for the squared-amplitude of any scalar field component.

Sticking to the electric-energy density W, we can measure a set of samples $\{W_i\}$ of electric-energy densities over a given position, obtained by means of any stirring technique. Assuming these samples to be iid, the diffuse-field hypothesis would require the samples to follow a chi-squared probability density function with 6 degrees of freedom. If the measurements were taken at sufficiently high frequency, the diffuse-field hypothesis would likely be taken for granted.

Current wisdom would require to assess this hypothesis by means of statistical tests, setting the diffuse-field hypothesis as the null hypothesis, i.e., the hypothesis assumed to hold against which the data will be tested. All of these tests will provide a measure

of the deviation of the experimental data from the theoretical distribution, by defining a sort of norm.

Let us focus on the most intuitive one, i.e., the idea of confidence interval [R40], i.e., the interval within which a random variable satisfying the null hypothesis will appear with a given probability $1-\alpha$; α is therefore the probability of observing a sample of a diffuse field outside the confidence interval, usually referred to as the significance level of a test. The confidence interval can be predicted for the arithmetic average (estimator) $\bar{W}$ computed from N_m samples measured at a given frequency

$$\bar{W} = \langle W_i \rangle_{N_m} = \frac{1}{N_m} \sum_{i=1}^{N_m} W_i, \tag{2.14}$$

with $\bar{W}$ asymptotically converging in probability to a Gaussian-distributed random variable with a variability $\varsigma^2_{\bar{W}}$ directly related to the variability of the samples $\{W_i\}$ as

$$\varsigma^2_{\bar{W}} = \frac{1}{N_m} \left(\frac{\langle W_i^2 \rangle}{\langle W_i \rangle^2} - 1 \right) = \frac{\varsigma^2_{W_i}}{N_m}. \tag{2.15}$$

The concept of outliers is based on these very ideas, by considering that the estimator $\bar{W}$ cannot belong to the reference distribution (null hypothesis) if it is significantly outside the confidence interval; significance takes here a statistical meaning as it is up to the experimenter to decide if unlikely extreme values should be regarded as significant or not. A typical choice is $\alpha = 5$ %.

Going back to the problem of spotting outliers, if a sample W_i falls outside the confidence interval, then three conclusions are possible:

1. the null hypothesis is valid : the definition of confidence interval allows samples to fall outside it with a probability α, so it is still possible to satisfy the null-hypothesis (perfect diffuse-field configuration) while observing some peculiar samples (rare events). Intrinsical to this picture is the idea of observing these outliers with a probability not significantly different from α;

2. the null hypothesis is assumed to be valid, while the observed rate of samples falling outside the confidence interval is significantly higher than α. The contradiction is solved by invoking experimental errors, such as unstirred components, operating as systematic errors (biases);

3. the null hypothesis is rejected by assuming the experimental work to be correct, applying in a strict manner a decision criterium set by statistical tests.

How could (2.13) help in this discussion? The answer is by proving that the confidence intervals computed from the null-hypothesis are too conservative, leading to a rejection rate that is *qualitatively* interpreted as a substantial deviation from the ideal state, while yielding in practice little difference.

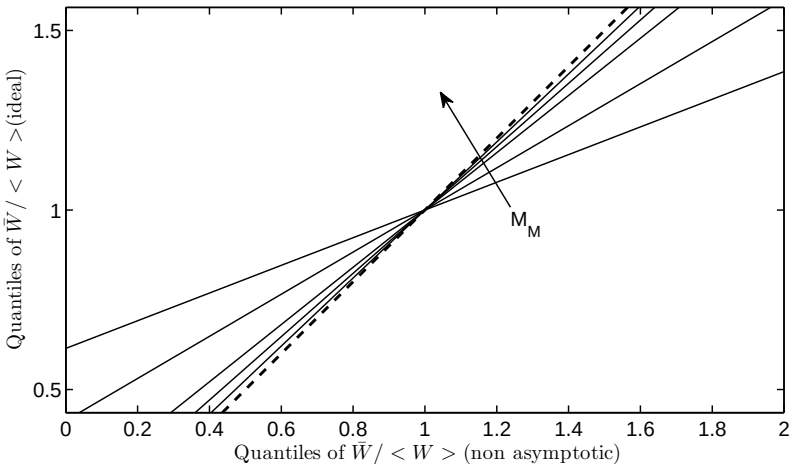

Figure 2.3 – Theoretical quantile-quantile plot of the asymptotic distribution laws for $\langle W \rangle$ in the asymptotic and non-asymptotic case, as based on (2.13), for a number of average overlapped modes $M_M = \{1, 3, 10, 20, 50\}$. The dashed line stands for the bisector, which is asymptotically approached as M_M increases. The size of the sample population is not needed in this type of plots, as it only intervenes in setting the confidence interval, with no effect on the relationship between the two quantile distributions.

We are talking about a distortion in the expectation of the confidence interval, which can be predicted in a straightforward manner. To this end, let us consider a number N_m of independent samples W_i large enough as to have their arithmetic average $\bar{W}$ approximating a Gaussian law, by virtue of the central-limit theorem. We aim at computing how a confidence margin defined for a significance level α under the hypothesis of a diffuse-field behavior, translates into another confidence margin whenever M_M happens not to be high enough. A good and intuitive way of assessing the effect of a finite M_M is to check how the quantiles of the asymptotic case, i.e., $M_M \to \infty$, relate to those of the modal description we have introduced. As we are dealing with this problem under the approximation of a normally distributed $\bar{W}$, the quantiles are given by [R40]

$$\frac{q_p}{\mu_{\bar{W}}} = 1 + \sqrt{2}\varsigma_{\bar{W}} \mathrm{erf}^{-1}(2p-1) \quad , \tag{2.16}$$

where $p = P(\bar{W} < q_p)$ is the probability associated to the quantile q_p, while $\mu_{\bar{W}}$ is the expected mean-value of $\bar{W}$ and $\varsigma^2_{\bar{W}}$ was defined in (2.15). The central-limit theorem allows to compute a good approximation of the quantiles of $\bar{W}$ just by knowing these two moments, for the case of an ideal χ^2_6-distributed W_i and for the more realistic case provided by (2.13). The result of this operation is presented in Fig. 2.3, where any

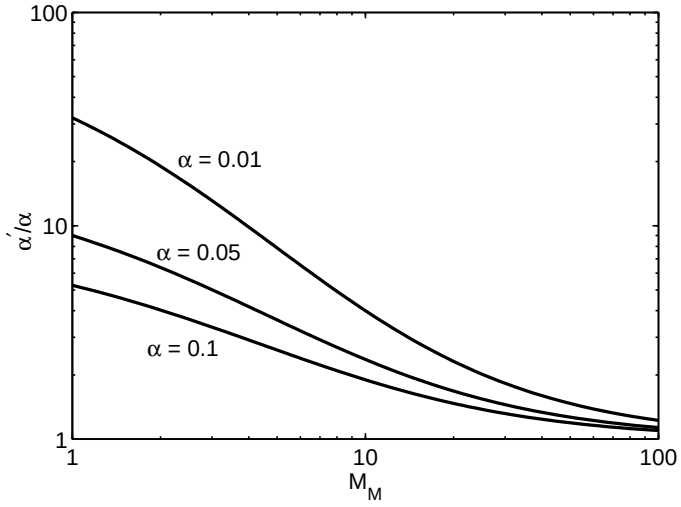

Figure 2.4 – Apparent significance level α' associated to the one based on asymptotic statistics (i.e.,the diffuse-field hypothesis), α. As the number of overlapped modes M_M decreases, the statistical interpretation of the arithmetic mean of experimental samples can be increasingly misleading, due to a higher variance with respect to the samples mean.

confidence margin established on the asymptotic case for a given significance level α is shown to lead to an inevitably larger margin with the same significance level as soon as M_M is found to be finite. It is interesting to notice that the case $M_M = 3$, often regarded as a good compromise for a diffused field in room acoustics, actually provides a more than twofold increase in the original confidence margin.

The other way round, choosing the same interval margin for the ideal and non-ideal cases, if this interval corresponds to a significance level α for the former case, this will lead to a corresponding significance level α' in the latter, related as

$$\alpha' = 1 - \mathrm{erf}\left(\frac{q_{1-\alpha/2}}{\sqrt{2}} \sqrt{\frac{M_M}{18/\pi + M_M}} \right) \quad . \tag{2.17}$$

This function is plotted in Fig. 2.4, for several values of α. These results provide a direct feeling about the increased probability of incurring into samples falling outside the originally intended confidence margin. The probability α' of this event increases not only when M_M is relatively low, but also when the significance level α is reduced. This type of interdependence has a potentially very harmful impact, as α is typically reduced in order to improve the significance of the results of a statistical test, thus reducing the number of samples that would be otherwise regarded as outliers: when expecting asymptotic results from a realistic RC, this risks leading to a higher rate of rejection of eventual hypothesis tests, i.e., the opposite effect expected in the first place, since the frequency of occurrence of outliers will inevitably increase.

The results in Fig. 2.4 should be considered with due care. As shown in [J7, App.], the average number of overlapping modes can be quite low, staying well below 3 at frequencies where a reverberation chamber is regarded (not only assumed!) as fully compliant with international standards [R2]. Still, Fig. 2.4 shows that for $M_M = 3$

the probability of estimating an average electric-energy density outside the confidence interval is 5 times higher for $\alpha = 5$ % and 13 times higher if $\alpha = 1$ %. In other words, despite the fact that in practice the cavity is working properly, the blind application of statistical concepts would lead to stronger rejection rates, yet not representative of a more or less important degradation of the performance of the cavity. Further elements have been added to this discussion in [C22], but the simple analysis here shown proves that statistical tests should not be used without linking them to practical measures of degradation of the performance. In the opposite case, the risk of depriving them of any quantitative meaning, hence usefulness.

2.3 Local statistical anomalies

The statistical anomalies (outliers) observed on a local scale in Fig. 2.1 are intriguing features of any reverberation chamber. In order to understand their origin, we need to go back to the definition of modal overlapping and hence of modal density. As recalled in § 1.3.1, the only estimate of the modal density easily accessible in practice is Weyl's approximation. It is therefore natural to wonder how far away from it is the *actual* modal density observed for a specific configuration; following this line of thought, what would be the effect of a deviation from Weyl's estimate? This issue was studied in [J7] and its major results are presented in § 2.3.1.

As soon as the idea of a random modal overlapping is considered, it becomes clear that the very existence of a LUF (or Schröder's frequency) as currently defined loses any physical ground. This point is discussed in § 2.3.2, where an alternative definition is suggested.

2.3.1 Random fluctuations in the modal overlapping

These questions can be answered by developing the results summarized in § 1.3.2: by knowing the probability density function of the distance between two consecutive frequencies of resonance, it should be possible to provide an estimate not only of their average number within a frequency bandwidth, but more generally to estimate the probability of observing more or less modes than expected on average from Weyl's approximation.

Recalling that the modes in which we are interested are those found within the average modal bandwidth $\bar{B}_M$, the above problem can be reformulated as a need to develop a probabilistic description of the number of modes found within $\bar{B}_M$. In order to stress the difference with the *average* number of such modes M_W predicted by Weyl's approximation, the *actual* number of modes overlapping will be referred to as M_{loc}, standing for the number of modes locally overlapping over $\bar{B}_M$.

Deriving the probability density function of M_{loc} from that of the spacing two consecutive resonant frequencies is more related to combinatorics than physics. The procedure developed in [J7] passes through the following steps:

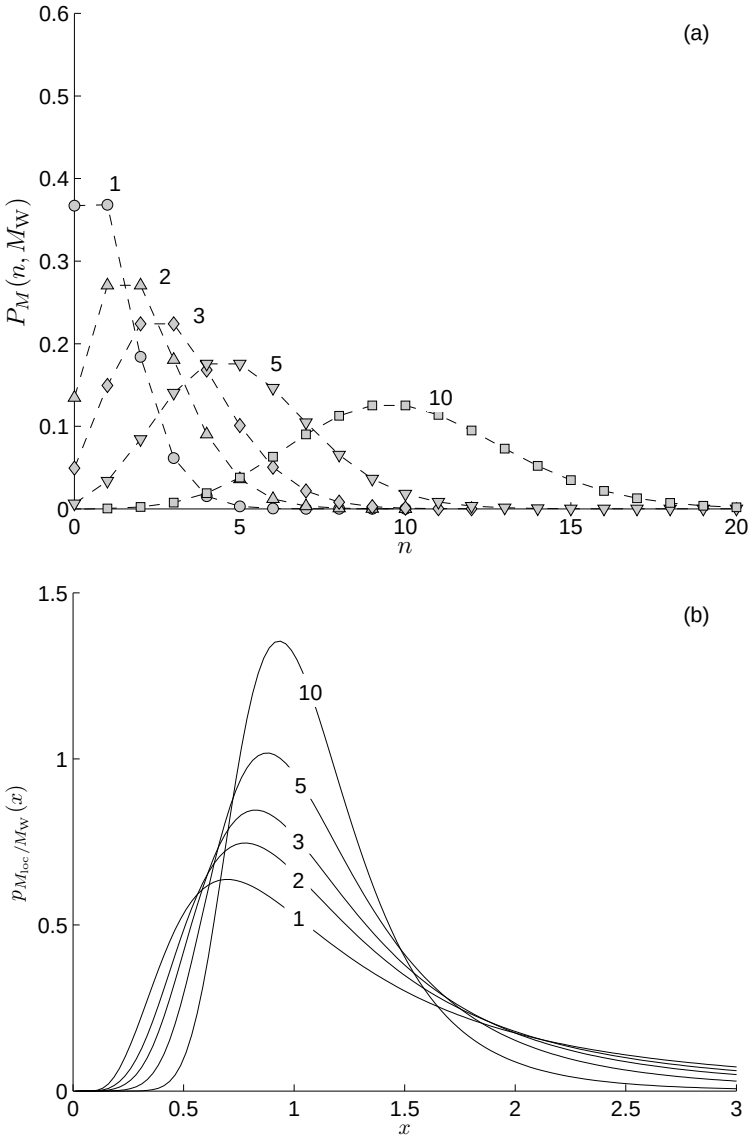

Figure 2.5 – Modal probability density functions for an integrable cavity : (a) number of modes observed over a given bandwidth, with respect to Weyl's formula estimation (numerical values close to each curve); (b) relative fluctuation of the local modal overlapping with respect to the estimate based on Weyl's formula.

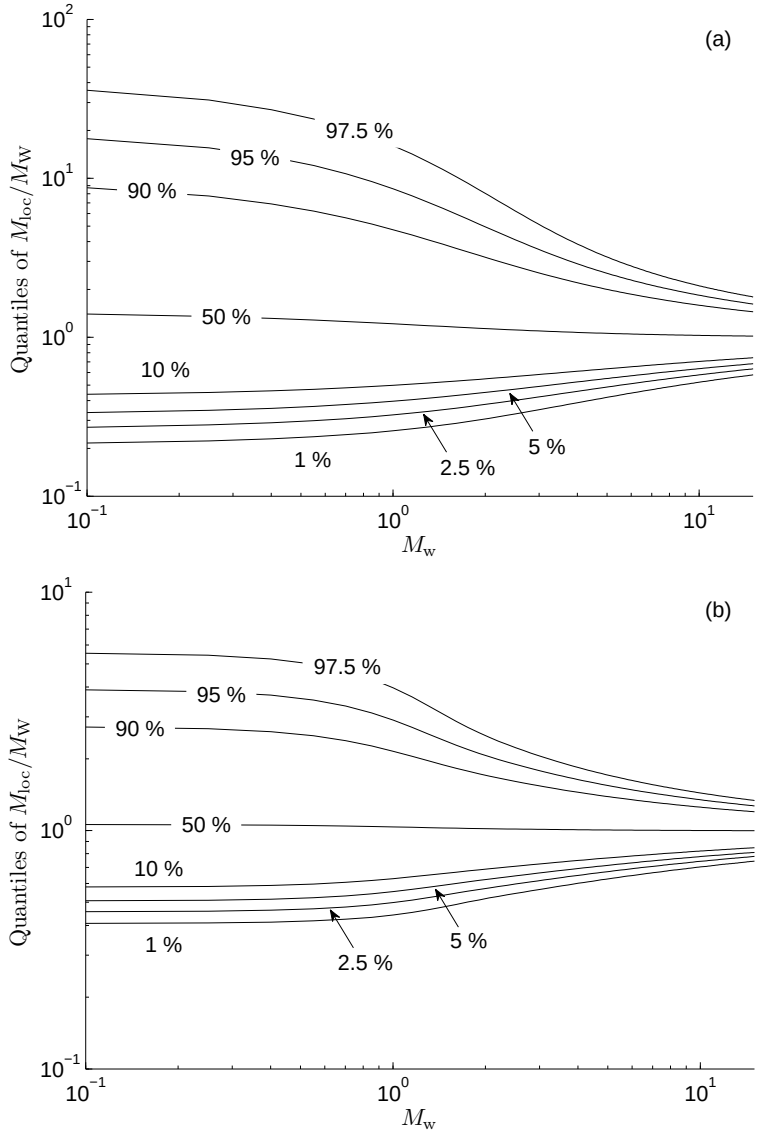

Figure 2.6 – Quantiles of the deviation of the local modal overlapping with respect to the estimate obtained from Weyl's formula, for (a) an integrable system and (b) a GOE chaotic one.

1. deriving the probability density function of the overall bandwidth S_n

$$S_n = \sum_{i=1}^{n} s_i \tag{2.18}$$

   covered by $n+1$ consecutive frequencies of resonance at distances $\{s_i\}$;

2. from S_n, the probability of observing n modes within a reference bandwidth B can be formulated as the probability of fulfilling the condition

$$S_{n-1} \leqslant B < S_n; \tag{2.19}$$

3. the effective number of modes observed over the bandwidth $\bar{B}_M$ is therefore directly obtained as

$$M_{\mathrm{loc}} = \frac{n}{S_n} \bar{B}_M, \tag{2.20}$$

   where the probability density functions of n and S_n are known by now from the previous steps.

Since the main point to ascertain here is to quantify the random fluctuations of M_{loc} with respect to M_W, it is natural to consider their ratio, implying

$$\frac{M_{\mathrm{loc}}}{M_W} = \frac{n}{S_n} \frac{1}{m_W}, \tag{2.21}$$

which is still, though not explicitly, dependent on the reference bandwidth B over which the local modal overlapping is studied. Examples of the probability density functions of n and M_{loc}/M_W computed for an integrable cavity (§ 1.3.2) for several values of M_W are presented in Fig. 2.5. It can be seen that for values of $M_W < 5$, the probability of observing no resonant mode is not negligible, while more in general the probability density functions of n are spread over a quite large range of values. The direct consequence is the appearance of fairly large fluctuations in the actual number of overlapping modes M_{loc} with respect to the values predicted by Weyl's approximation, as visible in Fig. 2.5(b).

The original motivation for this analysis is better served by Fig. 2.6, where some quantiles of the probability distribution of M_{loc}/M_W are shown for the two ideal cases of integrable and GOE chaotic cavities.

The median (50 % quantile) is very well approximated by the estimate M_W provided by Weyl's formula. Hence, there is an equal probability of observing either a higher or lower modal overlapping. In the context of deviations from the asymptotic statistics for field samples, the most important quantiles are those related to the probability of observing a lower modal overlapping. In this respect, when expecting $M_W = 1$, there is a 10 % probability of observing an actual modal overlapping below 49 % and 63 % of M_W, for an integrable and a GOE cavity, respectively. Such strong reduction is proven by our derivation to be a normal phenomenon in a large cavity, and not related to any non-ideality in its use. A 50 % reduction in the modal overlapping leads to a twofold increase in the additional term of the variability of the electric-energy density, as demonstrated in [J4] and recalled in (2.13). Worse, but perfectly normal scenarios can appear : with a probability of 1 % the modal overlapping can be found below 25 % and 44 % of M_W.

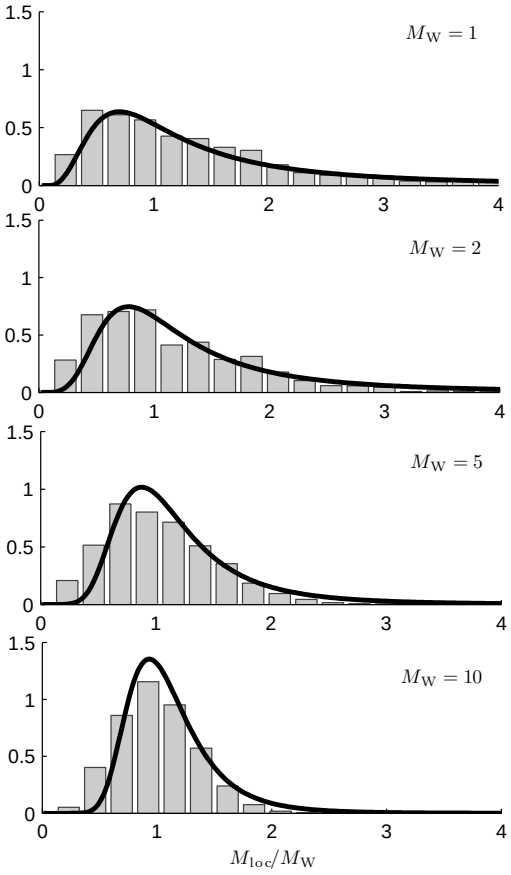

Figure 2.7 – Empirical probability distributions of the number of overlapped modes M_{loc} found in a rectangular cuboid cavity. These results pertain to the local modal overlapping M_{loc} counted over a frequency bandwidth where a reference overlapping M_{W} is predicted by means of Weyl's formula. The thick curves represent the theoretical probability density functions shown in Fig. 2.5(b).

These results could be expected to improve when a higher modal overlapping of $M_W = 3$ is considered. This value is often taken as a reference for the appearance of a diffuse-field condition in room acoustics [R75]. Even in this case, M_{loc} can be lower than 58 % and 72 % of M_W with a 10 % probability; with a probability of 1 %, below 34 % and 56 %, again for integrable and GOE cavities. Hence, even at relatively high modal overlappings, the probability of observing *normal* strong deviations in the field statistics should not be underestimated. Recalling that $M_W = 3$ is expected only at relatively high frequency [J7, App.], the appearance of statistical anomalies from a

local lack of modal overlapping seems to be very likely in the lower frequency range of operation of a reverberation chamber.

A probability of 1 % is compatible with the rate of appearance of local non-compliancies observed in practice, and could thus provide a physical explanation to the observation of outliers [R42]. It could also serve as an explanation for the existence of local non-compliancies even at higher frequencies, where the concept of diffuse field is usually taken for granted.

These predictions were verified by computing the local modal overlapping expected in a canonical cuboid cavity; analytical formulae are available to predict the frequencies of resonance of such a cavity [R33]. The bandwidths over which this operation was carried out were computed by taking Weyl's approximation (1.43), imposing a given M_W, finding out the bandwidth $M_W/m_W(f)$ over which this number of modes are expected to overlap at a given frequency and counting the *actual* number of modes. The four values $M_W = \{1, 2, 5, 10\}$ were considered, and the actual count $M_{\text{loc}}(f)$ was computed over 1000 frequencies (see [J7] for details). The empirical probability distributions thus obtained are shown in Fig. 2.7, where they are compared to the theoretical probability density functions shown in Fig. 2.5(b). Disagreements appear as M_W increases: in this case the spacings between adjacent resonance frequencies can no longer be regarded as independent random variables. Higher-order statistics should be included, as described in [R81], taking in to account longer-range correlation between spacing realizations.

Among the several approximations employed in this analysis, the hypothesis of a constant quality factor has hefty consequences on our results, since the quality factor of resonant modes are known to be strongly fluctuating quantities, too [R13, R25, R3]. This further source of randomness implies that the average modal bandwidth $\bar{B}_M$ should also be treated as a random variable, linked to that of the quality factor. Therefore, an extended model can be proposed by regarding all previous probability density functions as conditional to a fixed value $\bar{B}_M$, e.g.,

$$p_{M_{\text{loc}}/M_W}(x) \rightsquigarrow p_{M_{\text{loc}}/M_W}(x|\bar{B}_M). \tag{2.22}$$

The probability density function for the modal overlapping could thus be computed as

$$p_{M_{\text{loc}}/M_W}(x) = \int p_{M_{\text{loc}}/M_W}(x|y) p_{\bar{B}_M}(y) \mathrm{d}y. \tag{2.23}$$

This idea is still a proposal and it has not been pushed further. Nonetheless, (2.23) can be expected to present an increased statistical dispersion with respect to the simplified case of a fixed average quality factor, thus suggesting that the above results are in fact best-case results. The rate of increased probability in observing modal-depleted conditions requires solving (2.23).

2.3.2 Considerations about the definition of the LUF

It is useful to recall the trajectory of our investigations. We started from the observation that the usual approach of assuming a threshold frequency beyond which a cavity supports a diffuse-field model is flawed. The rationale behind this conclusion is that statistical anomalies appear even at frequencies well above this threshold frequency; tentative explanations of faulty setups appear rather unconvincing. The establishment of a formal relationship between modal overlapping and excess statistical dispersion in the electric-field intensity, while taking into account the random behaviour of modal spacing, has led to a statistical description of the probability of occurrence of the anomalies observed in the first place.

The natural consequence of this line of investigation is that the idea of a minimum frequency (LUF), as currently done, has no physical support. There is no minimum frequency above which the ability of a cavity to behave as a diffuse-field generator will improve *monotonously*, since there will always be a probability, though weak, of observing a local statistical anomaly at a given frequency.

An alternative idea can be introduced, based on our analysis: the LUF can be defined in probabilistic terms as the minimum frequency above which the *probability* of observing statistical anomalies reduces below a given value deemed reasonable. This idea is just a proposal, and is currently under investigation; still, it seems more natural, and physical, than all of the current rather arbitrary definitions. More importantly, it has a practical side, since knowledge of the probability of observing statistical anomalies is fundamental in order to assess the accuracy of any experimental result obtained in a cavity.

Chapter 3

Coherent field generation

Simplicity does not precede complexity, but follows it

Alan Perlis

REVERBERATING cavities are not always operated in conjunction with harmonic excitations. For example, multi-tone signals and wide-band noise [R44] are also used in acoustic reverberating rooms. These non-harmonic excitations are mainly introduced as an effective way of averaging out the random fluctuations found in the operation of reverberation chambers, e.g., in the case of radiated-power measurements, or as a randomization procedure, and are also used in the context of EMC tests when introducing frequency stirring procedures [R31].

In this chapter, we are rather concerned with a very different issue, that of using non-harmonic excitations in order to control the response of a cavity. The focus will be on the idea of making *coherent* applications possible. By this term we consider the generation of field distributions and propagating wavefronts that appear to be occurring in a free-space environment, as generated by deterministic sources.

So far we have kept stating that the field distributions generated within a large reverberating cavity is of non-coherent nature, resulting from a large number of reflection/diffraction interactions of propagating waves with the cavity boundaries. We have argued about the more or less diffusive nature of the field distribution in § 2, but have always taken for granted the non-coherent nature of any field distribution generated in a cavity, as a requirement for their use as standardized test facilities.

The idea of having coherent wavefronts propagating within a reverberating cavity as in free-space should therefore definitely come as a surprise. If any harmonic excitation results into a non-coherent field distribution, how could it be possible that a

collection (eventually continuous) of such distributions at different frequencies could resemble to free-space propagation conditions? The answer to this apparent paradox relies upon self-averaging properties of random media, when excited by means of special non-harmonic signals. As shown in § 3.2.1, this property is made possible by the existence of a large number of degrees of freedom over the excitation bandwidth, as discussed in § 1.2.3. Not only coherent fields can be generated, but their polarization can also be controlled in a manner that has no equivalent in free-space environments, as shown in § 3.2.4.

In order to access these properties, the concept of time-reversed excitation will be introduced in § 3.1, as the fundamental technique upon which the techniques here discussed are defined. The guiding principle along this chapter will be the idea that the use of complex media can, under certain conditions, simplify the generation of field distributions of interest in practical scenarios. All of these properties are possible only because the diffuse-field approximation can be invoked, as discussed in § 3.3, turning upside-down the received wisdom that free-space-like environments, e.g., anechoic chambers, provide the simplest conditions for the generation of coherent field distributions.

It should be clear from the beginning that our aim is not only to *emulate* free-space conditions within a reverberating cavity but more generally, as discussed in § 3.3.2, to define new procedures capable of offering properties that are not easily found in free-space environments, bridging the gap between anechoic and reverberating chambers.

3.1 Time reversal of waves

In this section we do not pretend to provide a thorough summary of time reversal, nor of all of its applications. We rather aim at recalling some of the assumptions that are necessary in order to have access to the properties of time reversal; moreover, we want to highlight some issues that are often neglected and that play a fundamental role in the limitations of this type of technique, particularly in the context herein considered for tests based on predefined wave configurations. A panoramic view of available time-reversal applications is necessary in order to get a better grasp of our contributions to this technique.

Time reversal is fundamentally the same technique previously known as phase-conjugation, which originated in optics in the late 70s [R95], primarily intended to compensate distortions (self-healing) in wavefronts propagating through complex media, particularly with the aim of focusing energy towards a given position in space. All of the applications of time reversal are based on one fundamental property of Helmholtz equation, namely its being time-reversal symmetric, implying an invariance of its solutions to a change of sign in the time variable. This property is apparent when looking

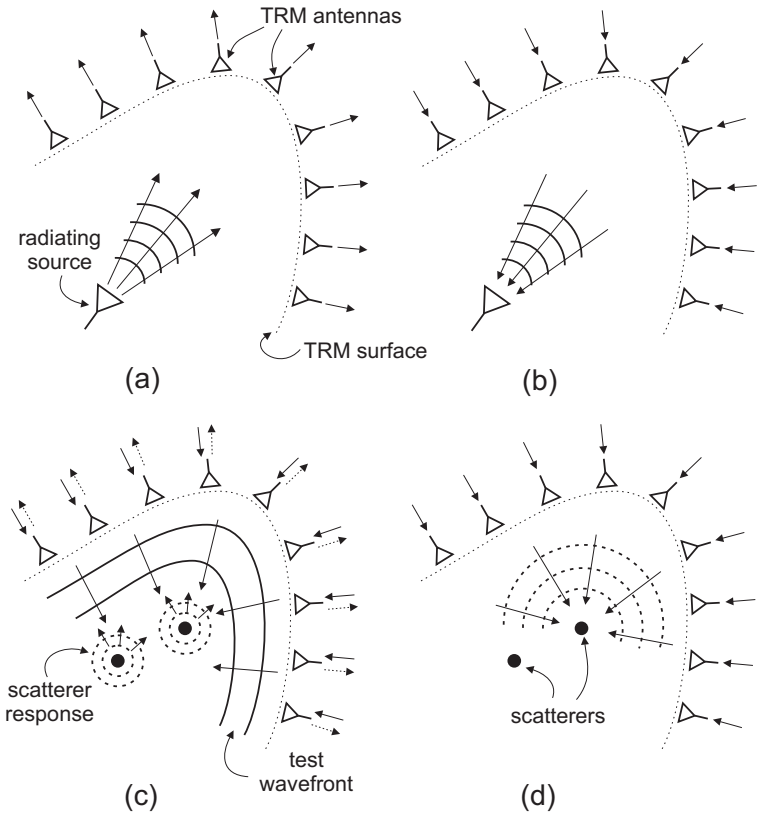

Figure 3.1 – A schematic representation of the two main time-reversal techniques currently available: (a)-(b) time-reversal of a radiating source; (c)-(d) selecting focusing over a point scatterer by means of the DORT approach.

at the definition of the equation in a homogeneous and source-less medium

$$\left(\nabla^2 + \frac{1}{c^2}\frac{\partial^2}{\partial t^2}\right)\boldsymbol{u}(\boldsymbol{r},t) = 0, \tag{3.1}$$

where $\boldsymbol{u}(\boldsymbol{r},t)$ is a generic vector solution, or wavefront, and c is the speed of light in the medium. Time-reversal applications typically exploit this property by coupling it to Huygens' principle: as depicted in Figs. 3.1(a)-(b), we can define a two-step procedure where the first step involves a source of radiation generating a diverging wavefront *recorded* by an ideally continuous set of transducers (e.g., antennas) deployed over a closed surface Σ. These transducers are usually referred to, in the context of time-reversal applications, as a time-reversal mirror (TRM) [R9]. Coupling Huygens' principle to the time-reversal symmetry of Helmholtz equation implies that by exciting the transducers with the time-reversed version of the signals received during the first phase, the TRM will generate an ideally perfect replica of the original wavefront, but this time converging back at the source, as a consequence of our inverting the direction of evolution of the time variable [R9].

The time-reversal symmetry of (3.1) is apparently always satisfied: in fact, this property is not shared by every solution $\boldsymbol{u}(\boldsymbol{r},t)$ of (3.1), since the time-reversal symmetry

is broken at least in two cases: 1) for wavefronts involving evanescent waves (source region); 2) when dealing with lossy media. This fundamental limitation implies that focusing wavefronts generated by means of time reversal cannot provide any focusing beyond the diffraction limit [R79, R58], i.e., the minimum size of the focusing spot is about the wavelength of the central frequency involved in $\boldsymbol{u}(\boldsymbol{r}, t)$, since the spatial information related to the evanescent waves cannot survive to the distance from the source to the TRM and back again. Only evanescent waves allow the reproduction of spatial field distributions with "faster" spatial variations than those associated to propagative contributions, i.e., related to a wavelength.

An important step in our proposal is the passage from the usually open media addressed when using the paradigm we just recalled, towards bounded ones, e.g., closed cavities. This issue was studied in several papers, e.g., [R19, R48], where it was shown that time reversal can still be applied in configurations where the notion of a continuous TRM surface is lost, as long as the cavity can be treated as highly-reverberant, in order to ensure a large number of independent degrees of freedom. In this case, the TRM can be shrunk to a few transducers with no need to share a portion of a continuous surface. Without going into details, as this is out of the scope of this dissertation, it is now the array of images of the actual transducers that constitutes a generalized TRM; the main difference is that the signals "applied" or "received" by each of these images are inevitably replicas of the few signals actually applied/received by the real transducers. The consequences of this strong interdependence are explored in §§ 3.2 and 3.3, by means of frequency and spatial correlation functions.

Image theory allows establishing a close relationship between open media and cavities; hence, the properties of time reversal can be expected to apply to the latter case, as equivalence theorems [R30] do not require to consider a continuous surface of equivalent sources (here, the TRM transducers). As a result, pulsed wavefronts can be generated in reverberating cavities, a surprising result that has received much attention during the last ten years, in particular within the acoustics community [R67, R19]. Concerning the case of electromagnetic reverberation chambers, the first experimental demonstration was provided in [R48], while theoretical investigations dealing with a realistic description involving losses was presented in [J2].

The ability to generate pulsed fields within a reverberation chamber is a topic that deserves a full investigation in its own: as a matter of fact, it is well-known that it is currently very hard to generate short-pulsed fields as required by some standards [R1] when testing immunity for EUTs closely exposed to high-power radar pulses: not only pulsed fields can be generated with time reversal, but it has been demonstrated that by focusing a part of the energy into a portion of the cavity, the already high energy efficiency of RCs can be dramatically increased when operating them with wide-band excitation signals [J3], as recalled in § 3.2.3. Furthermore, it has been recently shown that the polarization of the field thus generated in an RC can be easily controlled, with a remarkably pure polarization [J13], a fact discussed in § 3.2.4.

A last point to recall when dealing with time reversal is the development of the

DORT technique [R64], a French acronym meaning expansion of the time-reversal operator. This approach introduced a new paradigm for time reversal: standard time reversal considers that what will be the target of the focusing wave during the second phase (Fig. 3.1(b)), needs to be a source during the first one (Fig. 3.1(a)). The DORT allows avoiding the target to be a source, whenever it behaves as a *point* scatterer, i.e., as a passive device that will respond with a spherical wavefront to an externally excited locally plane wave. Under these conditions, the DORT technique implies using the TRM to generate a testing wavefront (Fig. 3.1(c)), to which the EUT will respond behaving as a passive scatterer. The DORT has been shown to allow focusing over one among several targets (Fig. 3.1(d)) as long as these are sufficiently separated in order to resolve them from an imaging point of view [R27]. The DORT may appear to have some interest for testing applications, particularly when dealing with passive EUTs that cannot be operated as active sources.

The problem with these two methods is that in the available literature time-reversal applications always aim at producing a focusing wavefront at some position in space. The motivation is never the generation of a wavefront for testing purposes: the reason why focusing is under consideration is typically either a clearer transmission of signals through complex media at a given position (e.g., a receiver in underwater [R43] and wireless communication schemes [R49]) or to improve imaging techniques [R64, R27, R96]. As we argue in § 3.3, this is not compatible with EUT testing, since EUTs are often electrically large and present distributed scattering features rather than localized ones.

3.2 Time-reversed transmissions through complex media

Albeit its being usually defined for the focusing of a wavefront, most (if not all) applications of time reversal aim at the reproduction of pulsed fields at a given position in space. For a signal-theory point of view, this problem is equivalent to the transmission of a signal from a transmitter to a receiver; in the case of pulsed-field generation, the receiver will just be characterized by an ideal field probe sampling the field without introducing any alteration. Hence our regarding all these applications as a point-to-point transmission problem.

In this respect, there is hardly any difference between time reversal and a matched-filter approach. Differences exist, but are to be found not at the position of the receiver, but around it: time reversal also aims at maximizing the amount of energy observed around the focal point, where the receiver stands, but this fact has no impact on the analysis of the quality of the transmission as a matched-filter application.

The transmission by means of any type of wave, be it scalar or vector in nature, will result in a scalar transfer function, relating the inevitably scalar signals at the transmitting and receiving ends. We will consider in the following that our objective is to transmit the best reproduction possible of a template signal $x(t)$ through a medium

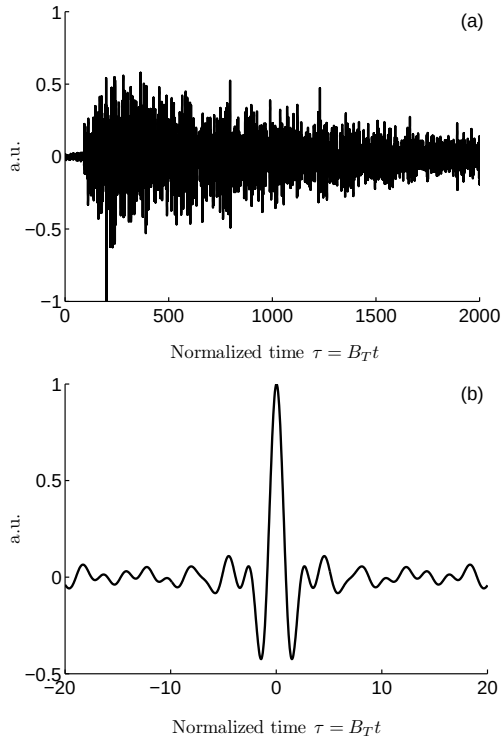

Figure 3.2 – An example of impulse responses measured in Supelec's reverberation chamber, for $f_c = 1.1$ GHz and $B_T = 0.5$ GHz: (a) direct impulse response $h(\tau)$ and (b) equivalent impulse response $g(\tau)$ for time-reversal transmissions. Time is normalized to the coherence time $1/B_T$.

with an impulse response $h(t)$. The output signal

$$y(t) = x(t) * h(t) \tag{3.2}$$

is typically a very poor reproduction of $x(t)$ when dealing with complex media, due to random fluctuations in the transfer function $H(\omega)$, especially random phase shifts that are capable of destroying the coherence of any non-harmonic signal. Clearly, this working assumption implies that the bandwidth B_T of $x(t)$ be much larger of the coherence bandwidth B_c of the medium transfer function; conversely, $x(t)$ would be properly transmitted even through complex media, a fact exploited in sub-carrier communication schemes, such as in orthogonal frequency-division multiplexing.

In the case of time-reversal communications, the received signal is rather given by

$$y(t) = h(t) * h(-t) * x(t), \tag{3.3}$$

having applied the signal $x(t) * h(-t)$ at the transmitter input port. Therefore the received signal could be interpreted as being transmitted trough an equivalent medium characterized by an *equivalent* transfer function

$$G(\omega) = |H(\omega)|^2, \tag{3.4}$$

directly applying the signal $x(t)$ originally intended for transmission. What has changed in between a direct transmission and the time-reversal one is that the equivalent transfer function is now real and positive, so that the main mechanism by which coherence was lost, namely random phase-shifts, is now absent. The Fourier spectrum of the received signal is still subject to random fluctuations, but as discussed in § 3.2.1, if $B_T/B_c \gg 1$, the received signal will be a good replica of $x(t)$.

A simple way of understanding this property requires looking back at (3.3): the equivalent impulse response is

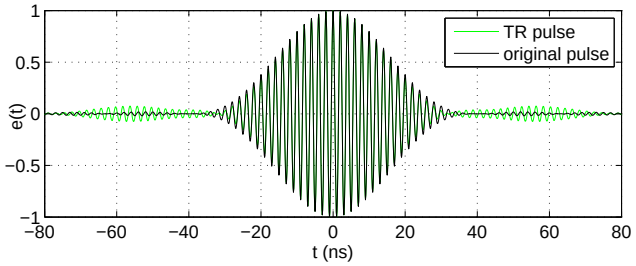

Figure 3.3 – An example of time-reversal transmission of a Gaussian pulse through Supélec's reverberation chamber, for a bandwidth $B_T = 50$ MHz. Random fluctuations outside the central-pulse region are visible.

$$g(t) = h(t) * h(-t), \tag{3.5}$$

i.e., the autocorrelation function of the original impulse response. In this last expression, as in the rest of this work, we will use an anti-causal representation, since $h(-t)$ should in practice be written as $h(T-t)$, where T is the duration of the impulse response. This choice is intended to simplify our notations and has no impact on our conclusions.

While $g(t)$ has no remarkable difference from $h(t)$ in the case of a free-space environment, in the case of random media it can be very different. If $h(t)$ bears no self-resemblance, then its autocorrelation function $g(t)$ will be characterized by a peak around $t \simeq 0$, while for $t \gtrsim T_c$, the coherence time of the medium, it will typically present a very low average value, fluctuating around the value zero. An example of these impulse responses is shown in Fig. 3.2, expressed in normalized time $\tau = B_T t$: while $h(\tau)$ is dominated by the relaxation time of the cavity with a time-constant of about 1000, $g(\tau)$ weakly fluctuates around zero as soon as $\tau \gtrsim 2$, implying that the latter is dominated by the coherence time of the cavity impulse response, which is indeed much shorter than its relaxation time.

It is clear from these ideas that the use of $g(t)$ rather than $h(t)$ in random media has a strong appeal, since $g(t)$ appears to be a fair approximation of a Dirac delta, thus potentially allowing the proper transmission of $x(t)$ at the receiver. Hence one of the reasons for the strong interest time reversal has suscitated in applications involving complex media. An example of the reproduction of a wide-band pulse within a reverberation chamber is shown in Fig. 3.3, where it is compared to the original one: the signal is indeed very well transmitted, even though random fluctuations appear at the two sides of the pulse. The problem of predicting the average intensity of residual fluctuations in time-reversal transmissions is addressed in § 3.2.2.

3.2.1 Self-averaging in time-reversal transmissions

Before looking more closely to the characteristics of time-reversal transmissions through a cavity, it is instructive to push the analysis of the point-to-point transmission a little further. To this effect, the equivalent transfer function $G(\omega) = |H(\omega)|^2$ will be regarded as a random function, subtended by unknown physical phenomena. In this respect, the

tools introduced in § 1.2.3 will be applied as a suitable black-box approach, by studying the statistics of the received signal at the time of focusing, i.e., $t = 0$, and the late-time statistics.

We first bring our attention over the value recorded at the receiver at the time of focusing,

$$y(0) = \int_{B_T} G(\omega)X(\omega)\mathrm{d}\omega. \tag{3.6}$$

Some interesting conclusions can be obtained by writing the above integral as a discrete summation, discretizing the integral over finite cells $B_c^{(i)}$ of identical bandwidth equal to B_c centered around the frequencies $\omega_i/2\pi$

$$y(0) \simeq \sum_{i=1}^{N_c} \int_{B_c^{(i)}} G(\omega)X(\omega)\mathrm{d}\omega. \tag{3.7}$$

with $N_c = \lceil B_T/B_c \rceil$ the number of coherence cells covered by the excitation bandwidth. In the rest of this chapter, we will always assume that the spectrum $X(\omega)$ of the excitation signal evolves slowly within a single coherence bandwidth. Moreover, since the signals targeted at the receiving end are often of pulsed nature, their spectra are typically flat over most of their bandwidth B_T, thus providing a further justification for this assumption.

Using the notations

$$X_i = X(\omega_i) \tag{3.8}$$

$$G_i = 2\mathrm{Re}\left\{\int_{B_c^{(i)}} G(\omega)\mathrm{d}\omega\right\}, \tag{3.9}$$

$$\tag{3.10}$$

(3.7) can be approximated as

$$y(0) = \sum_{i=1}^{N_c} X_i G_i, \tag{3.11}$$

having considered, for the sake of simplicity, $X_i \in \mathbb{R}^+$.

The value taken by $y(0)$ is a random function of the random transfer function $G(\omega)$. Ideally, $y(0)$ should be deterministic and predictable in a simple manner from basic information about the cavity. This condition can be expressed in statistical terms as

$$\sigma_y^2(0) = \left\langle \left[y(0) - \left\langle y(0) \right\rangle \right]^2 \right\rangle = 0. \tag{3.12}$$

The presence of a residual statistical dispersion of $y(0)$ can serve as a measure of the ability of time reversal in ensuring a proper transmission of a signal through a complex medium. Taking as example what is done in optics [R26], we will consider the contrast

$$\Lambda_p = \frac{\langle y(0)\rangle^2}{\sigma_y^2(0)}, \tag{3.13}$$

as a figure of merit of the quality of the transmission, with a meaning closely related to the concept of signal-to-noise ratio used in signal theory. Here no noise source has been assumed to exist, so the analogy should not be pushed too far; the role of "noise" is here played by the statistical dispersion of the received signal, and should be regarded as a speckle superposed to the ideal transmission expected in (3.12). The contrast (3.13) is noted by a subscript p since it is measured at the expected time of arrival of the peak of the signal, for what is typically a pulse around $t = 0$, thus related at its instantaneous power; an alternative definition pertaining to the received energy will be proposed in § 3.2.2.

The peak contrast Λ_p can be evaluated by substituting (3.11) into (3.13). The computation is very straightforward, but the variance $\sigma_y^2(0)$ deserves a little attention; it takes the shape

$$\sigma_y^2(0) = \sum_i X_i^2 \left\langle \left| G_i - \langle G_i\rangle \right|^2 \right\rangle + \sum_{i\neq j} X_i X_j \left\langle \left(G_i - \langle G_i\rangle\right)\left(G_j - \left\langle G_j\right\rangle\right)^* \right\rangle. \tag{3.14}$$

The initial choice of breaking the integral in (3.6) over coherence cells implies that random values taken by the $\{G_i\}$ can be expected to be weakly correlated, simplifying (3.14) into

$$\sigma_y^2(0) = \sum_i X_i^2 \sigma_{G_i}^2, \tag{3.15}$$

where $\sigma_{G_i}^2$ are the variances of the N_c iid random variables $\{G_i\}$. When dealing with large cavities, even for relatively large bandwidths with $B_T \gg B_c$, the statistical moments of the random function $G(\omega)$ can be expected to be independent of the frequency of observation, resulting in identical $\sigma_{G_i}^2$, $\forall\ i$. Hence

$$\langle y(0)\rangle = \bar{G}_i \sum_{i=1}^{N_c} X_i = N_c \bar{G}_i \bar{X} \tag{3.16}$$

$$\sigma_y^2(0) = \sigma_{G_i}^2 \sum_{i=1}^{N_c} X_i^2 = N_c \sigma_{G_i}^2 X_{\text{rms}}^2, \tag{3.17}$$

where $\bar{X}$ and X_{rms} are, respectively,the arithmetic and quadratic averages of $X(\omega)$ over B_T; thus (3.13) yields

$$\Lambda_p = \Lambda_{G_i} \frac{B_T}{B_c} \kappa^2, \tag{3.18}$$

where

$$\Lambda_{G_i} = \frac{\bar{G_i}^2}{\sigma^2_{G_i}}, \tag{3.19}$$

is the contrast of $G(\omega)$ sampled at the frequencies $\omega_i/2\pi$ and

$$\kappa = \frac{\bar{X}}{X_{\text{rms}}} \tag{3.20}$$

is a shape factor [J2], with $\kappa \leqslant 1$.

Equation (3.18), though resulting from a heavily simplified analysis, highlights some interesting properties of time-reversal transmissions. First of all, the received signal will be characterized by a decreasing uncertainty as the number of coherence bandwidths covered by the excitation signal increases. The reason for this property, often referred to as self-averaging [R16, R47, R60], is that in time-reversal transmissions the N_c degrees of freedom available are excited in a coherent way, i.e., in phase, since eventual random phase-shifts introduced by $H(\omega)$ are set to zero by phase-conjugated excitations. Second, (3.18) shows what is the role of the statistics of the propagation medium, as quantified by the contrast Λ_{G_i} of the transfer function. As we pass from a random to a deterministic medium the Λ_{G_i} increases asymptotically to infinity, as could be expected from the presentation of time-reversal propagation in open media in § 3.1. For the case of a cavity in a diffuse-field configuration, $H(\omega)$ is well modelled by a complex Gaussian process with iid real and imaginary parts; hence, $G(\omega)$ can be modelled as an exponential random process, i.e., $\Lambda_{G_i} = 1$. Third, the shape of the signal to be transmitted also plays a part that should not be underestimated; while for pulse-like signals $\kappa \simeq 1$, for more complex shapes with their energy not concentrated around the time $t = 0$ but spread over a larger support, the final contrast will be found to be lower than expected from simpler considerations [R7].

Time-reversed excitation signals appear to remarkably simplify the problem of transmission through complex media: while a direct transmission would result in a strongly distorted signal, with random amplitude and phase modulation (random transfer function), non-harmonic signals generated by means of the procedure described in § 3.2 lead to an asymptotically deterministic transmission of the original signal $x(t)$. This asymptotic value can be derived on the basis of energy-conservation considerations, i.e., macroscopic ones, which do no require any specific information about the fine structure of the medium [J5, App. A].

Can these results be expected to hold also for $t \neq 0$? The answer is no, and it can be understood by studying (3.7) at an instant t:

$$y(t) = 2\mathrm{Re}\left\{\sum_{i=1}^{N_c}\int_{B_c^{(i)}} X(\omega)G(\omega)\mathrm{e}^{+\mathrm{j}\omega t}\mathrm{d}\omega\right\} \simeq \sum_{i=1}^{N_c} X_i G_i \cos(\omega_i t). \tag{3.21}$$

The difference between (3.21) and (3.7) is that while the $\{G_i\}$ summed up coherently in (3.7), now they take part to a random-walk process, activated by the random phase-shifts introduced by the Fourier kernels. The sum passes from coherent at $t = 0$ to incoherent as soon as the phase-shifts are allowed to rotate rapidly, effectively behaving as a uniformly distributed random variable. It is the case, e.g., when between two consecutive sub-bandwidths $B_c^{(i)}$ the phase-shift is far greater than 2π, i.e., for $t \gtrsim 1/B_c$. In this case the received signal corresponds to the signal that would be received within a large cavity under a diffuse-field configuration, since the random-walk process destroys any would-be coherent transmission. No coherent component is present now, leading to a fully developed speckle signal [R26] with $\langle y(t)\rangle \to 0$ and an unchanged variance with respect to (3.16).

The reason for the absence of coherent transmission is not the fact that $x(t) \simeq 0$ at the time of sampling; even with a non-negligible coherent signal, it could not be observed at the receiving end, because of the random-walk process.

It is important to bear in mind that the use of non-harmonic signals should not be interpreted as a need for wide-band signals, as it has been the case in most of the investigations carried out in acoustics [R94, R22, R17], where relative bandwidths up to 100 % were considered. As proven by the analysis in § 3.2.1, the actual criterium is to ensure $B_T/B_c \gg 1$; the need for wide-band signals in acoustics is likely justified by a wider coherence bandwidth. In the case of *reverberating* media, the final bandwidth B_T can be narrow enough to regard the signal $x(t)$ as quasi-harmonic; as an example, for a standard electromagnetic reverberation chamber, at 1 GHz, with $\bar{Q} \simeq 10^4$, the coherence bandwidth would be of the order of 100 kHz, thus resulting in at least 100 degrees of freedom when applying a transmitting signal with $B_T/f_c \simeq 1$ %. The resulting peak contrast Λ_p would be around 20 dB, thus a fairly clear transmission.

3.2.2 Coherent-transmission efficiency through reverberating media

Most of the analyses of the self-averaging property observed in time-reversal transmissions through complex media consider the generation of a strong contrast at the time of focusing as the most important observable [R18, R23, R41]. Indeed, in some applications the objective can be to generate a spot of pulsed energy regardless of its time evolution.A more general approach is to assess the ability of time-reversal transmissions to reproduce specific pulsed shapes at the receiver; the transmission of data is an example of an application where it is not sufficient to generate a maximum in the instantaneous power observed at the receiver.

In this respect, an alternative analysis was presented in [J2] for the case of a reverberating cavity, where the received signal $y(t)$ was described as the superposition of a

term coherent with the original signal $x(t)$ and a residual part $n(t)$

$$y(t) = \rho x(t) + n(t). \tag{3.22}$$

An optimal transmission through time reversal would therefore require that for a given input energy at the transmitter end, the fraction of energy at the receiver maintaining a coherence with $x(t)$ be maximized. It is therefore sensible to introduce a slight modification of the idea of contrast: rather than just assessing the ratio between the signal at $t = 0$ over the rms value of the residual late-time fluctuations as done in (3.18), we will consider the ratio between the energy of the coherent part of the received signal and the total energy value of the residual part, i.e.,

$$\Lambda = \frac{\mathscr{E}_c}{\mathscr{E}_n} \quad , \tag{3.23}$$

where the energy $\mathscr{E}_c$ of the coherent part is given by

$$\mathscr{E}_c = \rho^2 \mathscr{E}_X = 2\rho^2 \int_{B_T} |X(\omega)|^2 \mathrm{d}\omega \quad , \tag{3.24}$$

and the energy $\mathscr{E}_n$ of the residual part is

$$\mathscr{E}_n = 2 \int_{B_T} |X(\omega)|^2 |H(\omega)|^4 \mathrm{d}\omega - \mathscr{E}_c \quad . \tag{3.25}$$

In practical terms, Λ is important since it assesses how much of the energy of the received signal can be used to extract information, as part of a coherent transmission system. The coherent-transmission efficiency η_c can be defined as

$$\eta_c = \frac{\mathscr{E}_c}{\mathscr{E}_c + \mathscr{E}_n} = \frac{\Lambda}{1+\Lambda}, \tag{3.26}$$

as a figure of merit assessing the fraction of received energy that is coherent, as opposed to the random-like behaviour of the residual fluctuations.

Moreover, the original definition of contrast (3.18) can be related to Λ by approximating the residual part with an exponential profile, with a time-constant $\bar{Q}/\omega_c$, where $\bar{Q}$ is the average composite quality factor of the cavity. Knowing $\mathscr{E}_n$ and its time-constant, its rms amplitude at $t = 0$ can be directly computed, yielding

$$\Lambda_p = \frac{\bar{Q}}{\pi} \frac{B_T}{f_c} \kappa^2 \Lambda \quad , \tag{3.27}$$

where κ was introduced in (3.20).

We can gain some insight into the values taken by these three figures of merit, namely Λ_p, Λ and η_c, by applying the random spectral model introduced in § 1.3. In this respect, the transfer function $H(\omega)$ can be represented as a discrete sum

$$H(\omega) = \sum_{i=1}^{M} \alpha_i \psi_i(\omega), \tag{3.28}$$

where $\{\psi_i(\omega)\}$ is the set of modal responses related to resonance frequencies $\{f_i\}$ and $\{\alpha_i\}$ constant coefficients. Modelling the sets $\{\alpha_i\}$ and $\{f_i\}$ as two sets of iid random variables leads to a random transfer function $H(\omega)$, with random figures of merit Λ_p, Λ and η_c.

Proceeding in that same manner, the sets of modal coefficients and the frequencies of resonance can be modelled as random variables, leading to a random transfer function $H(\omega)$ and random figures of merit Λ_p, Λ and η_c. Their average values have been studied in [J2, J6], proving that

$$\langle \Lambda \rangle = \frac{M_M}{M_M + 1/\pi} \tag{3.29}$$

$$\langle \eta_c \rangle = \frac{M_M}{2M_M + 1/\pi}, \tag{3.30}$$

with M_M the average number of overlapped modes over B_T (see § 1.3.1). A direct consequence of (3.29) and (3.30) is that for an increasing number of overlapping modes

$$\langle \Lambda \rangle \rightarrow 1 \tag{3.31}$$

$$\langle \eta_c \rangle \rightarrow \frac{1}{2}, \tag{3.32}$$

a result that can therefore be expected to hold under a diffuse-field approximation. Hence, the best-case performance of a time-reversal transmission system will be limited to half the received energy following a time-evolution set by the original signal $x(t)$, while at least the same amount of energy will be wasted in fluctuations that have no use. The result is a coherent-transmission efficiency limited to $1/2$.

Recalling the example of Fig. 3.3, these asymptotic results could seem counterintuitive, since the rms amplitude of the fluctuations appears to be negligible with respect to the coherent part around $t = 0$. In fact, the support over which the fluctuations maintain an almost constant average intensity is, typically, much larger than that of the coherent part of the signal; while the former is proportional to the relaxation time of the cavity, i.e., $\bar{Q}/\omega_c$, the latter is proportional to $1/B_T$, for a pulsed signal $x(t)$. Therefore, the application of time reversal to reverberating cavities though allowing the reception of clear reproductions of a template signal $x(t)$, does that at the expenses of a reduced energy efficiency, since at least the same amount of energy is wasted into residual random fluctuations running over a long span of time.

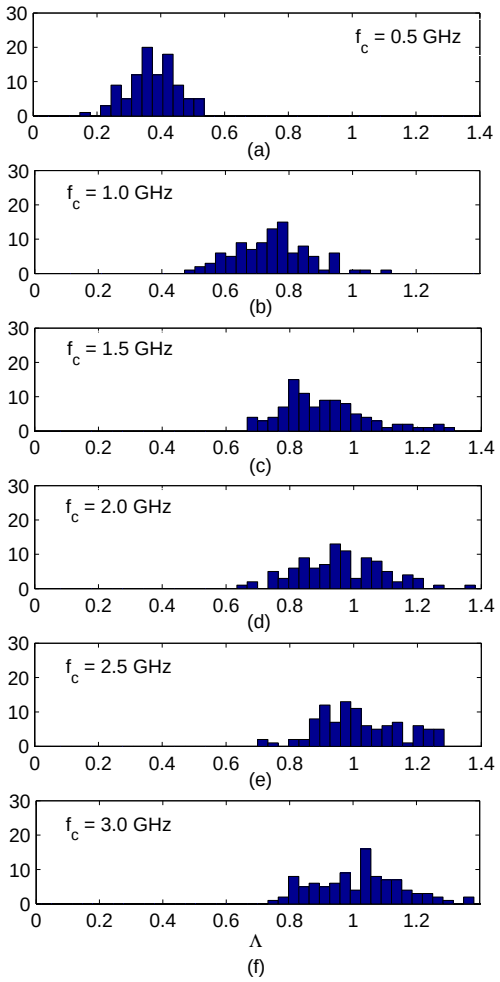

Figure 3.4 – Frequencies of occurrence for the energy contrast Λ as computed from experimental data measured over a bandwidth $B_T = 100$ MHz, centered around the frequencies $f_c = \{0.5, 1, 1.5, 2, 2.5, 3\}$ GHz (top to bottom). Each histogram was obtained from a population of 100 sample transfer functions as measured between a fixed transmitter antenna and a moving electro-optical probe.

Results demonstrating the validity of this prediction are shown in Fig. 3.4, where Λ has been computed from experimental data and represented as histograms. As the frequency increases, so does the average number of overlapping modes, thus leading to predicted saturation in the value of Λ; the statistical dispersion of Λ is limited to less than ± 1 dB.

A direct comparison between theoretical and experimental values observed for η_c is presented in Fig. 3.5, proving the accuracy of (3.30). Fig. 3.5 also proves another important point: the energy efficiency Λ does not depend on the bandwidth of the excitation signal, but is uniquely identified by the statistical properties of the medium. The effect of an increasing bandwidth over the peak efficiency Λ_p is therefore heavily dependent on the shape of the template signal $x(t)$, as measured by κ: as a conclusion, it is not at all enough to increase the bandwidth in order to improve the accuracy of the transmission, but it is rather more important to ensure an efficient use of the bandwidth, in the sense of providing the maximum peak intensity for a fixed amount of energy.

3.2.3 Conversion efficiency

While in a harmonic steady-state the energy-density is on average evenly distributed over the entire volume of a cavity (perfect diffusion), the fact that time reversal can generate a focusing field distribution, implies that at a given time a

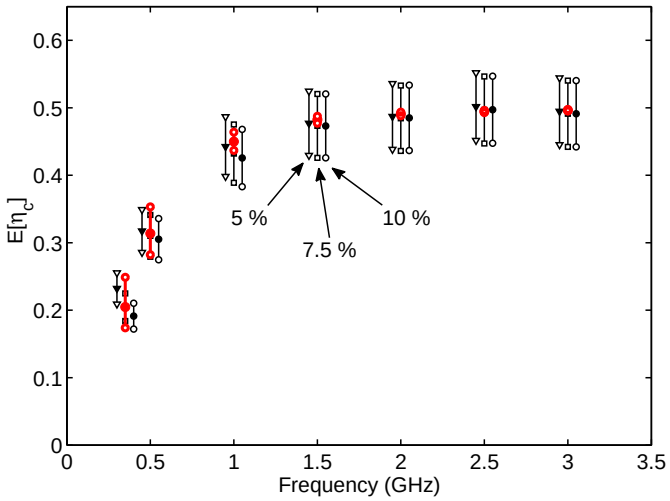

Figure 3.5 – Experimental results for the coherence efficiency of time-reversal transmissions within an electromagnetic reverberation chamber. Results for a 5 % (▽), 7.5 % (□) and 10 % (○) relative bandwidth are shown; results predicted by (3.30) are indicated by a full red dot. The bars on the experimental results refer to measurement uncertainty estimated at ±10 % of the nominal value, those on theoretical ones were obtained by propagating an uncertainty of ±30 % on the estimated $\bar{Q}$.

non-negligible fraction of the overall electromagnetic energy $\mathscr{E}_{\text{in}}$ injected into the cavity will be more strongly concentrated within a smaller region of space. As a result, one can expect that time-reversed signals could be used as a straightforward technique to improve the ability of reverberation chambers in generating high-intensity fields.

This idea was explored in [J3], by means of a diffuse-field approximation, imposing the same input energy $\mathscr{E}_{\text{in}}$ injected in the case of a harmonic and time-reversed excitation. In the case of a harmonic excitation, this input energy was set in order to ensure that a steady-state response was practically reached with a 95 % level. A conversion efficiency was introduced, defined as

$$\eta = \frac{\max\limits_{t} \|\mathbf{e}(t)\|^2}{\mathscr{E}_{\text{in}}}, \tag{3.33}$$

and computed for the two types of excitation signals.

The ability of time reversal in improving the conversion efficiency was therefore measured by the conversion gain

$$G = \frac{\eta_{\text{TR}}}{\eta_{\text{CW}}}, \tag{3.34}$$

which was proven to be equal to

$$G = \frac{B_T \bar{Q}}{\pi f_c}, \tag{3.35}$$

i.e., $G \propto N_c$. Once again, a figure of merit for time-reversal applications to reverberation chambers appear to be proportional to the number of coherence bandwidths covered by the Fourier spectrum of the excitation signal.

The validity of (3.35) was proven with experimental results in [J3]. The direct consequence is the prediction that time-reversal excitations of a reverberation chamber can easily outperform harmonic-driven ones by several orders of magnitude, by concentrating part of the stored energy within a smaller region, for a short instant. It could be argued that this is not really useful, since reverberation chamber already enable higher conversion efficiencies than free-space configurations; in fact, when testing aeronautical devices, field levels as high as 11 kV/m can be required [R1], in order to simulate the response of an EUT when passing in close range of radar systems, as well as to test its hardening to high-power microwaves that could be used in electronic warfare. The generation of such field levels is not a trivial problem, and the power amplifier required in harmonic-driven chambers are often prohibitively expensive; the extra margin provided by time-reversed excitations therefore constitute a promising solution to this problem.

3.2.4 Polarization control

Being capable of transmitting pulsed signals through a complex medium is a remarkable feat, but in the case of a vector field it would be even more interesting if its polarization could be controlled, too. This possibility, first investigated in [J13] and [C18], can be studied by assuming the vector transfer function $\boldsymbol{H}(\omega)$ between the input port of an antenna and the electric field measured by an observer within a cavity as known.

Let define an excitation signal $w(t)$ whose Fourier spectrum $W(\omega)$ be

$$W(\omega) = X(\omega)\boldsymbol{H}^{\mathrm{H}}(\omega) \cdot \hat{\boldsymbol{p}}, \tag{3.36}$$

where $\hat{\boldsymbol{p}}$ is a complex unit vector representing the polarization of the field to be generated at the observer position. $X(\omega)$ is the Fourier spectrum of the signal to be transmitted. The resulting electric field observed at the time $t \simeq 0$, generated by applying $w(t)$ at the antenna, can be written as

$$\boldsymbol{e}(0) = \int_{B_T} X(\omega)\boldsymbol{H}(\omega)\boldsymbol{H}^{\mathrm{H}}(\omega) \cdot \hat{\boldsymbol{p}}\, \mathrm{d}\omega. \tag{3.37}$$

Using the same approach introduced in § 3.2.1, breaking B_T into a discrete sequence of coherence bandwidths of the scalar components $H_i(\omega)$ of $\boldsymbol{H}(\omega)$, yields

$$\boldsymbol{e}(0) \simeq \bar{X} \left(\sum_{m=1}^{N_c} \boldsymbol{H}(\omega_m) \boldsymbol{H}^{\mathrm{H}}(\omega_m) \right) \cdot \hat{\boldsymbol{p}}, \tag{3.38}$$

which, by virtue of the law of large numbers, can be approximated, for $N_c \gg 1$ as

$$\boldsymbol{e}(0) \simeq \bar{X} \frac{B_T}{B_c} \left\langle \boldsymbol{H}(\omega_m) \boldsymbol{H}^{\mathrm{H}}(\omega_m) \right\rangle \cdot \hat{\boldsymbol{p}}, \tag{3.39}$$

as long as $\left\langle \boldsymbol{H}(\omega) \boldsymbol{H}^{\mathrm{H}}(\omega) \right\rangle$ is independent of ω over B_T. The averaged quantity was already considered in § 1.4.1 for an ideally diffusive medium, with

$$\left\langle \boldsymbol{H}(\omega) \boldsymbol{H}^{\mathrm{H}}(\omega) \right\rangle = S(\omega) \underline{\mathbf{1}}, \tag{3.40}$$

where $S(\omega)$ is the spectral power density observed in the medium for a unit-power excitation. Therefore, for a diffusive medium with $S(\omega) \simeq S(\omega_c)$ and $B_T/B_c \gg 1$,

$$\boldsymbol{e}(0) \simeq \bar{X} S(\omega_c) \frac{B_T}{B_c} \hat{\boldsymbol{p}}, \tag{3.41}$$

i.e., an electric field with a polarization corresponding to a perfect reproduction of the vector $\hat{\boldsymbol{p}}$. Clearly, residual statistical fluctuations must be expected for this asymptotic result, with an average intensity reducing as $1/\sqrt{N_c}$, as already discussed in § 3.2.1.

The most interesting implication of (3.41) is that thanks to the definition (3.36) of the excitation signal $w(t)$, the polarization of the electric field at a given position can be controlled just by means of a signal synthesis approach, rather than by relying on the mechanical alignment of a source with a high cross-polarization rejection. An experimental demonstration of this possibility is given in Fig. 3.6, where the electric field generated at a fixed position within Supelec's reverberation chamber is shown for three different choices of the polarization vector $\hat{\boldsymbol{p}}$; it is clear that for $t \simeq 0$ not only the field is no longer incoherent and, more importantly, it presents a deterministic polarization, oriented along the direction pointed by $\hat{\boldsymbol{p}}$.

What is remarkable is that it is not the source that ensures the generation of a polarized field, but the diffuse nature of the field propagating within the cavity. This statement could seem paradoxical, but the above mathematical demonstration shows that it is the property (3.40), intrinsic to a diffuse-field configuration, that ensures this result.

3.3 Emulating free-space propagation

The results presented in § 3.2 seem to imply that time-reversed excitation of diffusive cavities should be regarded as a promising field of investigation with practical applications. Within the framework of device testing, the ability to generate short pulses in a

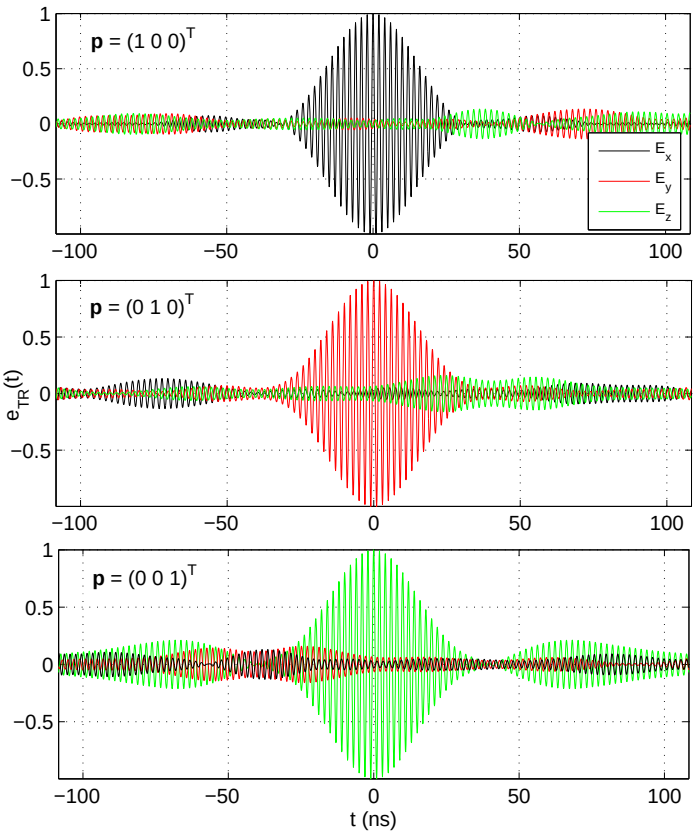

Figure 3.6 – The field components obtained from experimental results measured at one position, for a Gaussian pulse. Each plot corresponds to a weight vector **p** with just one non-null element. Top to bottom, the x, y and z components of the fields are ideally the only components excited when the pulse attains its peak value.

weakly lossy medium together with an accurate control of the field polarization have a direct appeal to EMC testing, particularly for defense applications.

Unfortunately, such conclusions miss at least two important issues : devices are seldom smaller than a wavelength and it is not especially useful to control the field over just one point in space. Test facilities rather require the ability to generate known and repeatable wavefronts, since most often the characteristics of EUTs are expressed as functions of their response to extended incident wavefronts.

The problem is that time-reversal techniques in their present state are not suitable for device testing: they are actually mismatched to practical needs, as they have been designed to deal with mainly point scatterers, rather than electrically extended ones, as it is often the case when dealing with real-life EUTs, and this goes without taking into account the issue of polarization, which leads to an even more complex scenario when compared to the scalar-wave propagation and scattering undergoing in acoustics.

The standard implementation of time-reversal techniques implies that each time we wish to generate a new converging wavefront, its diverging version needs to be generated by a real source in the first phase. Furthermore, as the characteristics of the

wavefront change, e.g., the direction of arrival or the polarization, the first phase is to be carried out again. This is clearly a strong limitation when proposing time reversal for testing applications, since as soon as a wide range of configurations is to be tested, the repetition of the two phases and the ensuing longer test duration could outweigh the benefits of time-reversal excitations. Moreover, the question of how to generate the diverging wavefront in the first place is far from trivial, since the testing wavefront (i.e., the converging version) will need to be radiated by a *real* source that therefore needs to be tailored to this purpose.

The solution to this mismatch is to shift our attention from the idea of reproducing a wavefront focusing over one point to the idea of *directly* generating *any* focusing wavefront. By this last term, we consider the ability to control all of the parameters defining a wavefront, e.g., its time-dependence, polarization, directivity and direction of arrival. This reflection has motivated our proposing an alternative approach based on the use of synthetic sources, leading to a new paradigm for time reversal that is not only suitable for EMC purposes but also brings in new advantages for any test based on submitting an EUT to impinging wavefronts. This approach, that we have named the Time-Reversal Electromagnetic Chamber (TREC) was originally introduced in [C25] while the first experimental demonstration was proposed in [J15].

3.3.1 A change of perspective : wavefront generation

The general case of *coherent* wavefront generation within a diffusive cavity was the subject of a recent paper [J5], where the diverging wavefront to be time-reversed is regarded through the lens of the equivalence theorem [R30]; the idea is to move the focus from the source to the wavefront it generates. With reference to Fig. 3.7, a *virtual* source can be defined, together with a surface Σ over which equivalent currents can be defined in such a way as to generate a wavefront radiating away from Σ identical to that of the virtual source.

Based on the assumption of knowing the vector transfer functions relating the excitation voltages applied to discrete TRM antennas to the electric and magnetic fields over Σ, and that all points over Σ stand in the far-field region of the virtual source, it can be shown that the voltages V_i that should be applied to the i-th TRM antenna during the *second* phase is [J5]

$$V_i(\omega) = \int_\Sigma \boldsymbol{N}_{\mathrm{eq},i}(\boldsymbol{r}', \omega) \cdot \boldsymbol{E}^*_{\mathrm{wf}}(\boldsymbol{r}', \omega) \mathrm{d}\boldsymbol{r}', \tag{3.42}$$

with

$$\boldsymbol{N}_{\mathrm{eq},i}(\boldsymbol{r}, \omega) = \frac{\boldsymbol{N}_{e,i}(\boldsymbol{r}, \omega)}{\zeta_0} + \hat{\boldsymbol{r}} \times \boldsymbol{N}_{m,i}(\boldsymbol{r}, \omega), \tag{3.43}$$

where $\boldsymbol{N}_{e,i}(\boldsymbol{r}, \omega)$ and $\boldsymbol{N}_{m,i}(\boldsymbol{r}, \omega)$ are the vector transfer functions relating the electric and magnetic fields to the input port of the i-th TRM antenna, respectively.

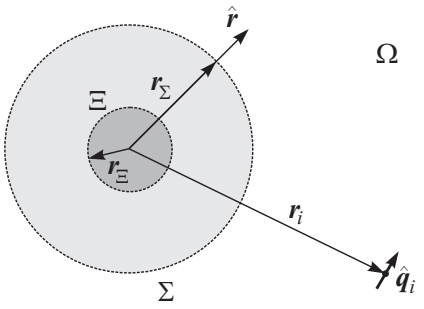

Figure 3.7 – Configuration for the application of Love's equivalence theorem. Equivalent electric and magnetic currents are defined over the surface Σ, representing the wavefront $\boldsymbol{E}_{\mathrm{wf}}(\boldsymbol{r},\omega)$ that would have been generated by a synthetic source contained in the volume bounded by the surface Ξ. These elements are embedded into a complex medium Ω. The i-th TRM antenna is modelled as an elementary dipole in $\boldsymbol{r}_i$, oriented along $\hat{\boldsymbol{q}}_i$.

Equation (3.42) is of direct practical importance because it implies that the first phase can be totally removed and more specifically that there is no need for a physical source in the first place. Our proposal of using equivalent sources over Σ as a proxy of a virtual source could lead to assuming that a distributed-source network is now necessary; in fact, knowledge of the transfer functions $\boldsymbol{N}_{e,i}(\boldsymbol{r},\omega)$ and $\boldsymbol{N}_{m,i}(\boldsymbol{r},\omega)$ as measured by means of field probes allow avoiding such a complex scenario. Moreover, (3.42) also states that potentially *any* wavefront can be generated when adopting this improved version of time reversal; no assumption has been made on the shape of the target wavefront $\boldsymbol{E}_{\mathrm{wf}}(\boldsymbol{r},\omega)$, nor on the type of vector transfer functions imposed by the propagation medium. In other words, (3.42) could be regarded as a wavefront-synthesis procedure, directly taking into account the behaviour of the medium as a weighting function.

Since we are rather interested in the case of wave-diffusive media, and specifically large cavities, the transfer functions $\boldsymbol{N}_{e,i}(\boldsymbol{r},\omega)$ and $\boldsymbol{N}_{m,i}(\boldsymbol{r},\omega)$ can be modelled, as done throughout this dissertation, as random functions of the space and frequency variables. Recalling the property of self averaging discussed in § 3.2.1, in the case of $B_T/B_c \gg 1$, it is possible to assume that all field-related quantities, if excited by means of time-reversed excitations, will asymptotically converge to deterministic values, with vanishingly small random fluctuations. Therefore, by only considering the average values at which these quantities converge, it can be shown that [J5]

$$\left\langle \boldsymbol{E}_{\mathrm{TR,i}}(\boldsymbol{r},\omega)\right\rangle = \int_{\Sigma} \underline{\boldsymbol{T}}_{\mathrm{i}}(\boldsymbol{r},\boldsymbol{r}',\omega)\cdot\boldsymbol{E}^{*}_{\mathrm{wf}}(\boldsymbol{r}',\omega)\mathrm{d}\boldsymbol{r}', \tag{3.44}$$

i.e., the wavefront generated by each TRM antenna is a functional of the target wavefront through the dyadic operator $\underline{\boldsymbol{T}}_{\mathrm{i}}(\boldsymbol{r},\boldsymbol{r}',\omega)$, defined as

$$\underline{\boldsymbol{T}}_{\mathrm{ee,i}}(\boldsymbol{r},\boldsymbol{r}',\omega) = \left\langle \boldsymbol{N}_{e,i}(\boldsymbol{r},\omega)\boldsymbol{N}^{*}_{e,i}(\boldsymbol{r}',\omega)\right\rangle \tag{3.45}$$

$$\underline{\boldsymbol{T}}_{\mathrm{em,i}}(\boldsymbol{r},\boldsymbol{r}',\omega) = \left\langle \boldsymbol{N}_{e,i}(\boldsymbol{r},\omega)\left[\hat{\boldsymbol{r}}'\times\boldsymbol{N}^{*}_{m,i}(\boldsymbol{r}',\omega)\right]\right\rangle \tag{3.46}$$

$$\underline{\boldsymbol{T}}_{\mathrm{i}}(\boldsymbol{r},\boldsymbol{r}',\omega) = \frac{1}{\zeta_0}\underline{\boldsymbol{T}}_{\mathrm{ee,i}}(\boldsymbol{r},\boldsymbol{r}',\omega) - \underline{\boldsymbol{T}}_{\mathrm{em,i}}(\boldsymbol{r},\boldsymbol{r}',\omega). \tag{3.47}$$

The above results point out once again that time reversal entirely relies upon the spatial and frequency correlation properties of the medium; indeed, the three dyadic operators are nothing else than spatial covariance matrices.

What are the roles of frequency and spatial correlations? The latter sets the spatial resolution of the method, in the sense that it operates as a point-spread function in (3.44), modifying the target wavefront into the eventually distorted replica $\left\langle \boldsymbol{E}_{\mathrm{TR,i}}(\boldsymbol{r},\omega)\right\rangle$ observed in practice.

Conversely frequency correlation has a fundamental role, already highlighted in § 3.2.1: ensuring that the bandwidth B_T of the wavefront will activate enough degrees of freedom to yield a quasi-deterministic result, with negligible random fluctuations.

Spatial correlation is therefore important since it provides a limit to the generation of wavefronts with rapid spatial variations, of importance when dealing with directive wavefronts. In the ideal case of a perfectly diffusive cavity, (3.45) can be expressed in closed form; to this end we need to introduce the local reference system depicted in Fig. 3.8, defined by a longitudinal unit vector $\hat{\boldsymbol{\rho}} = \boldsymbol{d}/\|\boldsymbol{d}\|$, where $\boldsymbol{d} = \boldsymbol{r}' - \boldsymbol{r}$, a transversal unit vector $\hat{\boldsymbol{v}}$ lying on the plane defined by the vectors $\boldsymbol{r}$ and $\boldsymbol{r}'$ and a third unit vector $\hat{\boldsymbol{\eta}} = \hat{\boldsymbol{\rho}}\times\hat{\boldsymbol{v}}$. The only non-null components of (3.45) are therefore

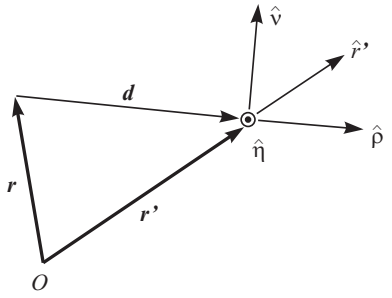

Figure 3.8 – The local reference system based on the orientation of the $\boldsymbol{r}$ and $\boldsymbol{r}'$ vectors, defined by the right-hand set of unit vectors $\hat{\boldsymbol{v}}$, $\hat{\boldsymbol{\eta}}$ and $\hat{\boldsymbol{\rho}}$. This choice is at the basis of the results derived for the case of a wave-diffusive medium.

$$\left(\underline{\boldsymbol{T}}_{\mathrm{ee}}\right)_{\hat{\boldsymbol{\rho}}\hat{\boldsymbol{\rho}}}(\boldsymbol{r},\boldsymbol{r}',\omega) = \frac{N_{\mathrm{e,av}}^2}{3}\rho_l(d,\omega) \tag{3.48}$$

$$\left(\underline{\boldsymbol{T}}_{\mathrm{ee}}\right)_{\hat{\boldsymbol{\nu}}\hat{\boldsymbol{\nu}}}(\boldsymbol{r},\boldsymbol{r}',\omega) = \frac{N_{\mathrm{e,av}}^2}{3}\rho_t(d,\omega) \tag{3.49}$$

$$\left(\underline{\boldsymbol{T}}_{\mathrm{ee}}\right)_{\hat{\boldsymbol{\eta}}\hat{\boldsymbol{\eta}}}(\boldsymbol{r},\boldsymbol{r}',\omega) = \left(\underline{\boldsymbol{T}}_{\mathrm{ee}}\right)_{\hat{\boldsymbol{\nu}}\hat{\boldsymbol{\nu}}}(\boldsymbol{r},\boldsymbol{r}'(\boldsymbol{r},\boldsymbol{r}',\omega)), \tag{3.50}$$

$$\left(\underline{\boldsymbol{T}}_{\mathrm{em}}\right)_{\hat{\boldsymbol{\nu}}\hat{\boldsymbol{\nu}}}(\boldsymbol{r},\boldsymbol{r}',\omega) = \frac{N_{\mathrm{e,av}}^2}{3\zeta_0}\rho_m(d,\omega)\hat{\boldsymbol{r}}'\times\hat{\boldsymbol{\nu}}\cdot\hat{\boldsymbol{\eta}} \tag{3.51}$$

$$\left(\underline{\boldsymbol{T}}_{\mathrm{em}}\right)_{\hat{\boldsymbol{\nu}}\hat{\boldsymbol{\rho}}}(\boldsymbol{r},\boldsymbol{r}',\omega) = \frac{N_{\mathrm{e,av}}^2}{3\zeta_0}\rho_m(d,\omega)\hat{\boldsymbol{r}}'\times\hat{\boldsymbol{\eta}}\cdot\hat{\boldsymbol{\rho}} \tag{3.52}$$

$$\left(\underline{\boldsymbol{T}}_{\mathrm{em}}\right)_{\hat{\boldsymbol{\eta}}\hat{\boldsymbol{\eta}}}(\boldsymbol{r},\boldsymbol{r}',\omega) = \left(\underline{\boldsymbol{T}}_{\mathrm{em}}\right)_{\hat{\boldsymbol{\nu}}\hat{\boldsymbol{\nu}}}(\boldsymbol{r},\boldsymbol{r}'(\boldsymbol{r},\boldsymbol{r}',\omega)), \tag{3.53}$$

where $\rho_l(d,\omega)$, $\rho_t(d,\omega)$ and $\rho_m(d,\omega)$ are spatial correlation functions that were introduced in (1.73)-(1.75), whereas $N_{\mathrm{e,av}}(\omega)/\sqrt{3}$ represents the rms amplitude of any scalar components of the electric field that would be generated within the cavity by a unitary-power harmonic excitation; its value can be easily predicted from power-conservation considerations, as shown in [J5, App. A].

Whence, the operator $\underline{\boldsymbol{T}}(\boldsymbol{r},\boldsymbol{r}',\omega)$ reads, for the case of an ideally diffused field

$$\underline{\boldsymbol{T}}(\boldsymbol{r},\boldsymbol{r}',\omega) = \frac{N_{\mathrm{e,av}}^2}{3\zeta_0}\underline{\boldsymbol{\rho}}(\boldsymbol{r},\boldsymbol{r}',\omega), \tag{3.54}$$

with

$$\begin{aligned}\underline{\boldsymbol{\rho}}(\boldsymbol{r},\boldsymbol{r}',\omega) = {}& \hat{\boldsymbol{\rho}}\hat{\boldsymbol{\rho}}\rho_l(d,\omega) - \hat{\boldsymbol{\nu}}\hat{\boldsymbol{\rho}}\rho_m(d,\omega)\hat{\boldsymbol{r}}'\times\hat{\boldsymbol{\eta}}\cdot\hat{\boldsymbol{\rho}} + \\ & + (\hat{\boldsymbol{\nu}}\hat{\boldsymbol{\nu}} + \hat{\boldsymbol{\eta}}\hat{\boldsymbol{\eta}})\left[\rho_t(d,\omega) + \rho_m(d,\omega)\hat{\boldsymbol{r}}'\times\hat{\boldsymbol{\nu}}\cdot\hat{\boldsymbol{\eta}}\right],\end{aligned} \tag{3.55}$$

introducing the normalized dyadic response $\underline{\boldsymbol{\rho}}(\boldsymbol{d},\omega)$. As a result, the real and imaginary parts of the scalar components of this function are now bounded to one, since they correspond to the degree of spatial coherence of the medium [R93].

The dyadic operator $\underline{\boldsymbol{T}}_{\mathrm{i}}(\boldsymbol{r},\boldsymbol{r}',\omega)$ appearing in (3.44) is therefore independent, on average, of the position and orientation of the TRM antenna, thanks to the isotropic and depolarization properties of diffused fields. In particular, all the quantities in (3.48) are deterministic, so that (3.44) can be solved in order to study the accuracy of the TREC technique in reproducing a given wavefront.

A graphical representation of $\underline{\boldsymbol{\rho}}(\boldsymbol{r},\boldsymbol{r}',\omega)$ is shown in Fig.3.9, where its angular spreading action is well apparent. The question of how accurately a target wavefront will be distorted is therefore natural, as well as the reflection about the eventual existence of a class of wavefronts that will be less subject to these distortions. A qualitative

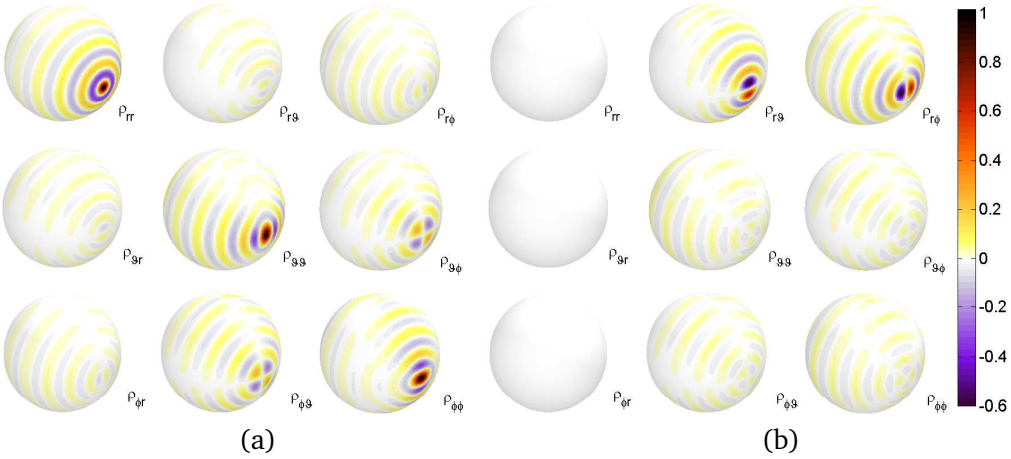

Figure 3.9 – Normalized dyadic function $\underline{\boldsymbol{\rho}}(\boldsymbol{r},\boldsymbol{r}',\omega)$ computed for $\boldsymbol{r} \in \Sigma$ and $\boldsymbol{r}' = r_\Sigma \hat{\boldsymbol{x}}$, with $r_\Sigma = 3\lambda$: (a) real and (b) imaginary parts. The 9 terms of the dyadic response are shown, matrix-wise, considering standard spherical unit vectors, following the order $\hat{\boldsymbol{r}}$, $\hat{\boldsymbol{\vartheta}}$ and $\hat{\boldsymbol{\varphi}}$, defined with respect to a polar axis vertically oriented.

answer was proposed in [J5], showing that the resolution of the point-spread function is consistently better than that potentially generated by any virtual source for which Σ stand in its far-field region.

An example of resulting wavefront is shown in Fig. 3.10, where the target wavefront was that of a square aperture of side λ, with uniform electric field linearly polarized. The electric field distribution was computed over a continuous range of distances from $\lambda/10$ up to 3 λ, limited to a horizontal cut, along the xy plane, starting from an equivalent-source surface at $r_\Sigma = 3\lambda$. In Fig. 3.10 the two spherical components $E_\varphi(\boldsymbol{r},\omega)$ and $E_r(\boldsymbol{r},\omega)$ of the electric field are shown, $E_\vartheta(\boldsymbol{r},\omega)$ being identically null by virtue of symmetry. It is possible to conclude that a focusing of the propagating energy is indeed occurring, as the electric field builds up converging towards the phase-center of the synthetic source.

Two notable distances are marked in Fig. 3.10: $r_\Sigma = 2\lambda$ and $r_\Xi = \lambda/2$. The target wavefront (far field) should only present a φ-oriented field, which is indeed found in the TREC-generated wavefront, as shown in Fig. 3.10(a)-(b); the purity of the polarization appears to start degrading as the wavefront crosses r_Ξ, when the focusing wavefront approximates the original field distribution found in what would be the reactive part of the synthetic source. Since the TREC can only produce propagative waves by means of distant sources (i.e., the TRM antennas), the diffraction limit ensues, leading to a focal spot about one wavelength wide. The appearance of a radial component in Fig. 3.10(b) is due to this phenomenon of approximation of the original source distribution, and it

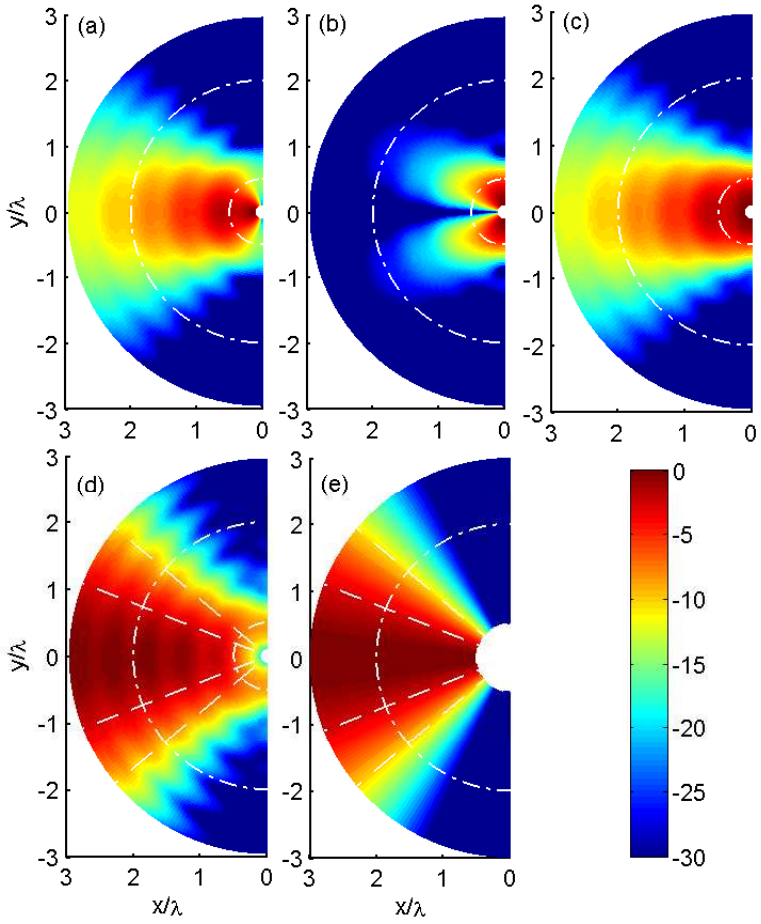

Figure 3.10 – Numerical solution of (3.44) for the case of the radiation pattern of a wideband linearly-polarized square-aperture antenna, one wavelength wide at the central frequency. The evolution of the electric field is studied over the half-plane of the xy cut (E-plane cut) along which the time-reversed wavefront is expected to focus, for radial distances going from $\lambda/10$ up to 3λ: (a) $E_\varphi(\boldsymbol{r},\omega)$; (b) $E_r(\boldsymbol{r},\omega)$; (c) $\|\boldsymbol{E}(\boldsymbol{r},\omega)\|$; (d) $\|\boldsymbol{E}(\boldsymbol{r},\omega)\|r$; (e) angular dependence $\|\boldsymbol{F}(\boldsymbol{r},\omega)\|$, proportional to $\|\boldsymbol{E}_{\text{wf}}(\boldsymbol{r},\omega)\|r$. The outer dashed line represents the Fraunhofer distance for the synthetic source, whose volume is marked by the inner dashed line. All results are normalized to the peak-value of E_φ and expressed in dB. Radial dashed lines represent the -3 dB and the -10 dB angles. For further details, refer to page 155.

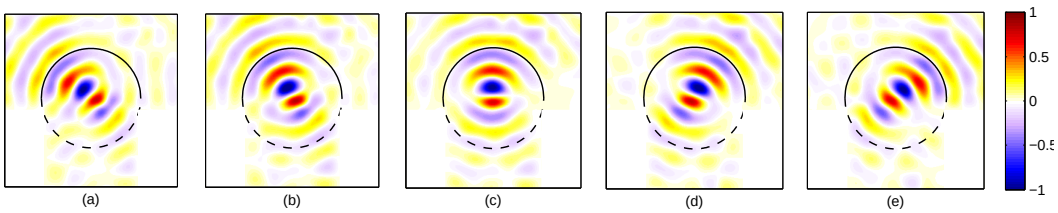

Figure 3.11 – Experimental results obtained for a same virtual source oriented along different directions. A 200 MHz bandwidth with a central frequency of 1.1 GHz was used.

becomes more evident when looking at the total field in Fig. 3.10(c): the wavefront focuses back onto the source region, with an almost uniform intensity.

The accuracy of the angular distribution of the focusing wavefront is more easily observed in Fig. 3.10(d), where the wavefront is normalized to Green's scalar function, yielding the radiation pattern to be compared to that shown in Fig. 3.10(e). The comparison is very good, with the converging wavefront accurately reproducing a radially-invariant radiation pattern over its far-field region within a ± 0.2 dB range over the main lobe. Fig. 3.10(d) also provides a clear picture of the focal spot due to diffraction limit: directivity is lost, with energy almost equally spread over all directions, and particularly with a reduction in its increase with respect to an ideal spherical convergence.

These results imply that the loss of directivity is not due to an intrinsic limitation of the method, as could have been expected from the point-spread function shown in the previous section. It actually appears that the point-spread function is effectively capable of reproducing all the phenomena leading to wave focusing under physical conditions, including the diffraction limitation over the near-field region of the synthetic source. Practically, no significant distortion occurs over the main-lobe outside the surface Ξ of the virtual source.

In short, the TREC approach allows emulating a free-space environment within a diffusive medium; as discussed in § 3.3.2, this result should not be regarded as a complicated manner of using a reverberation chamber as an anechoic one, but rather as the first step towards new possible applications. Let just consider the fact that at no point in the above derivation the direction of arrival of the converging wavefront was linked in any manner to the position of the TRM antennas. As a result, the TREC is not just emulating a free-space environment, but it is offering the possibility of generating wavefronts propagating along any direction without having a source in the line-of-sight of the observer. Though counterintuitive, this result is a direct consequence of the use of a diffusive medium: its properties, in particular spatial correlation, is independent of direction, polarization and position. Hence, wavefronts generated by means of the TREC approach can emulate any propagation pattern, as long as these wavefronts sat-

isfy Helmholtz equation. An example of this property is given in Fig. 3.11, where the wavefront of a virtual source was generated for a varying orientation; the resulting wavefronts are practically invariant to the rotation.

3.3.2 Potential applications

In the introduction to this chapter we have stated that it is our intention not to apply time reversal merely as a way of emulating free-space propagation within reverberating cavities, but rather in order to define a new test facility. As pointed out at the end of the previous section, the TREC is not only capable of emulating a free-space propagation, but it allows a direct synthesis of wavefronts without requiring a line-of-sight configuration, a condition that would be necessary in any anechoic environment. The TREC can therefore be regarded as an alternative to anechoic environments for radiated tests (e.g., radiated immunity in EMC testing), where the proper test phase would not require any mechanical movement of sources, nor a collection of sources covering the EUT along all directions of interest. Its intrinsical ability in providing a higher conversion efficiency is a welcome by-product that highlights the successful merging of reverberating and anechoic features.

In practice, there is a last problem to be solved: the transfer functions $\boldsymbol{N}_{\mathrm{eq},i}(\boldsymbol{r},\omega)$, needed for the synthesis of the excitation signals (3.42). A feasible solution is to excite each TRM antenna with a unitary harmonic excitation and measure the tangential electric and magnetic field components over Σ, e.g., by means of a moving probe. Such an approach would provide all the information needed for the synthesis (3.42); a preliminary demonstration of the feasibility of this approach was presented in [J15].

Mechanical movements would therefore be still necessary. In order to better understand the difference between standard approaches and the TREC one, Fig. 3.12 presents the flow of operations needed: while for multiple test configurations anechoic environments typically require mechanical movements repeated for each test, in a TREC all movements would be limited to a preliminary phase during which the transfer functions $\boldsymbol{N}_{\mathrm{eq},i}(\boldsymbol{r},\omega)$ are collected once and for all; the actual test phase would require no mechanical movement, speeding it up.

Still, the overall number of movements could be expected to be the same, so that one could wonder what are the advantages of this procedure. Two points come to mind: first, since the preliminary phase involves the displacement of a probe rather than a source, the lighter weight of a probe implies a simpler mechanics and faster displacement rates, thus an overall shorter duration. Second, (3.42) does not require any assumption on the nature of the wavefront; it is therefore uncorrect to assume that one position of the probe corresponds to just one test configuration, as inevitable for anechoic environments. In fact, (3.42) does not provide for any limitation in this respect, allowing the generation of a larger number of test wavefronts than possible in an anechoic environment with a single source. Parameters such as a varying directivity, polarization, time-dependence, etc., can be changed from data acquired for a single

direction, whereas for an anechoic environment this would require mechanical modifications in the source, eventually the use of a collection of sources, resulting in longer test durations.

Moreover, the TREC being a linear system, it is also possible to imagine rather peculiar scenarios, e.g., with multiple incidences, with more than one wavefront impinging over the EUT along different directions. This possibility is of direct practical importance, since in practice an EUT is seldom operated in a free-space environment; more often, it interacts with boundaries at least partially reflective, e.g., walls, the ground, neighbouring devices, etc. As a result, tests within anechoic environments are bound to represent an approximate estimate of the actual response of the EUT within more realistic environments. The TREC can therefore emulate more complex environments than anechoic ones, by reproducing echoes corresponding to reflections upon *virtual* boundaries.

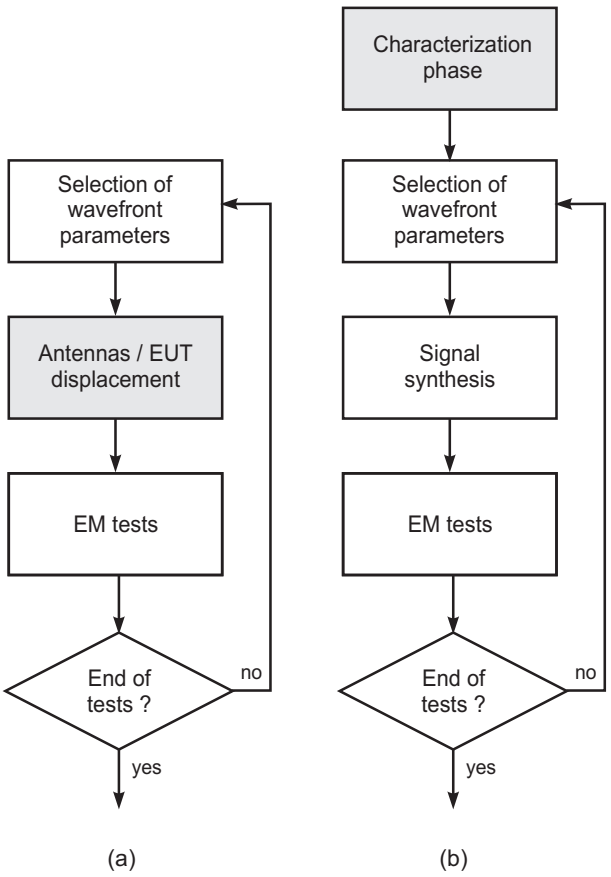

Figure 3.12 – Sequences of necessary steps to follow when using (a) an anechoic test environment and (b) a TREC. Shaded blocks represent operations based on mechanical displacements or substitution of devices.

The case we want to make is that the TREC should not be regarded only as an emulation of free-space propagation, since it also comes with advantages of its own, not found with other test facilities. Furthermore, it paves the way to new applications such as the identification of coupling paths in an EUT and the measurement of its scattering cross-section. Preliminary tests during the last two years have proven the feasibility of these ideas. The feasibility of fast antenna measurement have also been demonstrated in [J9]. For all these reasons, we can conclude by stating that having chosen to work with a complex environment allows to simplify a number of problems that have not yet

a simple practical solution. As discussed in § 4, these themes need to be investigated and will constitute the basis for future investigations.

Chapter 4

Discussions and perspectives

THE previous chapters were intended to summarize our main contributions to the field of large cavities over the last 4 years. A special attention was placed upon the use of these media as testing facilities, particularly for radiated tests as defined for EMC applications. Fundamentally, two topics have been presented : non-perfectly diffusive cavities under a harmonic steady-state and the generation of coherent fields within diffusive cavities.

The main tool used for this purpose was a random spectral representation of fields propagating within these media. It has allowed not only to understand the reasons of certain non-idealities in field statistics and to predict some remarkable features of time-reversal driven cavities, but has also shown that without recurring to complex models, the gap between plane-wave representations and modal ones could be bridged, providing a simple explanation of the difficulties observed in the low-frequency analysis of large cavities.

A complete review of our work is out of the scope of this dissertation; indeed, the same approach has been also used in order to prove the possibility of controlling the field statistics in the lower-frequency range of a cavity [C15], setting an alternative to the use of electrically large scatterers as field stirrers, implying the possibility of reducing the LUF without major modifications in the cavity geometry. Further work on non-idealities has also highlighted the importance of taking into account even very weak correlation levels that are typically found between field samples measured in a cavity [C7] and the debatable use of statistical goodness-of-fit tests as tools for assessing the correct functioning of a reverberation chamber [C22].

Our aim was to stress the transversal approach we have applied in studying cavities, without recurring to approaches and assumptions that are too often taken for granted, at least within the EMC community. An *outsider* point of view is needed, in our opinion, if we are to go further in the physical understanding of phenomena that have not yet been fully taken into account.

Our investigations clearly indicate that the understanding of cavity-based applications can be improved by taking advantage of the results summarized in the previous

chapters. In this respect, the ideas we will prospect in the next few years are presented in § 4.1, and concern field statistics as well as coherent applications based on time reversal. Conversely, a long-term vision is presented in § 4.2, where we argue about how the tools developed in the context of our work on large cavities could be applied to other domains outside EMC testing.

4.1 Short-term projects

We have highlighted the need for sounder models of cavities in non-perfect diffusive regime. In this respect, we will work in the next few years on the physics of cavities. In particular, we aim at completing the track opened, introducing a global statistical model taking into accounts often neglected effects, e.g., residual spatial/stirrer correlation. As shown in § 1.4.2, there is room for hybrid models bridging the gap between perfect diffuse-field random PWS and random spectral models capable of assessing the actual number of modes actively taking part in the response of a cavity. Such models are needed in order to introduce a statistically-based definition of the LUF of a reverberation chamber: as discussed in § 2.3.2, none of the current definitions is capable of accounting for the imperfect diffusion observed even in very large cavities. Random fluctuations in the modal density and the modal overlapping are one of the reasons for the use of statistical approaches; acknowledging the impossibility of observing no local statistical anomaly requires models capable of predicting the probability of observing a given number of such anomalies, as a function of macroscopic parameters experimentally accessible without a priori assumptions.

Hybrid models would also be needed for another issue, namely understanding how a loaded cavity, i.e., with lossy material inserted in it, behaves. Current models do not account for the intermediate regime where a cavity is no longer resonant enough to provide a diffusive environment. This issue should not be confused with that of weak modal overlapping; on the contrary, increasing losses can be expected to increase modal overlapping. The problem is rather due to the fact that in the case of substantial losses, the usual weak-perturbation approach is no longer viable. As a result, predictions of field uniformity and sample independence based on the use of spectral/plane-wave models based on the assumption of independent degrees of freedom fail, because there is no way of estimating beforehand the actual number of degrees of freedom. Correlation between modes or plane waves should be expected, but the issue is how to set the correlation, and what relationship should be expected with higher loss levels? An answer to this problem should be possible using hybrid plane-wave spectra models as the one introduced in § 1.4.2, where wave propagation and interaction with lossy boundaries can be accounted for and used as a proxy for assessing the effective number of *independent* propagation paths observed in practice. A similar idea is used in multiple-scattering theory, where the ratio between the average length of propagation of a wave to the average free-path between scattering interactions is used just in the same man-

ner, i.e., to assess how many degrees of freedom can be expected to be ensured by a complex medium, for example in the study of the fluctuations in electric conductivity in mesoscopic quantum systems [R78].

Another issue still open within the EMC community is that of predicting the performance of a mechanical stirrer. It is hardly exaggerated to claim that stirrer design is as random as the samples it is expected to generate: current rules are limited to rather generic guidelines [R97, R4, R91, R55, R37] whose main merit is to avoid the use of electrically small stirrers. The main reason for these difficulties lies in the assumption that the response of a stirrer can be studied only either by experimental tests or by numerical simulations, both to be carried out within the targeted reverberation chamber. We would rather attempt a different approach, by exploiting the possibility of using image theory, thanks to the rectangular boundaries preferred by the EMC community: it seems feasible to link *analytically* the scattering response of a scatterer in free space to that it will produce when included within a cavity. To this end, it will likely be necessary to make reference to the literature on propagation in periodic media. Numerical simulations of a scatterer in a free-space environment would be dramatically faster than those carried out within a reverberating cavity, because of well-known numerical difficulties in the simulation of systems with strongly pronounced resonances and/or long relaxation times.

Concerning our work on time-reversal excitation of cavities, but not restricted to the TREC approach, there are several developments that are already under way. We will just refer to two of them that constitute the heart of two Ph.D. theses that have only very recently started. The first topic is the use of cavities with long relaxation times used in conjunction with time reversal as the basic elements in the amplification of short high-power microwave pulses. Two novelties are introduced by this work: the first one is the use of a cavity for the time-spreading of pulses, enabling higher amplification rates, while the low spatial correlation of large cavities is expected to allow the excitation of multiple radiation sources at the same time.

The second topic aims at using a TREC as a fast antenna-test facility. The approach chosen will be opposite to that already explored in [J9]. In this work the TREC is examined under the lens of estimation/decision theory, by setting up a problem of identification of the radiation pattern of a source exposed to complex wavefronts generated by the TREC. The main novelty will be the absence of any simple test wavefront, e.g., plane waves, currently used in anechoic facilities. Initial explorations support the idea that from an estimation point of view, complex wavefronts could outperform local plane waves when trying to estimate radiation patterns. The flexibility of the TREC in generating arbitrary wavefronts that could not be easily generated in a free-space environment is the main asset of this work.

In both the physics of harmonic-driven cavities and applications of the TREC, the concepts and results summarized in this dissertation will constitute the foundations upon which new researches will be based. The availability of simple statistical tools of broad applicability and capable of reproducing experimentally-observed phenomena is

a fundamental point in the success of these new projects.

4.2 Long-term vision

The TREC approach is expected to require a longer planning for its further development. Several axis have already been identified; we will just present the main ideas at the basis of two of them that look particularly promising.

The first development will turn around a feature of the TREC that we have so far been neglecting, namely wave focusing. Actually, we have made use of it repeatedly, as soon as a high contrast Λ was required, as well for high conversion efficiencies and for any quantity that relies on self-averaging. Still, focusing was a property not exploited in itself, but rather was a manner of ensuring an almost deterministic response. What we have neglected in focusing is the idea of spatial resolution it offers; this should be compared with the total lack of spatial resolution offered by plane waves. Spatial resolution has a direct practical appeal when recalling that an open problem in EMC testing is the identification of localized paths through which external waves couple to the internal space of an EUT; a typical example is a slot in a metallic shielding. The TREC was conceived as a general tool for the generation of focusing wavefronts; if these wavefronts were defined in such a way at to focus over a controllable position, it would be possible to generate wavefronts that would excite only a limited region of space over the external boundary of an EUT. The idea is therefore to scan an EUT by using a moving focal spot, and to observe under what conditions the EUT is maximally stressed; coupling paths could therefore be identified without human intervention, as the standard approach is still, surprisingly, to manually scan the surface of an EUT with electric and magnetic probes/sources.

A preliminary investigation was presented in [C14], and has supported the feasibility of this idea. In that work we considered a box where a half-wavelength slot was cut into it. Generating a focusing wavefront moving across the slot, and sensing the field level transmitted within the box, it was possible to identify the position of the slot within a quarter-of-wavelength resolution. The fact that the aperture was a slot rather than a hole was detected by using two orthogonal polarizations for the electric field: the anisotropic response of the slot pointed to its orientation in space and its actual shape.

That preliminary work is the basis for a much more ambitious project. Treating an EUT as a black-box, it is possible to derive an equivalent macromodel capable of describing its behaviour in every detail, if a suitably conceived learning phase is considered. Similar ideas are routinely used in electronics [R80, R85], where even nonlinear responses can be accurately extracted from a few responses of the EUT, excited by means of cleverly designed stimuli. The appeal of this idea is that if a *behavioural* macromodel of an EUT were available, then its response to any configuration could be extrapolated without requiring further tests: from complex propagation scenarios to

the case of complex electromagnetic stimuli, the EUT response could be estimated from its macromodel. The extraction of such an equivalent model is made feasible by the flexibility of the TREC approach. It would result in a paradigm shift in EUT testing: no longer using plane wave as the simplest way of interpreting the response of the EUT, but rather conceiving complex test scenarios in order to extract the maximum amount of information from a limited number of tests.

The second long-term project we envisage is again based on the TREC and deals with the estimation of the full scattering response of an EUT. In this case EMC is no longer the main beneficiary, as this topic is rather found within the core of radar measurements. In order to appreciate the interest of this idea, we should recall that current radar tests are typically limited to monostatic radar cross sections, where the field scattered by the EUT is measured along the same direction along which it is illuminated. Although monostatic measurements serve a number of applications, bistatic radars have been suggested as interesting extensions that would provide more detailed information about the EUT, particularly in their identification. It is therefore important to be capable of assessing the bistatic response of an EUT, in laboratory conditions, e.g., during R&D phases. The problem is that bistatic measurements involve a heavy experimental setup: for each direction of illumination over a 4π-steradian range of angles, measurements of the scattered field should be taken again over 4π steradian, giving raise to an overall number of samples that goes like $\mathcal{O}(f^4)$, while requiring a complex mechanical system for the joint displacement of the transmission and reception antennas over two concentric spheres.

The TREC is expected to provide a simpler solution by limiting the number of mechanical movements to $\mathcal{O}(f^2)$, and just during an initial phase. Preliminary tests were carried out in 2010 and in 2012, within the framework of Master thesis. Though not yet published, and still in an embryonic stage, it appears that the idea is indeed feasible, leading to a simpler and faster procedure to estimate bistatic responses within a facility.

Simpler access to the scattering response of an object has clearly a broader spectrum of applications than just radar imaging. Use of the TREC for non-destructive testing, as well as medical imaging does not seem a too far-fetched idea.

Appendices

Appendix A

Curriculum vitæ

Andrea Cozza

Associate Professor
Département de Recherche en Électromagnétisme (DRE)
Laboratoire des Signaux et Systèmes
SUPELEC
3 rue Joliot-Curie
Plateau de Moulon, 91192 Gif-sur-Yvette
France

Telephone : +33 (0)1 69 85 15 77
Fax : +33 (0)1 69 85 15 69
E-mail : andrea.cozza@supelec.fr

Education

2002 - 2005	**Ph.D.**, Université des Sciences et Technologies de Lille (France), jointly with Politecnico di Torino (Italy).
1996 - 2001	**Diploma di Laurea in Ingegneria Elettronica**, Politecnico di Torino (Italy).

Experience

2010 -	**Associate Professor** at Supélec (Gif-sur-Yvette campus), Département de Recherche en Électromagnétisme.

2007 - 2009	**Assistant Professor** at Supélec (Gif-sur-Yvette campus), Département de Recherche en Électromagnétisme.
2005 - 2007	**Post-doctorate student** at Supélec (Gif-sur-Yvette campus): theoretical analysis, design and development of a fast measurement system for electromagnetic dosimetry, based on near-field techniques.
2002 - 2005	**Ph.D. student** in Electromagnetic Compatibility: theoretical analysis of the propagation and radiation of electromagnetic interferences along railway lines.

Honors and awards

- Graduated, Summa Cum Laude, Politecnico di Torino, 2001
- Recipient, Prix Coron-Thévenet, Académie des Sciences, 2012

Appendix B

Selected papers

This Appendix reproduces six papers that I deem important for my research activities. They also showcase my contributions to the modelling of wave propagation in large cavities. These papers are, in order of appearance:

1. A. Cozza, "The Role of Losses in the Definition of the Overmoded Condition for Reverberation Chambers and Their Statistics", *IEEE Transactions on Electromagnetic Compatibility*, Vol. 53, No. 2, 2011. Reproduced at page 107.

2. A. Cozza, "Probability Distributions of Local Modal-Density Fluctuations in an Electromagnetic Cavity", *IEEE Transactions on Electromagnetic Compatibility*, Accepted for publication, 2012. Reproduced at page 119.

3. A. Cozza, "Statistics of the performance of time reversal in a lossy reverberating medium", *Physical Review E: Statistical, Nonlinear, and Soft Matter Physics*, Vol. 80, No. 5, 2009. Reproduced at page 135.

4. A. Cozza, "Increasing peak-field generation efficiency of reverberation chamber", *IET Electronics Letters*, Vol. 46, No. 1, 2010. Reproduced at page 147.

5. A. Cozza, H. Moussa, "Enforcing a deterministic polarization in a reverberating environment", *IET Electronics Letters*, Vol. 45, No. 25, 2009. Reproduced at page 151.

6. A. Cozza, "Emulating an Anechoic Environment in a Wave-Diffusive Medium through an Extended Time-Reversal Approach", *IEEE Transactions on Antennas and Propagation*, Accepted for publication, 2012. Reproduced at page 155.

1

The Role of Losses in the Definition of the Overmoded Condition for Reverberation Chambers and Their Statistics

Andrea Cozza

Département de Recherche en Électromagnétisme, SUPELEC
3 rue Joliot-Curie, 91192 Gif-sur-Yvette, France

***Abstract*—It is commonly acknowledged that in perfectly-stirred reverberation chambers the energy density of the electric field follows a χ^2_6 law, as long as the overmoded condition applies. This concept, never defined properly, is often confused with the idea of a threshold on the modal density, regardless of the quality factor of the cavity. This interpretation is here proven to be inaccurate, as losses play a fundamental role in the nature of the field statistics and not, as often assumed, just in its scaling. In particular, it is shown how the overmoded condition should be stated mathematically, highlighting how the cavity quality factor and the number of eigenmodes excited cannot be regarded as quantities intervening independently on the field statistics, but should rather be considered jointly. These results are derived by means of a modal analysis, with a limited number of assumptions. A quantitative relationship is established between average modal overlapping and the rate of convergence of the electric energy density towards a χ^2_6 law. Rather than setting an arbitrary threshold on modal overlapping as a necessary condition for an overmoded behaviour, the statistical uncertainty due to the limited number of available field samples is shown to affect the very definition of the overmoded condition.**

***Index Terms*—Statistics, Cavities, Losses, Error analysis.**

I. Introduction

Current use of reverberation chambers is based on a number of commonly accepted rules. Among these, the fact that an overmoded condition is necessary to achieve isotropy, uniformity and depolarization of the electromagnetic field in a test volume can be regarded as one of the most fundamental [1], [2], [3]. It is hence surprising that the study of this condition has not received much attention: to the best of our knowledge, no clear definition has yet been given in the field of Electromagnetic Compatibility, even though a similar criterium exists in acoustical reverberation chambers [4], albeit unable to provide an assessment of the rate of convergence of field statistics to theoretically justified asymptotic laws.

As a matter of fact, going through the literature, it appears that the concept of an overmoded cavity is somewhat regarded as related to a threshold value in the modal density [2]. This likely comes from the fact that the availability of a large number of modes resonating at the working frequency is necessary, if the field distribution inside the cavity is to be complex enough to behave as a random distribution under the use of a stirring technique, e.g., by rotating an electrically large mechanical paddle [1], [3]. To the best of our knowledge, no study has yet clearly defined this threshold level, although the strong ties between a high modal density and a well-stirred cavity are known in practice [1]. A significant example of the low interest the overmoded condition aroused in most previous works is given in [1], where the overmoded condition is dismissed as something seemingly trivial, fulfilled as soon as a cavity is electrically large. Interestingly, Lehman [3] regarded the assessment of the validity of the overmoded condition as an open issue.

Fulfilling the requirement for an overmoded cavity allows the use of simplified models, as the one presented in [5], based on the description of the electromagnetic field as a continuous plane-wave spectrum: it links in a straightforward manner the idea of a well-stirred cavity to field statistics: an environment where an infinite number of plane waves propagate with the same probability along all the directions and polarizations, implies that the electric energy density follows a χ^2_6 law, as a direct consequence of the central-limit theorem [6], [3]. Since this theoretical result is based on the assumption of a well-stirred cavity, the limited efficiency of the stirring technique is often regarded as the most likely source of non-compliancy, especially in the lower frequency range, because of the statistical correlation of contiguous stirrer positions [7].

But another potential reason of non-compliancy could come from the inadequacy of the assumption of an infinite number of propagating plane waves (intrinsically linked to the use of a continuous plane-wave spectrum) as this condition is approximatively fulfilled only asymptotically. In practice, depending on the number of resonant modes excited at the working frequency, the number of plane waves into which the field can be decomposed is finite, hence resulting in a non-perfect matching between a χ^2_6 probability law and what is observed from experimental data about electric energy density. Users of reverberation chambers widely consider that working at frequencies above the Lowest Usable Frequency (LUF), as defined in [8], is a sufficient condition to make a cavity overmoded. This idea has already been proven to be incorrect [9], [10], as the statistical properties of the field generated at frequencies close to the LUF can be quite different from the ideal asymptotic case treated in most statistical models of reverberation chambers. Nevertheless, it is well accepted that working at frequencies well above the LUF ensures an overmoded condition.

All these results point to the fact that the occurrence of a non-compliancy at high frequency is unlikely, as both the

modal density and the stirrer efficiency are expected to be high. These facts seem to support again the idea that the overmoded condition is linked to a threshold in the modal density, without taking into account the role of losses. Losses are merely included *a posteriori*, when computing the efficiency of a cavity in converting an input power into a high-intensity field. An exception is the analysis of how increasingly high losses impact statistical uniformity, presented in [11], where the requirement for a minimum quality factor was investigated. In this paper, we deal with configurations that are on the other end of the scale: as a matter of fact, the reverberation chamber will always be assumed to be highly resonant, with a quality factor much higher than one, typically several hundreds. Additional losses will always be assumed only to affect the relative bandwidth of resonant modes, with no influence on the way resonances are established.

Under these conditions, experimental data have been presented in [12], [13], [14], [15], providing clear clues that the overmoded condition is actually not based on a threshold level for the modal density and that losses can have a beneficial impact on field statistics [12], [13]. A similar conclusion was also suggested in a study based on a canonical modal representation [16], though the lack of an analytic approach hindered the development of predictive/design tools; moreover, the possibility of non-compliancy above the LUF was not pointed out. Indeed in [14], [15], no doubt could subsist about the stirrer efficiency at those frequencies where the field statistics was shown not to comply with the asymptotic probability laws predicted by continuous plane-wave spectrum models, especially because they occurred over a small subset of scattered frequencies.

This gives room to the idea that the overmoded condition is not just a matter of having a large number of modes and an ideally perfect stirrer. An eventual role of losses in field statistics would also cast some doubts on the often invoked idea of unstirred components. As soon as field statistics do not comply with asymptotic ones, this is regarded as due to a bad stirring. The results shown in this paper prove that statistical non-compliance can also be explained by a weak modal overlapping, even though a perfect stirring is assumed and a large number of resonant modes are potentially available.

This paper proposes a theoretical analysis linking in a formal way the statistical properties of the electromagnetic field within a reverberation chamber and two of its most important quantities: the composite quality factor and the number of modes excited at the working frequency. It will be shown that losses must be included into modal representations, in order to derive a meaningful statistical analysis of the field within a reverberation chamber. A modal approach is employed to this effect, staging a finite number of resonant modes excited at a given frequency. We will not address the question of statistical uniformity, but rather that of statistical convergence for the electric energy density measured at a given position.

The paper is organized as follows: Section II recalls the basics of modal analysis as derived for metallic enclosures; some important notations and concepts are introduced for the benefit of the derivations presented in the rest of the paper. Section III makes use of this modal representation, applying the concept of statistical excitation of the chamber, in order to derive the standardized variance of the electric energy density. Following these results, it is shown how the composite quality factor and the modal density of the chamber impact field statistics, and in particular the fact that the theoretical asymptotic behaviour predicted in [5] can be disproved. This leads to a quantitative definition of the overmoded condition in Section IV, as the one ensuring a limited error with respect to asymptotic statistics. Section V then seeks to assess how this deviation affects the probability of rejection in goodness-of-fit tests on field samples. This is achieved by means of numerical simulations based on the proposed modal representation. Experimental results are then presented in Section VI to check the validity of these ideas.

II. Modal representation and notations

As we are interested in the statistical properties of the field excited within a cavity, we will make use of a modal representation, being an effective tool to this effect. We shall thus express the electric field as follows [17], [18]

$$\mathbf{E}(\mathbf{r}, f) = \sum_{i=1}^{\infty} \gamma_i(f)\mathbf{e}_i(\mathbf{r}, f)\psi_i(f) \quad , \tag{1}$$

where $\mathbf{r}$ is the position at which the field is being observed and f the working frequency for a harmonic excitation. Three sets of modal quantities are involved in (1): 1) the modal weights $\{\gamma_i(f)\}$, which depend only on frequency for a given configuration of the excitation sources; 2) the modal topographies $\{\mathbf{e}_i(\mathbf{r}, f)\}$ describing the spatial dependence of the field for each mode and 3) the frequency responses $\{\psi_i(f)\}$ of the resonant modes. The computation of the modal weights requires a precise knowledge of the modal topographies $\{\mathbf{e}_i(\mathbf{r}, f)\}$ as the former are obtained by projecting the equivalent current distribution of the sources over the modal topographies [17].

As rightfully recalled in [2], though this approach is exact, in practice it is hardly usable, as the computation of the modal topographies comes, apart for canonical configurations, as a computational burden for most numerical codes. This notwithstanding, the modal approach allows deriving some fundamental results, as will be proven here. To this end, a number of simplifications are required, enforced on three sets of modal parameters.

Let us recall that the $\{\psi_i(f)\}$ represent the responses of second-order systems, defined as follows

$$\psi_i(f) = \frac{f}{f_i^2(1 + \mathrm{j}/2Q_i)^2 - f^2} \quad , \tag{2}$$

where f_i is the resonance frequency of the i-th mode and Q_i its quality factor. The first set of modal parameters is thus given by the $\{f_i\}$. For the sake of simplicity, it is often assumed that the quality factors are equal for all the modes close to the frequency of analysis, approximating them with a composite quality factor [19]. This is, clearly, not physical, as the losses of each mode strongly depend on the field topography, a well-known fact in waveguide theory [17]; nevertheless, this approximation is usually capable of capturing the behaviour

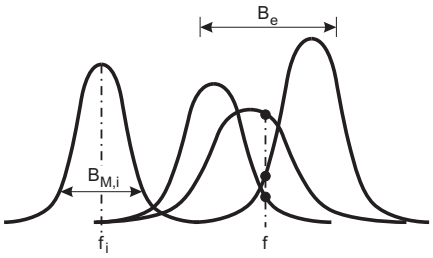

Fig. 1. A graphical depiction of the modal decomposition of a random realization of the electric field and some of the notations used. The dots represent the level of contribution of the three modes dominating the field at the working frequency f.

of a cavity and we will make use of a modified version in Appendix A.

We will limit our analysis to a generic position $\mathbf{r}$. Introducing the following factorization for the modal topographies

$$\mathbf{e}_i(\mathbf{r}, f) = e_i(\mathbf{r}, f)\hat{\boldsymbol{\xi}}_i(\mathbf{r}, f) \quad , \tag{3}$$

we can hence restate (1) as

$$\mathbf{E}(\mathbf{r}, f) = \sum_{i=1}^{\infty} \tilde{\gamma}_i(\mathbf{r}, f)\psi_i(f)\hat{\boldsymbol{\xi}}_i(\mathbf{r}, f) \quad , \tag{4}$$

having introduced the equivalent weights

$$\tilde{\gamma}_i(\mathbf{r}, f) = \gamma_i(f)e_i(\mathbf{r}, f) \quad . \tag{5}$$

The second set of parameters is given by the modal weights $\{\tilde{\gamma}_i\}$, while the modal polarizations $\{\hat{\boldsymbol{\xi}}_i\}$ are the third and last set of parameters that we will consider.

The use of (4) allows studying field statistics in a simple way, as soon as the three modal parameter sets are treated as random variables. This approach is often used when studying the asymptotic properties of complex systems, as in [5], a common practice in statistical mechanics. Under this paradigm, (4) is entirely defined by the three sets of modal parameters $\{\tilde{\gamma}_i\}$, $\{f_i\}$, $\{\hat{\boldsymbol{\xi}}_i\}$ and the composite quality factor Q.

Recalling that the contribution of each mode is weighted by its frequency response $\{\psi_i(f)\}$, the influence of each mode is localized around each resonance frequency f_i, as shown in Fig. 1. The extent of the influence of each mode is set by its quality factor Q_i, as the mode can be effectively excited only for working frequencies at most at a distance $|f_i - f| < B_{M,i}$ from the resonance frequency. The distance $B_{M,i}$ is the bandwidth covered by each mode, from its peak at f_i, to a reduction of a factor ρ. Typical values of ρ are -3 dB and -10 dB. For the case of $\rho = -3$ dB,

$$B_{M,i} = \frac{f_i}{Q_i} \quad , \tag{6}$$

a result that will be used later.

As we will show, the introduction of the bandwidths $B_{M,i}$ is not necessary, nor the definition of a level ρ; nevertheless, this approach simplifies the mathematical derivation, while effectively pointing out that it is not necessary to carry out the sum in (4) over all of the modes, but just over a reduced subset $\mathscr{M}$

$$\mathscr{M} = \{i : |\psi_i(f)| > \rho|\psi_i(f_i)|\} \quad , \tag{7}$$

where ρ is chosen in order to give a significant contribution from the modes. Hence, (4) is limited to a number of modes $M = \#\mathscr{M}$, i.e., the cardinality of $\mathscr{M}$, spanning a frequency bandwidth B_e

$$B_e = \max_{i \in \mathscr{M}} B_{M,i} \quad , \tag{8}$$

hereafter referred to as the equivalent bandwidth of the reverberation chamber. This concept will be shown to play an important role, as it accounts for the fact that a harmonic signal excites a number of modes that are to be found over this bandwidth. These concepts are illustrated in Fig. 1, for a random realization of (1).

III. Statistical modal analysis

Following the previous discussions, we will consider the simplified model in (9) as the reference for our statistical analysis

$$\mathbf{E} = \sum_{i \in \mathscr{M}} \tilde{\gamma}_i \psi_i \hat{\boldsymbol{\xi}}_i \quad , \tag{9}$$

where the indexes i now span the set $\mathscr{M}$, and having dropped the spatial and frequency dependencies, as our analysis will deal with the field statistics at one specific position and frequency at a time.

We focus our analysis on electric energy density

$$W(\mathbf{r}, f) = \epsilon_0 \|\mathbf{E}(\mathbf{r}, f)\|^2 \quad , \tag{10}$$

where ϵ_0 is the dielectric constant for the medium filling the cavity, and the electric field is expressed in root-mean-square units. The model proposed in (9) is fit for studying any quantity related to the electric field. The rationale for choosing the electric energy density lies in its asymptotic convergence to a six-degree-of-freedom chi-square law, thus with a standardized variance equal to 1/3, as opposed to the squared amplitude of Cartesian components (directly related to the received power for polarized electrically small antennas, such as dipoles) which follow a two-degree chi-square law, with a standardized variance equal to 1. Although this has no impact from a theoretical point of view, it makes a big difference in practice, as the statistical uncertainty affecting moments estimated from a finite sample population is directly dependent on the relative statistical dispersion of the samples, as recalled in Appendix B. The experimental results presented in Section VI, dealing with the electric energy density, are indeed already affected by a non-negligible statistical uncertainty; use of single Cartesian components of the electric field would have resulted in a even higher uncertainty.

The average spatial uniformity properties of W can be obtained straightforwardly from a continuous modal representation, as done in [5], where it is proven that W follows a six-degree-of-freedom chi-squared probability law, or χ^2_6. Although such approach allows to understand and explain in a simple way some of the most important properties of reverberation chambers, it is incapable of providing results but

for asymptotic conditions. As such, it cannot explain why field statistics can deviate from the asymptotic χ^2_6 probability law in practical scenarios, where the electromagnetic field within a reverberation chamber is given by a discrete plane-wave spectrum.

Let us now consider (9) under a similar statistical viewpoint. We will consider the three sets of modal parameters as random variables. The main assumptions required are that: 1) the modal parameters of different sets are independent and 2) the parameters within the same set are independent and identically distributed (iid). Recalling the physical meaning of these parameters, it is clear that they are not independent, as they are all related to the position and spatial distribution of the sources. Nevertheless this approach is commonly regarded as sound, and it is the foundation for statistical analysis for reverberation chambers [2].

The modal weights will be regarded as defined by an iid real and imaginary part

$$\tilde{\gamma}_i = \alpha_i + \mathrm{j}\beta_i \quad . \tag{11}$$

No specific assumption is required on the type of law followed by the $\{\alpha_i\}$ and $\{\beta_i\}$. We define

$$\mu_n = \mathsf{E}\left[|\tilde{\gamma}_i|^n\right] \quad , \tag{12}$$

as the n-th order moment of the modulus of the modal weights $\{\gamma_i\}$. These moments are identical for all the modal weights, following the iid assumption for the modal quantities.

The modal polarizations $\{\hat{\boldsymbol{\xi}}_i\}$ will be considered as uniformly distributed over a 4π-steradian angle, as done in [5], so that all polarizations are equally likely. Resonance frequencies will be assumed to be distributed uniformly over a bandwidth B_e around the working frequency f. These are best-case assumptions, as they imply that a perfect stirring is available. Indeed, in order to meet these requirements, the stirring technique must be capable of providing perfectly uncorrelated samples, following exactly the same probability law. Hence, the following results are not only non-conservative, but rather optimistic, and they should be regarded as lower-bounds for any use in error estimation. Such choices are meant to model a perfect stirring technique, where for each random realization the frequencies of resonance of the cavity will be modified, with equal probability of finding them over the bandwidth B_e.

Actually, the probability density function for the $\{f_i\}$ should account for the fact that the probability of finding a resonance at a given frequency increases with the modal density of the cavity. As the modal density is not linear with frequency [2], resonance frequencies cannot, in general, be distributed uniformly. But as long as the bandwidth B_e over which the $\{f_i\}$ are observed is small enough (i.e., for a highly-resonant cavity), the distribution can indeed be approximated as uniform. The actual problem with the use of simple probability density functions is that the phenomenon of mode clustering cannot be modelled properly. For the sake of simplicity this is going to be neglected in the remainder of this paper; again, this implies that we are setting our analysis in a best-case configuration, as mode clustering would yield a stronger deviation from asymptotic results.

Modelling the $\{f_i\}$ as random variables leads to having $\{\psi_i(f)\}$ behaving as random functions. Subsequent analysis will show that their squared modulus play a central role. Hence, we introduce the moments

$$\nu_n = \mathsf{E}\left[|\psi_i(f)|^n\right] \quad , \tag{13}$$

which, for $n = 2$, represent the average power of the modes, and it accounts for how effectively they are made to resonate on average, as their frequencies of resonance $\{f_i\}$ are randomly scattered around the working frequency f. This should be regarded as a sort of available power, as the actual amount of power in the modes depends on the modal weights $\tilde{\gamma}_i$. At the same time, ν_2^2 summarizes how power is shared among the different modes. Indeed the average mutual power shared by two any modes is

$$\mathsf{E}\left[|\psi_i^\star(f)\psi_j(f)|^2\right] = \mathsf{E}\left[|\psi_i(f)|^2\right]\mathsf{E}\left[|\psi_j(f)|^2\right] = \nu_2^2 \quad , \tag{14}$$

recalling the independence assumption for the resonance frequencies $\{f_i\}$. As mutual power is a measure of the overlapping of the modes, it has an important place in field statistics.

Let us now consider (10). By introducing the Cartesian unit vectors $\hat{\boldsymbol{u}}_k$, the electric energy density W can be written as

$$W = \epsilon_0 \sum_{k=1}^{3} |\mathbf{E}\cdot\hat{\boldsymbol{u}}_k|^2 \quad . \tag{15}$$

Following (9)

$$\begin{aligned} W &= \epsilon_0 \sum_{k=1}^{3} \left| \hat{\boldsymbol{u}}_k \cdot \sum_{i\in\mathscr{M}} \tilde{\gamma}_i \psi \hat{\boldsymbol{\xi}}_i \right|^2 \\ &= \epsilon_0 \sum_{k=1}^{3} \left\{ \sum_{i\in\mathscr{M}} |\tilde{\gamma}_i|^2 |\psi_i|^2 |\hat{\boldsymbol{\xi}}_i\cdot\hat{\boldsymbol{u}}_k|^2 + \right. \\ &+ \left. \sum_{\substack{i,j\in\mathscr{M}\\ j\neq i}} \tilde{\gamma}_i\tilde{\gamma}_j^\star \psi_i\psi_j^\star (\hat{\boldsymbol{\xi}}_i\cdot\hat{\boldsymbol{u}}_k)(\hat{\boldsymbol{\xi}}_j^\star\cdot\hat{\boldsymbol{u}}_k) \right\} \end{aligned} \tag{16}$$

which can be restated as

$$\begin{aligned} W &= \epsilon_0 \sum_{i\in\mathscr{M}} |\tilde{\gamma}_i|^2 |\psi_i|^2 + \\ &+ \epsilon_0 \sum_{\substack{i,j\in\mathscr{M}\\ j\neq i}} \tilde{\gamma}_i\tilde{\gamma}_j^\star \psi_i\psi_j^\star \sum_{k=1}^{3} (\hat{\boldsymbol{\xi}}_i\cdot\hat{\boldsymbol{u}}_k)(\hat{\boldsymbol{\xi}}_j^\star\cdot\hat{\boldsymbol{u}}_k) \end{aligned} \tag{17}$$

recalling that

$$\sum_{k=1}^{3} |\hat{\boldsymbol{\xi}}_i\cdot\hat{\boldsymbol{u}}_k|^2 = \|\hat{\boldsymbol{\xi}}_i\|^2 = 1 \quad . \tag{18}$$

This model can be used in order to study the actual role of losses in electric energy density statistics. To this end, we propose to compute the first two moments of the electric energy density, and to check under what conditions the standardized variance converges to the theoretical results recalled in [1], [2].

The average electric energy density can be computed by taking the ensemble average of (17). Recalling the assumption of independence between the modal weights and the frequencies

of resonance, as well as the fact that the modal weights are iid random variables, we get

$$\mathsf{E}\left[W\right] = \epsilon_0 M \mu_2 \nu_2 \quad , \tag{19}$$

having applied (12) and (13).

Getting on with the computation of the variance of the electric energy density, by squaring (17) and proceeding again by separating the coherent and incoherent parts of the sum, yields

$$\begin{aligned} \mathsf{E}\left[W^2\right] &= \epsilon_0^2 M \mu_4 \nu_4 + \\ &+ \epsilon_0^2 M(M-1)\mu_2^2 \nu_2^2 \Bigg(1 + \\ &+ \mathsf{E}\left[\left| \sum_{k=1}^{3} (\hat{\boldsymbol{\xi}}_i \cdot \hat{\boldsymbol{u}}_k)(\hat{\boldsymbol{\xi}}_j^{\star} \cdot \hat{\boldsymbol{u}}_k) \right|^2 \right] \Bigg) \end{aligned} \tag{20}$$

The ensemble average in (20) can be simplified taking note of

$$\sum_{k=1}^{3} (\hat{\boldsymbol{\xi}}_i \cdot \hat{\boldsymbol{u}}_k)(\hat{\boldsymbol{\xi}}_j^{\star} \cdot \hat{\boldsymbol{u}}_k) = \hat{\boldsymbol{\xi}}_i \cdot \hat{\boldsymbol{\xi}}_j^{\star} \tag{21}$$

and since

$$\mathsf{E}\left[|\hat{\boldsymbol{\xi}}_i \cdot \hat{\boldsymbol{\xi}}_j^{\star}|^2 \right] = \frac{1}{3} \quad \forall\, i \neq j \quad , \tag{22}$$

equation (20) can be expressed as

$$\mathsf{E}\left[W^2\right] = \epsilon_0^2 M \mu_4 \nu_4 + \frac{4}{3} \epsilon_0^2 M(M-1) \mu_2^2 \nu_2^2 \quad , \tag{23}$$

so that the standardized variance is given by

$$\left(\frac{\sigma}{\mu} \right)_W^2 = \frac{\mathsf{E}\left[W^2\right]}{(\mathsf{E}\left[W\right])^2} - 1 = \frac{1}{M} \frac{\mu_4}{\mu_2^2} \frac{\nu_4}{\nu_2^2} + \frac{M-4}{3M} \quad . \tag{24}$$

Based on the results demonstrated in Appendix A, the following result holds for $Q \gg 1$ (meaning several hundreds)

$$\frac{\nu_4}{\nu_2^2} \simeq \frac{B_e}{\pi} \frac{Q}{f} \quad , \tag{25}$$

where Q is the composite quality factor of the cavity. Attention should be paid about the fact that the definition of this composite quality factor is not the same currently used in EMC, i.e., as defined in [8], [2]. In fact, this considers the average efficiency of a reverberation chamber in converting an input power into an electric energy density. This efficiency being based on the notion of average electric energy density over the test volume, it is not suitable for statistical convergence at a specific position. We rather deal with the average time constant of the cavity at a given point. Hence, it is a function of frequency and position, with a non-smooth behaviour in these variables, presenting a large dynamics of values. The notion of average is thus applied to the Q_i of the dominant modes at the working frequency f.

From (25)

$$\left(\frac{\sigma}{\mu} \right)_W^2 = \frac{1}{\pi} \frac{\mu_4}{\mu_2^2} \frac{B_e}{M} \frac{Q}{f} + \frac{M-4}{3M} \quad . \tag{26}$$

As we anticipated in the beginning of this Section, the definition of B_e is redundant. As a matter of fact, (26) is approximated as long as we limit the sum in (9) to a finite number of modes around the working frequency. We should rather consider a level $\rho \to 0$, leading to $B_e \to \infty$ and, as a consequence, $M \to \infty$, i.e., let all the modes intervene. Clearly, this implies an increasing number of modes involved in (9), but with a level of energy getting lower as their frequency of resonance gets further away from the working frequency f. This is not in contradiction with our derivation, as this fact is accounted for by the ν_n moments. The use of the limit is valid as long as Q is high enough to have the dominant modes confined into a narrow bandwidth around f, so that the idea of an average composite Q is still physically acceptable.

Under these conditions, we can introduce the standardized variance ς_W^2 of the electric energy density, taking the limit of (26) as

$$\varsigma_W^2 = \lim_{\rho \to 0} \left(\frac{\sigma}{\mu} \right)_W^2 = \frac{1}{3} + \frac{1}{\pi} \frac{\mu_4}{\mu_2^2} \lim_{M \to \infty} \frac{B_e}{M} \frac{Q}{f} \quad . \tag{27}$$

Since for $Q \gg 1$

$$\lim_{M \to \infty} \frac{B_e}{M} = \frac{1}{m(f)} \quad , \tag{28}$$

where $m(f)$ is the modal density, expressed in Hz^{-1}, equation (27) can now be written as

$$\varsigma_W^2 = \frac{1}{3} + \frac{1}{\pi} \frac{\mu_4}{\mu_2^2} \frac{1}{M_M} \quad . \tag{29}$$

If a resonant mode were centered on f, thus with a -3 dB bandwidth $B_{3\mathrm{dB}} = f/Q$, then $M_M = m(f) B_{3\mathrm{dB}}$ would be equal to the number of modes found on average within this bandwidth. In other words, M_M assesses how strongly the modes overlap on average.

IV. On the overmoded condition

The result in (29) must be capable of predicting the asymptotic results expected from the theoretical and experimental analyses presented in [5], [20]. This is the case, as

$$\lim_{M_M \to \infty} \varsigma_W^2 = \frac{1}{3} \quad , \tag{30}$$

which is the result expected for a χ_6^2 probability distribution law [6]. Hereafter, we will refer to this asymptotic value as $\varsigma_{\chi_6^2}^2$.

This asymptotic result is met only when the number of overlapped modes increases, as opposed to common understanding, where modal density is regarded as the actual dominating parameter. This points to the true conditions that must be enacted for the cavity to be overmoded: requiring a large number of resonant modes is a necessary but not sufficient condition, as long as they are not overlapped. As this last event is tightly linked to the bandwidth of the mode response, the overmoded condition is strongly dependent on the losses experienced in the reverberation chamber.

The roles of the modal density and the composite quality factor Q are clarified by Fig. 2, where the standardized variance of the electric energy density ς_W^2 predicted by (29) is plotted against a varying modal density and quality factor. These results show how the idea of the overmoded region

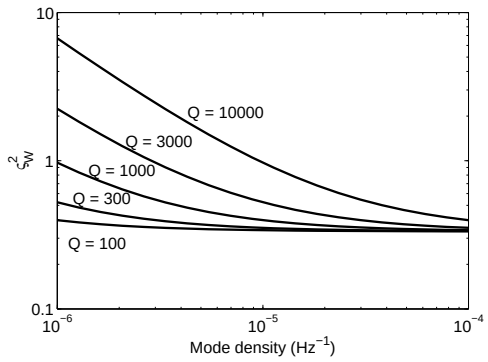

Fig. 2. The standardized variance predicted by (29), for a varying modal density and composite quality factor. A working frequency $f = 1$ GHz was assumed.

as a threshold condition could be easily thought as a correct definition, since increasing the modal density ultimately leads to an asymptotic convergence to the standardized variance expected for a χ^2_6 law, i.e., the value $1/3$.

It is noteworthy that common understanding looks at modal density and frequency as being univocally related: this wrong interpretation has likely originated because of the use of Weyl's formula [2], a smooth approximation not accounting for mode clusters. Actually, modal density broadly increases with frequency, but it can locally decrease or increase with respect to the smooth behaviour predicted by Weyl's formula, resulting in a non-monotonous function of frequency.

Fig. 2 also shows that an increasing modal density is not the only way of achieving the convergence in (30), since for a given modal density a relatively small increase of losses also leads to convergence.

This phenomenon is not new: in acoustics, this idea is expressed by Schroeder frequency [4], as the minimum frequency for which three modes are overlapped within their -3 dB bandwidth. The problem is that this definition is arbitrary and unable to quantify how strongly the actual electric energy density statistics will diverge from the asymptotic results obtained for an infinite number of resonating modes.

As opposed to this approach, we consider the relative error ϵ_{ς^2} between the result predicted by (29) and the asymptotic one

$$\epsilon_{\varsigma^2} = \frac{\varsigma^2_W - \varsigma^2_{\chi^2_6}}{\varsigma^2_{\chi^2_6}} = \frac{3}{\pi}\frac{\mu_4}{\mu_2^2}\frac{1}{M_M} \quad . \tag{31}$$

The ratio μ_4/μ_2^2 is related to the kurtosis κ of the real (or imaginary) part of the modal weights as

$$\frac{\mu_4}{\mu_2^2} = \frac{1}{2}(\kappa + 1) \quad . \tag{32}$$

In order to compute this error, we need to make some assumptions on the type of probability law followed by the modal weights. Although not justified by any physical phenomenon, they are usually assumed to be normally distributed [5]. Adopting this same approach $\mu_4/\mu_2^2 = 2$, yielding

$$\epsilon_{\varsigma^2} = \frac{6}{\pi}\frac{1}{M_M} \quad . \tag{33}$$

The ratio μ_4/μ_2^2 would not change much with the probability distribution law; e.g., for the case of uniformly distributed modal weights $\mu_4/\mu_2^2 = 7/5$.

The relationship between M_M and the divergence from the asymptotic law is actually intuitive. Chi-squared laws are a direct consequence of the central-limit theorem, as recalled in [3], a condition approached as the number of degrees of freedom increases. For a cavity, modal representations provide a clear insight, as the number of degrees of freedom is just the number of modes effectively resonating (on average) at the working frequency. Clearly, this requires a potentially high number of modes (modal density), but also the possibility to make them resonate at the working frequency: this is directly dependent on the average quality factor of the modes, the dominant parameter for making a mode accessible when working at a frequency not equal to the one at which it resonates. The merit of (33) is that it provides a quantitative formula, indispensable in order to give a meaningful definition of the overmoded condition.

Indeed, (33) clearly shows that the overmoded condition is not given by a universal threshold, but rather dependent on the admissible error on the standardized variance. This topic will be the object of a more detailed discussion in Section V. If we consider a 10 % error ϵ_{ς^2} on the standardized variance as acceptable, then at least about 20 modes must overlap within their average -3 dB bandwidth, centered around the working frequency. A quick computation allows to check that this condition is often not met in unloaded chambers, unless the working frequency is conspicuously higher than the (LUF). Experimental results supporting this claim are presented in Section VI.

These conclusions are coherent with the findings reported in [9], where it was shown that testing against the need of χ^2 distribution laws, the minimum frequency for which the test is passed can be higher than the conventional LUF derived by applying the standard [8]. In a similar way, experimental results such as those presented in [15] go in this direction: they showed that by applying goodness-of-fit tests to the samples collected in what was considered as an overmoded cavity (in the sense of standard [8]), the test would fail for certain frequencies. This implied that the overmoded condition is not ensured by passing a threshold value, but that it depends more finely on the properties of the cavity at each frequency. Indeed, considering the paradigm we have introduced in this Section, the well-known fact that the composite quality factor of a cavity follows a frequency trend far from being smooth, implies that at frequencies where the quality factor increases, the probability of not passing a goodness-of-fit test can be expected to be higher. This conclusion is clearly submitted to the joint variation of the modal density and the composite quality factor, as the two can compensate each other.

The way (33) is defined implies that a high modal density can be a sufficient condition, when it goes to infinity, as

required in asymptotic models [5]. But it also proves that for a given maximum error, the same statistical compliancy can be attained by controlling the losses within the cavity. As most of the time the modal density is not a design parameter, (33) can play an important role in the design of reverberation chambers.

The attentive Reader should avoid thinking that (33) implies that increasing losses is a certain and good solution to the limitations of reverberation chambers. From an energetic point of view, increasing losses is obviously a non-desirable policy, as it would impair the ability of a reverberation chamber in efficiently generating a high-level electromagnetic field.

But at the same time, as demonstrated in Section VI, increasing losses provide some benefits, speeding up the convergence towards an asymptotic chi-square law. This notwithstanding, (33) holds true as long as modal-weight statistics and modal density can be regarded as unaffected by increased losses. Such condition is realistic if losses have a perturbative effect, implying a relatively small increase. Actually, this scenario occurs and is of interest in practice, as the inclusion of lossy EUTs within a reverberation chamber affects the statistics of the field the latter generates. The availability of a theory capable of predicting how the field statistics is modified should come of use in understanding under what conditions the behaviour of an unloaded chamber is not too sensitive to the inclusion of EUTs. This clearly is a matter of practical concern.

As opposed to the case of a perturbative effect, it has been highlighted how a strong increase in losses has a negative impact on field statistics, as in [21]. It is noteworthy that in that study the quality factor was reduced by a factor up to ten, thus strongly modifying the reverberation chamber behaviour, whose relationship with the unloaded configuration should be questioned. Again, our analysis is incapable of predicting how a strong reduction of the quality factor affects the modal description of a cavity, so that this type of effects are out of the scope of our work.

Attention should be paid to the fact that our analysis is optimistic, as it is based on the assumption that the stirrer technique be capable of ensuring that all the dominant modes will have the same probability to span the -3 dB bandwidth around the working frequency. This means that in the case of mode clustering, the actual number of modes required might be higher.

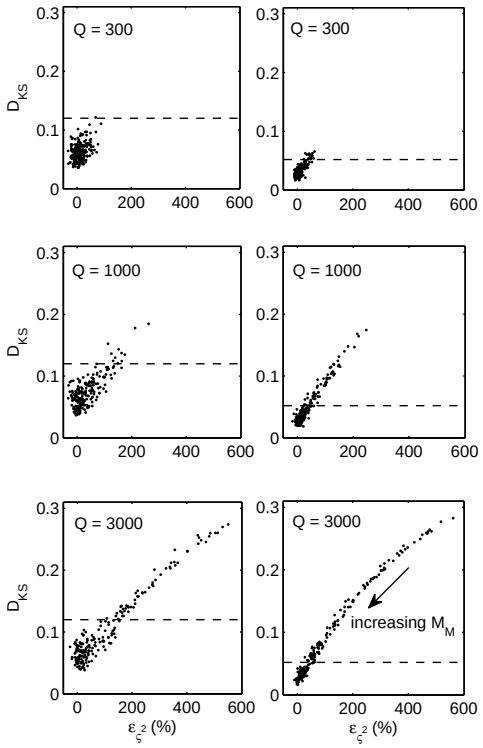

Fig. 3. Scatter plots representing the close relationship existing between the standardized variance of W and Kolmogorov-Smirnov statistics D_{KS}. The model (9) was employed with three different values for the quality factor (300, 1000 and 3000), for 200 values of modal density, spanning the range from 10^{-6} Hz^{-1} to 10^{-4} Hz^{-1}. For each configuration, 100 independent samples (left column) or 500 independent samples (right column) were generated, from which the relative error ϵ_{ς^2} on the standardized variance and Kilmogorov-Smirnov statistics D_{KS} were computed, and plotted as an individual point. All results have been computed for a working frequency $f = 1$ GHz. Dashed lines represent the threshold associated to Kilmogorov-Smirnov test, for accepting the null hypothesis of a χ^2_6 distribution law with a 95 % confidence margin.

V. Relationship with probability-law testing

The results presented so far assess the deviation from a χ^2_6 law focusing on the standardized variance. Although this is a meaningful measure of statistical compliance, it is known from the "moment problem" that two probability laws can be expected to be identical only if all their moments are identical [22]. Hence, from a theoretical point of view, we cannot draw any conclusion on how close the empirical and asymptotic laws are, unless all of their moments were available. Our analysis is limited to the first two moments of the electric energy density; as the estimation of higher moments from experimental data is a critical issue [6], we regarded such approach as practically unfeasible, as the resulting higher moments would be overwhelmed by statistical uncertainty.

It is nevertheless fundamental to have a clue about how good (33) is as an estimator of the deviation of the entire probability law. As the actual (opposed to the asymptotic) probability distribution law of W cannot be expressed in closed-form, the link between these two quantities must be ascertained directly studying the electric energy density of field samples. To this end, we have used (9), generating random values for the three modal parameter sets (as introduced in Section III), obtaining a population of random samples for the electric energy density W, as generated within a perfectly stirred cavity. This allowed us to estimate two different pieces of information: 1) the standardized variance and 2) the standardized empirical distribution function $F_W(W)$ of

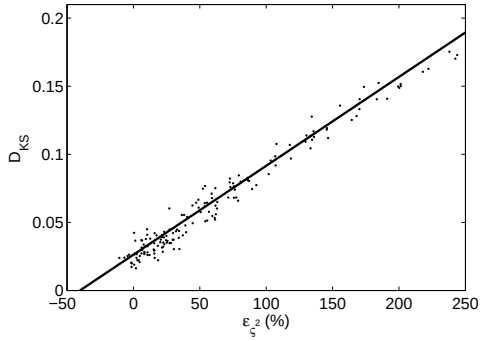

Fig. 4. Numerical data generated by (9), from 500-sample populations (as in Fig. 3), and the approximation (36) obtained by means of a least-squared linear regression (solid line).

W. From the latter we computed the Kolmogorov-Smirnov statistic D_{KS}, defined as [23]

$$D_{KS} = \max_{W} \left| F_W(W) - F_{\chi^2_6}(W) \right| \quad , \tag{34}$$

where $F_{\chi^2_6}(W)$ is the standardized probability distribution function of the asymptotic χ^2_6 law. Standardization of random variables, and hence of their associated probability distributions, is a necessary step, in order to apply goodness-of-fit tests in a meaningful way, as the reference asymptotic distribution moments are not known and configuration-dependent.

The correlation between ϵ_{ς^2} and D_{KS} was investigated by means of scatter plots, as those shown in Fig. 3. These results show unmistakably that the Kolmogorv-Smirnov statistics is tightly related to the error on the standardized variance. The parametric analysis in Fig. 3 proves that an increasing Q leads to a stronger deviation from the asymptotic χ^2_6 law. The scatter plots are actually parametric curves in the variable M_M, as pointed out in Fig. 3, rather than directly dependent on variables m, f and Q. Hence, the results in Fig. 3 are not valid only for a specific configuration, but in general.

The fact that the points in Fig. 3 rather than laying on a curve are scattered should not be interpreted as a hint of a partial correlation between D_{KS} and ϵ_{ς^2}: as a matter of fact, these two quantities have been estimated from a finite population, implying that these estimators are affected by residual statistical uncertainty (see Appendix B). Indeed, increasing the population from 100 to 500 samples shows a substantial reduction in the uncertainty of the data correlation. Hence, we think that the variance error ϵ_{ς^2} could be used for assessing the deviation of the entire distribution law, although it only brings information about the first two moments of W. The accuracy of this approach is clearly dependent on the number of available samples.

In any case, the strong link between Kolmogorov-Smirnov statistics and the standardized variance error validates the idea of using (33) for predicting how changing losses would affect the statistical behaviour of a reverberation chamber, thus extending the purpose of (33) from an analysis tool for meaningful physical understanding, to potentially a prediction/design tool for practically ensuring the statistical compliance of a reverberation chamber.

The hypothesis of statistical compliance is based on the validity of the following condition [23]

$$\sqrt{N} D_{KS} < K_\alpha \quad , \tag{35}$$

where N is the number of independent field samples and K_α is a threshold value for a significance level equal to α. Typical values of K_α for $\alpha = 0.05$ are about 1.15. This means that for $N \geqslant 100$, the most important region in Fig. 3 is for $\epsilon_{\varsigma^2} \lesssim 150$ %, where the correlation between ϵ_{ς^2} and D_{KS} is close to linear. As establishing a closed-form expression linking these two quantities is likely difficult, we have rather opted for a simple linear regression model

$$D_{KS} \simeq \eta_1 + \eta_2 \epsilon_{\varsigma^2} \quad \epsilon_{\varsigma^2} \geq 0 \quad , \tag{36}$$

which is valid only for $\epsilon_{\varsigma^2} \lesssim 250$ %. The regression parameters $\eta_1 = 2.6 \cdot 10^{-2}$ and $\eta_2 = 6.5 \cdot 10^{-2}$ refer to the model showed in Fig. 4.

Plugging (36) into (35) yields the maximum acceptable error $\epsilon_{\max}$ ensuring statistical compliance

$$\epsilon_{\varsigma^2} < \epsilon_{\max} = \frac{K_\alpha}{\eta_2 \sqrt{N}} - \frac{\eta_1}{\eta_2} \quad . \tag{37}$$

Apart as a tool for checking the statistical compliance of a reverberation chamber, (37) is also important in the definition of the overmoded condition. As a matter of fact (37) states that in order to pass Kolmogorov-Smirnov test, it is not necessary to have a negligible error on the standardized variance. The actual upper-bound $\epsilon_{\max}$ to apply to ϵ_{ς^2} can be quite high, as the number of samples N decreases. This does not mean that the conclusions in Section IV are incorrect: as a matter of fact, this higher threshold just accounts for the fact that the true ϵ_{ς^2} is not known, having been estimated from a finite population. Hence, it is pointless to try to enforce a condition on ϵ_{ς^2} stronger than the precision with which this quantity is known.

As an example, using the data shown in Fig. 3, a 500-sample population would require a relative error $\epsilon_{\varsigma^2} < 39$ % in order to accept the hypothesis of an electric energy density following the asymptotic chi-square distribution. Applying (33), this maximum error threshold is translated into a need for about 5 overlapped modes, a result well looser than the 20 modes required by setting a 10 % error on the standardized variance. As a consequence, the definition of overmoded region cannot be dissociated from the statistical uncertainty that is inevitably present when dealing with estimators based on a finite population of random samples. In other words, it is not statistically meaningful to set a general and arbitrary threshold on the number of overlapped modes M_M.

Equation (37) can also be used for designing additional losses aiming at improving the statistics of the electric energy density. Given a working frequency f and an estimate of the modal density m, and computing from (37) the maximum error $\epsilon_{\max}$ leading to passing the Kolmogorov-Smirnov test, a maximum composite quality factor $Q_{\max}$ is found

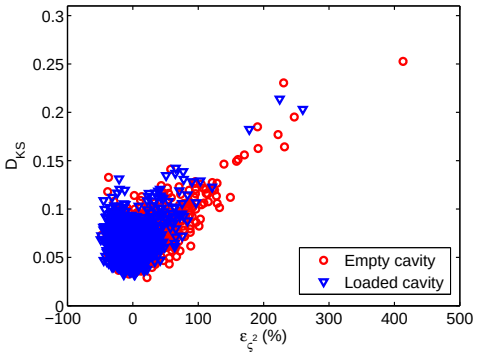

Fig. 5. Scatter plots of D_{KS} and ϵ_{ς^2} as derived from experimental data for the case of the empty and absorber-loaded chamber. The samples are related to the entire frequency range 0.7-3 GHz.

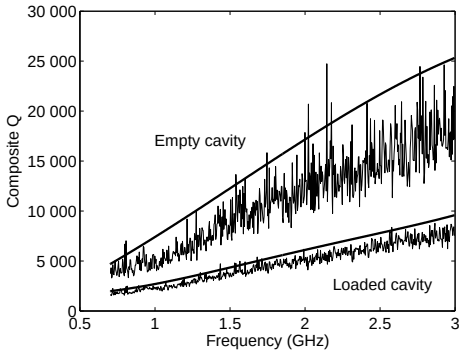

Fig. 6. Quality factors for the empty and loaded chambers. The smooth curves represent the loose majorants used for deriving the maximum-error results in Fig. 7.

$$Q_{\max} = \frac{\pi}{6} m f \epsilon_{\max} \quad . \tag{38}$$

Considering a lower Q would be pointless, as the improvement on statistics would be undetectable, due to unavoidable statistical uncertainty, while field-strength would degrade.

These discussions clearly hold as long as (9) is physically sound, i.e., as additional losses have a perturbative effect on the field within the cavity. An experimental validation of this model is presented in the next Section.

VI. Experimental results

In order to validate our findings, experimental tests were carried out in Supelec's reverberation chamber. This cavity, measuring 13.8 m^3, and equipped with a 100-step mechanical stirrer, has its LUF around 550 MHz. In our setup, a log-periodic dipole antenna was used as a source exciting the cavity, over the frequency range 0.7-3 GHz. An optical-link field probe was used in order to collect data about the three field components at one position within the test volume of the chamber, while the stirrer was made to move over its entire range of rotation.

This approach was used for two configurations, for an empty cavity and with a small piece of RF absorber, made up of 4 pyramids about 30 cm high, standing in the center of the floor of the cavity. As the field probe used was phase sensitive, we were able to compute the composite quality factor for the cavity over the entire frequency range of test, by post-processing the frequency-spectrum data in time domain (see Fig. 6).

The field samples were used in order to compute the electric energy density samples. The same procedure exposed in the previous Section was then applied: the aim was to check whether the same correlation between D_{KS} and ϵ_{ς^2} was to be found in practice. The results of this analysis, shown in Fig. 5, confirm those presented in Fig. 3. As the number of steps is limited to 100, the statistical uncertainty associated to the estimations of ϵ_{ς^2} and D_{KS} is not negligible, as already discussed in the previous Section and detailed in Appendix B. Moreover, the actual number of independent samples generated by the mechanical stirrer is frequency-dependent, going from about 30 around 700 MHz, to about 100 at 3 GHz, thus leading to an even higher statistical uncertainty in the lower frequency range.

Having validated the close relationship between D_{KS} and ϵ_{ς^2}, we went further in our validation by focusing on the relative error ϵ_{ς^2}. The next step was to look at how well (33) allows to predict the maximum deviation of the standardized variance, knowing a fair estimate of the modal density and the composite quality factor of a reverberation chamber. Though the latter can be estimated by means of measurements, modal density is not something that is routinely measured, although a solution to this problem has recently been proposed [24]. In the context of this paper, we have stuck to the current approach consisting in using Weyl's approximation, and we have considered the simplest of Weyl's formulas [2]

$$m(f) \simeq \frac{8\pi V f^2}{c^3} \quad . \tag{39}$$

With no access to a precise estimate of modal density, any attempt at finely predicting the standardized deviation error is bound to an error that cannot be estimated easily. For this reason we rather focused on the ability to provide results bounding the error, and thus capable of giving a warning about the global trend of ϵ_{ς^2} over a given frequency range. Following this point of view, rather than using the quality factor estimate obtained from experimental characterization of our chamber, we considered a smooth majoring curve. The rationale behind this approach is that, according to (33), the maximum error occurs when a minimum number of overlapped modes is present, which in turn occurs when the ratio of the modal density and the composite quality factor is at a minimum. The use of a smooth curve is justified by our interest in the trend of the error, and not its fine modelling. Furthermore, the information available on the quality factor is often provided

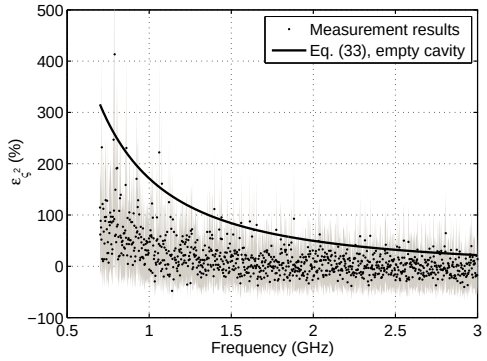

(a)

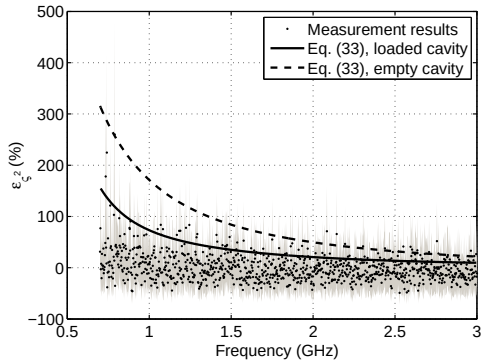

(b)

Fig. 7. Experimentally estimated relative error ϵ_{ς^2} as a function of frequency: (a) for the empty cavity and (b) for the one loaded with the small absorber. The results from (33) have been computed from the smooth curves majoring the composite Q derived from the experimental data and shown in Fig. 6. Shaded areas stand for the 95 % statistical uncertainty of the estimated ϵ_{ς^2}, computed for a 95 % confidence margin as shown in Appendix B.

by simple predictive models [2], particularly during a design phase.

Fig. 6 shows that we did not use a true majorant. The reason for this is that it would have provided too conservative results, as a few points higher than average can lead to a strong overestimation of Q. The approximations we employed were chosen as a compromise between the need of a majoring curve and that of not considering a too strongly overestimated quality factor. As a consequence, for certain frequencies the relative error ϵ_{ς^2} can be higher than the estimated upper bound. This outcome can also be caused by modal depletion, whose frequencies of occurrence are unknown.

From these data and (39) we computed the curves shown in Fig. 7, predicting the maximum deviation of the electric energy density from the asymptotic chi-square law. The actual error ϵ_{ς^2} was directly estimated from the experimental data. The statistical uncertainty associated to these results has been

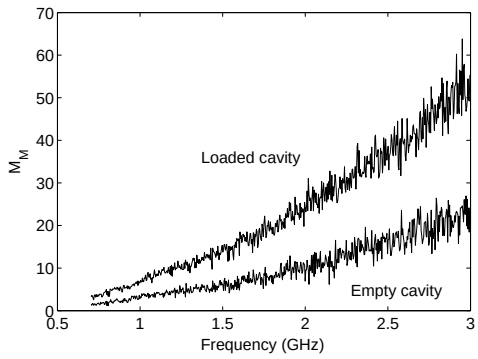

Fig. 8. Estimated average number of overlapped modes M_M, for the unloaded and loaded configurations.

estimated with a 95 % confidence margin as detailed in Appendix B, and is shown in Fig. 7 as shaded areas.

Fig. 7 proves that (33) is indeed capable of predicting the trend of the maximum ϵ_{ς^2}, as the composite quality factor and the modal density evolve in frequency, and this for two chamber configurations. The comparison between the error ϵ_{ς^2} in the case of the empty and loaded chamber is especially interesting as it is clear that the results predicted by (33) are indeed closely following the global trend of the maximum deviation of the statistics of the electric energy density. These results also prove that (33) can be used in practice as a design tool, as the majorant of the error computed in the case of inclusion of additional losses correctly predicts the improvement in the worst-case statistical performance of the loaded cavity.

The statistical uncertainty cannot be neglected, as it is the main reason for the residual error at the higher frequency range. The procedure proposed in Appendix B allows estimating a residual error of about 46 % on ϵ_{ς^2}, even though this latter is expected to be close to zero. This result is independent of the proposed model, and merely based on statistical considerations. This statistical uncertainty, present even when the reverberation chamber is expected to behave ideally, is the reason of existence of the ambiguity in the definition of the overmoded condition. It is meaningless to require an error ϵ_{ς^2} smaller than this statistical uncertainty, as the former cannot be measured precisely enough. It is interesting to notice that this statistical uncertainty appears to be smaller than the threshold imposed by (37) for accepting the asymptotic condition (and thus the overmoded condition), as it would be expected, since they are intimately related.

Looking at the ϵ_{ς^2} estimated from measurements, there exist a lower frequency for which the error seems not to reduce anymore. This frequency is about 2 GHz and 1.5 GHz for, respectively, the empty and loaded chambers. It is worthwhile checking what is the number of overlapped modes M_M at these frequencies. An estimate of M_M is shown in Fig. 8, based on the experimentally evaluated composite quality fac-

tors and the modal density given by (39). For the two frequencies previously mentioned, it seems that a minimum number of 10 overlapped modes is required, in order to have the better performance possible, according to the limited accuracy provided by the residual statistical uncertainty. These results are actually too restrictive, as a more statistically motivated choice would make use of (37), obtaining 800 MHz for the empty chamber and a frequency below 700 MHz for the loaded one. This example is meaningful in depicting the intrinsical ambiguity of a single definition of the overmoded condition, and the fundamental insight brought in by (33) and (37).

A final discussion is worthwhile: the validity of (33) implies that if the error it predicts is comparable with the one found in practice in a mode-stirred reverberation chamber, then it would be wrong, from a statistical point of view, to conclude anything about the eventual inefficiency of the stirring technique. As a matter of fact, (33) has been derived under a perfect-stirring assumption, so that the eventual presence of a poor stirring is expected to provide an error ϵ_{ς^2} higher than that due to a limited modal overlapping. This is all the more true in the lower frequency range, where the ineffectiveness of field stirring is often regarded as the major source of statistical non-compliancy in reverberation chambers: interestingly, the lower frequency range is also where poor modal overlapping appears more strongly.

VII. Conclusions

A discrete modal description of the field within a cavity has allowed us to quantify the role that losses play in the statistics of the electric energy density generated within reverberation chambers. The proposed model has led to the derivation of a simple formula expressing the error between the actual standardized variance and the asymptotic one. This error was shown to be dominated by the number of modes superposed within the -3 dB bandwidth of the dominant modes; as such, this result goes against common understanding that the overmoded condition is a mere matter of available resonating modes. We have proven that the definition of the overmoded condition is not universal, but depends on the maximum acceptable deviation from asymptotic laws, as well as on the number of independent samples generated by the stirring technique.

By linking the standardized variance error ϵ_{ς^2} to Kolmogorov-Smirnov statistics, it was proven that ϵ_{ς^2} is a meaningful metric for assessing how likely electric energy density samples are to deviate from an asymptotic χ^2_6 probability law. This same analysis has led to the definition of a maximum composite quality factor that should not be exceeded in order to ensure statistical compliancy. A fundamental result is that even starting with a perfect-stirring assumption and a high modal density, an electrically large reverberation chamber can still present a non-asymptotic statistical performance. These conclusions have major consequences on other commonly accepted ideas, such as that non-compliance with asymptotic laws is always a matter of poor stirring and that the Q should always be as high as possible.

Experimental results support our findings, both for the soundness of the proposed deviation metric and the fact that it allows to predict the actual error incurred in field samples. This latter result is fundamental, as it could lead to a simple way of assessing the statistical compliance of a reverberation chamber, and how relatively small changes in its composite quality factor would affect its statistics.

Acknowledgements

We wish to acknowledge the contribution of the anonymous Reviewers to the present version of this paper, in particular the suggestion of the existence of an optimal composite quality factor.

Appendix A
Moments of the $|\psi_i(f)|$ random variables

Following the derivation given in Section IV, two moments are needed, the second and the fourth. The second-order moment of $|\psi_i(f)|$ reads

$$\mathsf{E}\left[|\psi_i(f)|^2\right] = \int |\psi_i(f)|^2 p(f_i)\mathrm{d}f_i \quad , \tag{40}$$

where $p(f_i)$ is the probability density function for the frequency of resonance f_i. As recalled in [11], there exist minimum requirements for the composite quality factor of a cavity, for it to be compliant with EMC standards. This being coherent with our study, we can assume $Q_i \gg 1$. As a consequence, the average relative bandwidth $B_{M,i} = f_i/Q_i$ of each mode can be expected to be much smaller than one. Hence, the $|\psi_i(f)|$ give a non-negligible contribution over an equivalent bandwidth $B_e/f_i = 1/Q_i \ll 1$. The ensemble integral in (40) can thus be limited over a finite and narrow bandwidth B_e; this implies that it is reasonable to assume that over this bandwidth all of the modes have the same bandwidth. In other words, one can consider that the $\psi_i(f)$ functions are frequency-shifted replicas of the same template $\psi_0(f)$, i.e., $\psi_i(f) = \psi_0(f - f_i)$. At the same time, the narrow-band requirement, together with the perfect-stirrer assumption at the heart of our work, allows to consider resonance frequencies uniformly distributed over B_e. As such

$$\mathsf{E}\left[|\psi_i(f)|^2\right] = \frac{1}{B_e}\int_{B_e} |\psi_i(f)|^2 \mathrm{d}f_i \quad . \tag{41}$$

The frequency-replica paradigm implies that

$$\int_{B_e} |\psi_i(f)|^2 \mathrm{d}f_i = \int_{B_e} |\psi_0(f-f_i)|^2 \mathrm{d}f_i = \int_{B_e} |\psi_0(f)|^2 \mathrm{d}f \quad . \tag{42}$$

The last integral is now recognizable as the energy of the template function; clearly, this leads to modal functions $\psi_i(f)$ with the same energy. This was shown to be given by [25]

$$\int_{B_e} |\psi_0(f)|^2 \mathrm{d}f = \frac{1}{B_{M,i}}\frac{\pi}{2}\frac{Q_i^2}{Q_i^2+1} \simeq \frac{\pi}{2B_{M,i}} \quad . \tag{43}$$

Hence

$$\nu_2 \simeq \frac{\pi}{2B_{M,i}B_e} \quad . \tag{44}$$

The fourth-order moment can be obtained by means of the same approach [25], yielding

$$\nu_4 \simeq \frac{\pi}{4B_{M,i}^3 B_e} \tag{45}$$

and finally

$$\frac{\nu_4}{\nu_2^2} \simeq \frac{B_e}{\pi}\frac{Q}{f} \quad , \tag{46}$$

having introduced the approximation $B_{M,i} \simeq B_M$, where $B_M = f/Q$ is the average -3 dB bandwidth of the dominant modes at the working frequency f and Q the associated composite quality factor.

APPENDIX B
STATISTICAL UNCERTAINTY FOR A FINITE POPULATION

In the experimental evaluation of the error ϵ_{ς^2} in the standardized variance, estimators are used for the average value and the variance of W. Having been derived from a finite population of N independent samples, these estimators are affected by a residual statistical uncertainty that is important to acknowledge and estimate. This can be done by applying a local linearization of the definition of the error ϵ_{ς^2}, obtaining the following propagation-of-error model [6]

$$\sigma^2_{\hat{\epsilon}_{\varsigma^2}} = \left(\frac{\partial \epsilon_{\varsigma^2}}{\partial \mu_W}\right)^2 \sigma^2_{\hat{\mu}_W} + \left(\frac{\partial \epsilon_{\varsigma^2}}{\partial \sigma^2_W}\right)^2 \sigma^2_{\hat{\sigma}^2_W} \quad , \tag{47}$$

where $\hat{\mu}_W$ and $\hat{\sigma}^2_W$ are unbiased estimators of, respectively, μ_W, the average electric energy density and σ^2_W, its variance, as derived from the N available samples [6]. The derivatives are evaluated over the average values of these estimators. These estimators behave as random variables, with average values equal to those they should estimate (unbiased estimators) and variances $\sigma^2_{\hat{\mu}_W}$ and $\sigma^2_{\hat{\sigma}_W}$. Assuming the N samples to be iid, the estimator variances can be approximated as [6]

$$\sigma^2_{\hat{\sigma}^2_W} = \sigma^4_W \left(\frac{2}{N-1} + \frac{\kappa_W - 3}{N}\right) \tag{48}$$

$$\sigma^2_{\hat{\mu}_W} = \frac{\sigma^2_W}{N} \tag{49}$$

where κ_W is the kurtosis of the random variable W. As this value is not known for the random variable W, we will approximate it by means of its asymptotic value for a χ^2_6 distribution law, i.e., $\kappa_W = 5$. This yields

$$\sigma^2_{\hat{\epsilon}_{\varsigma^2}} \simeq \frac{4}{3N}\left(1+\epsilon_{\varsigma^2}\right)^3 + \left(\frac{2}{N-1} + \frac{\kappa_W - 3}{N}\right)\left(1+\epsilon_{\varsigma^2}\right)^2 \quad , \tag{50}$$

which is the square of the root-mean-square uncertainty of the ϵ_{ς^2} estimator. Attention should be paid to the fact that (50) depends on the exact error ϵ_{ς^2}, which is only known by means of its estimate $\hat{\epsilon}_{\varsigma^2}$. In the higher frequency range, as $\epsilon_{\varsigma^2} \to 0$, (50) simplifies to

$$\lim_{\epsilon_{\varsigma^2}\to 0} \sigma^2_{\hat{\epsilon}_{\varsigma^2}} \simeq \frac{16}{3N} \quad , \tag{51}$$

which is the residual statistical uncertainty that hinders the enforcement of a single definition of the overmoded condition. For $N = 100$ the standard deviation of the estimation error is about 23 %. Assuming it to be normally distributed, the maximum residual error is about twice as such, for a 95 % confidence level, i.e., about 46 %.

REFERENCES

[1] J. Kostas and B. Boverie, "Statistical model for a mode-stirred chamber," *Electromagnetic Compatibility, IEEE Transactions on*, vol. 33, no. 4, pp. 366 –370, nov 1991.
[2] D. Hill, "Electromagnetic theory of reverberation chambers," *NIST Technical note*, no. 1506, 1998.
[3] T. Lehman, "A statistical theory of electromagnetic fields in complex cavities," *Interaction Notes, Note 494*, 1993.
[4] M. Schroeder, "Statistical parameters of the frequency response curves of large rooms," *J. Audio Eng. Soc*, vol. 35, no. 5, pp. 299–305, 1987.
[5] D. Hill, "Plane wave integral representation for fields in reverberation chambers," *IEEE Transactions on Electromagnetic Compatibility*, vol. 40, no. 3, pp. 209–217, 1998.
[6] F. James, *Statistical methods in experimental physics*. World Scientific, 2006.
[7] N. Wellander, O. Lundén, and M. Bäckström, "Experimental investigation and mathematical modeling of design parameters for efficient stirrers in mode-stirred reverberation chambers," *Electromagnetic Compatibility, IEEE Transactions on*, vol. 49, no. 1, pp. 94 –103, feb. 2007.
[8] *Reverberation chamber test methods*, International Electrotechnical Commission (IEC) Std. 61 000-4-21, 2003.
[9] C. Lemoine, P. Besnier, and M. Drissi, "Investigation of reverberation chamber measurements through high-power goodness-of-fit tests," *Electromagnetic Compatibility, IEEE Transactions on*, vol. 49, no. 4, pp. 745 –755, nov. 2007.
[10] G. Orjubin, E. Richalot, S. Mengue, and O. Picon, "Statistical model of an undermoded reverberation chamber," *Electromagnetic Compatibility, IEEE Transactions on*, vol. 48, no. 1, pp. 248 –251, feb. 2006.
[11] C. Holloway, D. Hill, J. Ladbury, and G. Koepke, "Requirements for an effective reverberation chamber: unloaded or loaded," *Electromagnetic Compatibility, IEEE Transactions on*, vol. 48, no. 1, pp. 187 –194, feb. 2006.
[12] B. Zhang, W. Li, X. Li, Z. Yuan, J. He, and R. Zeng, "Load effect investigation of a reverberation chamber," in *Antennas, Propagation and EM Theory, 2008. ISAPE 2008. 8th International Symposium on*, November 2008, pp. 1115–1118.
[13] D. Zhang, E. Li, T. Yeo, W. Chow, and J. Quek, "Influences of loading absorber on the performances of a reverberation chamber," in *Electromagnetic Compatibility, 2003 IEEE International Symposium on*, vol. 1, August 2003, pp. 279–281 vol.1.
[14] O. Lundén and M. Bäckström, "How to avoid unstirred high frequency components in mode stirred reverberation chambers," in *Electromagnetic Compatibility, 2007. EMC 2007. IEEE International Symposium on*, July 2007, pp. 1–4.
[15] V. Primiani, F. Moglie, and V. Paolella, "Numerical and experimental investigation of unstirred frequencies in reverberation chambers," in *Electromagnetic Compatibility, 2009. EMC 2009. IEEE International Symposium on*, August 2009, pp. 177–181.
[16] J. Dawson, T. Konefal, M. Robinson, A. Marvin, S. Porter, and L. Chirwa, "Field statistics in an enclosure with an aperture - effect of Q-factor and number of modes," in *Electromagnetic Compatibility, 2005. EMC 2005. 2005 International Symposium on*, vol. 1, 8-12 2005, pp. 141 – 146 Vol. 1.
[17] N. Marcuvitz, *Waveguide handbook*. Inspec/Iee, 1986.
[18] J. Van Bladel, *Electromagnetic fields*. IEEE, 2007.
[19] B. Liu, D. Chang, and M. Ma, "Eigenmodes and the composite quality factor of a reverberating chamber," *US Nat. Bur. Stand. Tech. Note*, vol. 1066, 1983.
[20] P. Corona, G. Ferrara, and M. Migliaccio, "Reverberating chambers as sources of stochastic electromagnetic fields," *Electromagnetic Compatibility, IEEE Transactions on*, vol. 38, no. 3, pp. 348 –356, Aug 1996.
[21] O. Lundén and M. Bäckström, "Absorber loading study in FOI 36.7 m^3 mode stirred reverberation chamber for pulsed power measurements," in *IEEE EMC Symposium, Detroit, USA*, 18-22 August 2008.
[22] K. Chung, *A course in probability theory*. Academic Pr, 2001.
[23] R. D'Agostino and M. Stephens, *Goodness-of-fit techniques*. CRC, 1986.
[24] A. Cozza, "An experimental method for assessing the modal density in a reverberation chamber," in *Electromagnetic Compatibility (APEMC), 2010 Asia-Pacific Symposium on*, 12-16 April 2010, pp. 578 –581.
[25] ——, "Statistics of the performance of time reversal in a lossy reverberating medium," *Physical Review E*, vol. 80, no. 5, p. 56604, 2009.

Probability Distributions of Local Modal-Density Fluctuations in an Electromagnetic Cavity

Andrea Cozza, *Member, IEEE*

***Abstract*—Results from random-matrix theory are applied to the modeling of random fluctuations in the modal density observed in an electrically large cavity. By starting from results describing the probability distribution of the modal spacing between adjacent frequencies of resonance, or nearest-neighbor spacing, we introduce a simple procedure allowing to pass from the modal spacing to the local modal density as measured over a finite bandwidth. This local definition of the modal density is more consistent with the physics of reverberation chambers, since it has been recently shown that the deviation from asymptotic statistics of field samples is dependent on the number of modes overlapping within a modal bandwidth. It is shown that as opposed to current interpretation, the number of overlapping modes is a strongly fluctuating quantity, and that estimating it by taking the frequency derivative of Weyl's formula can lead to non-negligible errors and misunderstandings. Regarding these fluctuations as second-order effects is therefore not sound from a physical point of view, since the existence of modal depleted scenarios can easily explain the appearance of local anomalies in the field statistics, particularly, but not exclusively, in the lower frequency range of operation of reverberation chambers.**

***Index Terms*—Cavities, mode-stirred reverberation chambers, stochastic fields, test facilities, field statistics, random-matrix theory, random fluctuations.**

GLOSSARY

$N(f)$	Cumulative number of modes up to the frequency f.
$N_{\mathrm{W}}(f)$	Weyl's smooth approximation of $N(f)$.
$N_{\mathrm{f}}(f)$	Residual fluctuations $N(f) - N_{\mathrm{W}}(f)$ not accounted for by Weyl's approximation.
$m_{\mathrm{W}}(f)$	First derivative of $N_{\mathrm{W}}(f)$, used as an estimate of the modal density.
$M_{\mathrm{W}}(f)$	Average number of modes overlapping in a bandwidth B, estimated as $B\, m_{\mathrm{W}}(f)$.
$M_{\mathrm{loc}}(f)$	Actual number of modes overlapping in a bandwidth B.
$m_{\mathrm{loc}}(f)$	Homogenized local modal density $M_{\mathrm{loc}}(f)/B$.
$\varsigma^2_W(f)$	Normalized variance σ^2/μ^2 of the electric-energy density W.

I. INTRODUCTION

THE prediction of the performance of mode-stirred (or tuned) reverberation chambers (MSRCs) as generators of random electromagnetic test scenarios is a fundamental topic both from a theoretical and practical point of view in the operation of these facilities. The main issue here is the reproducibility of tests carried out in them and in particular the need to ensure that the fields generated by any MSRC belong to the same type of probability law. The current understanding of MSRCs is that at suitably high frequencies the electric and magnetic fields can be accurately described as complex-valued (circular) Gaussian random variables.

Such a probability law is typically assumed as a reasonable choice due to the (expected) availability of a large number of normal modes at high frequencies [1], [2], [3], as opposed to what are regarded as undermoded scenarios, where alternative reference probability laws have been proposed [4], [5], [6].

Still, as recalled in [7], the Gaussian hypothesis is only but an approximate model and it is incapable to explain the appearance of frequencies at which the field statistics proves to deviate substantially from those of a Gaussian random variable. Excluding the existence of unconventional setup configurations where the excitation source is strongly coupled to the equipment under test (EUT) [8], experimental observations of local anomalies in field statistics, appearing as glitches, have been reported in several papers [9], [10], [11]: these phenomena, though partially tolerated in the current operation of MSRC [12], have not yet received a satisfying physical explanation. Anomalies of this kind usually imply statistical dispersions higher than expected for a diffuse field (perfect reverberation), taking the form of local deviations rather than systematic ones over a bandwidth: these are usually referred to as outliers [2], i.e., as samples not belonging to the reference law and suspected to indicate a problem of some sort in the setup.

A rather different explanation can be proposed as soon as we remember that modal representations of the electromagnetic field generated within a MSRC are accurately reproduced by considering a finite number of modes, and in particular the average number of modes M_{loc} overlapping within the -3 dB bandwidth of a mode [13]. Theoretical and experimental results presented in [13] proved that M_{loc} can be quite low (a few units) even at frequencies where a MSRC is regarded as fully functional: as a result, the hypothesis of a Gaussian-distributed field is no longer justified, and its use should be limited to an educated guess for approximate predictive models.

Our previous work in [13] proved that the standardized (or normalized) variance, or variability for simplicity, of the electric-energy density, can be predicted on the basis of a few macroscopic parameters, such as the frequency, the geometrical dimensions of the cavity and an estimate of its average quality factor. It was intended as a first step in a better understanding of anomalous field statistics, suggested as being basically due to a poor local modal overlapping, a

A. Cozza is with the Département de Recherche en Électromagnétisme, Laboratoire des Signaux et Systèmes (L2S), UMR 8506 SUPELEC - Univ Paris-Sud - CNRS, 3 rue Joliot-Curie, 91192 Gif-sur-Yvette, France. Contact e-mail: andrea.cozza@supelec.fr.

fact already recognized [12], [6], without having been more deeply explored.

The accuracy of the modal density estimated from Weyl's formula is often taken for granted. In fact, as shown in this paper, this is not a sound approach, as the modal density should rather be treated as a random quantity, subjected to non-negligible random fluctuations. The apparent lack of any available model capable of predicting the likeliness of observing a strong reduction (or increase) in the local modal density makes any prediction of the probability of observing these phenomena practically impossible.

It is the aim of this paper to introduce the probability laws of the modal density as observed *locally*, over a finite bandwidth, an approach that is better matched to the concept of modal overlapping. The average number of modes and ultimately the local modal density are considered as random quantities, according to the concepts of random-matrix theory (RMT) [14], [15]. Our results are completely general and independent from the details of implementation of the MSRC, as they are based on universality classes, as defined in the context of RMT. Interestingly, the probability law of the local modal density is entirely characterized by the average modal density predicted by Weyl's formula and the class of statistics of the MSRC. A priori knowledge of the average quality factor, the volume of the cavity and the frequency of operation are thus sufficient to derive a complete description of the statistics of the local modal density.

The interest of these models is not merely relegated to a better physical understanding of MSRCs, but also has a direct impact on their practical use. The results here proposed can be invoked when studying how likely it is that the field statistics in a reverberation chamber deviates from the ideal case usually taken as a reference, by means of the procedure introduced in [13]: clearly, the model here proposed being derived on physical grounds, the probability of appearance of anomalous field statistics can be predicted without recurring to phenomenological approaches, such as those based on the idea of fitting empirical field distributions to general theoretical laws [11].

The paper is organized as follows: Section II discusses various definitions of modal density and overlapping, while summarizing some major results derived in the context of random-matrix theory at the basis of the derivation presented in the rest of this paper. Sections III and IV introduce auxiliary results later used in Section V in the derivation of the probability distributions of the local modal density. An empty cuboid cavity is used as a test case in Section VI, supporting our predictions of a strongly fluctuating local modal density. Some considerations about the practical impact of these results are presented in Section VII, with an emphasis on the concept of outliers and local anomalous field statistics. The Appendix presents a detailed general calculation of the number of overlapping modes that should be expected in a cavity, supporting our claim that weak modal overlapping should not be expected only in the lower frequency range, but even in what is usually expected to be the overmoded region.

II. Preliminary discussions

Our analysis takes its start from results already available in the literature: on the one hand the link between the variability of the energy density and the average number of overlapped modes observed at the working frequency, and on the other the statistics of modal-related quantities derived in the context of RMT. The purpose of this Section is to briefly recall these tools while emphasizing some physical concepts and limitations that play a fundamental role in the subsequent derivations.

A. Local modal density and overlapping

When thinking about the modal density, one intuitively associates it to a certain number of modes resonating around the working frequency. The modal density can therefore be defined as the average number M_B of modes found in a bandwidth B,

$$m_B(f) = \frac{M_B(f)}{B}, \tag{1}$$

and is therefore dependent on B itself. As long as B is large enough to encompass several modes, then (1) is an average that can be expected to converge to a single value, for B large enough, predicted by Weyl's approximation [16]

$$m_{\mathrm{W}}(f) = \frac{8\pi V}{c_0^3} f^2 + o(f) = \frac{8\pi V_\lambda}{f} + o(f), \tag{2}$$

with V the volume of the cavity, c_0 the speed of light in the filling medium and V_λ the volume measured in cubic wavelengths.

The definition (1) provides a more general framework than (2), since the modal density is considered in a local setting: for this reason, it will be referred to as the local modal density, associated to a specific bandwidth.

It is often practical to associate a specific value to the modal density $m(f)$, e.g., by taking the limit for $B \to 0$: the discrete nature of the set of frequencies $\{f_i\}$ at which a cavity resonates implies that in practice $m(f)$ can only take two values, i.e., zero if no mode resonates at the working frequency f or infinity otherwise [14], i.e.,

$$m(f) = \lim_{B\to 0} m_B(f) = \sum_{i=1}^{\infty} \delta(f - f_i). \tag{3}$$

This outcome is inevitable as the distribution of the normal modes cannot approach the completeness of real numbers, thus leaving inevitable "gaps" between them.

The estimate $m_{\mathrm{W}}(f)$ is in general different from $m_B(f)$ because it is not derived as in (3), but in a less direct manner, by first introducing the function $N(f)$ describing the overall number of modes of a cavity up to the frequency f

$$N(f) = \#\{f_i : f_i \leqslant f\}, \tag{4}$$

with $\#$ the cardinality of a set. This function can be represented as the sum of a smooth approximation $N_{\mathrm{W}}(f)$ and a fluctuating function $N_{\mathrm{f}}(f)$ with zero average value

$$N(f) = N_{\mathrm{W}}(f) + N_{\mathrm{f}}(f). \tag{5}$$

This smooth approximation was first derived by Weyl and was intended to provide an approximate solution asymptotically exact at infinite frequency [16]. The fact that the intensity of the residual fluctuations grows less quickly than $N_{\mathrm{W}}(f)$ as $f \to \infty$, thus ensuring

$$\lim_{f\to\infty} \left| \frac{N_{\mathrm{f}}(f)}{N_{\mathrm{W}}(f)} \right| = 0, \tag{6}$$

should not be mistaken for an indication that modal density can be defined as often done, by taking the derivative of $N_{\mathrm{W}}(f)$ at the working frequency f, leading to the approximation

$$m(f) = \lim_{B\to 0} \frac{M_B}{B} \cong \frac{\mathrm{d}N_{\mathrm{W}}(f)}{\mathrm{d}f} = m_{\mathrm{W}}(f). \tag{7}$$

As a matter of fact, the residual $R_m(f) = |m_{\mathrm{W}}(f) - M_B/B|$ does not converge to zero, since $N_{\mathrm{f}}(f)$ takes on the discrete nature of $N(f)$, thus preserving the results in (3). It could be expected that the accuracy of the approximation (7) improves as the frequency, and thus $N(f)$, increases, hence leading to modes getting close enough to provide a sort of approximate continuity. Unfortunately, this is not the case, as well witnessed by the number variance, a measure of the intensity of the fluctuations of the modal density $m(f)$ around a smooth approximate, e.g., $m_{\mathrm{W}}(f)$, as it will be recalled in Section II-B. Not only fluctuations do not vanish with the frequency, but they actually increase in absolute intensity, though their relative intensity decreases, as proven by studying the number variance, a measure of modal fluctuations discussed in Section II-B. A practical example is given in Section VII for a cuboid cavity.

As it will be shown in the rest of this paper, these fluctuations cannot be dismissed as minor approximation errors, particularly when the average number of overlapped modes is not high enough, as happens to be the case even at frequencies well above the lowest usable frequency (LUF) as usually defined by thumb rules proposed in practice within the framework of EMC tests [12] (see the Appendix for more details).

The differences between $m(f)$ and $m_{\mathrm{W}}(f)$ play a central role when studying the average local modal overlapping $M_{\mathrm{loc}}(f)$. This quantity represents the average number of modes found within a bandwidth B_M equal to the average -3 dB width of a mode, i.e., $B_M = f/\bar{Q}$, hence

$$M_{\mathrm{loc}}(f) = m_{B_M}(f)\frac{f}{\bar{Q}(f)}, \tag{8}$$

with $\bar{Q}(f)$ the ensemble-average composite quality factor of a MSRC; the use of ensemble[†] averages will be indicated by means of an overhead bar.

As proven in [13], a high modal density in itself is not a guarantee of a diffuse field, ensuring Gaussian-distributed scalar field components; the dominant parameter is rather $M_{\mathrm{loc}}(f)$, which is required to be $M_{\mathrm{loc}}(f) \gg 1$ in order to support a diffuse field. Therefore, it makes more sense to directly count the number of modes overlapping over B_M, rather than passing through (8), since it requires an estimate of the local modal density $m_{B_M}(f)$, as defined in (1). This subtle distinction makes all the difference and should not be underestimated: it could seem more natural to assume $m_{B_M}(f) \simeq m_W(f)$ and derive $M_{\mathrm{loc}}(f)$ from (8), but in this way we would implicitly accept the notion of a deterministic and smoothly increasing modal density, with no random fluctuations, with a $m_W(f)$ not depending on B_M. On the other hand, it is tempting to just consider the average modal density (and overlapping), since in practice the ensemble-average of $m_{B_M}(f)$ can be quite close to $m_W(f)$; as discussed in Section VII, such an approximation directly leads to a fundamental misunderstanding about the origin of statistical anomalies, or outliers, originated by strong random fluctuations in the modal density expected for single realizations of the cavity.

When directly considering the number of modes overlapping over B_M, the corresponding modal density should rather be defined as in (1), with an implicit local definition depending on B_M. In practice, (1) is an average modal density, but in this context the average is not over the realizations (ensemble average), but rather over the bandwidth B_M for a single realization. In other words, it represents a sort of locally homogenized modal density, spread equally over the entire modal bandwidth B_M rather than as a set of singularities as in (3). For this reason, we will refer to it as a *local* average, in contrast to the *ensemble* average. It will be shown in Section VII that this apparently redundant distinction makes a big difference.

B. Random matrix theory and universality classes

Following these discussions, what is needed is a probabilistic description of the local modal density $m_{B_M}(f)$, as defined in (1). A theory answering to this need is provided in the next three Sections. The starting point is the probability distribution of the spacing between the frequencies of resonance of two adjacent modes, often referred to as nearest-neighbor spacing, as derived by means of RMT [14].

This short summary is certainly not intended to serve as an introduction to RMT, and the interested Reader may refer to the first three chapters in Stöckmann's seminal book [14]. Nonetheless, we will give a brief overview of the reasons why we can apply in practice the results derived in the context of quantum chaos to our problem of field statistics in mode-stirred reverberation chambers.

RMT was developed to deal with structures where a direct solution of Schrödinger equation is regarded as complex or simply ill-defined, e.g., when the Hamiltonian operator is unknown. This is the case for complex quantum structures, such as large nuclear compounds or mesoscopic structures (e.g., quantum dots). A solution to this type of problems was found by approximating the unknown Hamiltonian operator by means of a matrix, eventually of asymptotic infinite dimensions, whose entries are assumed to follow specific probability distributions [17]. This idea is directly related to a previous and very successful approach, namely statistical mechanics, where in a similar manner the problem of studying

[†]By this term we consider the ensemble of all the random realizations of cavities generated by varying boundary conditions, due to any stirring procedure, but sharing the same macroscopic properties, i.e., average quality factor, volume, average energy density, average modal density, etc. [6].

the (thermo)dynamics of a large collection of interacting particles was solved by considering a random description of the state variables of the particles. The drive in these approaches is not having a fine-level information of the system at the scale of the individual elements it is composed of: the focus is rather on its macroscopic behavior, described by means of statistical quantities related to the statistical moments of physical quantities of interest and in general by means of probability distribution functions.

RMT has been widely successful in this respect, and at least in its basic idea surprisingly simple; the same cannot be said for the mathematical details. The structural similarity existing between Helmholtz and Schrödinger equations has motivated studies comparing the results predicted by RMT to those observed in microwave experiments [18]. It is important to notice that a major difference between these two equations is the absence of an Hamiltonian operator in Helmholtz equation: the structure is the same, but the lack of an Hamiltonian hinders the drawing of a direct parallel between the two equations. It is for this reason that the application of RMT to cavities where classical waves (of any nature) propagate had virtually to wait for a fundamental piece of work, namely the Bohigas-Giannoni-Schmidt conjecture [19], where it was postulated that the results of RMT should apply to any complex system. A number of experimental validations have confirmed this conjecture, which is today widely accepted as a physical fact. Of particular interest for the EMC community are the works dealing with microwave cavities, i.e., unstirred reverberation chambers, where the accuracy of the prediction of RMT was proven beyond any doubt (e.g., [18]).

The rationale behind recalling these points is that the nomenclature used in RMT is somewhat cryptic, with definitions that make sense in the context of quantum chaos without having any correspondence in classical wave theory. The apparent validity of the Bohigas conjecture allowed a direct transfer of the RMT ideas from the former to the latter, hence the potentially confusing terminology.

In this framework, we need to recall that RMT is based on universality classes allowing to define fundamental symmetry properties of the random matrix approximation of the Hamiltonian, according to fundamental physical properties of the system under consideration, e.g., energy conservation, reciprocity, etc., independently from the fine details of the system. In this respect, we will consider two configurations of practical interest, the case of integrable systems, also referred to (improperly) as the Poissonian ensemble [20], and that of the Gaussian Orthogonal Ensemble (GOE) [14], characterized by time-reversal invariance, i.e., energy conservation. A precise definition of the first class is apparently not yet available outside the context of quantum chaos, but the analogy with microwave structures is still maintained. The important point to consider is that under the category of integrable systems is considered any system that do not present any trace of the features of wave-chaotic systems, in particular level repulsion and of course exponential sensitivity to initial conditions. In practice, the fact that frequencies of resonance can cross each other's path when a dynamical perturbation (stirring) is operating, is a direct measure of absence of a fully chaotic behavior. Integrable systems are actually regarded as an extreme case of non-chaotic systems, whereas in practice a certain amount of chaos is often observed [21]. In practice, completely empty rectangular cuboid cavities are a good example of integrable systems, while the inclusion of a scatterer spurs partially chaotic responses as soon as its dimensions are comparable to the wavelength. The GOE provides the other extreme representation for the ideal case of a fully chaotic system.

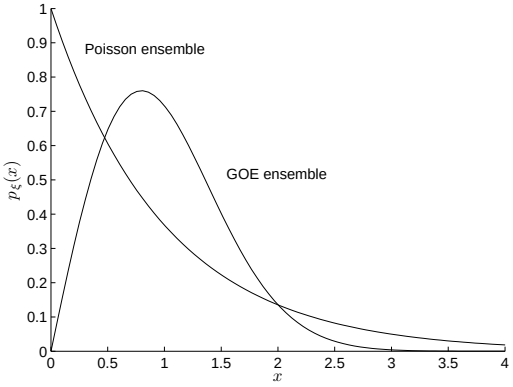

Fig. 1: Nearest-neighbor spacing probability density functions for an integrable and a GOE system, normalized to the ensemble-average spacing.

An example of direct interest for the EMC community was provided in [22], where it was shown through numerical simulations that a mechanical stirrer is not capable of providing a fully chaotic behavior, with traces of integrable features. It should be clear that the notion of integrable system is by no means related to the idea of degeneracy in the frequencies of resonance of a cavity, as in the case of an empty rectangular cavity with widths in rational proportion. Even in the case of irrational ratios, such a system will present the same behavior than any other integrable system.

The theory introduced in this paper is entirely based on the statistics of the nearest-neighbor spacing, defined as

$$s_i = f_{i+1} - f_i, \tag{9}$$

where s_i can be regarded, according to RMT, as the i-th realization of a random variable s, the probability density functions (pdfs) of the normalized nearest-neighbor spacing $\xi = s/\bar{s}$, with $\bar{s} = 1/m_{\mathrm{W}}$ the average nearest-neighbor spacing between adjacent modes, are [14]

$$p_\xi(x) = \mathrm{e}^{-x}, \tag{10}$$

for a Poisson ensemble and

$$p_\xi(x) = \frac{\pi}{2} x \mathrm{e}^{-\pi x^2/4}, \tag{11}$$

for the GOE case. We are thus confronted to either an exponential distribution or a Rayleigh one with a parameter

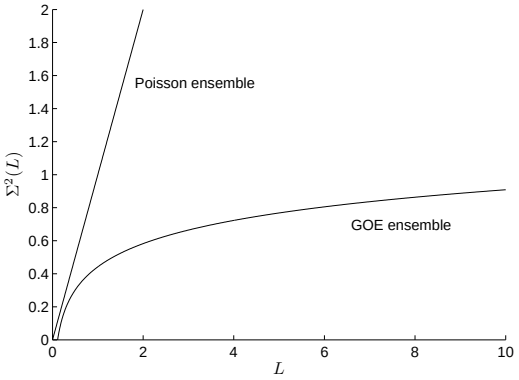

Fig. 2: Number variances $\Sigma^2(L)$ for an integrable and a GOE chaotic system.

$\sigma^2 = 2/\pi$. These two functions are plotted in Fig. 1 where it is clear that the nil probability of superposed modes in chaotic systems is a direct consequence of level repulsion.

Two major differences can be noticed in these functions and will have a major impact on the statistics of the local modal density: 1) for chaotic systems, the modal spacing is decidedly less dispersed than for an integrable system, with a probability distribution presenting a mode (peak) close to the average spacing $\xi = 1$; 2) for an integrable system, it is clear that modes can come in clusters due to a high probability of superposition [20], so that in order to maintain a fixed average spacing, the clusters must be relatively isolated one from the other, as justified by the longer exponential tail. We can refer to this phenomenon as modal depletion, i.e., the local lack of resonant modes, and it can be conjectured that the probability of incurring into what are often regarded as outliers [2] can be explained by this phenomenon. In other words, it is a natural and inevitable phenomenon in an integrable system, whereas it is to be expected less likely in chaotic systems.

According to the type of system we are dealing with, a higher probability of observing a wider nearest-neighbor spacing has a direct impact on the number of modes that can be observed in a fixed bandwidth, as will be derived in Section III.

As already recalled, practical systems are often in between these two extreme configurations, although a Poisson ensemble behavior should be expected in the lower frequency range when dealing with rectangular cavities: this result holds as long as eventual scatterers in the cavity are electrically small, after which the system moves gradually towards a chaotic one, as shown experimentally in [18]. Several methods have been devised to assess the degree of chaoticity of a cavity: in the context of this work, we will restrict our discussions and computations to the two extreme classes already introduced. The following results are directly applicable to the more general case of intermediary statistics for the modal nearest-neighbor spacing.

A direct measure of the impact on the fluctuations of the modal density for the two universality classes can be obtained by studying their number variance $\Sigma^2(L)$, defined as the variance in the number of modes observed over a bandwidth containing on average L modes, i.e., $L\bar{s} = L/m_{\mathrm{W}}$. The number variance is equal to

$$\Sigma^2(L) = L, \tag{12}$$

for an integrable system and

$$\Sigma^2(L) = \frac{2}{\pi^2}\ln(2\pi L) + 0.0696 + O(L^{-1}), \tag{13}$$

for a GOE chaotic one, as proven in [15].

The number variance is a measure of the standard deviation of fluctuations in the modal density with respect to the average one defined by means of Weyl's formula. As made clear by Fig. 2, for an increasing L the fluctuations can be quite severe for an integrable system, as opposed to a chaotic one. In particular, the fact that the variance in the number of modes increases with an increasing bandwidth is a direct proof of the non-convergent behavior of the approximate modal density (2). The increasing intensity of the fluctuations supports our claim that assuming the average modal density as an accurate and reliable measure of the availability of a large number of modes at high frequency is not correct. Modal depleted frequency bandwidths can pop out at any frequency leading to increased variability in the field statistics [13], even at frequencies above the usual LUF definitions.

Unfortunately, the number variance cannot be employed as a predictive tool in the study of the probability of observing anomalous field statistics, since it does not give any measure of the way fluctuations evolve for rare events, i.e., towards the tails of the pdf of the local modal density.

RMT is an asymptotical theory capable of accurately predicting the statistical properties of the spectrum of a system (here the frequencies of resonance of a cavity) as long as it admits a sufficiently large number of states. It should be clear that RMT cannot pretend to be exact when the electrical dimensions of a cavity become small, i.e., in its lower frequency range where it mainly behaves as a high quality factor resonator, allowing only a very limited number of resonances. Hence, RMT can be applied successfully even at frequencies below the LUF, since the modal density is typically high enough to justify a statistical description.

Other universality classes could be considered, such as the Gaussian unitary ensemble, or GUE, but it is of minor interest in practice, as it is useful only in the case of non-reciprocal systems. It could nevertheless find some applications in the case of the testing of devices with ferromagnetic properties or in general employing non-reciprocal materials. This case will not be addressed in this paper, but the procedures here developed are valid in any other type of nearest-neighbor spacing statistics and can be readily applied to any other universality class.

III. Bandwidth covered by n modes

Access to the nearest-neighbor spacing probability distribution allows deriving that of the bandwidth covered by n modes. Knowledge of the latter is instrumental in the computation of

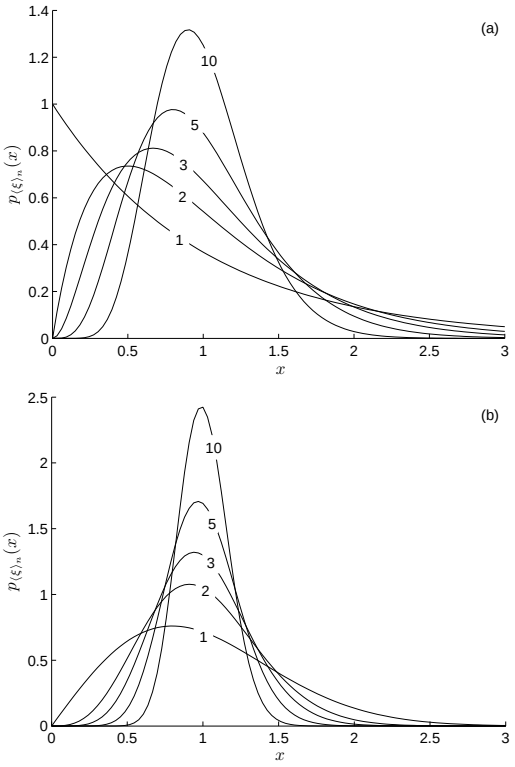

Fig. 3: Probability density functions of the normalized local-average nearest-neighbor spacing $\langle\xi\rangle_n$, for (a) an integrable system and (b) a GOE chaotic one. Several values of n are considered, showing the rate of convergence of the two universality classes towards the ensemble average value expected from Weyl's formula, corresponding to $x = 1$.

the number of modes found within a fixed bandwidth and ultimately for the local modal density.

The total bandwidth S_n covered by $n + 1$ modes can be defined as

$$S_n = \sum_{i=1}^{n} s_i = \frac{1}{m_{\mathrm{W}}} \sum_{i=1}^{n} \xi_i, \tag{14}$$

where the $n + 1$ modes define n random intervals or sub-bandwidths obeying to the parent laws introduced in the previous Section. We stick to the use of the normalized nearest-neighbor spacing ξ, as this choice allows deriving completely general results. In this respect, it is better introducing the local-average of the spacing of n consecutive modes,

$$\langle s\rangle_n = \frac{1}{n} \sum_{i=1}^{n} s_i = \frac{\langle\xi\rangle_n}{m_{\mathrm{W}}}, \tag{15}$$

where the normalized local average nearest-neighbor spacing $\langle\xi\rangle_n = \langle s\rangle_n/\bar{s}$ will have a central role in Section V.

The pdf $p_{\langle\xi\rangle_n}(x)$ implies carrying out n convolutions of the original pdf of the random variable ξ/n,

$$p_{\xi/n}(x) = n p_{\xi}(nx), \tag{16}$$

since $\langle\xi\rangle_n$ involves the sum of n such random variables that will be assumed to be iid. This procedure implies an approximation, as higher-order statistics, involving the mutual correlations between spacings at different distances is usually not identically equal to zero [14]. As the average modal density increases, with more packed resonances, the omission of their correlation can be expected to have an increasing importance.

In the case of an integrable system, where an exponential distribution is predicted for the nearest-neighbor spacing, the result of such operation is available in closed form and is the Gamma probability distribution, with $\langle\xi\rangle_n \in \Gamma(n, 1/n)$. In the other cases, i.e., the GOE and any other intermediate non-fully chaotic system, no closed-form solution is available. A simple way of deriving the pdf of $\langle\xi\rangle_n$ is to pass through the characteristic function $\varphi_{\xi/n}(t)$ of $p_{\xi/n}(x)$ [23]

$$\varphi_{\xi/n}(t) = \mathcal{F}\left\{p_{\xi/n}\right\}(t), \tag{17}$$

by means of a Fourier transform. In the Fourier domain the n convolutions correspond to

$$\varphi_{\langle\xi\rangle_n}(t) = \left[\varphi_{\xi/n}(t)\right]^n. \tag{18}$$

The pdf of the local-average normalized nearest-neighbor spacing can be retrieved by inverse-transforming its characteristic function

$$p_{\langle\xi\rangle_n}(x) = \mathcal{F}^{-1}\left\{\varphi_{\langle\xi\rangle_n}\right\}(x), \tag{19}$$

with the total random bandwidth covered by $n+1$ modes given by

$$S_n = n\bar{s}\langle\xi\rangle_n. \tag{20}$$

Some examples are given in Fig. 3, for the case of integrable and GOE systems. As expected for iid random variables, as n increases, the central-limit theorem requires the pdf of their average to converge towards a bell-shaped function, asymptotically approaching a Gaussian function. What is important to notice is that the two groups of functions inherit the features of their respective parent law for the modal nearest-neighbor spacing. As a result, for the same ensemble-average modal nearest-neighbor spacing $\bar{s} = 1/m_{\mathrm{W}}$, the integrable case shows a sensibly larger statistical dispersion, with a much heavier tail for large nearest-neighbor spacings. Reciprocally, this implies that for a fixed bandwidth, the probability of finding a given number of modes should be expected to be smaller in the case of an integrable system than for a chaotic one. Again, this is related to the higher probability of close modes found in integrable systems, leading to clusters interleaved with modal depleted regions. A higher rate of modal-cluster formation is visible in Fig. 3(a), where the probability of finding n modes packed into a bandwidth narrower than the average one is clearly higher than in the GOE case, especially for a small n. Although this could be

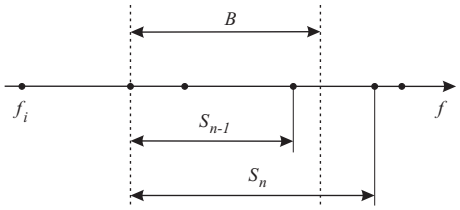

Fig. 4: Definitions of some modal-related quantities, showing the convention adopted in order to predict the number of modes appearing within B. Each dot represents a frequency of resonance of a cavity. The first resonance on the left of B is taken as a reference in the count, and does not belong to B, being at its left.

interpreted as an advantage of integrable systems with respect to GOE ones, generating a higher modal density with non-negligible probability, this comes with an also increased rate of depletion, as clear in the tail of the distributions.

IV. Number of modes in a finite bandwidth

The second element needed to derive the probability distribution of the local modal density is the probability law $p_M(n, B)$ of finding no more that n modes within a fixed bandwidth B (see Fig. 4). It can be derived straightforwardly by recalling that a bandwidth B contains no more than n modes if

$$S_{n-1} \leqslant B < S_n. \tag{21}$$

In order to provide an unambiguous procedure for counting these modes, the lower end of the bandwidth B will be assumed to coincide with a resonance frequency, as shown in Fig. 4. Clearly, this definition provides a different count when other configurations are considered; in fact, this is not important, as the count is meant as an auxiliary parameter in the definition of the local modal density. The statistics of this latter is actually invariant with respect to translations along the frequency axis, since we are here talking about a fraction of the average spacing, so that our convention does not lead to any bias in the pdf of the local modal density. As a result of this choice, the first mode will not be counted as belonging to B, so that of the n modes found in B, only $n-1$ will be counted. In other words, the first frequency of resonance is assumed to be on the left of B.

Hence, according to this convention, the probability law $p_M(n, B)$ is given by

$$\begin{aligned} p_M(n, B) &= P(\{S_{n+1} > B\} \cap \{S_n \leqslant B\}) \\ &= \int_{S_n=0}^{B} \int_{S_{n+1}=B}^{\infty} p(S_n, S_{n+1}) \mathrm{d}S_n \mathrm{d}S_{n+1}, \end{aligned} \tag{22}$$

where the joint pdf $p(S_n, S_{n+1})$ is needed. It can be derived by expressing it as a function of conditional probabilities

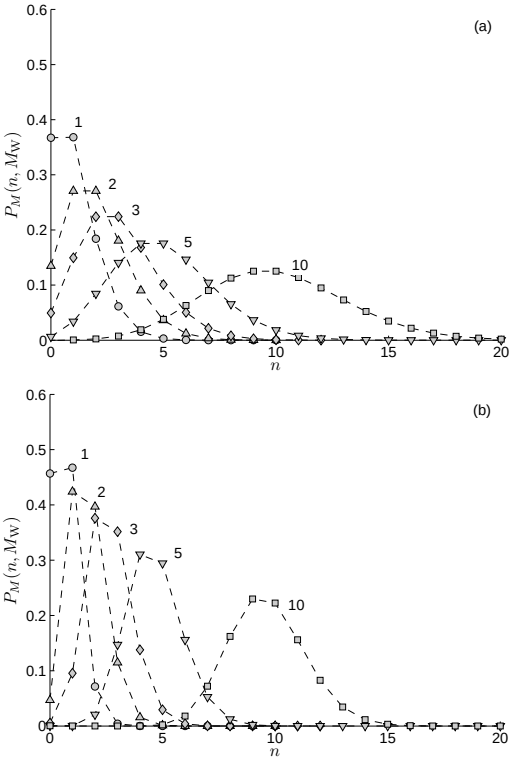

Fig. 5: Probability density functions $p_M(n, M_\mathrm{W})$ for (a) an integrable system and (b) a GOE chaotic one for several values of the average number of modes M_W. Notice the relatively high probability of finding no mode in the case of integrable systems with $M_\mathrm{W} < 5$, with respect to the GOE case.

$$\begin{aligned} p(S_n, S_{n+1}) &= P(S_{n+1}|S_n) p_{S_n}(S_n) \\ &= p_s(S_{n+1} - S_n) p_{S_n}(S_n), \end{aligned} \tag{23}$$

where the conditional probability of observing a bandwidth S_{n+1} covered by $n+2$ modes (counting the reference one) knowing that $n+1$ modes cover the bandwidth S_n is actually equivalent to the probability of observing a further modal nearest-neighbor spacing $s = S_{n+1} - S_n$ between the last two modes. Hence

$$\begin{aligned} p_M(n, B) &= \int_{S_n=0}^{B} \int_{s=B-S_n}^{\infty} p_s(s) p_{S_n}(S_n) \mathrm{d}S_n \mathrm{d}s \\ &= \int_0^B p_{S_n}(x) \left[1 - F_s(B-x)\right] \mathrm{d}x, \end{aligned} \tag{24}$$

where $F_s(x)$ is the cumulative distribution function of the nearest-neighbor spacing s. Setting $y = x/\bar{s}$, this result can be recast as

$$p_M(n, M_{\rm W}) = \int_0^{M_{\rm W}} p_{\langle\xi\rangle_n}(y)\,[1 - F_\xi\,(M_{\rm W} - y)]\,{\rm d}y, \quad (25)$$

where

$$M_{\rm W} = \frac{B}{\bar{s}} = m_{\rm W} B \quad (26)$$

is the average number of modes expected over B from an ensemble point of view. In the rest of this paper we will consider the case where $M_{\rm W} = m_{\rm W} B_M$, i.e., the average number of overlapped modes predicted by means of Weyl's formula (2).

Attention should be paid to the fact that the derivation of the probability function (25) is exact and applies for any number of modes, but for the case $n = 0$. This case implies that the closest modes to the bandwidth are just outside it, i.e., the event (21) should now be substituted by the event $\{s > B\}$. Since (25) applies to any $n \in \mathbb{N}\backslash 0$, the normalization property of a pdf can be rather used to derive

$$p_M(0, M_{\rm W}) = 1 - \sum_{i=1}^{\infty} p_M(i, M_{\rm W}). \quad (27)$$

Another property of (25) is that the average number of modes $\mathsf{E}[n]$ must coincide with that predicted by Weyl's formula, i.e., $M_{\rm W}$. This property has been numerically verified for the examples shown in Fig. 5.

The results obtained from (25) are shown in Fig. 5, where the increased statistical dispersion encountered for integrable systems is remarkably higher than for a chaotic one. Of particular interest is the non-negligible probability of observing no mode when $M_{\rm W} < 5$ in an integrable system, i.e., of experiencing a modal depletion. This fact is important in practice, since an average overlapping $M_{\rm W} > 5$ is not automatically achieved even at relatively high frequencies, as shown in the Appendix.

V. Local modal density distributions

The local definition introduced in (1) can only account for an integer number of modes in B_M, whereas in practice we are rather interested in fractional values, too. With reference to Fig. 4, the local modal density can be defined as the ratio n/S_n, where S_n is the bandwidth covered by $n+1$ modes (the first one being used as a reference), according to the definition (21). Hence the actual number of overlapping modes over a finite bandwidth, observed on a local scale, reads as

$$M_{\rm loc} = \frac{n}{S_n} B_M. \quad (28)$$

This definition is now capable of capturing all the intermediated cases where B_M intercepts a fraction of the spacing separating two adjacent modes. For a given $M_{\rm loc}$, an infinite number of modal scenarios can provide the same result. The distribution function $F_{M_{\rm loc}}(x)$ can now be computed by considering the entire set of events yielding the same equivalent modal overlapping over B_M, i.e.

$$\begin{aligned}\{M_{\rm loc} = x\} &= \bigcup_{n=1}^{\infty} \left\{ \frac{n}{S_n} B_M = x \right\} \\ &= \bigcup_{n=1}^{\infty} \left\{ \frac{n}{S_n} \bar{s} = \frac{x}{M_W} \right\} \\ &= \bigcup_{n=1}^{\infty} \left\{ \langle\xi\rangle_n^{-1} = \frac{x}{M_W} \right\},\end{aligned} \quad (29)$$

recalling (15). Whence, partitioning the above event, we obtain

$$\begin{aligned}F_{M_{\rm loc}}(x) &= P\,(M_{\rm loc} \leqslant x) = \\ &= \sum_{n=1}^{\infty} P\left(\langle\xi\rangle_n \geqslant \frac{M_W}{x} \right) p_M(n, M_{\rm W}) \\ &= \sum_{n=1}^{\infty} \left[1 - F_{\langle\xi\rangle_n}\left(\frac{M_W}{x} \right) \right] p_M(n, M_{\rm W}),\end{aligned} \quad (30)$$

with $M_{\rm W}$ defined by (26). Needless to say, since

$$\frac{M_{\rm loc}}{M_W} = \frac{m_{\rm loc}}{m_{\rm W}}, \quad (31)$$

the same probability function holds also for the local modal density.

The pdf of $M_{\rm loc}$ can then be straightforwardly retrieved by taking the derivative of (30) with respect to its argument. Expressing it in terms of the deviation from the overlapping $M_{\rm W}$ predicted by means of Weyl's formula yields

$$p_{M_{\rm loc}/M_{\rm W}}(x) = x^{-2} \sum_{n=1}^{\infty} p_{\langle\xi\rangle_n}\,(1/x)\, p_M(n, M_{\rm W}). \quad (32)$$

Some examples of this pdf are presented in Fig. 6: it is hence possible to assess the large domain of variability of the modal density, spanning more than one octave with a non negligible probability even at a relatively high modal overlapping of 10 modes, and up to two octaves for the integrable case.

The ensemble average $\bar{M}_{\rm loc}$, mode and standard deviation of the local modal overlapping are shown in Fig. 7, as functions of $M_{\rm W}$. The mode and the ensemble average are on either side of the value predicted by Weyl's formula, indicating that although the modal density can be higher than expected for a weak modal overlapping, the most likely issue (mode) is lower.

The fact that the average local modal density is higher than predicted by Weyl's approximation (2) is a direct consequence of Jensen inequality [24], since the modal density is related to the nearest-neighbor spacing by means of a convex function.

In practice, a statistical mode systematically below the average implies that even with a GOE chaotic cavity the number of overlapping modes is likely lower than $M_{\rm W}$. The ensemble average for the case of an integrable system is much higher than expected, due to a strong skewness in the probability distributions in Fig. 6. Even more important is the fact that the standard deviation is still comparable with $M_{\rm W}$ even when $M_{\rm W} \gtrsim 10$, in both cases. This result implies that even a relatively strong modal overlapping is still affected

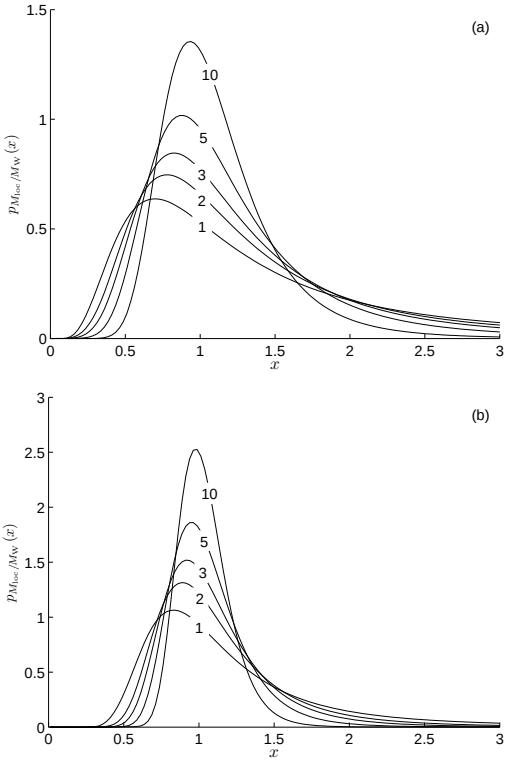

Fig. 6: Probability density functions of the local modal density, normalized to the ensemble-average modal density predicted by Weyl's formula, i.e., $M_{\rm loc}/M_{\rm W}$, for (a) an integrable system and (b) a GOE chaotic one.

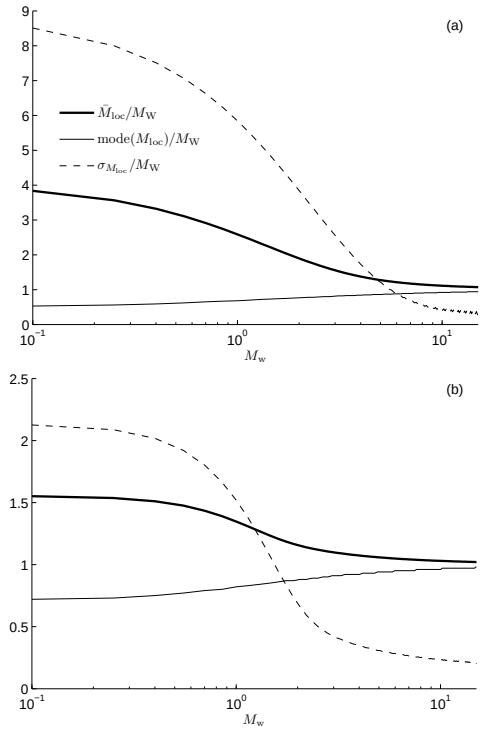

Fig. 7: Average value, mode and standard deviation of the local modal overlapping $M_{\rm loc}$, normalized to the expected value $M_{\rm W}$ predicted by means of Weyl's formula, for (a) an integrable system and (b) a GOE chaotic one.

by non-negligible random fluctuations, of the same order of magnitude as the average. Of course, their impact decreases with $M_{\rm W}$: as discussed in [13], when $M_{\rm loc} \gtrsim 3$, although the field will not be yet completely diffused, its deviation from the asymptotic statistics will become less sensitive to the actual number of overlapped modes. A much higher dependence from $M_{\rm loc}$ is to be expected at a weak modal overlapping, where a large statistical dispersion can lead to a dramatic increase in the variability of the electric field.

These results, requiring no specific assumption on the fine details of the geometry of a cavity, give an insight into three important issues: 1) for a weak modal overlapping, the deviation of the field statistics predicted in [13] should be expected to present a strong statistical dispersion, and in particular a high probability of leading to even larger deviations than those predicted when using $M_{\rm W}$ as an estimate of the modal overlapping; 2) even at high frequencies where a large number of modes are expected to overlap, their actual number is still affected by a non-negligible statistical dispersion; 3) the differences between Poisson and GOE statistics vanish asymptotically for a large overlapping, e.g., mode and mean value converge to the same result, as expected by invoking the central-limit theorem. In particular for this last point, the standard deviation expected for the GOE case is about half of that in the integrable case.

We want to stress that these fluctuations in the field statistics must not be interpreted as non-compliancies or shortcomings of reverberation chambers, as they just belong to the normal range of physical responses expected for such systems. As made clear by Fig. 6, albeit the probability of experiencing a very low number of modes over B_M decreases as $M_W \to \infty$, the probability is never equal to zero. In other words, it is unphysical to expect a reverberation chamber to present no anomalous statistics even at high frequency. We can conclude that the concept of outliers as suggested in [2] appears to originate from a biased interpretation of otherwise physically justified deviations in the field statistics generated by a reverberation chamber. While unlikely, these extreme scenarios due to mode-depleted frequencies are perfectly within the physiological response of a cavity.

VI. Validation for a cuboid cavity

An experimental validation involving modal quantities is far from being a trivial task, since as soon as two consecutive

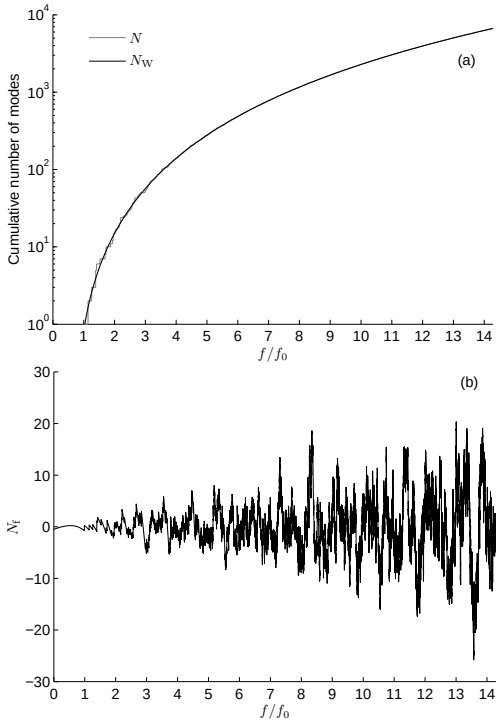

Fig. 8: Cumulative number of modes for the rectangular cuboid cavity taken as an example in Section VI: (a) comparison between the actual count $N(f)$ computed with (4) and (33) and Weyl's approximation (34); (b) the residual fluctuations $N_{\mathrm{f}}(f)$.

resonance frequencies are closer than the average modal bandwidth B_M, modal overlapping ensues making it hardly possible to distinguish and thus count the actual number of resonant frequencies.

A numerical validation is possible exclusively in the case of regular geometries, e.g., where Helmholtz equation can be solved by the method of separation of variables. A cavity in the shape of an empty rectangular cuboid is of practical interest within the framework of EMC test facilities, and will thus be taken as an example to illustrate the validity of our results.

A note of caution is nevertheless necessary, since the analysis of a regular geometry implies an integrable system, hence a Poisson class. As already pointed out, there is experimental evidence [18], [21], [22] that the behavior of real-life reverberation chambers is at least partially chaotic. Unfortunately, in this case no closed-form expression for the resonance frequencies is available.

For lateral dimensions (a, b, c) of the cuboid cavity its frequencies of resonance can be computed by [25]

$$f_{mnp} = \frac{c_0}{2}\sqrt{\left(\frac{m}{a}\right)^2 + \left(\frac{n}{b}\right)^2 + \left(\frac{p}{c}\right)^2}, \qquad (33)$$

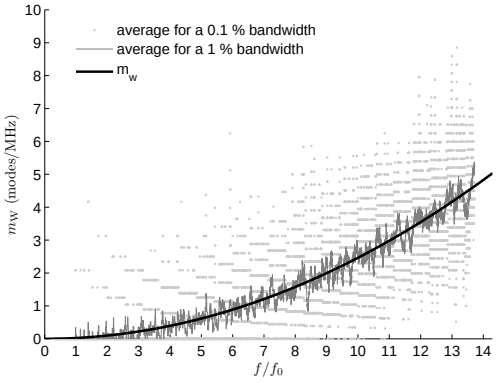

Fig. 9: Local modal density computed from $N(f)$, averaged over 0.1 % and 1 % relative bandwidths. The thick black curve is the result predicted by deriving Weyl's approximation (35). The relative bandwidth over which the average modal density should be computed is rather $1/\bar{Q}$, which is usually much smaller than the 0.1 % value here considered. Much stronger fluctuations should be expected in this case, making their graphical representation by far less clear.

It is therefore straightforward to compute the cumulative number of normal modes $N(f)$, by taking due care in counting in the degeneracies and allowed combinations of the triplet (m, n, p) [25]. For the sake of providing a quantitative example, the choice $a = 2.8$ m, $b = 2.5$ m, $c = 3.2$ m, corresponding to a volume $V = 22.4$ m^3 and a fundamental resonance $f_0 = 71.2$ MHz will be considered throughout this Section. The resulting cumulative number of modes $N(f)$ is shown in Fig. 8(a).

A more accurate Weyl's approximation valid for the special case of an empty cuboid [25] will be used as a reference,

$$N_{\mathrm{W}}(f) = \frac{8\pi V_\lambda}{3} - \frac{(a+b+c)}{\lambda} + \frac{1}{2}, \qquad (34)$$

predicting a modal density

$$m_{\mathrm{W}}(f) = \frac{8\pi V}{c_0^3} f^2 - \frac{(a+b+c)}{c_0}. \qquad (35)$$

A comparison between the cumulative number of modes predicted by (34) and those obtained by directly counting them from (4) and (33) is shown in Fig. 8(a): the well-known ability of Weyl's approximation in accurately predicting the cumulative number of modes is retrieved. The residual error, i.e., the fluctuating part $N_{\mathrm{f}}(f)$ of $N(f)$ is shown in Fig. 8(b), where it is clear that $N_{\mathrm{f}}(f) \ll N(f)$, at least when $f/f_0 \gtrsim 1$. Note how the intensity of the fluctuations increases with the frequency, as predicted by the number variance recalled in Section II-B.

Nevertheless, as already recalled in Section II, this should not be taken as a gauge of the accuracy of Weyl's approximation when dealing with modal densities. Fig. 9 shows a comparison between the results predicted by (35) and the

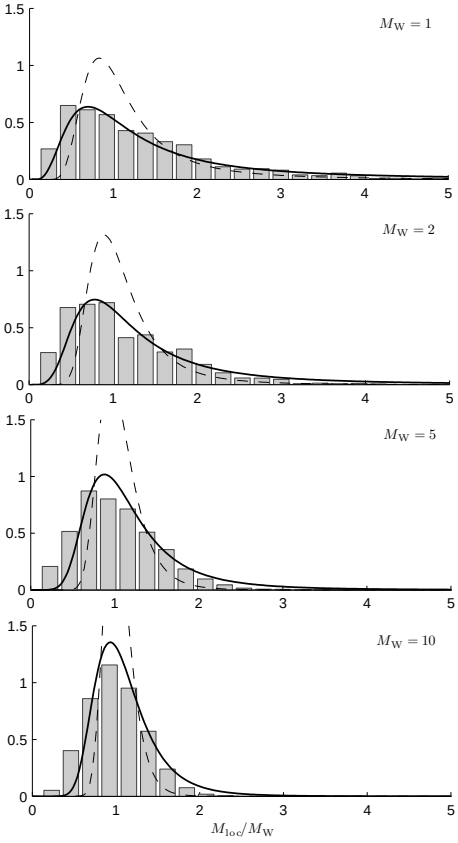

Fig. 10: Empirical probability distributions of the number of overlapped modes $M_{\rm loc}$ observed for the rectangular cuboid cavity discussed in Section VI, obtained by observing 1000 bandwidths over the entire frequency range shown in Fig. 9. These results pertain to the local modal overlapping $M_{\rm loc}$ counted over a frequency bandwidth where a reference overlapping $M_{\rm W}$ is predicted by means of Weyl's approximation (35). Four values of $M_{\rm W}$ are shown. The thick black curves represent the probability density functions predicted by our model and shown in Fig. 6(a) for an integrable cavity, while the dashed ones are for a GOE cavity, as given in Fig. 6(b).

actual local average modal density obtained over a relative bandwidth of 0.1 % and 1 % around a continuously varying frequency f. As discussed in Section II, the fluctuations are now far from negligible, with a high frequency of occurrence of regions of modal depletion, where even at relatively high frequency the modal density observed can be very close to zero.

The minimum frequency at which a cavity can be expected to be in an overmoded condition is often estimated at 5 to 10 times the fundamental resonance f_0. Fig. 9 proves that the actual average local modal density is still very strongly fluctuating around the value predicted by (35). It is noteworthy that the relative bandwidth over which the actual modal density should be averaged is equal to $1/\bar{Q}$. Now, $\bar{Q}$ is never as low as just a few hundred units. Therefore, even the results computed over a 0.1 % bandwidth are optimistic in their display of a strongly fluctuating local modal density, since the value of $1/\bar{Q}$ should rather be expected into the $10^{-6} - 10^{-4}$ range, with even wider fluctuations.

In order to validate our prediction about the pdf of the number of overlapping modes, we proceeded to a direct count based on the definition (28). The bandwidths over which this operation was carried out were computed by taking Weyl's approximation (35), imposing a given $M_{\rm W}$ and finding out the bandwidth $M_{\rm W}/m_{\rm W}(f)$ over which this number of modes should be expected to overlap at a given frequency. The four values $M_{\rm W} = \{1, 2, 5, 10\}$ were considered, and the actual count $M_{\rm loc}(f)$ was computed over 1000 bandwidths distributed over the entire frequency range, starting at $f = 2f_0$. The empirical probability distributions thus obtained are shown in Fig. 10(a)-(d), where they are compared to the pdfs shown in Fig. 6(a). The good agreement between these results prove that in practical configurations the actual number of overlapping modes can definitely be smaller than expected when using Weyl's approximation, even when a relatively high average modal overlapping is expected.

The question of what average modal overlapping should be expected in practice is treated in detail in the Appendix, where it is shown that a weak modal overlapping, i.e., $M_{\rm W} < 3$, is far from unlikely. Experimental results pertaining to this issue have also been shown in [13].

VII. Practical considerations

As already recalled in Section I, these discussions about random fluctuations in the modal overlapping have a direct practical impact, because of the direct link existing between the average local modal density over B_M, and thus the modal overlapping, and the variability ς^2_W of the energy density $W = \epsilon_0 \|\boldsymbol{E}\|^2$, as measured at any position inside at least a subvolume of a MSRC, a region usually referred to as working volume, with

$$\varsigma^2_W = \left(\frac{\sigma_W}{\bar{W}}\right)^2 \tag{36}$$

and σ_W the standard deviation of W.

As demonstrated in the Appendix and already shown in [13], the number of overlapped modes actually intervening can be quite low even at frequencies above the LUF estimated by means of the usual thumb rules. Under such conditions, the variability of W is bound to be higher than expected, as demonstrated in [13]

$$\varsigma^2_W = \frac{1}{3} + \frac{2}{\pi M_{\rm loc}}. \tag{37}$$

The ensemble-average modal density was considered in [13], with $m_{B_M}(f)$ in (8) approximated by its ensemble average, $\bar{m}_{B_M}(f) \simeq m_{\rm W}(f)$, thus neglecting the random fluctuations that inevitably affect it, as proven in the previous Sections. Having only access to the estimate of the modal density provided by Weyl's formula, only the average deviation

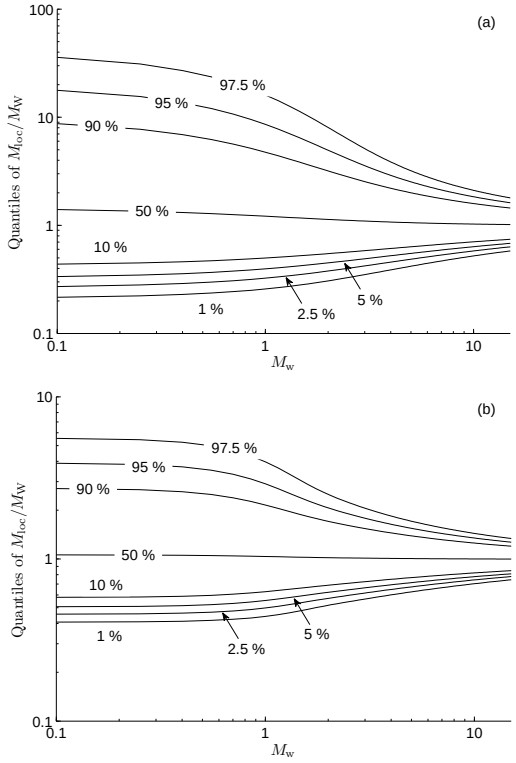

Fig. 11: Quantiles of the deviation of the local modal overlapping with respect to the estimate obtained from Weyl's formula, for (a) an integrable system and (b) a GOE chaotic one.

can be predicted, or an upper bound, as done in [13]. The non-negligible probability of observing a modal overlapping even weaker than expected has thus a direct and measurable impact on the statistics of the field generated by a reverberation chamber. As long as the actual number of overlapping modes $M_{\rm loc} \gg 1$, this error can be entirely negligible, since (37) converges to the value $1/3$ expected for a diffuse field; but in the case of weak modal overlapping, as already discussed and proved in [13], very strong statistical deviations can ensue, particularly when $M_{\rm loc} \lesssim 3$.

The following example should make this point clearer. In a cavity with an average modal overlapping $\bar{M}_{\rm loc} = 1$, (37) predicts an increase in the variability of W equal to 0.63, corresponding to a 191 % relative deviation in the variability ς^2_W. Of all the random realizations generated by a stirring technique, sharing the same average modal density, those presenting $M_{\rm loc} = 1/2$ will be affected by an electric energy density with a statistical variability amplified by a factor 2, i.e., about 380 %, which can easily explain anomalous field statistics on a local scale. As clear from Fig. 6, such an event is not unlikely. If $\bar{M}_{\rm loc} = 3$, than the relative deviation in the variability would rather pass from 63 % to 126 %, if a realization featured half the average density. Therefore, depending on the average modal overlap, fluctuations can have a very different impact, with fields behaving with an increased statistical dispersion than expected from ideal reverberation models [2]. From this example it is clear that the strongest effect will be felt when $\bar{M}_{\rm loc} \lesssim 3$.

A useful summary of the probability of occurrence of random fluctuations is given in Fig. 11, where the quantiles of the random variable $M_{\rm loc}/M_{\rm W}$ are computed for a varying $M_{\rm W}$. The median (50 % quantile) is very well approximated by the estimate $M_{\rm W}$ provided by Weyl's formula. Hence, there is an equal probability of observing either a higher or lower modal overlapping. In the context of deviations from the asymptotic statistics for field samples, the most important quantiles are those related to the probability of observing a lower modal overlapping. In this respect, when expecting $M_{\rm W} = 1$, there is a 10 % probability of observing an actual modal overlapping below 49 % and 63 % of $M_{\rm W}$ for an integrable and GOE cavity, respectively. Such strong reduction is proven by our derivation to be a normal phenomenon in a large cavity, and not related to any non-ideality in its use. A 50 % reduction in the modal overlapping leads to a twofold increase in the additional term of the variability of the electric energy density, as demonstrated in [13] and recalled in (37). Worse, but perfectly normal, scenarios can appear : with a probability of 1 % the modal overlapping can be found below 25 % and 44 % of $M_{\rm W}$. In other words, rare phenomena of very strong modal depletion can explain the existence of anomalous field statistics in a MSRC that is otherwise standard compliant.

These results could be expected to improve when a higher modal overlapping of $M_{\rm W} = 3$ is considered. This value is often taken as a reference for the appearance of a diffuse-field condition in room acoustics [26]. Even in this case, $M_{\rm loc}$ can be lower than 58 % and 72 %, and with a probability of 1 %, below 34 % and 56 %. Hence, even at relatively high modal overlappings, the probability of observing *normal* strong deviations in the field statistics should not be underestimated.

A probability of 1 % is compatible with the rate of appearance of local non-compliancies as tolerated in current practice [12], and could thus provide a physical explanation to the observation of outliers [2]. It could also serve as an explanation for the existence of local non-compliancies even at higher frequencies, where the concept of overmoded cavity is usually taken for granted.

Of notable importance is the observation of a much higher statistical dispersiveness for an integrable case. In practice, this scenario is to be expected only when the scatterers within a reverberation chamber are no longer electrically large, i.e., towards their lower frequency range of operation, close to the LUF. It is thus pertinent to wonder if the inclusion of large passive scatterers within a chamber could improve at least the field statistics, by making the cavity chaotic rather than integrable. A similar idea was already vented in previous papers, but it was rather based on the hope of increasing the modal density [27], [28]. Our suggestion is of a different order: to reduce the statistical dispersion in modal overlapping

by making a cavity chaotic, in order to avoid even stronger local deviations in the field statistics, due to modal depletions justified by stronger random fluctuations for the integrable case.

VIII. Conclusions

In this paper we have applied universal results from RMT in order to derive the probability distributions of modal-related quantities of interest to the physics of MSRC. These laws are entirely general and just require a handful of macroscopic parameters to be used in practice: the volume of the cavity V, its average composite quality factor $\bar{Q}$, etc. The two universality classes representing an integrable and a GOE chaotic system serve as extremes in the actual behavior of real-life MSRCs.

The rationale for our analysis is the link proven in [13] between the average number of overlapped modes over the average bandwidth of a mode, directly depending on the local modal density and the deviation in the parent law of field samples, as assessed by their increased variability.

It was shown that the estimate of local modal density, and thus modal overlapping, yielded by Weyl's formula has a far from negligible probability of overestimating the availability of resonant modes, particularly when modes are already scantly overlapped, i.e., for $M_{\mathrm{W}} \lesssim 3$. Interestingly, the statistical dispersion of the modal density appears to be non-negligible even at frequencies where a relatively large number of modes is already overlapping, on average.

The inevitable consequence is the appearance of large deviations from the asymptotic Gaussian behavior expected for the field generated in an overmoded reverberation chamber. These results are expected to be the basis for a better understanding of anomalous field statistics; moreover, the fact of being firmly based on physical grounds makes them appealing in the study of the links existing between the physics of large cavities and the statistical properties of real-life reverberation chambers.

Acknowledgements

The Author is grateful to the anonymous Reviewers for their constructive remarks and suggestions.

Appendix

Average modal overlapping M_{W} from Weyl's approximation

The average number M_{W} of overlapping modes in a cavity can be estimated by means of Weyl's approximation. Since we are mainly interested in knowing the order of magnitude of M_{W}, we will consider the basic approximation (2), yielding

$$M_{\mathrm{W}}(f) = m_{\mathrm{W}}(f)\frac{f}{\bar{Q}} = \frac{8\pi V_\lambda}{\bar{Q}}. \tag{38}$$

The average composite quality factor $\bar{Q}$ can be expressed as the harmonic sum of the three main loss/leakage mechanisms [29]

$$\frac{1}{\bar{Q}} = \sum_{i=1}^{3}\frac{1}{\bar{Q}_i}, \tag{39}$$

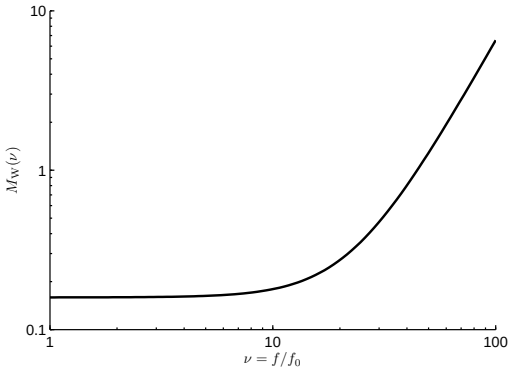

Fig. 12: Average modal overlapping predicted by (47) for dissipation in antenna loads and non-perfectly conductive metallic boundaries, neglecting the inclusion of additional lossy material into a cavity. These results refer to the case of a fundamental resonance at 20 MHz.

with

$$\bar{Q}_1 = 16\pi^2 V_\lambda \tag{40a}$$

$$\bar{Q}_2 = \frac{3V}{2\delta\mu_w S} \tag{40b}$$

$$\bar{Q}_3 = \frac{2\pi V}{\lambda\bar{\sigma}_{\mathrm{eq}}}, \tag{40c}$$

where V is the volume of the cavity and S the surface of its metallic boundary.

$\bar{Q}_1$ models the dissipation in the antenna load (single antenna, here), for the special case of a perfectly matched antenna; $\bar{Q}_2$ represents Joule dissipation over imperfectly conductive walls, with μ_w the relative magnetic permeability of the metal covering the cavity surface and δ its effective skin-depth; $\bar{Q}_3$ accounts for power loss due to leakage through the cavity surface and dissipation in lossy materials within the cavity (e.g., absorbers) through an average absorption cross section, since they essentially behave in the same manner. We obtain from (38) - (40)

$$M_{\mathrm{W}}(f) = \frac{1}{2\pi} + 4\frac{\bar{\sigma}_{\mathrm{eq}}}{\lambda^2} + \frac{16\pi}{3}\mu_w\frac{S\delta}{\lambda^3}. \tag{41}$$

In the lower frequency range, the dominant term in (41) is $\bar{Q}_1$, i.e., dissipation in antenna loads. In this case

$$\lim_{f\to 0} M_{\mathrm{W}}(f) = \frac{1}{2\pi} \simeq 0.16, \tag{42}$$

a result well below the average overlapping of 3 modes that is often regarded as ensuring a diffuse-field regime in a reverberating cavity [26].

In order to derive a simple closed-form expression, we will consider a cubic cavity, with side a and non-magnetic metal surfaces, i.e., $\mu_w = 1$. In this case the fundamental resonance frequency is

$$f_0 = \frac{c_0}{\sqrt{2}a}. \tag{43}$$

Expressing the frequency in terms of f_0, as $f = \nu f_0$, the wavelength becomes $\lambda = \lambda_0/\nu$, where $\lambda_0 = \sqrt{2}a$. Hence (41) can be recast into

$$M_{\rm W}(\nu) = \frac{1}{2\pi} + 4\frac{\bar{\sigma}_{\rm eq}}{\lambda_0^2}\nu^2 + \frac{16\pi}{3}\frac{S\delta}{\lambda_0^3}\nu^3. \qquad (44)$$

The last term includes the skin depth, which is frequency dependent. A simplification is possible by writing

$$\frac{S\delta}{\lambda^3} = \frac{\nu^{2.5}}{\sqrt{\lambda_0}}\frac{3}{\sqrt{\pi\mu_0\sigma_w c_0}}, \qquad (45)$$

where σ_w is the conductivity of the metallic surfaces. For a conductivity $\sigma_w = 3.5 \cdot 10^7$ S/m (aluminium), (44) becomes

$$M_{\rm W}(\nu) = \frac{1}{2\pi} + 4\frac{\bar{\sigma}_{\rm eq}}{\lambda_0^2}\nu^2 + 2.47 \cdot 10^{-4}\frac{\nu^{2.5}}{\sqrt{\lambda_0}}. \qquad (46)$$

We are now in condition to assess the average number of overlapping modes predicted by Weyl's approximation. For a cavity with $f_0 = 20$ MHz, i.e., $\lambda_0 = 15$ m, with negligible leakages and no absorbing materials, we should expect

$$M_{\rm W}(\nu) = \frac{1}{2\pi} + 6.37 \cdot 10^{-5}\nu^{2.5}, \qquad (47)$$

which can now be evaluated at multiples of the fundamental resonance. We shall consider the two most widely applied thumb rules for overmoded conditions: 1) a frequency about 5 or 10 times f_0, i.e., $\nu = 5$ or $\nu = 10$; 2) a frequency where the cumulative number of modes is $N \geq 60$, for which Weyl's approximation (2) implies

$$V_\lambda = \frac{45}{2\pi} \qquad (48)$$

corresponding for a cubic cavity to $a/\lambda \simeq 1.92$ and $\nu = 2.7$. We obtain $M_{\rm W}(2.7) = 0.16$, $M_{\rm W}(5) = 0.17$ and $M_{\rm W}(10) = 0.18$. In all of these cases, $M_{\rm W} < 1$, thus making the case for strong fluctuations in the modal density an important issue, as implied by the results shown in Fig. 11 for weak average modal overlapping and discussed in Section VII. Fig. 12 shows $M_{\rm W}(\nu)$ for a varying frequency, in the case where $\bar{Q}_3 \to \infty$: based on dissipation in the antenna load and finite conductivity over the cavity boundary, a modal overlapping $M_{\rm W} = 1$ is to be expected only above 45 times f_0.

Clearly, the presence of a lossy EUT or absorbers within the cavity would increase $M_{\rm W}$. Indeed, for a perfectly absorbing material, the absorption cross-section would be approximately equal to its geometrical cross section. Hence, an additional factor $4\bar{\sigma}_{\rm eq}/\lambda^2$ should be included and could be expected to be the dominant one around the LUF. This conclusion agrees with the observations made in [13], where it was shown that an unloaded cavity can be incapable of supporting a diffuse-field condition even above the lowest usable frequency defined in the IEC standard [12]. The inclusion of additional losses seems to be necessary in the lower frequency range, for the sake of creating more easily reproducible conditions for the field statistics, i.e., with field statistics approaching the asymptotic ones derived in [2], [30].

REFERENCES

[1] T. Lehman, "A statistical theory of electromagnetic fields in complex cavities," *Interaction Notes, Note 494*, 1993.

[2] J. Kostas and B. Boverie, "Statistical model for a mode-stirred chamber," *IEEE Transactions on Electromagnetic Compatibility*, vol. 33, no. 4, pp. 366 –370, nov 1991.

[3] P. Corona, G. Ferrara, and M. Migliaccio, "Reverberating chambers as sources of stochastic electromagnetic fields," *IEEE Transactions on Electromagnetic Compatibility*, vol. 38, no. 3, pp. 348 –356, Aug 1996.

[4] G. Orjubin, E. Richalot, S. Mengue, and O. Picon, "Statistical model of an undermoded reverberation chamber," *IEEE Transactions on Electromagnetic Compatibility*, vol. 48, no. 1, pp. 248 –251, feb. 2006.

[5] L. Arnaut, "Compound exponential distributions for undermoded reverberation chambers," *IEEE Transactions on Electromagnetic Compatibility*, vol. 44, no. 3, pp. 442 – 457, aug 2002.

[6] ——, "Limit distributions for imperfect electromagnetic reverberation," *IEEE Transactions on Electromagnetic Compatibility*, vol. 45, no. 2, pp. 357 – 377, may 2003.

[7] J. Ladbury, G. Koepke, and D. Camel, *Evaluation of the NASA Langley Research Center mode-stirred chamber facility*, ser. NIST technical note. US Department of Commerce, National Institute of Standards and Technology, 1999, no. 1508.

[8] P. Corona, G. Ferrara, and M. Migliaccio, "Reverberating chamber electromagnetic field in presence of an unstirred component," *IEEE Transactions on Electromagnetic Compatibility*, vol. 42, no. 2, pp. 111 –115, may 2000.

[9] O. Lundén and M. Bäckström, "How to avoid unstirred high frequency components in mode stirred reverberation chambers," in *Electromagnetic Compatibility, 2007. EMC 2007. IEEE International Symposium on*, July 2007, pp. 1–4.

[10] V. Primiani, F. Moglie, and V. Paolella, "Numerical and experimental investigation of unstirred frequencies in reverberation chambers," in *Electromagnetic Compatibility, 2009. EMC 2009. IEEE International Symposium on*, August 2009, pp. 177–181.

[11] R. Serra and F. Canavero, "Bivariate statistical approach for good-but-imperfect electromagnetic reverberation," *IEEE Transactions on Electromagnetic Compatibility*, vol. 53, no. 3, pp. 554 –561, aug. 2011.

[12] *Testing and measurement techniques - Reverberation chamber test methods*, International Electrotechnical Commission (IEC) Std. 61 000-4-21, 2011.

[13] A. Cozza, "The Role of Losses in the Definition of the Overmoded Condition for Reverberation Chambers and Their Statistics," *IEEE Transactions on Electromagnetic Compatibility*, no. 53, pp. 296–307, 2011.

[14] H. Stöckmann, *Quantum chaos: an introduction*. Cambridge Univ Pr, 1999, vol. 3.

[15] M. Mehta, *Random matrices.*, ser. Pure and Applied Mathematics. Amsterdam: Elsevier, 2004, vol. 142.

[16] C. Vaa, P. M. Koch, and R. Blümel, "Weyl formula: Experimental test of ray splitting and corner corrections," *Phys. Rev. E*, vol. 72, p. 056211, Nov 2005.

[17] E. Wigner, "Random matrices in physics," *Siam Review*, vol. 9, no. 1, pp. 1–23, 1967.

[18] H.-J. Stöckmann and J. Stein, "Quantum chaos in billiards studied by microwave absorption," *Physical Review Letters*, vol. 64, pp. 2215–2218, May 1990.

[19] O. Bohigas, M. Giannoni, and C. Schmit, "Characterization of chaotic quantum spectra and universality of level fluctuation laws," *Physical Review Letters*, vol. 52, no. 1, pp. 1–4, 1984.

[20] M. Berry and M. Tabor, "Level clustering in the regular spectrum," *Proceedings of the Royal Society of London. A. Mathematical and Physical Sciences*, vol. 356, no. 1686, pp. 375–394, 1977.

[21] F. Haake, G. Lenz, P. Seba, J. Stein, H. Stöckmann, and K. Życzkowski, "Manifestation of wave chaos in pseudointegrable microwave resonators," *Physical Review A*, vol. 44, no. 10, pp. 6161–6164, 1991.

[22] G. Orjubin, E. Richalot, O. Picon, and O. Legrand, "Chaoticity of a reverberation chamber assessed from the analysis of modal distributions obtained by FEM," *Electromagnetic Compatibility, IEEE Transactions on*, vol. 49, no. 4, pp. 762–771, 2007.

[23] A. Papoulis, *Stochastic processes*. McGraw-Hill, New York, 1965.

[24] J. Pečarić, F. Proschan, and Y. Tong, *Convex functions, partial orderings, and statistical applications*. Academic Press, 1992, vol. 187.

[25] B. Liu, D. Chang, and M. Ma, "Eigenmodes and the composite quality factor of a reverberating chamber," *US Nat. Bur. Stand. Tech. Note*, vol. 1066, 1983.

[26] M. Schroeder, “Statistical parameters of the frequency response curves of large rooms,” *J. Audio Eng. Soc*, vol. 35, no. 5, pp. 299–305, 1987.
[27] L. Arnaut, “Operation of electromagnetic reverberation chambers with wave diffractors at relatively low frequencies,” *Electromagnetic Compatibility, IEEE Transactions on*, vol. 43, no. 4, pp. 637 –653, nov 2001.
[28] W. Petirsch and A. Schwab, “Investigation of the field uniformity of a mode-stirred chamber using diffusers based on acoustic theory,” *Electromagnetic Compatibility, IEEE Transactions on*, vol. 41, no. 4, pp. 446 –451, nov 1999.
[29] D. Hill, “Electromagnetic Theory of Reverberation Chambers,” National Institute of Standards and Technology, Tech. Rep., 1998.
[30] ——, “Plane wave integral representation for fields in reverberation chambers,” *IEEE Transactions on Electromagnetic Compatibility*, vol. 40, no. 3, pp. 209–217, 1998.

Statistics of the Performance of Time Reversal in a Lossy Reverberating Medium

Andrea Cozza*
SUPELEC, Département de Recherche en Électromagnétisme, 3 rue Joliot-Curie, 91192 Gif-sur-Yvette, France.
(Dated: October 20, 2009)

It has been proposed [J. Derosny, Ph.D. Thesis, Université Paris VI, 2000] that the performance of time reversal at recreating a coherent pulse in a strongly reverberating medium is directly proportional to the number of resonant modes M actively taking part at the transmission of energy. This idea is here tested against experimental results, showing that as soon as losses are taken into account, the quality of the focused pulse is a sublinear function of M, leading to a saturation phenomenon that was previously unacknowledged. This is here proven to be caused by mutual coupling between lossy resonant modes, thanks to a statistical modal description of the transmission of signals through the medium. Closed-form relationships are proposed for the first two moments of the pulse signal-to-noise ratio, linking them to the occupied bandwidth, the number of active modes and the degree of resonance of the medium. These formulae, supported by experimental and numerical results, prove that the performance of time reversal can be affected by a strong statistical dispersion. The proposed analysis also predicts that time reversal is a self-averaging process when applied to a reverberating medium, thus allowing the use of models developed in an ensemble-average framework.

I. INTRODUCTION

The interest of time-reversal techniques has been demonstrated in the fields of acoustics as well as electromagnetics, giving rise to a host of applications as diverse as pulsed-energy focusing in complex media [1], imaging techniques [2], and selective focusing [3]. Among these, one of the most surprising features of time reversal is its ability to ensure the transmission of coherent pulses through reverberating media [1, 4]. In the context of this paper, we will consider a reverberating medium as a generally inhomogeneous medium where the propagation of electromagnetic or acoustic energy is strongly constrained into a finite volume. This region of space can be identified by an ideally closed surface imposing highly reflective boundary conditions, a configuration often referred to as a cavity. The provision of a finite volume does not exclude the existence of small apertures, through which a limited amount of the energy can leak out of the reverberating environment leading to a small perturbation of its behaviour assimilable to an energy loss. Coherently with this scenario, the media filling the cavity, as well as its boundary surface, will be regarded as lossy, introducing power dissipation along wave propagation. Following this description, a cavity is characterized by an infinite but countable set of resonances, associated to the eigenmodes of Helmholtz equation when the reflective-surface boundary conditions are enforced [5].

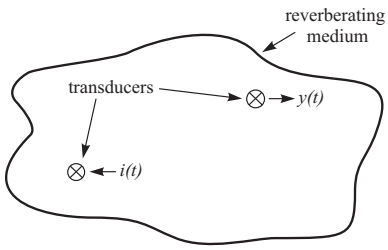

FIG. 1: Synoptic of a generic communication system embedded into a reverberating environment. A pulse $y(t)$ is to be focused at the receiver location by feeding the transmitter with an *ad hoc* signal $i(t)$ defined by means of time-reversal techniques.

Typically, for a pulse transmitted within such a medium, the signal received would be dominated by a long non-coherent tail, made up of a large number of echoes of the original pulse; conversely, use of time-reversal techniques allows a predominantly coherent transmission of the pulse. Applications of this property to electromagnetics range from new signal-forming schemes for telecommunications in multipath channels [6] to the generation of high-intensity local fields for device/material testing [7]. Although the basics for the physical interpretation of time-reversal in such context are known [4], there is no available model allowing to predict the statistical behaviour of this technique when used in a reverberating medium, and in particular how its performance depends on the relative position of the receiver-transmitter pair within the system (see Fig. 1). In particular, the analyses found in the literature focus just on the mean asymptotic performance, without giving any hint of its statistical dispersion. Furthermore, to the best of our knowledge, these models assume the system to be lossless [4].

In this paper we fill this gap by proposing a study of the performance of time reversal for more realistic scenarios, assessing how the signal-to-noise ratio (SNR) of received pulses evolves while changing, on the one hand, the positions of the transducers and, on the other hand, the properties of the medium. This is done by studying the statistics of the performance, in particular by proposing closed-form expressions for the first two moments of the SNR of the received pulse. These results should allow predicting more thoroughly the way time reversal behaves in a reverberating medium, especially thanks to the knowledge of the variance of the SNR: indeed, this is a fundamental piece of data for ensuring, within a certain confidence margin, a given performance for any po-

*andrea.cozza@supelec.fr

sition of the receiver and transmitter. Moreover, by acknowledging the existence of non-negligible loss mechanisms, the proposed model predicts phenomena that were not previously highlighted, such as the fact that losses lead to a saturation of the SNR, because of the mutual coupling between resonant modes through the tails of their frequency spectra. A major point is the generality of these results, which are valid for any system obeying to a modal resonant description, be it acoustic or electromagnetic, while requiring a very limited number of simplifying assumptions.

The paper starts with the introduction of tools for assessing the quality of the received pulse, generalized to the case of lossy media by applying novel definitions with respect to [4]. These tools are then applied for the analysis of experimental results obtained in an electromagnetic reverberation chamber, pointing out some of the previously recalled phenomena that have not yet been acknowledged. A theoretical analysis based on a modal description is then proposed in Section III, leading to the first two statistical moments of the SNR; subsequently, we focus in Section IV on the asymptotic response, proving that thanks to the self-averaging properties of time reversal, its statistical description is asymptotically independent on the actual realization of the reverberating medium, and entirely describable through few global parameters. Numerical results, as well as experimental ones are presented in Section V, validating the accuracy of the proposed analysis. Finally, a simple heuristic interpretation of our findings is given in Section VI, providing a framework for intuitively understanding the reasons for the saturation of the SNR.

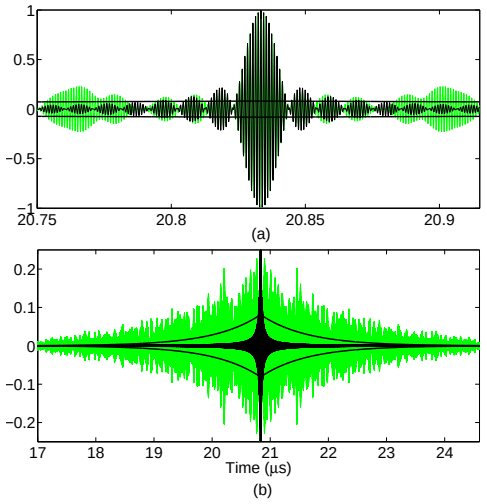

FIG. 2: An example of a pulse transmitted through a reverberating medium using time reversal, for the case of $Q = 5000$, $M = 500$, $B_T = 100$ MHz, central frequency 1 GHz: the region around the peak of the pulse (a) and a wider perspective highlighting the residual noise distribution (b). The dark trace is the original pulse to be transmitted, whereas the light one is the signal actually received, affected by residual noise. The thicker line represents the equivalent noise $n_e(t)$.

II. ON THE QUALITY OF RECEIVED PULSES

A. Mathematical tools for quality assessment

In this Section we are concerned by the use of time-reversal techniques for transmitting a coherent pulse to a given receiver placed in a reverberating medium. Hereafter, this will be supposed to be reciprocal. The configuration we deal with is depicted in Fig. 1: two transducers are placed within the medium, one acting as a transmitter and the other one as a receiver. Defining $h(t)$ as the impulse response between the two transducers, it was shown in [4] that by transmitting the signal $i(t) = x(-t) \star h(-t)$, the received signal $y(t)$ will be a fair replica of $x(-t)$, even in a strongly reverberating medium. Due to this feature, time reversal has been proposed as a way of communicating through complex media, and in particular multipath channels, whose characteristics are well represented by reverberating media [8]. An example of pulse received for this setup is shown in Fig. 2, where $x(t)$ is a cardinal sinus modulating an harmonic carrier. Indeed, it appears that the received signal is almost undistinguishable from the original one around its peak region, whereas it is affected by a stronger modification over the signal tails.

In the following, we will consider the pulse $x(t)$ to have a spectral content comprised in the frequency range $[f_1, f_2]$, i.e., with a frequency bandwidth $B_T = f_2 - f_1$ centered around the frequency $f_c = (f_1 + f_2)/2$. A total number of M resonant modes will be assumed to exist over this frequency range, with resonance frequencies given by the set $\{f_k\}$. In a general way, a transfer function $H(f)$ in a reverberating medium can be expressed as a superposition of these modes, weighted by complex coefficients $\gamma_k = \alpha_k + \mathrm{j}\beta_k$ [5], i.e.,

$$H(f) = \sum_{k=1}^{M} \gamma_k(f)\phi_k(f) \quad , \quad f \in [f_1, f_2] \quad . \qquad (1)$$

The response $\phi_k(f)$ of the k-th mode will be assumed, with no loss of generality, to be a Lorentzian function. By considering the main effect of losses to lead to a small perturbation of these functions, one can write [5]:

$$\phi_k(f) = \frac{f_k^2/Q_k}{f_k^2(1 + \mathrm{j}/2Q_k)^2 - f^2} \quad , \qquad (2)$$

where Q_k is the quality factor associated to the k-th mode, which thus has a -3 dB bandwidth $B_{M,k} = f_k/Q_k$. The modal weights $\{\gamma_k\}$ are functions of the transmitter and receiver positions and of the spatial field distribution associated to each resonant mode.

In order to simplify the notations in the following analysis, we will consider the reference signal to be $x(-t)$, so that the received one is rather linked to $x(t)$. For the same reason, we

will avoid delaying the time-reversed pulse, and consider a non-causal description, as this does not affect the final results. Bearing these definitions in mind, the fitness of the focused pulse can be assessed by computing the component $s(t) = \rho x(t)$ that is coherent with respect to $x(t)$, leading to

$$y(t) = \rho x(t) + n(t) \quad , \tag{3}$$

where $n(t)$ is the residual noise due to the distortion of the pulse introduced by the non-flat transfer function $H(f)$ of the medium, with $H(f)$ the Fourier transform of $h(t)$. Residual $n(t)$ being orthogonal to $x(t)$ by definition, ρ can be computed as

$$\rho = \frac{\langle Y, X \rangle}{\langle X, X \rangle} = \frac{\displaystyle\int_{f_1}^{f_2} X|H|^2 X^\star \mathrm{d}f}{\displaystyle\int_{f_1}^{f_2} |X|^2 \mathrm{d}f} \quad , \tag{4}$$

having applied Parseval equality, where $X(f)$ and $Y(f)$ are the Fourier spectra of the respective time-domain signals. The brackets stand for the projection operator. It is interesting to notice that because of the quadratic form in the previous result, $\rho \in \mathbb{R}^+$, so that the sign of the peak of the received pulse will always be unchanged. Defining the energy $\mathcal{E}_G$ of a spectrum $G(f)$ as

$$\mathcal{E}_G = 2 \int_{f_1}^{f_2} |G(f)|^2 \mathrm{d}f \quad , \tag{5}$$

the energy $\mathcal{E}_S$ of the coherent part is thus given by

$$\mathcal{E}_S = \rho^2 \mathcal{E}_X = 2\rho^2 \int_{f_1}^{f_2} |X|^2 \mathrm{d}f \quad , \tag{6}$$

whereas the energy $\mathcal{E}_N$ of the residual noise is

$$\mathcal{E}_N = 2 \int_{f_1}^{f_2} |X|^2 |H|^4 \mathrm{d}f - \mathcal{E}_S \quad , \tag{7}$$

so that we can introduce the energy SNR Λ as

$$\Lambda = \frac{\mathcal{E}_S}{\mathcal{E}_N} \quad . \tag{8}$$

While the energy ratio Λ will be extensively used in the rest of the paper, the ability of time reversal in transmitting coherent pulses is better assessed by means of the peak SNR Λ_p as defined as follows [4]:

$$\Lambda_p = \frac{s^2(0)}{n_{\mathrm{rms}}^2} \quad , \tag{9}$$

having assumed that the peak of the received pulse occurs in $t = 0$. The quantity n_{rms} is the root-mean-square (rms) value of $n(t)$:

$$n_{\mathrm{rms}}^2 = \lim_{T \to \infty} \frac{1}{T} \int_{-T/2}^{T/2} n^2(t) \mathrm{d}t \quad . \tag{10}$$

Equation (9) thus measures how much the coherent part of the transmitted pulse stands out of the residual noise. Now, the use of the rms value is consistent only in the case of a lossless system, as done in [4], since in this case $n(t)$ would have an infinite energy but a finite non-zero average power. Conversely, for the case of a lossy system, n_{rms} would be equal to zero, since the noise has finite energy; as a matter of fact, the time-constant characterizing the decay of a mode with quality factor Q_k is $\tau_k = Q_k/(\pi f_k) = 1/(\pi B_{M,k})$. We will assume that all the modes involved have the same bandwidth, and as a consequence the same time-constant $\tau = \tau_k, \forall k$; this assumption is valid as long as B_T/f_c is sufficiently smaller than one, i.e., for configurations that cannot yet be regarded as wide-band, though not strictly narrow-band. Under such conditions, $n(t)$ will also obey to a time-decay with constant τ; therefore, we introduce the equivalent noise signal $n_e(t)$:

$$n_e(t) = n_0 \mathrm{e}^{-\pi f_c t/Q} \quad , \tag{11}$$

where Q is the average quality factor, and by imposing the same overall energy for the two noise signals, we get

$$n_0^2 = \frac{\mathcal{E}_N \pi f_c}{Q} \quad . \tag{12}$$

The equivalent noise $n_e(t)$ behaves as a smoothed version of the actual noise $n(t)$, maintaining the same overall time-decay, and thus the same average instantaneous power content. The example shown in Fig. 2 illustrates this approach. It is now possible to define the peak SNR by considering the equivalent instantaneous noise energy at the signal peak in $t = 0$,

$$\Lambda_p = \frac{s^2(0)}{n_e^2(0)} = \frac{Q}{\pi f_c} \chi \Lambda \quad , \tag{13}$$

where $\chi = x^2(0)/\mathcal{E}_X$ is a factor related to the shape of $x(t)$. This simple relationship between the two SNR definitions allows focusing on the energy SNR, which is much simpler to compute in the frequency domain.

Thanks to these definitions, it is possible to predict the performance of time-reversal transmission for any pulse $x(t)$, just by knowing the transfer function $H(f)$. Most remarkably, this just requires having access to the absolute values of the spectra $X(f)$ and $H(f)$.

B. Experimental investigations in a reverberation chamber

In general, the pulse SNR will depend on the relative position of the transmitter and the receiver within the system; in order to exploit the time-reversal technique for real-life applications, it is of paramount importance to be able to ensure that a given minimum SNR be respected for any transducers position, at least with respect to a certain confidence margin. In order to assess the variability of the SNR, we carried out experimental tests, by considering an electromagnetic reverberation chamber, with a fixed antenna acting as the transmitter and a linearly polarized electro-optical sensor (connected to

an optical fiber) as a receiver. This last choice was imposed by the fact that a receiving antenna being moved inside the chamber would have changed its fundamental characteristics, modifying the sets $\{f_k\}$ and $\{\gamma_k\}$, and as thus impairing the validity of any comparison. The very weak interaction ensured by the optical sensor means that it can be regarded as an almost ideal electric-field probe, minimizing the modification of the quantity being measured.

A total of 100 randomly chosen positions and orientations of the receiver were considered, measuring the respective transfer functions over six frequency ranges, centered at frequencies from 0.5 GHz to 3 GHz, by steps of 0.5 GHz. For each central frequency, two bandwidths B_T were considered, namely 100 MHz and 200 MHz.

We assumed, for the sake of simplicity, $x(t)$ to have a flat spectrum over the frequency range $[f_1, f_2]$; this would be the case, e.g., for cardinal sinus pulses. The energy SNR was computed by means of (8), leading to the empirical statistical distributions shown in Fig. 3, and the first two statistical moments of Λ resumed in Table I, together with the average peak SNR Λ_p. These results point to three important facts: 1) while the average energy SNR increases with the frequency, its progression slows down at the same time, converging on an asymptotic value close to one, 2) the actual value of Λ is strongly dispersed, depending on the position of the receiver and, 3) an increasing bandwidth has apparently little effect on the average energy SNR, whereas its dispersion decreases. To the best of our knowledge, these conclusions have never been discussed before, and no theoretical framework is available for interpreting them.

The only available model is the one proposed in [4] for a lossless configuration. It predicts a direct proportionality between the number of modes M and the average peak SNR Λ_p. In order to apply this model to our experimental results, we estimated the number M_{w} of resonant modes existing in the chamber for a given frequency range through Weyl's formula [9]

$$M_{\mathrm{w}}(f_c) \simeq \frac{8\pi V}{c^3} f_c^2 B_T \left(1 + \frac{B_T^2}{12 f_c^2}\right) \quad , \qquad (14)$$

where V is the volume of the reverberation chamber and c is the speed of light in the medium filling it. Results obtained for the case of Supelec's chamber ($V = 3.08 \times 1.84 \times 2.44$ m^3) are shown in Table I. By comparing M_{w} to the average Λ_p, it is clear that their relationship is more complex, and characterized by a form of saturation of the performance, since even for large increases in M_{w}, Λ_p is barely affected.

The reasons for such a peculiar behaviour are to be sought in the existence of loss mechanisms in actual reverberation chambers; we will show in the next Section that this leads to mutual couplings between resonant modes, and ultimately to a saturation of the performance.

Concerning the statistical dispersion discussed in points 2) and 3), it has never been addressed before. It is worthwhile noticing that the orientation of the probe has little effect on the dispersion, since the cavity was over-moded for all the frequency ranges, apart for $f_c = 0.5$ GHz. For such configurations, the field is statistically isotropic, and it presents very similar statistical properties along its three Cartesian components [10].

f_c (GHz)	B_T (MHz)	mean Λ	std Λ	mean Λ_p	Q	M_{w}
0.5	100	0.37	0.074	187	3900	322
	200	0.30	0.051	300		644
1.0	100	0.75	0.12	272	5700	1287
	200	0.72	0.080	130		2574
1.5	100	0.91	0.14	243	6300	2896
	200	0.90	0.10	481		5792
2.0	100	0.96	0.13	192	6300	5149
	200	0.95	0.12	380		10297
2.5	100	1.02	0.13	187	7200	8045
	200	1.00	0.10	365		16090
3.0	100	1.02	0.14	188	8700	11584
	200	0.98	0.10	358		23169

TABLE I: Statistical moments of the energy SNR Λ and average peak SNR Λ_p, as computed from the experimental data presented in Fig. 3. The approximate number of modes M_{w} was computed by means of Weyl's formula (14), whereas the average quality factor Q was directly estimated from the time constant of the residual noise $n(t)$.

These results point out that apart from being able to explain the limitations of time reversal, it is of paramount importance to have a model predicting the statistical dispersion of the SNR. These are indeed the basic motivations of this paper.

III. STATISTICAL MOMENTS OF Λ

As often done in statistical descriptions, the parameters of the model will need to be regarded as random variables. This approach is not just dictated by mathematics, but it comes with physical meaning. In particular, the resonance frequencies $\{f_k\}$ are indeed distributed over the bandwidth B_T in a way that is hardly predictable, unless in canonical configurations. For the associated modal weights $\{\gamma_k\}$, since describing the projection of the transducer characteristic response over the modal topographies, a modification in the position of the receiver or the transmitter leads to a modification of the $\{\gamma_k\}$, so that a random position of the transducers implies a random set of modal weights. Moreover, the fact that the modal topographies, as well the excitation of the transducers are, in general, sign-changing functions, implies that the $\{\alpha_k\}$ and $\{\beta_k\}$ should be treated as zero-mean random variables, and they will be assumed to be independent and identical distributed (iid). No further assumption will be necessary about the type of distributions.

In order to simplify the model, the $\phi_k(f)$ will be assumed to be frequency-shifted replica, with approximately the same bandwidth $B_M = f_k/Q_k, \forall k$. This also implies that all the modal responses $\phi_k(f)$ have the same energy $\mathcal{E}_\phi$. In principle, this assumption holds only when relatively narrow bands are considered, although the results shown in Section V prove that

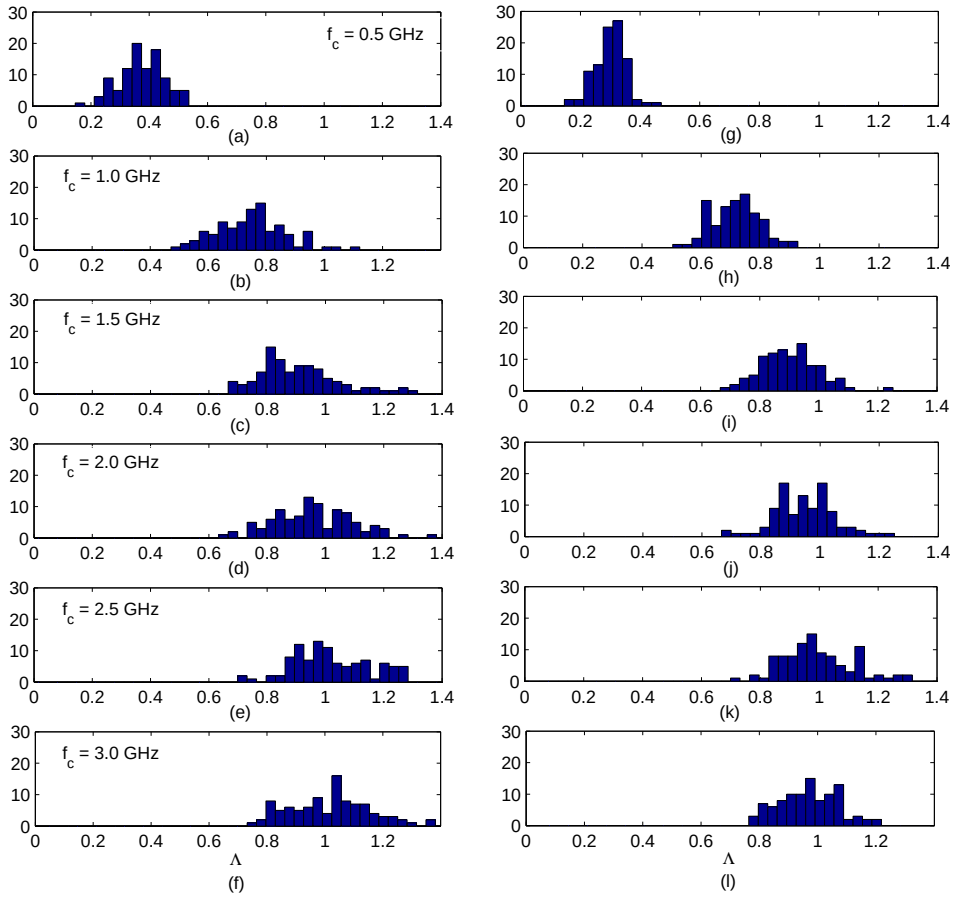

FIG. 3: Frequencies of occurrence for the energy SNR Λ as computed from experimental data measured over a bandwidth $B_T = 100$ MHz (left column) and $B_T = 200$ MHz (right column), centered around the frequencies $f_c = \{0.5, 1, 1.5, 2, 2.5, 3\}$ GHz (top to bottom). Each histogram was obtained from a population of 100 sample transfer functions as measured between a fixed transmitter antenna and a moving electro-optical probe.

this is not necessarily the case.

It is important to understand the physical role of the following statistical analysis, which aims at accounting for the impact of the random position of the transducers on the received pulse SNR. Indeed, equation (1), when coupled with equations (6)-(8), leads to the definition of Λ as a random function, depending on the probability density functions (pdfs) of $\{\gamma_k\}$ and $\{f_k\}$.

We start our analysis by considering a specific configuration for the reverberating medium, i.e., for a given set of known deterministic $\{f_k\}$, whereas the $\{\gamma_k\}$ will be regarded as random variables. This scenario corresponds to the case of a single realization for the medium, while the positions of the transducers are let free to change, so that all the statistical moments will be conditional to the set $\{f_k\}$. The ensemble behaviour of the SNR considering random $\{f_k\}$ will be studied in Section IV.

In order to simplify our analysis, but with no loss of generality in the conclusions, we will assume the modulus of $X(f)$ to be directly proportional to the characteristic function of the interval $[f_1, f_2]$, leading to $\chi = 2B_T$. This choice corresponds, e.g., to a cardinal sine excitation in the time-domain, modulating an harmonic carrier of frequency f_c, as for the example shown in Fig. 2. Attention should be paid to the fact that the definitions of the SNR actually depends just on the modulus of $X(f)$, so that an infinite number of pulse shapes

sharing the same spectral occupation would be characterized by the same SNR.

Following this assumption, (8) can be recast as

$$\Lambda = \frac{\left(\int_{f_1}^{f_2} |H|^2 \mathrm{d}f\right)^2}{B_T \int_{f_1}^{f_2} |H|^4 \mathrm{d}f - \left(\int_{f_1}^{f_2} |H|^2 \mathrm{d}f\right)^2} \quad . \tag{15}$$

Thus Λ is entirely defined by the properties of the random function $|H(f)|^2$ over the frequency-range $[f_1, f_2]$. In order to study the statistical properties of Λ, we introduce the auxiliary random variables $W_i \in \mathbb{R}^+$, as defined as

$$W_i = \int_{f_1}^{f_2} |H|^{2i} \mathrm{d}f \quad , \tag{16}$$

yielding

$$\Lambda = \frac{W_1^2}{B_T W_2 - W_1^2} \quad . \tag{17}$$

The rationale for introducing these auxiliary variables is that the statistical moments of Λ cannot be expressed as a direct function of the $\{\gamma_k\}$ and $\{f_k\}$ moments. Nevertheless, the moments of W_i can be linked more easily to those of $\{\gamma_k\}$ and $\{f_k\}$; an estimation of the moments of Λ can then be given by linearizing (17) around the W_i ensemble averages [11]. For the sake of simplicity, the following convention is introduced:

$$\overline{W}_i = \mathrm{E}[W_i|\{f_k\}] \quad . \tag{18}$$

Applying this approach to the average of Λ conditional to a given realization $\{f_k\}$ yields

$$\mathrm{E}[\Lambda|\{f_k\}] \simeq \frac{\overline{W}_1^2}{B_T \overline{W}_2 - \overline{W}_1^2} \quad . \tag{19}$$

In the same way, the conditional variance $\sigma^2_{\Lambda|\{f_k\}}$ can be approximated as

$$\sigma^2_{\Lambda|\{f_k\}} = \mathrm{E}[\Lambda^2|\{f_k\}] - \mathrm{E}[\Lambda|\{f_k\}]^2 \simeq \mathbf{J}^{\mathrm{T}} \mathbf{\Sigma} \mathbf{J} \quad , \tag{20}$$

where $\mathbf{\Sigma}$ is the covariance matrix of the random vector $[W_1, W_2]^{\mathrm{T}}$. The column vector $\mathbf{J}$ is the Jacobian of Λ as computed with respect to W_1 and W_2, evaluated at $(\overline{W}_1, \overline{W}_2)$:

$$\mathbf{J} = B_T \frac{\overline{W}_1}{\left(B_T \overline{W}_2 - \overline{W}_1^2\right)^2} \begin{bmatrix} 2\overline{W}_2 \\ -\overline{W}_1 \end{bmatrix} \quad . \tag{21}$$

A higher-order estimate of Λ could be given, but the resulting expression would be quite unwieldy without delivering considerable improvement in the final accuracy. For the same reason, we just consider the first two moments of W_1 and W_2. Thanks to the following expansion

$$\begin{aligned} |H(f)|^2 &= \sum_{k=1}^{M} |\gamma_k|^2 |\phi_k(f)|^2 + \\ &+ 2 \sum_{k=1}^{M} \sum_{m=k+1}^{M} \mathrm{Re}\left\{\gamma_k \gamma_m^\star \phi_k(f) \phi_m^\star(f)\right\} \end{aligned} \tag{22}$$

and assuming the $\{\gamma_k\}$ to be independent from the $\{f_k\}$, while recalling the hypothesis of all the modes having the same energy $\mathcal{E}_\phi$, as defined in (5), we can write

$$\mathrm{E}[W_1|\{f_k\}] = 2M\mu_2 \mathcal{E}_\phi \tag{23}$$

$$\begin{aligned} \mathrm{E}[W_2|\{f_k\}] &= 2M(\mu_2^2 + \mu_4)\mathcal{E}_{|\phi|^2} + \\ &+ 16\mu_2^2 \sum_{k=1}^{M} \sum_{m=k+1}^{M} \mathcal{E}_{\phi_k \phi_m} \end{aligned} \tag{24}$$

having introduced the moments μ_i

$$\mu_i = \mathrm{E}[\alpha_k^i] = \mathrm{E}[\beta_k^i] \quad . \tag{25}$$

Equation (24) differs from (23) in a fundamental aspect, i.e., the presence of the mutual energies $\mathcal{E}_{\phi_k \phi_m}$ shared between each couple of modes of the system. This term can be shown to be the source of the limitations of the SNR as the modal density M/B_T increases enough to lead to non-negligible interactions between the modes.

The same type of analysis was carried out for the elements $\Sigma_{ij} = \mathrm{E}[(W_i - \mathrm{E}[W_i])(W_j - \mathrm{E}[W_j])]$ of the covariance matrix, but this led to too complex expressions, especially for Σ_{22}. We would rather propose approximate results, where the mutual-energy terms are neglected:

$$\mathbf{\Sigma} \simeq 4M\boldsymbol{\nu} \quad , \tag{26}$$

having defined the elements of $\boldsymbol{\nu}$ as

$$\nu_{11} = \mathcal{E}_\phi^2(\mu_4 - \mu_2^2) \tag{27}$$

$$\nu_{12} = \mathcal{E}_\phi \mathcal{E}_{|\phi|^2}(\mu_2\mu_4 + \mu_6 - 2\mu_2^3) \tag{28}$$

$$\nu_{22} = \mathcal{E}_{|\phi|^2}^2(\mu_8 + 4\mu_2\mu_6 + \mu_4^2 - 2\mu_2^4 - 4\mu_2^2\mu_4) \tag{29}$$

It is worth noting that although interactions between modes have been neglected in $\mathbf{\Sigma}$, the Jacobian in (21) takes them into account. It will be shown in Section V that when applied as an input to (20), these expressions provide a good estimate of the variance of Λ, and as thus they are a useful tool in stating the uncertainty that affects time-reversal performances in a reverberating medium.

IV. AVERAGE ASYMPTOTIC PERFORMANCE

The formulae presented in the previous Section were derived considering a given deterministic set of resonant frequencies $\{f_k\}$, and as thus (19) and (20) depends, in principle,

on the actual realization of $\{f_k\}$. In fact, this dependence subsists only in the mutual energies $\mathcal{E}_{\phi_k\phi_m}$ in (24).

In this Section, we consider the performance of time-reversal when averaged over all the realizations of $\{f_k\}$, hence related to its general trend rather than for a specific configuration, proving that under certain conditions, the statistics of a single realization are well approximated by the simpler ensemble statistics.

To this end, let us consider the ensemble average of Λ with respect to the random set $\{f_k\}$; thanks to the linearization of Λ, it will suffice to carry out this averaging over the W_i, leading to:

$$\begin{aligned} \mathrm{E}[W_1] &= 2M\mu_2\mathcal{E}_\phi \qquad (30) \\ \mathrm{E}[W_2] &= 2M(\mu_2^2+\mu_4)\mathcal{E}_{|\phi|^2} + \\ &\quad + 8\mu_2^2M(M-1)\mathrm{E}[\mathcal{E}_{\phi_k\phi_m}] \quad . \qquad (31) \end{aligned}$$

The double sum in (24) is thus simplified by introducing the average mutual energy $\mathrm{E}[\mathcal{E}_{\phi_k\phi_m}]$. The result in (24) and (31) would then be identical if the following condition were satisfied:

$$\frac{2}{M(M-1)}\sum_{k=1}^{M}\sum_{m=k+1}^{M}\mathcal{E}_{\phi_k\phi_m} \simeq \mathrm{E}[\mathcal{E}_{\phi_k\phi_m}] \quad . \qquad (32)$$

This requirement corresponds to assuming the system to be ergodic, approximating the ensemble average over all the realizations with the average carried out over the set of mutual energies within a single realization. The strong law of large numbers [12] states that, if the system is ergodic, the left hand of (32) converges in probability to the ensemble average of the mutual energy; therefore, for a sufficiently high number of active modes M one gets

$$\mathrm{E}[\Lambda|\{f_k\}] \simeq \mathrm{E}[\Lambda] \quad . \qquad (33)$$

This phenomenon, often referred to as self-averaging, had already been experimentally highlighted in [13], although in a different context, as one of the most interesting features of time reversal, and it implies that its performance in transmitting coherent pulses in a reverberating medium is asymptotically independent from the actual realization of the set of the resonance frequencies $\{f_k\}$, underpinning the robustness of this technique.

An example highlighting this property is given in Fig. 4, where empirical pdfs are shown for 10 different realizations $\{f_k\}$, for three values of M, namely 50, 100 and 200, with $f_c = 2$ GHz, $B_T = 200$ MHz and $Q = 1000$. For each realization of $\{f_k\}$, ten thousand sets of modal weights $\{\gamma_k\}$ were considered. It appears that indeed the pdfs converge toward the ensemble average as M increases, even for such small values of M.

We can now write

$$\mathrm{E}[\Lambda] = \frac{2M\mathcal{E}_\phi^2}{B_T\left[(1+\mu_4/\mu_2^2)\mathcal{E}_{|\phi|^2} + 4(M-1)\mathrm{E}[\mathcal{E}_{\phi_k\phi_m}]\right] - 2M\mathcal{E}_\phi^2} \qquad (34)$$

It is clear that the behaviour of $\mathrm{E}[\Lambda]$ could be easily predicted should the three energy terms be known. As a matter of fact, a closed-form expression can be given for $\mathrm{E}[\mathcal{E}_{\phi_k\phi_m}]$ by exchanging the order of integration:

$$\mathrm{E}[\mathcal{E}_{\phi_k\phi_m}] = \int_{f_1}^{f_2}\left(\int_{f_1}^{f_2}|\phi_k(f)|^2p(f_k)\mathrm{d}f_k\right)^2\mathrm{d}f \quad , \qquad (35)$$

having exploited the fact that the $\{f_k\}$ are iid random variables. Noticing that the inner integral does not depend on the actual frequency f at which it is computed, as long as $B_T \gg B_M$, (35) becomes

$$\mathrm{E}[\mathcal{E}_{\phi_k\phi_m}] = B_T\left(\int_{f_1}^{f_2}|\phi_k(f_c)|^2p(f_k)\mathrm{d}f_k\right)^2 \quad , \qquad (36)$$

and by assuming a uniform distribution for the $\{f_k\}$ over the bandwidth B_T, this yields

$$\mathrm{E}[\mathcal{E}_{\phi_k\phi_m}] = \frac{\mathcal{E}_\phi^2}{B_T} \quad . \qquad (37)$$

The two remaining energies $\mathcal{E}_\phi$ and $\mathcal{E}_{|\phi|^2}$ can also be ex-

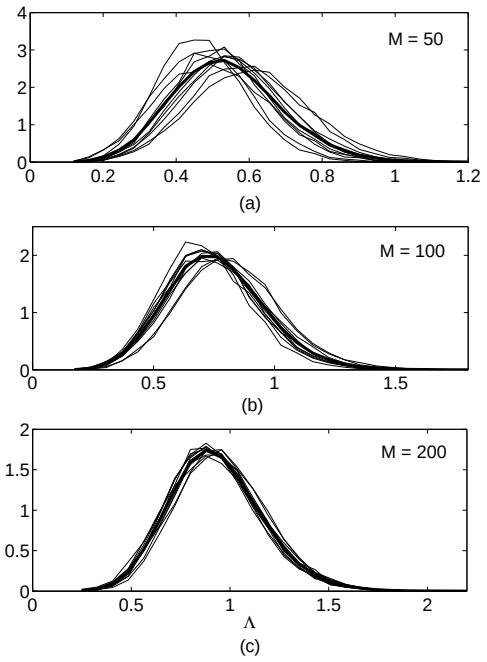

FIG. 4: Empirical conditional pdfs $p(\Lambda|\{f_k\})$ for $Q = 1000$, $f_c = 2$ GHz and $B_T = 200$ MHz, obtained for an increasing number of active modes. The thicker curve stands for the ensemble average of each group of realizations.

pressed in closed-form as

$$\mathcal{E}_{\phi_k} \;=\; f_k \frac{\pi}{2} \frac{Q_k}{Q_k^2+1} \simeq \frac{\pi}{2} B_M \qquad (38)$$

$$\mathcal{E}_{|\phi_k|^2} \;=\; f_k \frac{\pi}{4} \frac{Q_k^3 (Q_k^2+5)}{(Q_k^2+1)^3} \simeq \frac{\pi}{4} B_M \quad , \qquad (39)$$

so that (34) can be restated in a simpler form

$$\mathrm{E}[\Lambda] = \frac{M}{M + (1+\mu_4/\mu_2^2)\dfrac{B_T}{2\pi B_M}} \quad . \qquad (40)$$

Hence $\mathrm{E}[\Lambda]$ is linearly dependent on M at low modal density levels, whereas it converges to an asymptotic value for an higher M. Thus, in lossy reverberating media, the potential gain obtained by increasing the number of active modes (i.e., increasing the central frequency f_c) is put in jeopardy by the coupling existing between lossy resonant modes, with $\mathrm{E}[\Lambda]$ converging to a fixed value. Interestingly, this asymptotic value is simply equal to one. The physical significance of this result will be given a simplified explanation in Section VI.

Equation (40) is remarkably simple, and it shows that a handful of global parameters is sufficient for an accurate prediction of the quality of the received pulse. It is worth noting that the central frequency does not appear explicitly, as a consequence of the identical-mode assumption. These results also point to the fact that the most fundamental quantity for understanding the phenomena behind pulse focusing in a reverberating medium is B_T/B_M. This quantity will be hereafter referred to as N_s, for reasons that will be made clear in Section VI, yielding

$$\mathrm{E}[\Lambda] = \frac{M/N_s}{M/N_s + (1+\mu_4/\mu_2^2)/(2\pi)} \quad . \qquad (41)$$

This reformulation states that the average performance is entirely predicted by means of the ratio M/N_s. As soon as $M \gtrsim N_s$ the marginal gain brought by the availability of new modes is increasingly reduced, leading to a saturation for higher M.

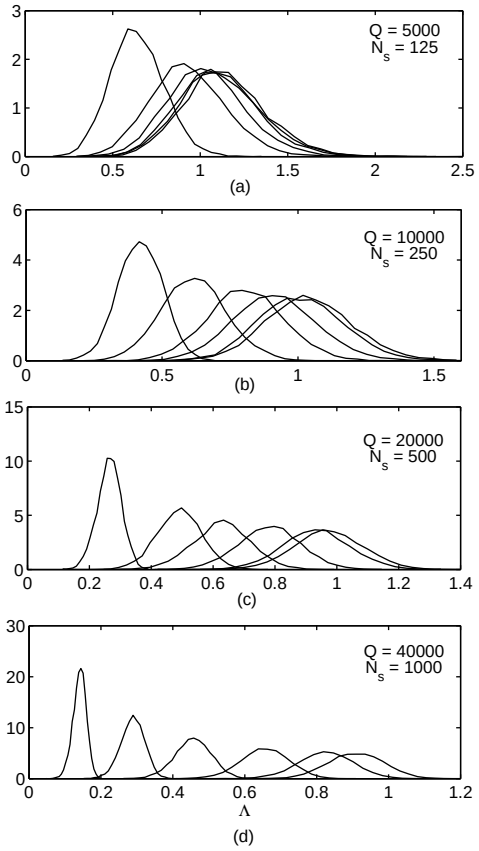

FIG. 5: Empirical pdfs for the energy SNR Λ, depending on the number M of active modes and the quality factor Q of the medium. The six curves presented in each picture correspond to $M = \{100, 250, 500, 1000, 2500, 5000\}$, respectively, from left to right.

V. MODEL VALIDATION

In order to check the accuracy of the proposed description, we considered numerical simulations, by synthesizing random realizations of transfer functions, thanks to (1). The rationale for this approach is the possibility to closely monitor the number of modes M, their quality factor, and so on. Indeed, as recalled later in this Section, experimental validations are impaired by the impossibility to assess the exact number of modes taking part to the transmission.

Thanks to the fact that (40) is not directly dependent on the central frequency f_c, but rather on the bandwidths B_T and B_M, the validation can be carried out at any value of f_c. We set for $f_c = 2$ GHz, with a varying bandwidth B_T and several average quality factors Q. Random complex weights γ_k are drawn accordingly to normally distributed α_k and β_k; the energy SNR for the transfer functions thus obtained are subsequently computed thanks to (8). Contrary to the assumption of a constant f_k/Q_k, the $\phi_k(f)$ were assumed to have a constant quality factor $Q = Q_k, \forall k$. Therefore, the modal responses $\phi_k(f)$ will not be identical as assumed in the model derivation.

The first tests aimed at showing how the energy SNR is distributed as M and $N_s = B_T/B_M$ vary, and is more of a qualitative investigation. A bandwidth B_T of 50 MHz was chosen, while four values of Q were tested, ranging from 5000 to 40000. The number of modes varied from 100 to 5000.

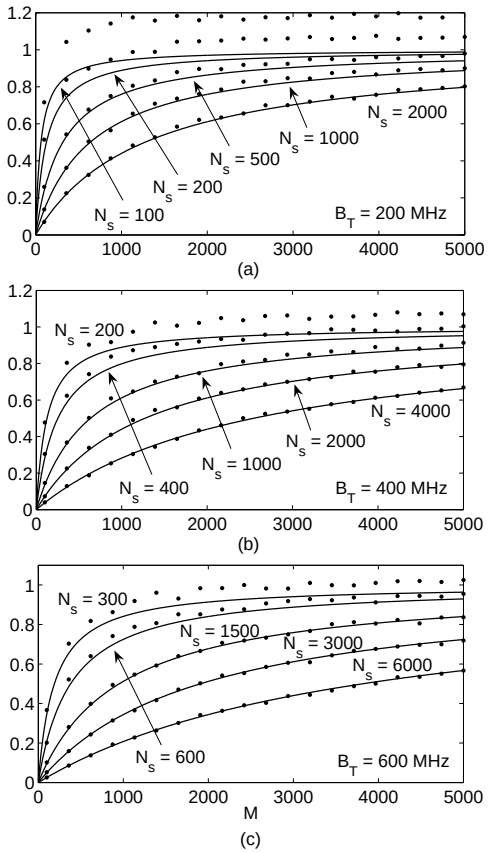

FIG. 6: Validation tests for $\mathrm{E}[\Lambda]$: numerical results obtained from 500 realizations (dots) and the values predicted by (40) (solid lines). All the presented results were computed for $f_c = 2$ GHz and for Q={1000, 2000, 5000, 10000, 20000}, while the corresponding N_s are displayed.

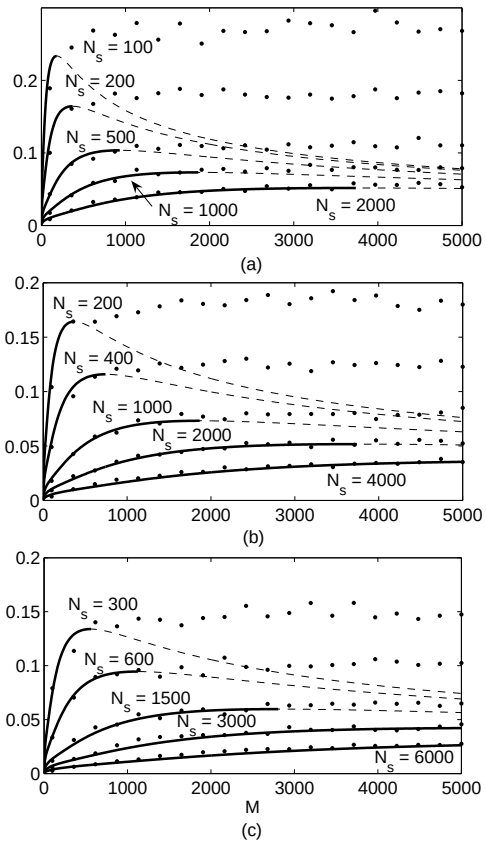

FIG. 7: Validation tests for the standard deviation of Λ, for the same configurations as in Fig. 6. The dashed lines correspond to the values predicted by (20), but considering ensemble-averaged W_i, whereas the thick solid ones highlight the model results up to the curve local maximum, for $M < M_\sigma$.

For each set of global parameters ten thousand realizations were generated, in order to establish empirical pdfs; these are shown in Fig. 5, and illustrate quite clearly that: 1) increasing losses tend to saturate the energy SNR faster, as M increases, 2) decreasing losses slow the saturation down, but reduce the average energy SNR, as the length of the residual-noise tails increases and so does the noise energy, and 3) the SNR experiences a standard deviation that is far from negligible when compared to the average value, although, as Q increases, the dispersion appears to decrease. The trend in the simulated pdfs recalls that of the experimental ones shown in Fig. 3.

Even though the energy SNR Λ decreases with Q, the peak SNR Λ_p increases monotonically, since the relationship between Λ and Q is actually sublinear. This fact is to be expected intuitively, and it also confirms the trend predicted by the model proposed in [4], since

$$\lim_{Q\to\infty} \mathrm{E}[\Lambda_p] = M \quad , \tag{42}$$

again, in the case of a cardinal-sinus pulse and gaussian statistics for the modal weights.

Quantitative validations were then carried out by considering $f_c = 2$ GHz, $Q = \{1000, 2500, 5000, 10000, 20000\}$, and a varying bandwidth $B_T = \{200, 400, 600\}$ MHz. The number of modes spanned the values 100 to 5000, and a population

of 500 random realizations $\{\gamma_k\}$ per configuration was considered, each configuration representing just a single realization of $\{f_k\}$. The results thus obtained for the average value and the standard deviation of Λ are shown in Fig. 6 and Fig. 7, respectively. Fig. 6 shows that the average value is predicted within a few percent points as long as $N_s \gtrsim 200$. Indeed, (40) is unable to predict any energy SNR greater than one; this is actually not due to a bad estimate of the moments of the auxiliary variables W_i, which are indeed precisely estimated in all of the considered tests, since (30) and (31) do not involve any approximation. This rather points directly to the conditions that are necessary for applying the linearization in (9), implying that it is necessary for the condition $N_s \gtrsim 200$ to be fulfilled. We investigated the possibility of including the Hessian term in the expansion (19), but we dropped this option, since it brought no tangible improvement, thus implying that the SNR as a non linear function of W_i would require terms higher than quadratic ones.

The standard deviation depicts a rather different scenario. Expression (20) neglects any modal interaction in the covariance matrix $\mathbf{\Sigma}$, but it includes them through the use of $\overline{W}_i$. For this reason, (20) is expected to underperform as soon as the modal interactions get more important, i.e., as the modal density M/B_T increases. The results in Fig. 7 support these ideas, showing that (20) is a very good estimate of the standard deviation, as long as it has not yet attained its maximum value $\sigma_{\max}$. After this point, (20) is no more a valid estimate, but the actual standard deviation gets to a plateau fairly approximated by $\sigma_{\max}$. In general, this value needs to be computed numerically, but for the case of modal weights distributed as Gaussian random variables, the number of modes M_σ for which the standard deviation reaches its maximum value can be approximated by

$$M_\sigma \simeq \frac{6}{\pi} N_s \quad . \tag{43}$$

Knowledge of the saturation point allows extending the validity of (20) over the entire range of values of M, i.e.,

$$\sigma^2_\Lambda \simeq \begin{cases} (\mathbf{J}^{\mathrm{T}} \mathbf{\Sigma} \mathbf{J})(M) & M \leq M_\sigma \\ \frac{1.7\pi}{N_s} & M > M_\sigma \end{cases} \quad . \tag{44}$$

Therefore, the maximum standard deviation goes like $1/\sqrt{N_s}$, whereas it is inversely proportional to N_s for $M \ll M_\sigma$. The former conclusion explains the behaviour previously highlighted, with the standard deviation decreasing when B_T and/or Q increase.

These numerical validations prove the effectiveness of the asymptotic models, even for a relatively low number of modes and with no ensemble averaging in $\{f_k\}$. This implies that the ergodic assumption formulated in the previous Section does indeed hold. The greatest limitation in the proposed models is the need for (9) to be well approximated by its tangent plane over the range of values spanned by the W_i, requiring $N_s \gtrsim 200$.

The last validation is a tentative experimental one. As recalled at the beginning of this Section, the exact number of modes excited in a reverberating system is usually not known. Therefore a direct validation is not feasible; nevertheless, it is current practice in electrical engineering to assumed that a linearly polarized antenna placed in an electrically large reverberating chamber will excite most of the modes existing over the frequency range of emission of the antenna. As a consequence, Weyl's formula is often used as a reference. Hence, we computed the moments of the energy SNR predicted by our model, considering a number of modes equal to three fractions of the estimate M_{w} given by Weyl's formula (14).

The results are resumed in Table II, together with the quantity N_s: the range of variation of the SNR is very well identified, both for the average value and the standard deviation, and the experimental results are consistently approached when considering a number of modes close to $0.9M_{\mathrm{w}}$. Furthermore, as expected from the numerical validation, as soon as N_s decreases towards 200 the experimental average Λ goes beyond one; in this case, the model will underestimate the statistical moments.

The fact that considering the same fraction of M_{w} over the six frequencies leads to good results, strongly reduces the odds that this accuracy be a random result; we thus consider that 90 % of the available modes were indeed effectively excited. The only exception is for $f_c = 0.5$ GHz and $B_T = 200$ MHz; in fact, the transmitting antenna had a cut-off frequency around 450 MHz, so that of the 200 MHz pulse to be received, it actually transmitted only three-quarters of the signal spectrum, hence exciting roughly three-quarters of the available modes. By taking into account this fact, the actual number of modes to be considered is rather $3/4 \cdot 0.9M_{\mathrm{w}} \simeq 2/3M_{\mathrm{w}}$: indeed, the results agree.

Overall, it appears that the average of Λ is hardly affected by an increase in B_T. Actually, this is predictable, since both N_s and M_{w} are linearly dependent on B_T, so that (41) is not modified. Conversely, the peak SNR will increase proportionally to B_T. At the same time, the standard deviation is sensitive to an increasing B_T. This was predicted in (44), and the reduction of a factor $1/\sqrt{2}$ subsequent to a doubling B_T is indeed well confirmed by the experimental results. These findings are of the utmost importance should time-reversal techniques be used for pulse transmission.

VI. AN HEURISTIC INTERPRETATION

We will here try to give an interpretation of the reported phenomena from a more physical, yet approximate, point of view. To this end, let us recall that the maximum value attained by the peak SNR Λ_p, as long as $N_s \gtrsim 200$, is simply given by $N_s/(2\pi)$. It is thus not dependent on the actual number of modes M, but rather to a, usually, much lower quantity.

Let us look at N_s from a different perspective: knowing that B_M is the average bandwidth of the frequency response of each mode, N_s states the maximum number of modes that could be placed one after the other over the bandwidth B_T. The energy SNR corresponding to this configuration is equal to one, and it corresponds to the best efficiency time-reversal can provide in concentrating energy in the coherent part rather than in the residual noise.

f_c (GHz)	B_T (MHz)	experiments	mod. $2M_\mathrm{w}/3$	mod. $3M_\mathrm{w}/4$	mod. M_w	N_s	M_w/N_s
0.5	100	0.37 (0.074)	0.30 (0.082)	0.33 (0.083)	0.39 (0.083)	785	0.41
	200	0.30 (0.051)	0.30 (0.058)	0.33 (0.058)	0.39 (0.058)	1570	
1.0	100	0.75 (0.12)	0.70 (0.097)	0.73 (0.097)	0.78 (0.097)	570	2.3
	200	0.72 (0.080)	0.70 (0.069)	0.73 (0.069)	0.78 (0.069)	1140	
1.5	100	0.91 (0.14)	0.88 (0.11)	0.89 (0.11)	0.92 (0.11)	420	6.9
	200	0.90 (0.095)	0.88 (0.080)	0.89 (0.080)	0.92 (0.080)	840	
2.0	100	0.96 (0.13)	0.95 (0.013)	0.95 (0.13)	0.96 (0.13)	315	16
	200	0.95 (0.010)	0.95 (0.092)	0.95 (0.092)	0.96 (0.092)	630	
2.5	100	1.02 (0.13)	0.97 (0.14)	0.97 (0.14)	0.98 (0.14)	288	28
	200	1.00 (0.12)	0.97 (0.097)	0.97 (0.097)	0.98 (0.097)	576	
3.0	100	1.02 (0.14)	0.98 (0.14)	0.98 (0.14)	0.98 (0.14)	290	40
	200	0.97 (0.10)	0.98 (0.096)	0.98 (0.096)	0.98 (0.096)	580	

TABLE II: Experimental validation against the results presented in Table I: mean values are given directly, while standard deviations are in parenthesis. The results computed by means of (40) and (20) were obtained considering a number of active modes equal to $2M_\mathrm{w}/3$, $3M_\mathrm{w}/4$ and M_w, due to the uncertainty on the actual M. The reliability of the estimates can be tested by checking the condition $N_s \gtrsim 200$.

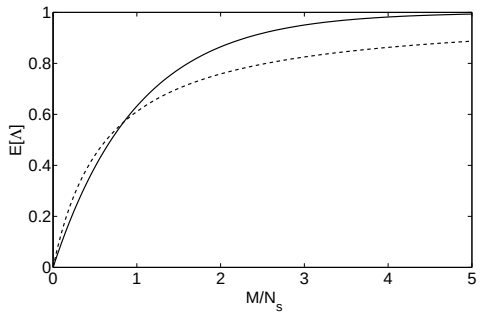

FIG. 8: Comparison between the mean energy SNR, as predicted by the modal approach (41) (solid line) and the slot occupancy description (46) (dashed line).

This fact can be used to give a simple intuitive interpretation, by introducing the idea of a number N_s of available slots, to be occupied by the actual number of active modes. Although simplistic, this vision of the spectrum as a quantified space makes sense. Hence, each mode introduces a further degree of freedom only if it can be allocated to a free slot; otherwise, it will be lost, just leading to a different modal weight, as a function depending on the weights of the modes previously allocated to the same slot. Therefore, the performance of time reversal is not related to the actual number of active modes, but rather to the number of slots being used, which could thus be regarded as an effective number of modes or degrees of freedom, or M_e, leading to an efficiency and, ultimately, to an energy SNR equal to M_e/N_s. The allocation of a mode to a specific slot being a "rare" event, this random process can be modelled by a Poisson law, with mean M/N_s. The mean number of occupied slots, and thus the effective number of modes M_e, is thus simply given by

$$M_e = N_s(1 - \mathrm{e}^{-M/N_s}) \quad , \tag{45}$$

and the related energy SNR

$$\mathrm{E}[\Lambda] \simeq \frac{M_e}{N_s} = 1 - \mathrm{e}^{-M/N_s} \quad , \tag{46}$$

highlighting the dominant role of the quantity M/N_s, as previously shown in (41). We could thus dub the quantity M/N_s as the modal slot occupancy: it defines completely the SNR and is sufficient for predicting the performance of time reversal in any configuration.

The validity of this reasoning is proven in Fig. 8. Indeed, for a low number of modes (with respect to N_s) the results predicted by (41) and (46) correspond fairly well. For higher slot occupancies, (46) saturates faster, since this model is incapable of acknowledging the partial superposition of two modes, something that would just lead to a partial loss of a degree of freedom. In spite of this over-simplification, this approach yields results consistent with those predicted by (41), while providing a simple framework for understanding the SNR saturation phenomenon.

VII. CONCLUSIONS

This paper has addressed the main phenomena underlying the quality of pulses received by a transducer as transmitted through a reverberating medium, when using time-reversal techniques. The quality of the received pulse has been analyzed with respect to global parameters identifying the properties of the medium, according to a modal description. Having included loss mechanisms, it was proven that the sharing of energy between finite-bandwidth resonant modes is at the origin of the limitations in the SNR of the received pulse. A

statistical approach has led to general results based on very few assumptions, mainly that of a sufficiently "wide-band" configuration with $B_T/B_M \gtrsim 200$: the developed model predicts correctly the first two statistical moments of the SNR, acknowledging its non-negligible statistical dispersion. Although mainly based on a mathematical approach, the physical meaning of these results were explained in plain terms by introducing a simplified heuristic description, proving that the SNR is in fact limited by the finite number of degrees of freedom available in a lossy reverberating system. These results should be useful for both the design of experiments and the interpretation of their results, and pertain to any type of wave propagation problem in a reverberating environment.

[1] G. Lerosey, J. De Rosny, A. Tourin, A. Derode, G. Montaldo and M. Fink, Radio Science **40**, RS6S12.1 (2005).
[2] L. Borcea, G. Papanicolaou, C. Tsogka and J. Berryman, Inverse Problems **18**, 1247 (2002).
[3] C. Prada and M. Fink, Wave Motion **20**, 151 (1994).
[4] J. De Rosny, Ph.D. Thesis, Université Paris VI, 2000.
[5] P.M. Morse and H. Feshback, Methods of Theoretical Physics, Feshback Publishing, 1981.
[6] A. Derode, A. Tourin, J. D. Rosny, M. Tanter, S. Yon and M. Fink, Phys. Rev. Lett. **90**, 014301-1 (2003).
[7] H. Moussa, A. Cozza and M. Cauterman, IEEE EMC Symposium, Austin, Texas (2009).
[8] C.L. Holloway, D.A. Hill, J.M. Ladbury, P.F. Wilson, G. Koepke and J. Coder, IEEE Trans. on Antennas and Propagation **54**, 3167 (2006).
[9] H. Weyl, Math. Ann. **71**, 441 (1912).
[10] D.A. Hill, IEEE Trans. on Electromagnetic Compatibility **40**, 209 (1998).
[11] A.I. Khuri, Advanced Calculus with Applications in Statistics, Wiley-Interscience, 2002.
[12] A. Leon-Garcia, Probability, Statistics, and Random Processes for Electrical Engineering, Prentice-Hall, 2008.
[13] A. Derode, A. Tourin and M. Fink, Phys. Rev. E **64** (2001).

Increasing the Peak-Field Generation Efficiency of a Reverberation Chamber

Andrea Cozza

ABSTRACT

The use of time-reversal techniques has been shown to allow focusing energy in a spot about half a wavelength wide. The fact of being able to concentrate energy into a reduced volume of space implies higher power densities and, ultimately, higher field levels. The use of this feature for improving the ability of a reverberation chamber in converting energy into high-intensity fields is investigated here. Experimental results are compared to those predicted by a simple asymptotic model, revealing the role played by losses and frequency bandwidth and how the performance of time-reversal techniques depends on these parameters.

I. INTRODUCTION

Among the several advantages presented by reverberation chambers (RCs), a special place is certainly held by their ability to produce high-intensity electromagnetic fields from relatively low-power sources. The standard harmonic excitation of an RC leads to a statistically uniform spreading of the electromagnetic energy over the entire volume of the cavity, essentially because of the fact that the cavity resonances are excited in an incoherent way. This implies that of all the energy stored in an RC driven by a continuous wave (CW) harmonic signal, only a fraction can be used for the "aggression" of the equipment under test (EUT). But while carrying out Electromagnetic Compatibility tests, as well as other types of radiated tests in RC, it would be typically more useful to be able of concentrating energy only over the EUT. This scenario can be modified thanks to recent advances brought by time-reversal techniques [1]: as a matter of fact, this approach allows to concentrate a bigger share of energy around and towards the EUT, thus increasing the efficiency of the RC as a high-intensity field generator for equipment testing.

In this letter, we prove that higher field-generation efficiencies are indeed made possible by using non-harmonic, time-reversal-based signals; we focus on how the physical parameters of the RC (quality factor Q, signal bandwidth, etc.) affect the performance of time-reversal driven RCs. To this end, we propose a simple asymptotic model capable of predicting the average improvement brought by time-reversal techniques over the standard use of RCs. Its validity is checked against experimental results obtained in an actual RC.

II. PEAK-FIELD GENERATION EFFICIENCY

For the purpose of our analysis the reverberation chamber will be represented as a black-box linear system. To this end, the vector electric field $\mathbf{E}(f)$ generated at a certain position, will be described as

$$\mathbf{E}(f) = X(f)\mathbf{\Phi}(f) = X(f)\left(\begin{array}{ccc}\phi_1 & \phi_2 & \phi_3\end{array}\right)^{\mathrm{T}} \qquad (1)$$

where $X(f)$ is the power-wave applied at the input port of the antenna exciting the chamber and $\phi_p(f)$ is the transfer function related to the p-th Cartesian component of the E field. Two cases will be considered for the excitation of the system: 1) $X_{\mathrm{CW}}(f)$, a harmonic steady-state signal of frequency f_c, with peak amplitude A, and 2) $X_{\mathrm{TR}}(f) = P(f)\phi_p^\star(f)$, with $P(f)$ the spectrum of a pulse signal $p(t)$, covering a bandwidth B_T around the central frequency f_c. This latter case, i.e., of a time-reversal-driven excitation, leads to the generation of a pulse approximating $p(t)$ [2], dominated by the field component along the p-th dimension [3]. Defining $p(t)$ as to attain its peak value at $t = 0$, the peak field generated by applying $X_{\mathrm{TR}}(f)$ is, in time-domain,

$$\max_t \|\mathbf{e}_{\mathrm{TR}}(t)\| = \|\mathbf{e}_{\mathrm{TR}}(0)\| = 2\int_{B_T} P(f)|H_p(f)|^2 \mathrm{d}f \qquad (2)$$

having carried out the integral over the positive-frequency region of the spectrum. Conversely, $X_{\mathrm{CW}}(f)$ yields a non-polarized field, whose peak value is given by

$$\max_t \|\mathbf{e}_{\mathrm{CW}}(t)\| = A\|\mathbf{\Phi}(f_c)\| \quad . \qquad (3)$$

Before being compared, the peak fields obtained through these two approaches need to be normalized to the energy $\mathcal{E}$ that is necessary to apply for their generation, thus leading to the definition of the peak-field generation efficiency

$$\eta = \frac{\max_t \|\mathbf{e}(t)\|^2}{\mathcal{E}} \quad . \qquad (4)$$

In the case of a harmonic excitation, 95 % of the steady-state amplitude is attained after a period equal to 3τ, with $\tau = Q/(\pi f_c)$ the average time-constant of the RC, Q being the average quality factor of the RC at f_c. Hence, an average applied energy

$$\mathcal{E}_{\mathrm{CW}} = \frac{3}{2}\frac{A^2 Q}{\pi f_c} \qquad (5)$$

which leads to

$$\eta_{\mathrm{CW}} = \frac{2}{3}\frac{\pi f_c}{Q}\|\mathbf{\Phi}(f_c)\|^2 \quad . \qquad (6)$$

Assuming an ideal reverberating chamber [4], the average quadratic field amplitude would be evenly distributed along the three field components, so that introducing the quadratic average $\phi_{\mathrm{av}}^2(f_c)$

$$\mathrm{E}\left[|\phi_p(f_c)|^2\right] = \phi_{\mathrm{av}}^2(f_c) \quad \forall p \in [1,3] \quad , \qquad (7)$$

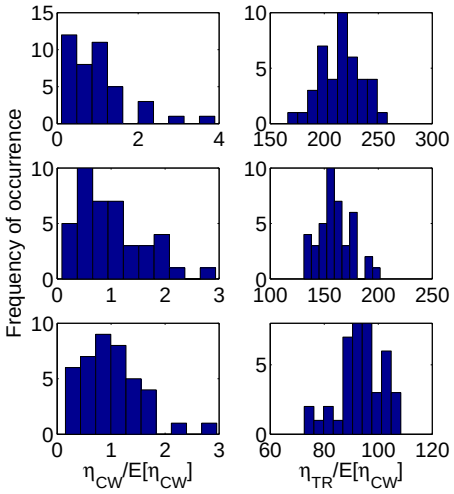

Fig. 1. Frequencies of occurrence distributions of η_{CW} (left column) and η_{TR} (right column), as obtained from transfer functions measured over a bandwidth $B_T = 100$ MHz, at a central frequency $f_c = \{1.0, 1.5, 2.0\}$ GHz (top to bottom, respectively). All the results have been normalized to the average values of η_{CW}.

yields

$$\mathrm{E}\left[\eta_{\mathrm{CW}}\right] = \frac{2\pi f_c}{Q}\phi_{\mathrm{av}}^2(f_c) \quad . \tag{8}$$

Conversely, time-reversal deals with a finite-energy excitation

$$\mathcal{E}_{\mathrm{TR}} = 2\int_{B_T} |X_{\mathrm{TR}}(f)|^2 \mathrm{d}f = 2\int_{B_T} |P(f)|^2 |\phi_p(f)|^2 \mathrm{d}f \quad , \tag{9}$$

so that its efficiency is given by

$$\eta_{\mathrm{TR}} = 2\frac{\left(\int_{B_T} P(f)|\phi_p(f)|^2 \mathrm{d}f\right)^2}{\int_{B_T} |P(f)|^2 |\phi_p(f)|^2 \mathrm{d}f} \quad . \tag{10}$$

Definitions (6) and (10) allow assessing how these two ways of using RCs manage to convert the same amount of energy into a peak field, just by knowing the transfer function between the excitation antenna and the E field component at a point of interest. It is therefore sensible to define the gain in the average peak-field efficiency $G = \mathrm{E}\left[\eta_{\mathrm{CW}}\right]/\mathrm{E}\left[\eta_{\mathrm{TR}}\right]$. Applying Cauchy-Schwarz inequality to (10) yields the following bound

$$\mathrm{E}\left[\eta_{\mathrm{TR}}\right] \leq 2\mathrm{E}\left[\int_{B_T} |\phi_p(f)|^2 \mathrm{d}f\right] = 2\int_{B_T} \phi_{\mathrm{av}}^2(f) \mathrm{d}f \quad . \tag{11}$$

This results in an equality for a constant $P(f)$. The term under the integral sign is the same as in (7) and assuming it to be constant over the entire bandwidth of the pulse $p(t)$, we obtain

$$G \leq \frac{B_T Q}{\pi f_c} \quad . \tag{12}$$

f (GHz)	B_T (MHz)	G	$\frac{B_T Q}{\pi f_c}$	$\frac{(\sigma/\mu)_{\mathrm{CW}}}{(\sigma/\mu)_{\mathrm{TR}}}$	Q
1.0	25	60	45	7.7	5700
	50	116	91	9.3	
	100	218	182	11.9	
1.5	25	39	34	6.3	6300
	50	80	68	7.0	
	100	161	135	7.7	
2.0	25	24	25	6.5	6300
	50	47	50	7.6	
	100	95	100	8.5	

TABLE I
COMPARISON OF THE EFFICIENCY GAIN G ASSESSED FROM EXPERIMENTAL DATA AND PREDICTED BY (12). ONLY THE RESULTS FOR THE FIELD GENERATED ALONG THE x-AXIS ARE SHOWN FOR TIME-REVERSAL EXCITATION. THE RATIO OF THE NORMALIZED STATISTICAL DISPERSIONS IS SHOWN IN THE FIFTH COLUMN.

This result is of paramount importance, since it allows assessing in a very simple way how time-reversal techniques would improve the performance of RC. Furthermore, it is a tool for designing the use of such techniques, as soon as the Q of the RC is known. In the following experimental validation we will consider a constant $P(f)$, in order to meet the upper bound.

III. EXPERIMENTAL RESULTS

The performance predicted by (12) was tested against experimental results measured in Supélec's RC ($3.08 \times 1.84 \times 2.44$ m^3), using a log-periodic dipole antenna positioned near one corner of the chamber, with the dipoles of the antenna aligned along the vertical direction (z axis), while the direction of maximum gain was aimed at a corner. The electric field was sampled by means of an optical E-field probe, manufactured by Enprobe, model EFS-105. This probe is linearly polarized, so that three transfer functions were measured for the three Cartesian field components; to this effect, a styrofoam support was used. A grandtotal of 40 positions were considered, uniformly distributed over the lower half of the RC, measuring the three Cartesian transfer functions by means of a network analyzer over three sub-bandwidths of $B_T = 100$ MHz, centered around central frequencies f_c equal to 1, 1.5 and 2 GHz. Equations (6) and (10) were applied to each transfer function, obtaining the peak-field generation efficiencies; these results are presented in Fig. 1, where for each f_c, the average η_{CW} was set as reference, with all the results presented normalized to this value.

This procedure was then repeated with a reduced B_T, namely for 50 MHz and 25 MHz bandwidths, and the gain G was computed. The results summarized in Table I prove that (12), despite its simplicity, allows assessing quite accurately the improvement in peak-field generation efficiency when adopting time-reversal techniques. The agreement is stronger at higher frequencies, where the field statistics in the RC are closer to an ideal reverberating medium [4]. Table I also demonstrates another interesting feature: time-reversal-driven RCs generate peak fields that are affected by a statistical dispersion by far lower than for a harmonic excitation. This feature is related to the self-averaging properties of time-reversal techniques, as already pointed out in [5] and [6].

IV. Conclusions

We have proven that time-reversal techniques are an interesting alternative to the standard harmonic excitation of RCs, by showing that higher peak-field values can be generated from the same amount of energy. This feature was demonstrated experimentally and predicted by means of a simple asymptotic model. More reliable performances were also observed, with a strong reduction of the statistical dispersion of the peak-field amplitude.

References

[1] H. Moussa, A. Cozza, and M. Cauterman, "Directive wavefronts inside a time reversal electromagnetic chamber," in *IEEE EMC Symposium, Austin, Texas*, 2009.

[2] G. Lerosey, J. De Rosny, A. Tourin, A. Derode, G. Montaldo, and M. Fink, "Time reversal of electromagnetic waves," *Physical Review Letters*, vol. 92, no. 19, p. 193904, 2004.

[3] A. Cozza and H. Moussa, "Polarization selectivity for pulsed fields in a reverberation chamber," unpublished, currently submitted to Asia-Pacific EMC Symposium 2010, Beijing.

[4] D. Hill, "Plane wave integral representation for fields in reverberationchambers," *IEEE Transactions on Electromagnetic Compatibility*, vol. 40, no. 3, pp. 209–217, 1998.

[5] J. Fouque, J. Garnier, G. Papanicolaou, and K. Solna, *Wave propagation and time reversal in randomly layered media*. Springer, 2007.

[6] A. Cozza, "Statistics of the Performance of Time Reversal in a Lossy Reverberating Medium," *Physical Review E*, accepted for publication.

Enforcing a Deterministic Polarization in a Reverberating Environment

Andrea Cozza and Houmam Moussa

Abstract

We report on a technique for generating coherently-polarized pulsed fields within highly reverberating environments. The ability of doing so is predicted theoretically, showing that the purity of the polarization of the electromagnetic field does not depend on the cross-polarization rejection of the source antenna, but only on the well-known depolarization properties of standard reverberation chambers. Experimental results are provided, proving that our theoretical model is sound, thus validating the first technique for generating a coherent arbitrarily polarized field in a reverberating environment.

I. Introduction

The success of standard reverberation chambers (RCs) as an Electromagnetic Compatibility facility is mainly due to two features: 1) the equipment under test is submitted by a large number of plane waves whose random directions of propagation and polarizations can be changed almost instantly through modal stirring, thus allowing the likely excitation of all of its weaknesses, 2) high-intensity fields can be generated from low-power sources. Nevertheless, the field they generate cannot be set in a deterministic way, and only its statistical moments are known [1]. In many applications it would be useful to be able to enforce a deterministic polarization, while keepipng point 2). This is unfeasible in standard RCs, due to the strongly incoherent nature of the field polarization. This notwithstanding, time-reversal techniques have been proven to be capable of enforcing deterministic properties in intrinsically complex and random media, as long as losses are low and the system is time invariant [2]. An example of this ability is given in Fig. 1, where a pulsed field is transmitted through a reverberation chamber, and compared to the desired waveform. In this paper, we prove for the first time that polarization coherence can also be reinstated, showing that it can be controlled with no limitations by simply modifying the excitation signal applied to the transmitting antenna, thus allowing a real-time coherent control of the field, with no need of either mechanical movements, or of antenna arrays.

II. Asymptotic polarization properties

We consider the same setup as for standard RC applications, i.e., a transmitting antenna placed within the RC in order to excite a field distribution. The vector electric field $\mathbf{E}(f,\mathbf{r})$ measured at any point $\mathbf{r}$ inside the RC can then be related to the signal $X(f)$ applied to the antenna as

$$\mathbf{E}(f,\mathbf{r}) = X(f)\mathbf{\Phi}(f,\mathbf{r}) = X(f)\begin{pmatrix}\Phi_x & \Phi_y & \Phi_z\end{pmatrix}^{\mathrm{T}}(f,\mathbf{r}) \quad , \tag{1}$$

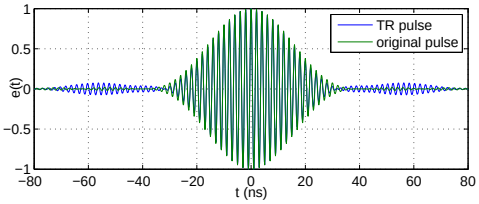

Fig. 1. An example of the ability of time-reversal techniques to generate coherent pulses in a reverberating environment. The blue curve represents the pulse received at a given location in a RC when applying time-reversal techniques, as computed by means of an experimentally measured transfer function. The green curve is the original pulse to be transmitted. The two peak-normalized curves are indistinguishable around the peak region.

where $\mathbf{\Phi}(f,\mathbf{r})$ is a vector transfer function, made up of three scalar transfer functions related to each Cartesian polarization component; these will be referred to as $\Phi_i(f,\mathbf{r})$ with $i = 1,...,3$ for, respectively, the x, y and z components. It is known that for an overmoded RC, the $\Phi_i(f,\mathbf{r})$ transfer functions are submitted to the following orthogonality condition [3]:

$$\mathrm{E}\left[\Phi_i(f,\mathbf{r})\Phi_j^{\star}(f,\mathbf{r})\right] = C\delta_{ij} \quad , \tag{2}$$

where $\mathrm{E}[\cdot]$ is the expected value operator and C is a normalization constant. This condition is satisfied only when averaging over the entire space of the random realizations of the transfer functions, e.g., such as when applying mode-stirring techniques. By recalling the modal theory underpinning the resonant phenomena occurring in an RC, a generic scalar transfer function can be expressed as

$$\Phi(f) = \sum_{i=1}^{M} \gamma_i \psi_i(f) \tag{3}$$

where $\psi_i(f)$ is the frequency response of the i-th resonant mode supported by the RC, centered around the frequency f_i, while $\gamma_i \in \mathbb{C}$ models how it is excited. Equation (3) is defined over a bandwidth B_T centered around f_0, where the RC supports M modes. Let us now assume that the $\{f_i\}$ and $\{\gamma_i\}$ are ergodic random processes, so that the average ensemble operator can be approximated through the arithmetic mean as applied to the different modes defining any transfer function. Recalling (2), the law of large numbers would then imply that

$$\lim_{M\to\infty} \int_{B_T} \Phi_i(f)\Phi_j^{\star}(f)\mathrm{d}f = M\mathrm{E}\left[\Phi_i(f_0)\Phi_j^{\star}(f_0)\right] \quad , \tag{4}$$

considering the equality as a convergence in probability. Equation (4) is the cornerstone of the proposed method, since

it implies that the same performance that would be obtained only by averaging over a large number of random realizations, can be fairly approximated when using wide-band signals in a single deterministic configuration, provided that the RC be in an overmoded state. This feature is in particular related to the self-averaging properties of time-reversal, as investigated in [2].

Having introduced ergodicity and (4), we can now describe how a coherent deterministic polarization can be enforced. Let us consider an excitation signal $X_{\mathrm{TR}}(f)$ defined as

$$X_{\mathrm{TR}}(f) = G(f) \sum_{i=1}^{3} p_i \Phi_i^\star(f) = G(f) \mathbf{\Phi}^{\mathrm{H}} \mathbf{p} \quad , \qquad (5)$$

where $G(f)$ is the spectrum of the pulse $g(t)$ to be generated at $\mathbf{r}$, with bandwidth B_T, and H is the Hermitian operator, while $\mathbf{p} = (p_1 \; p_2 \; p_3)^{\mathrm{T}}$ is a vector containing the complex weights of the desired polarization pattern to be enforced. Applying the signal (5) to (1) yields a received field

$$\mathbf{E}_{\mathrm{TR}} = G \mathbf{\Phi} \mathbf{\Phi}^{\mathrm{H}} \mathbf{p} \quad , \qquad (6)$$

having dropped the function arguments for the sake of simplicity. Since we are rather interested in the time-domain field, and especially over the peak of the pulse at $t = 0$, we get

$$\mathbf{e}_{\mathrm{TR}}(0) = \int_{-\infty}^{+\infty} G \mathbf{\Phi} \mathbf{\Phi}^{\mathrm{H}} \mathbf{p} \mathrm{d}f = \sqrt{\boldsymbol{\mathcal{E}}} \boldsymbol{\rho} \sqrt{\boldsymbol{\mathcal{E}}} \mathbf{p} \quad , \qquad (7)$$

having introduced the energy matrix $\boldsymbol{\mathcal{E}} = \mathrm{diag}\{\mathcal{E}_1, ..., \mathcal{E}_3\}$, with

$$\mathcal{E}_i = \int_{-\infty}^{+\infty} G |\Phi_i|^2 \mathrm{d}f = 2 \int_{B_T} \mathrm{Re}\left\{G\right\} |\Phi_i|^2 \mathrm{d}f \qquad (8)$$

and the polarization matrix $\boldsymbol{\rho}$, whose elements are defined as

$$\rho_{ij} = \frac{2 \int_{B_T} \mathrm{Re}\left\{G \Phi_i \Phi_j^\star\right\} \mathrm{d}f}{\sqrt{\mathcal{E}_i \mathcal{E}_j}} \quad . \qquad (9)$$

By applying (4), it can be proven that

$$\lim_{M \to \infty} \boldsymbol{\rho} = \mathrm{E}\left[\boldsymbol{\rho}\right] = \mathbf{1} \quad , \qquad (10)$$

where $\mathbf{1}$ is the identity matrix. Recalling that in an overmoded RC the field is statistically isotropic, i.e., $\mathrm{E}\left[|\Phi_i|^2\right] = \mathrm{E}\left[|\Phi_j|^2\right], \forall i, j$, by applying (4) to this last equation too, $\lim_{M \to \infty} \mathcal{E}_i = \mathcal{E}_0, \forall i$. We can hence claim that

$$\lim_{M \to \infty} \mathbf{e}_{\mathrm{TR}}(0) = \mathcal{E}_0 \mathbf{p} \qquad (11)$$

This result proves that without invoking any statistical averaging process, i.e., no stirring, the pulsed field generated through time-reversal converges, for a sufficiently overmoded RC, to a deterministic coherently polarized field, directly controlled by the weight vector $\mathbf{p}$, and this for any static configuration. In other words, the Φ_i functions approximate an orthogonal basis. This result has been derived as an asymptotic property, so that the actual received field is expected to fulfill (11) on average, while presenting a statistical dispersion inversely dependent on M.

f	1.0 GHz	1.5 GHz	2.0 GHz
$\mathcal{E}_1$	0.94 (0.12)	0.96 (0.13)	0.96 (0.11)
$\mathcal{E}_2$	0.92 (0.13)	0.94 (0.12)	0.97 (0.12)
$\mathcal{E}_3$	1.00 (0.14)	1.00 (0.14)	1.00 (0.14)
ρ_{12}	0.025 (0.056)	0.003 (0.061)	0.013 (0.074)
ρ_{13}	0.014 (0.045)	0.004 (0.061)	0.018 (0.076)
ρ_{23}	-0.021 (0.068)	-0.024 (0.070)	-0.012 (0.081)
M_e	570	420	315

TABLE I
STATISTICS OF THE PERFORMANCE IN PULSE TRANSMISSION AS OBTAINED FROM THE COLLECTED EXPERIMENTAL DATA. THE AVERAGE VALUES ARE PRESENTED FOR THE ENERGY MATRIX AND THE OFF-DIAGONAL TERMS OF MATRIX $\boldsymbol{\rho}$, WITH STANDARD DEVIATIONS GIVEN IN PARENTHESIS.

III. EXPERIMENTAL RESULTS

Experimental validation tests were carried out in Supélec's RC ($3.08 \times 1.84 \times 2.44$ m^3), using a log-periodic dipole antenna (LPDA) positioned near one corner of the chamber, with the dipoles of the antenna aligned along the vertical direction (z axis), while the direction of maximum gain was aimed at the corner. Concerning the receiving transducer, an all-optical E-field probe was used, manufactured by Enprobe, model EFS-105. This phase-preserving probe is linearly polarized, with a cross-polarization rejection of about 40 dB, thus allowing to measure accurately the cross-polarization of the received pulse. The probe was mounted over a styrofoam support, designed in order to ensure the measurement of the three Cartesian components of the E field. A total of 50 positions were considered, scattered uniformly over the lower half of the RC; for each of these, the transfer functions between the LPDA and the probe was measured along the three polarizations, by means of a vector network analyzer. Three frequencies were considered for f_0, namely 1, 1.5 and 2 GHz, considering a bandwidth $B_T = 100$ MHz. For all the f_0, M is expected to be higher than 1000, as predicted by Weyl's formula. The pulse $g(t)$ was set to be a Gaussian pulse, with a -20 dB frequency bandwidth B_T.

From the spectrum of $g(t)$ and the transfer functions, the energy matrix and the polarization matrix $\boldsymbol{\rho}$ were computed, as defined in (8) and (9), respectively. We first checked the validity of the isotropy assumption, by computing how the energy received along the three polarizations is distributed. The first two statistical moments were computed, and are shown in Table I, proving that this assumption makes sense for the three frequencies we chose, with a maximum error on the average energy of about 8 % and an average one of 5 %. A similar statistical analysis was carried out on the off-diagonal elements of $\boldsymbol{\rho}$: the results shown in Table I prove that indeed the field components orthogonal to the originally addressed one are on average very close to zero. These results prove that the ergodic assumption is indeed valid. The fact that the average is not exactly null is due to mechanical tolerances in the tracks of the styrofoam support housing the probe: a tilt of its axis of about 1 degree leads to a 0.02 cross-polarization, a value that closely matches the actual averages shown in Table I. Time-domain results are shown in Fig. 2, showing how the three Cartesian linear polarizations can be separately

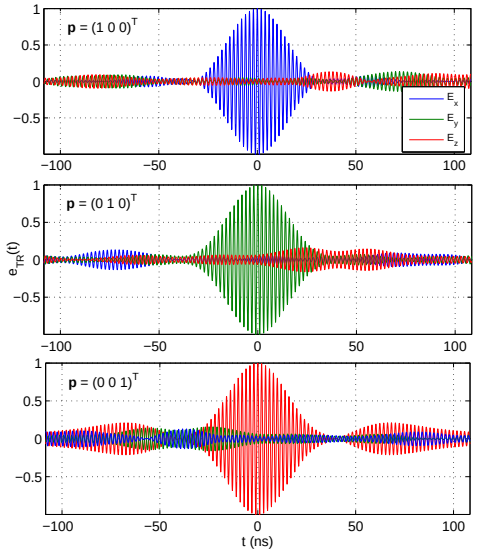

Fig. 2. The field components obtained from experimental results measured at one position, for a Gaussian pulse at 1.5 GHz. Each plot refers to a weight vector $\mathbf{p}$ corresponding to one Cartesian direction. Top to bottom, the x, y and z components of the fields are ideally the only excited when the pulse attains its peak value.

addressed by means of the proposed method.

Concerning the standard deviation of the rejection, it is directly related to the residual error when considering a finite number of modes. Nevertheless, it does not change much when doubling f_0. This is due to the limited number of degrees of freedom actually available when the quality factor Q of the modes is finite: it was indeed demonstrated in [4] that of M modes available, a maximum of about $M_e = B_T Q/f_0$ are actually independent. This interpretation is supported by the inverse trends followed by the standard deviation and M_e, as shown in Table I.

IV. Conclusions

We have introduced the first method for enforcing a coherent and deterministic polarization upon pulsed fields transmitted in a highly-reverberating environment. This novel approach is based jointly on the properties of time-reversal techniques and the strong depolarization experienced in reverberating media. In particular, we have proven that the polarization of the field can be controlled in a precise way by simply operating on the signal applied to the excitation antenna. Experimental results support this analysis, demonstrating that actual applications can be defined, such as high-power microwave testing with real-time polarization modification.

References

[1] D. Hill, "Electromagnetic theory of reverberation chambers," *NIST technical note*, no. 1506, 1998.

[2] J. Fouque, J. Garnier, G. Papanicolaou, and K. Solna, *Wave propagation and time reversal in randomly layered media*. Springer, 2007.

[3] D. Hill, "Plane wave integral representation for fields in reverberationchambers," *IEEE Transactions on Electromagnetic Compatibility*, vol. 40, no. 3, pp. 209–217, 1998.

[4] A. Cozza, "Statistics of the Performance of Time Reversal in a Lossy Reverberating Medium," *Physical Review E*, accepted for publication.

Emulating an Anechoic Environment in a Wave-Diffusive Medium through an Extended Time-Reversal Approach

Andrea Cozza, *Member*

***Abstract*—A generalized time-reversal (TR) technique for the generation of coherent wavefronts within complex media is presented in this paper. Although completely general, this method is primarily considered for testing purposes herein, where an equipment under test is submitted to a series of impinging wavefronts with varying features. Electromagnetic compatibility, antenna testing as well as telecommunications facilities where complex-wavefront schemes (e.g., multi-path configurations) are required, could benefit from the proposed approach. The main advantages and limitations of current standard TR approaches are reviewed in this respect, exposing their inadequacy for this particular context. The proposed alternative technique, named Time-Reversal Electromagnetic Chamber (TREC) is introduced and studied by means of a formal theoretical analysis, showing how a reverberation chamber (RC) supporting a diffused-field condition can be operated as a generator of deterministic pulsed wavefronts. The TREC is demonstrated to be capable of generating arbitrary wavefronts with a remarkable accuracy, allowing to revisit the RC as a deterministic facility: the main advantages of RCs and anechoic ones are merged, leading to a new facility capable of potentially generating in real-time pulsed wavefronts while using low input energies, without requiring neither mechanical displacements nor any special features of the sources.**

***Index Terms*—Cavities, random media, test facilities, time-domain measurements, dyadic Green's functions, wave focusing, time reversal.**

I. Introduction

THE idea of assessing the response of an equipment under test (EUT) to external electromagnetic radiations is fundamentally dependent on the availability of facilities capable of generating suitable testing scenarios in a reproducible and controllable manner. The most classical example is certainly the case of a locally-plane wave, typically assumed to propagate within an anechoic environment to simulate a free-space configuration. A number of solutions have been developed in the past, giving rise to such facilities as open-area test sites, compact ranges, TEM cells, and the like. All of these available solutions are somehow based on efforts to simulate an anechoic environment, a task often achieved by means of anechoic chambers (ACs), which rely on the use of electromagnetic absorbing materials.

Among the several reasons for choosing this type of environment is the simplicity of interpretation of the results of a test: having made use, at least ideally, of a single plane wave, the field scattered by the EUT, the currents induced over its external surface or at its interior are all straightforwardly linked to a single and well-defined external excitation.

Such an approach shows its limitations as soon as a large number of testing configurations is required (changing direction of arrival, polarization, etc.), thus leading to the need of complex and time-consuming mechanical displacements of the source or of the EUT. Albeit light-weight antennas and EUTs can be easily moved around, the case of large EUTs such as those considered in the aerospace industry (e.g., satellites, airplanes) or in electromagnetic compatibility (e.g., vehicles) requires complex mechanical solutions. A class of testing configurations in itself where a similar problem is observed is that involving the emulation of complex propagation environments, such as for telecommunication tests: the need to reproduce multi-path or fading environments comes with

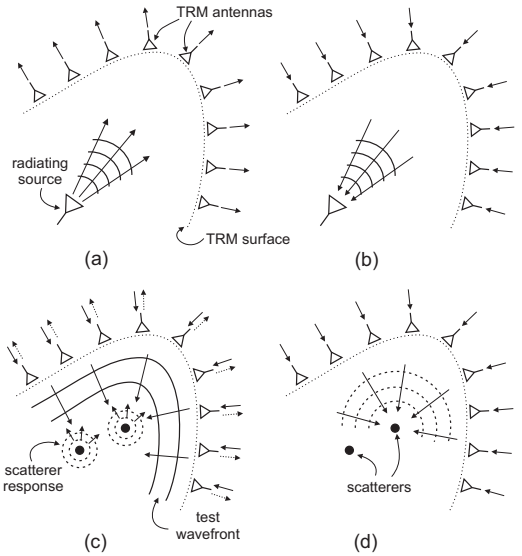

Fig. 1: A schematic representation of the two main TR techniques currently available: (a)-(b) TR of a radiating source; (c)-(d) selective focusing over a point scatterer by means of the DORT approach.

A. Cozza is with the Département de Recherche en Électromagnétisme, Laboratoire des Signaux et Systèmes (L2S), UMR 8506 SUPELEC - Univ Paris-Sud - CNRS, 3 rue Joliot-Curie, 91192 Gif-sur-Yvette, France. Contact e-mail: andrea.cozza@supelec.fr.

expensive solutions in ACs [1], [2].

For all these reasons, reverberation chambers (RCs) have gained a wide following even outside the electromagnetic compatibility (EMC) community, especially for the need of assessing the performances of telecommunication devices for data-transmission schemes through complex environments [3]. Here, the logic of the test is turned upside-down: the testing conditions do not require anymore moving the sources or the EUT, since it is considered that RCs can provide a testing scenario where a large number of plane waves propagate along ideally all possible directions [4], [5], [6]. The well-known price to pay for this simplification is the loss of intuitive understanding of the undergoing physical phenomena leading to the test results, and the important issue of having hardly repeatable testing conditions. We acknowledge the fact that the average testing conditions are repeatable, but the exact configuration is actually not.

As opposed to these two scenarios, in the last few years it has been shown that the preconceived idea of reverberating cavities as capable of supporting only narrow-band excitations and incoherent fields should be revisited. Time-reversal (TR) techniques have been shown to be capable of generating coherent wavefronts that can behave in a similar way to anechoic environments [7], [8], [9]. The availability of such a new way of using RCs is particularly exciting because it could be a way of accessing the main features of RCs and ACs at the same time, within the same facility, by taking advantage of a high energy efficiency while being able to generate simpler and more easily predictable wavefronts. Unfortunately, as we argue in the next two sections, currently available TR techniques are unsuitable for testing purposes, since they rely on a fixed two-step procedure that does not allow straightforwardly controlling the features of the generated wavefronts.

A more powerful technique disposing of these limitations was introduced in [10] and experimentally validated in [8]. It is based on the use of synthetic sources, leading to a generalized technique for the generation of time-reversed wavefronts whose features can be controlled in a very simple manner. In this paper, we present a formal analysis of how the equivalence theorem, coupled to a phase conjugation technique allows generating arbitrary wavefronts within random propagation media characterized by weak spatial correlation. Our theory is first introduced for a general medium, requiring only linearity and reciprocity, while in a second time we focus on the specific case of a medium supporting a diffused field distribution, e.g., an overmoded reverberation chamber. The dyadic operator describing how a target wavefront will be modified on average by the proposed technique is derived, and numerical examples are provided to illustrate our results. No experimental result is provided, since they are already available in the literature [8], [11].

As opposed to previous works dealing with the focusing of time-reversed waves in complex media [9], the proposed method is not limited by the intrinsical inability of standard TR techniques to generate arbitrary wavefronts. A major result is the proof that reverberation chambers are not only capable of generating wideband pulsed fields, but in a more general way to generate in an accurate way arbitrary coherent wavefronts, through a simple procedure. Our analysis leads to the conclusion that a paradigm shift can be introduced in TR applications when dealing with reverberation chambers (or more generally with wave-diffusive media), since the parameters defining the wavefront can be changed in real-time by means of standard signal-processing techniques, thus introducing the possibility of high-speed testing in reverberation chambers and the generation of complex, but deterministic, propagation scenarios.

II. Time-reversed wavefronts

In this section we do not pretend to provide a thorough summary of TR, nor of all of its applications. A panoramic view of available TR applications is necessary in order to get a better grasp of the advances proposed in this paper.

TR is fundamentally the same technique previously known as phase conjugation, which originated in optics in the late 70's [12], primarily intended to compensate distortions (self-healing) in wavefronts propagating through complex media, particularly with the aim of focusing energy towards a given position in space. All of the applications of TR are based on the TR symmetry of Helmholtz equation, implying an invariance of its solutions to a change of sign in the time variable.

TR applications typically exploit this property by coupling it to Huygens' principle: as depicted in Figs. 1(a)-(b), we can define a two-step procedure where the first step involves a source of radiation generating a diverging wavefront *recorded* by an ideally continuous set of transducers (e.g., antennas) deployed over a closed surface Σ. These transducers are usually referred to, in the context of TR applications, as a TR mirror (TRM) [13]. Coupling Huygens' principle to the TR symmetry of Helmholtz equation implies that by exciting the transducers with the time-reversed version of the signals received during the first phase, the TRM will generate an ideally perfect replica of the original wavefront, but this time converging back at the source, as a consequence of our inverting the direction of evolution of the time variable [13].

An important step in our proposal is the passage from the usually open media addressed when using the paradigm we just recalled, towards bounded ones, e.g., closed cavities. This issue was studied in several papers, e.g., [14], [15], [16], [11], where it was shown that the presence of reflective boundaries allows reducing the number of TRM transducers to just a few, typically one: this number is to be compared with the inevitably higher number of sources needed in wavefront synthesis in free-space environments [1], [2], a direct consequence of the spatial-sampling theorem [17]. The use of TR signals also allows the generation of short pulses within a reverberation chamber, which is of practical interest when testing EUTs closely exposed to high-power radar pulses [18].

The second approach to generating TR wavefronts is the DORT technique [19], [20]: while standard TR considers that what will be the target of the focusing wave during the second phase (Fig. 1(b)), needs to be a source during the first one (Fig. 1(a)), the DORT allows avoiding the target to be a source, whenever it behaves as a *point* scatterer, i.e., as a passive device that will respond with a spherical

wavefront (Fig. 1(d)) to an externally excited locally plane wave (Fig. 1(c)). The DORT may appear to have a potential for testing applications, particularly when dealing with passive EUTs that cannot be operated as active sources. In fact, as we argue in the next section, the DORT could hardly be applied for testing purposes.

The problem with all of these methods is that in the available literature TR applications always aim at producing a focusing wavefront at some position in space. The motivation is never the generation of a wavefront per se: the reason why focusing is under consideration is typically either a clearer transmission of signal through complex media at a given position (e.g., a receiver in sonar [21] or telecommunication schemes [22]) or to improve imaging techniques [19], [20], [23]. As we will argue in the next section, this is not compatible with EUT testing, since EUTs are often electrically large and present distributed scattering features rather than localized ones.

III. TR FROM A TESTING POINT OF VIEW

Following this short discussion about current TR techniques, one may think that it could be interesting to implement them within RCs for at least two reasons: 1) to provide a solution to the problem of pulsed field generation; 2) as a way of more effectively generating high-intensity fields within a reverberation chamber. Such points are apparently useful only in the context of EMC, where the absolute intensity of the testing wavefront is of paramount importance. As it will be shown in the rest of this paper, the proposed generalized approach provides a more powerful rationale for the idea of coupling TR to reverberation chambers; as a matter of fact, a further motivation is the ability to control the generated wavefront without any mechanical displacement of the sources, nor any need for complex sources.

Before passing to the advantages brought in by our method, let us us start by looking at the shortcomings of TR from a testing point of view. If the standard paradigm depicted in Figs. 1(a)-(b) were used, how to generate in the first place the diverging wavefront (first phase) that will be time-reversed in order to be focused over the EUT? The eventual solution of applying auxiliary sources over the EUT in order to radiate the first-phase wavefront are bound to fail, since the standard paradigm would require passing through the two phases we have recalled in the previous section: hence, as soon as a new direction of incidence is to be established, the auxiliary sources would need to be moved over the EUT, and a new cycle of test would start all over. This is hardly acceptable, as it would require an increased number of manipulations with respect to tests carried out in anechoic chambers.

A potential solution could be envisaged by recalling the DORT paradigm (Figs. 1(c)-(d)): in this case, it would not be possible to chose whatever direction of incidence on the EUT, as the DORT can merely select a wavefront among the scattering responses of the EUT. If this response is (as often is the case) dominated by a few bright points [24], the choice of the test wavefront will be limited to the intrinsical response of the EUT, rather than satisfying the need to identify the responses of the EUT to a varying, but predefined, testing wavefront.

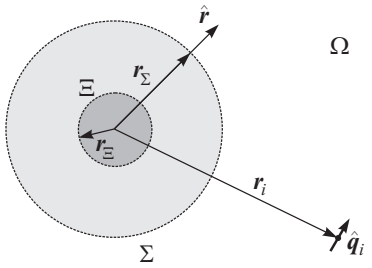

Fig. 2: Configuration for the application of Love's equivalence theorem. Equivalent electric and magnetic currents are defined over the surface Σ, representing the wavefront $\boldsymbol{\mathcal{E}}_{\mathrm{wf}}(\boldsymbol{r},t)$ that would have been generated by a synthetic source contained in the volume bounded by the surface Ξ. These elements are embedded into a complex medium Ω.

The problem is that TR techniques in their present state are not suitable for EUT testing: they are actually mismatched to practical needs, as they have been designed to deal with mainly point scatterers, rather than electrically extended ones, as it is often the case when dealing with real-life EUTs, and this goes without taking into account the issue of polarization, which leads to an even more complex scenario when compared to the scalar-wave propagation and scattering undergoing in acoustics.

The solution to this mismatch is to shift our attention from the idea of focusing over a point to the idea of generating a controllable wavefront. By this last term, we consider the ability to control all of the parameters defining a wavefront, e.g., its time-dependence, polarization, directivity and direction of arrival. This reflection has motivated our proposing an alternative approach based on the use of synthetic sources (section IV), leading to a new paradigm for TR that is not only suitable for EMC purposes but also brings in new advantages for any test based on submitting an EUT to impinging wavefronts. This approach, that we have named the Time-Reversal Electromagnetic Chamber (TREC) was originally introduced in [10] while the first experimental validation was proposed in [8].

IV. A GENERALIZED TR TECHNIQUE

Our analysis takes its start from the standard two-step approach recalled in section II. The application we envision is peculiar in the sense that we do not consider the usual retrieval of the wavefront generated by an elementary source, but rather a generic wavefront. In this respect, we introduce the function $\boldsymbol{\mathcal{E}}_{\mathrm{wf}}(\boldsymbol{r},t)$ describing the space-time dependence of the wavefront we aim at generating, i.e., the target wavefront: in fact, $\boldsymbol{\mathcal{E}}_{\mathrm{wf}}(\boldsymbol{r},t)$ is the diverging wavefront that would be generated in a free-space environment, whereas the TREC will rather be used in order to deliver, ideally, $\boldsymbol{\mathcal{E}}_{\mathrm{wf}}(\boldsymbol{r},-t)$, i.e., the converging version of the wavefront, used to test the EUT response in a number of potential applications. We are not

interested in specifying the nature of the source generating the original $\boldsymbol{\mathcal{E}}_{\rm wf}(\boldsymbol{r},t)$ wavefront, nor is it necessary: the wavefront $\boldsymbol{\mathcal{E}}_{\rm wf}(\boldsymbol{r},t)$ can be imagined as the result of an unspecified source, to be eventually found within a volume enclosed by the surface Ξ, introduced in Fig. 2. This surface will be assumed to be spherical for simplicity, with radius r_Ξ. Knowledge of the electrical dimension r_Ξ/λ provides a direct measure of the potential directivity of the wavefronts radiated by the source [25]. For reasons that will be clearer at the end of this section, we will refer to this source as the synthetic source.

The divergent wavefront thus radiated during the first phase can be regarded through the lens of Love's equivalence theorem [26]: by defining a closed surface Σ bounding the synthetic source (see Fig. 2), the sampling of the function $\boldsymbol{\mathcal{E}}_{\rm wf}(\boldsymbol{r},t)$ over Σ allows defining equivalent currents capable of exactly reproducing the same space-time dependence at any position outside Σ itself, independently from the eventual presence of an EUT.

Two assumptions will be introduced in order to simplify our analysis, with no loss of generality: the first one consists in regarding $\boldsymbol{\mathcal{E}}_{\rm wf}(\boldsymbol{r},t)$ over Σ as the far-field radiation of the synthetic source, while the second one is to assume that Σ be a spherical surface. The rationale for requiring a far-field radiation is twofold: first, our analysis will be greatly simplified, thanks to the simpler relationship existing between electric and magnetic fields, while the fact that time-reversed wavefronts are deprived of reactive components calls for the need to remove the reactive components off a wavefront before comparing it to the one generated at the end of the TR procedure, since only propagative components are conserved, as recalled in section II. The use of far-field wavefronts allows for a direct comparison of the target wavefront and the one actually generated by the proposed procedure.

According to these assumptions

$$\boldsymbol{\mathcal{H}}_{\rm wf}(\boldsymbol{r},t)=\frac{1}{\zeta_0}\hat{\boldsymbol{r}}\times\boldsymbol{\mathcal{E}}_{\rm wf}(\boldsymbol{r},t)\quad \boldsymbol{r}\in\Sigma, \tag{1}$$

where ζ_0 is the free-space wave impedance and $\hat{\boldsymbol{r}}$ is the radial unit vector coinciding with the outward pointing unit vector normal to Σ, as depicted in Fig. 2. As we are dealing with the generation of arbitrary wavefronts, and in particular pulsed ones, a time-domain description should be the final outcome of our analysis. Still, the intermediary steps of our analysis will be carried out in the frequency domain. We thus introduce the wavefront description for the electric field $\boldsymbol{E}_{\rm wf}(\boldsymbol{r},\omega)$ in Fourier frequency domain, defined as

$$\boldsymbol{E}_{\rm wf}(\boldsymbol{r},\omega)=\mathcal{F}\{\boldsymbol{\mathcal{E}}_{\rm wf}(\boldsymbol{r},t)\}, \tag{2}$$

where $\mathcal{F}\{\cdot\}$ is Fourier transform, with the magnetic-field spectrum similarly defined.

The equivalent electric and magnetic currents over Σ can thus be defined as

$$\boldsymbol{J}_e(\boldsymbol{r},\omega) = \boldsymbol{J}'_e(\boldsymbol{r},\omega)\delta(\boldsymbol{r}-\boldsymbol{r}_\Sigma) \tag{3a}$$
$$\boldsymbol{J}_m(\boldsymbol{r},\omega) = \boldsymbol{J}'_m(\boldsymbol{r},\omega)\delta(\boldsymbol{r}-\boldsymbol{r}_\Sigma), \tag{3b}$$

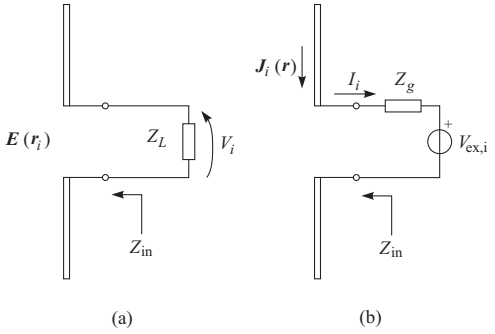

Fig. 3: Equivalent models of the TRM antennas used for the computation of the signals received during the first standard TR phase and the field generated by them in the second phase: (a) receiving-mode model; (b) transmission-mode model.

with

$$\boldsymbol{J}'_e(\boldsymbol{r},\omega) = -\frac{\boldsymbol{E}_{\rm wf}(\boldsymbol{r},\omega)}{\zeta_0} \tag{4a}$$
$$\boldsymbol{J}'_m(\boldsymbol{r},\omega) = \boldsymbol{E}_{\rm wf}(\boldsymbol{r},\omega)\times\hat{\boldsymbol{r}}. \tag{4b}$$

where $\boldsymbol{r}_\Sigma$ is a vector spanning the surface Σ and $\delta(\boldsymbol{r})$ is Dirac's delta distribution.

Given the distributions of electric and magnetic currents, the electric field $\boldsymbol{E}(\boldsymbol{r},\omega)$ they generate at any position within a propagation medium can be expressed by means of its dyadic Green's functions as

$$\boldsymbol{E}(\boldsymbol{r},\omega)=\int_\Sigma\tilde{\boldsymbol{G}}_{\rm ee}(\boldsymbol{r},\boldsymbol{r}',\omega)\cdot\boldsymbol{J}'_e(\boldsymbol{r}',\omega)\mathrm{d}^2\boldsymbol{r}'+\int_\Sigma\tilde{\boldsymbol{G}}_{\rm em}(\boldsymbol{r},\boldsymbol{r}',\omega)\cdot\boldsymbol{J}'_m(\boldsymbol{r}',\omega)\mathrm{d}^2\boldsymbol{r}'. \tag{5}$$

where the two dyadic functions $\tilde{\boldsymbol{G}}_{\rm ee}(\boldsymbol{r},\boldsymbol{r}',\omega)$ and $\tilde{\boldsymbol{G}}_{\rm em}(\boldsymbol{r},\boldsymbol{r}',\omega)$ refer to the Green's functions relating, respectively, electric and magnetic currents to the electric field.

The configuration depicted in Fig. 2 presents TRM antennas assimilable to elementary dipoles, positioned at $\boldsymbol{r}_i$ and oriented along $\hat{\boldsymbol{q}}_i$. These antennas will be operated in receiving and transmitting mode and can thus be described by means of the equivalent models shown in Fig. 3. In this framework, the electric field $\boldsymbol{E}(\boldsymbol{r}_i,\omega)$ related to the wavefront will eventually couple with them, leading to an output voltage $V_i(\omega)$

$$V_i(\omega)=\frac{Z_L(\omega)}{Z_L(\omega)+Z_{\rm in}(\omega)}\boldsymbol{E}(\boldsymbol{r}_i,\omega)\cdot\boldsymbol{h}_{e,i}(\omega), \tag{6}$$

where $\boldsymbol{h}_{e,i}(\omega)$ is the vector effective height of the TRM antennas

$$\boldsymbol{h}_{e,i}(\omega)=h_e(\omega)\hat{\boldsymbol{q}}_i, \tag{7}$$

having assumed all of the antennas to have an identical effective height $h_e(\omega)$.

As recalled in section II, TR applications require the output signals $V_i(\omega)$ to be time-reversed, or phase-conjugated in the frequency domain, and subsequently applied to the TRM

antennas. The TR of the $V_i(\omega)$ output signals would naturally require considering a delay T representing the duration of the first phase during which the output signals are recorded. This delay will be neglected in the rest of the paper, as it only leads to a phase-shift term shared by all of the output signals, with no impact on the results.

During the second phase of TR, the TRM antennas will be excited by means of the signals $V_{\mathrm{ex,i}}(\omega) = \bar{V}_i(\omega)$, where the overhead bar stands for phase conjugation. According to the equivalent model in Fig. 3(b), the antennas will be driven by a current $I_i(\omega)$

$$I_i(\omega) = -\frac{V_{\mathrm{ex,i}}(\omega)}{Z_g(\omega) + Z_{\mathrm{in}}(\omega)}, \tag{8}$$

leading to an equivalent electric-current density

$$\boldsymbol{J}_i(\boldsymbol{r}_i, \omega) = I_i(\omega)\boldsymbol{h}_e(\omega)\delta(\boldsymbol{r} - \boldsymbol{r}_i). \tag{9}$$

The electric field thus generated by each TRM antenna during the emission phase can be expressed as

$$\begin{aligned}\boldsymbol{E}_{\mathrm{TR,i}}(\boldsymbol{r}, \omega) &= \int_\Omega \tilde{\boldsymbol{G}}_{\mathrm{ee}}(\boldsymbol{r}, \boldsymbol{r}', \omega) \cdot \boldsymbol{J}_i(\boldsymbol{r}', \omega)\mathrm{d}^3\boldsymbol{r}' \\ &= h_e(\omega) I_i(\omega) \tilde{\boldsymbol{G}}_{\mathrm{ee}}(\boldsymbol{r}, \boldsymbol{r}_i, \omega) \cdot \hat{\boldsymbol{q}}_i.\end{aligned} \tag{10}$$

In order to simplify our notations, we introduce the electric and magnetic vector transfer functions

$$\boldsymbol{N}_{e,i}(\boldsymbol{r}, \omega) = \tilde{\boldsymbol{G}}_{\mathrm{ee}}(\boldsymbol{r}, \boldsymbol{r}_i, \omega) \cdot \hat{\boldsymbol{q}}_i \tag{11a}$$

$$\boldsymbol{N}_{m,i}(\boldsymbol{r}, \omega) = \tilde{\boldsymbol{G}}_{\mathrm{em}}(\boldsymbol{r}, \boldsymbol{r}_i, \omega) \cdot \hat{\boldsymbol{q}}_i, \tag{11b}$$

relating the electric or magnetic field observed at a generic position $\boldsymbol{r}$ to the signals applied to the input port of the i-th TRM antenna. They have units of $\Omega\mathrm{m}^{-2}$ and m^{-2}, respectively.

Inserting (5)-(8) into (10), and making use of (11), yields

$$\begin{aligned}&\boldsymbol{E}_{\mathrm{TR,i}}(\boldsymbol{r}, \omega) = \\ &- C(\omega)\left\{\int_\Sigma \boldsymbol{N}_{e,i}(\boldsymbol{r}, \omega)\bar{\boldsymbol{N}}_{e,i}(\boldsymbol{r}', \omega) \cdot \bar{\boldsymbol{J}}'_e(\boldsymbol{r}', \omega)\mathrm{d}^2\boldsymbol{r}'\right. \\ &\left.+ \int_\Sigma \boldsymbol{N}_{e,i}(\boldsymbol{r}, \omega)\bar{\boldsymbol{N}}_{m,i}(\boldsymbol{r}', \omega) \cdot \bar{\boldsymbol{J}}'_m(\boldsymbol{r}', \omega)\mathrm{d}^2\boldsymbol{r}'\right\}\end{aligned} \tag{12}$$

having exploited the spatial reciprocity of Green's functions, and thus of the vector transfer functions (11). The quantity $C(\omega)$ in (12) takes care of the electrical parameters of the TRM antennas

$$C(\omega) = \frac{|h_e(\omega)|^2}{Z_g(\omega) + Z_{\mathrm{in}}(\omega)} \frac{\bar{Z}_L(\omega)}{\bar{Z}_L(\omega) + \bar{Z}_{\mathrm{in}}(\omega)}. \tag{13}$$

It is noteworthy that the doublets of vector transfer functions under the integral signs are dyadic functions. Equivalent currents (4) can now be inserted, leading to

$$\begin{aligned}&\boldsymbol{E}_{\mathrm{TR,i}}(\boldsymbol{r}, \omega) = \frac{1}{\zeta_0}\int_\Sigma \boldsymbol{N}_{e,i}(\boldsymbol{r}, \omega)\bar{\boldsymbol{N}}_{e,i}(\boldsymbol{r}', \omega) \cdot \bar{\boldsymbol{E}}_{\mathrm{wf}}(\boldsymbol{r}', \omega)\mathrm{d}^2\boldsymbol{r}' + \\ &- \int_\Sigma \boldsymbol{N}_{e,i}(\boldsymbol{r}, \omega)\ \hat{\boldsymbol{r}}' \times \bar{\boldsymbol{N}}_{m,i}(\boldsymbol{r}', \omega) \cdot \bar{\boldsymbol{E}}_{\mathrm{wf}}(\boldsymbol{r}', \omega)\mathrm{d}^2\boldsymbol{r}'.\end{aligned} \tag{14}$$

having assumed excitation signals $V_{\mathrm{ex,i}}(\omega) = \bar{V}_i(\omega)/C(\omega)$.

This last result allows linking the space-time description of the target wavefront to the one actually generated after TR excitations are applied to the TRM antennas. Since we are interested in wave-diffusive media, the vector transfer functions (11) will be considered as random functions in section VI. The self-averaging property of TR [27], [28] implies that the wavefronts generated by a TREC converge towards their ensemble average, independently from the random realizations of Green's dyadic functions. This issue is discussed in Appendix B.

Hence, we introduce the average dyadic responses

$$\tilde{\boldsymbol{T}}_{\mathrm{ee,i}}(\boldsymbol{r}, \boldsymbol{r}', \omega) = \mathsf{E}\left[\boldsymbol{N}_{e,i}(\boldsymbol{r}, \omega)\bar{\boldsymbol{N}}_{e,i}(\boldsymbol{r}', \omega)\right] \tag{15a}$$

$$\tilde{\boldsymbol{T}}_{\mathrm{em,i}}(\boldsymbol{r}, \boldsymbol{r}', \omega) = \mathsf{E}\left[\boldsymbol{N}_{e,i}(\boldsymbol{r}, \omega)(\hat{\boldsymbol{r}}' \times \bar{\boldsymbol{N}}_{m,i}(\boldsymbol{r}', \omega))\right] \tag{15b}$$

$$\tilde{\boldsymbol{T}}_{\mathrm{i}}(\boldsymbol{r}, \boldsymbol{r}', \omega) = \frac{1}{\zeta_0}\tilde{\boldsymbol{T}}_{\mathrm{ee,i}}(\boldsymbol{r}, \boldsymbol{r}', \omega) - \tilde{\boldsymbol{T}}_{\mathrm{em,i}}(\boldsymbol{r}, \boldsymbol{r}', \omega), \tag{15c}$$

with $\mathsf{E}[\cdot]$ the ensemble-average operator. These functions are directly related to the autocorrelation functions of the generic random process $\boldsymbol{N}(\boldsymbol{r}, \omega)$ and are anisotropic. Finally, (14) gives place to

$$\mathsf{E}\left[\boldsymbol{E}_{\mathrm{TR,i}}(\boldsymbol{r}, \omega)\right] = \int_\Sigma \tilde{\boldsymbol{T}}_{\mathrm{i}}(\boldsymbol{r}, \boldsymbol{r}', \omega) \cdot \bar{\boldsymbol{E}}_{\mathrm{wf}}(\boldsymbol{r}', \omega)\mathrm{d}^2\boldsymbol{r}', \tag{16}$$

requiring no assumption on the nature of the medium, nor on the type of wavefront distribution, apart the simplifying assumption of a far-field configuration.

The possibility of obtaining an accurate transmission through a complex medium is feasible in the special case of a diffusive medium, which is characterized by a low spatial-correlation, thus ensuring an equivalent Green's function close to that of a free-space environment (see section VI). The fundamental point that we want to stress here is that the application of a TR approach allows reproducing a behavior that is actually closer to a free-space environment, but within a complex medium supporting a diffused-field configuration. This idea is illustrated in section VIII.

The far-field assumption was introduced as a way of simplifying the derivation of the above results, but the equivalence theorem is not affected by the region of radiation of a source, and will stay exact even in its reactive region, even though only the propagative part of the target wavefront will be reproduced, thus leading to the inevitable diffraction limit in the focus region [29].

V. A PARADIGM SHIFT FOR TR APPLICATIONS

The derivation of (16) implies that as soon as the dyadic Green's functions of the medium are known between the points over Σ and the positions of the TRM antennas, a direct relationship can be promptly established between the target wavefront distribution and the one generated by the TREC.

Moreover, the derivation leading to (16) paves the way for a change of paradigm in the use of TR techniques: indeed, as soon as the vector transfer functions $\boldsymbol{N}_{e,i}(\boldsymbol{r}, \omega)$ and $\boldsymbol{N}_{r,i}(\boldsymbol{r}, \omega)$ are known, it is no more necessary to undergo the two standard phases of TR. The signals $V_i(\omega)$ that would

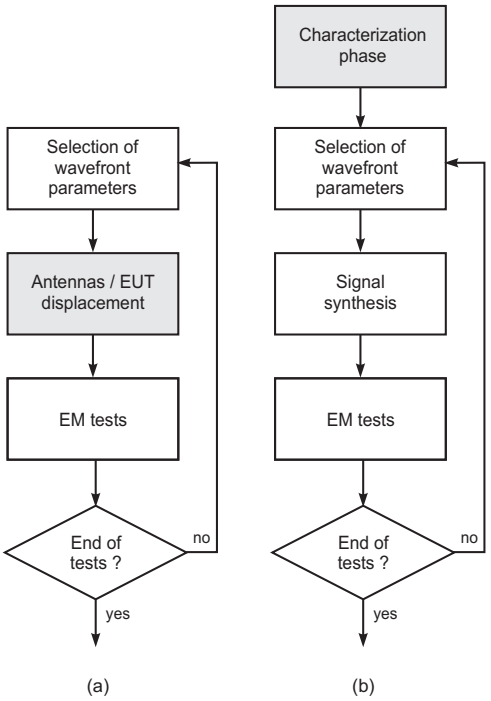

Fig. 4: Sequences of necessary steps to follow when using an (a) anechoic test environment or a (b) TREC. Shaded blocks represent operations based on mechanical displacements or substitution of devices.

result from the recording phase (or first phase) can be straightforwardly computed for any target wavefront without needing its actually being radiated, since

$$V_i(\omega) \propto \int_{\Sigma} \boldsymbol{N}_{\mathrm{eq},i}(\boldsymbol{r},\omega) \cdot \boldsymbol{E}_{\mathrm{wf}}(\boldsymbol{r},\omega)\mathrm{d}^2\boldsymbol{r}, \qquad (17)$$

with

$$\boldsymbol{N}_{\mathrm{eq},i}(\boldsymbol{r},\omega) = -\frac{\boldsymbol{N}_{e,i}(\boldsymbol{r},\omega)}{\zeta_0} + \hat{\boldsymbol{r}} \times \boldsymbol{N}_{m,i}(\boldsymbol{r},\omega), \qquad (18)$$

leading to a direct synthesis of the excitation signals for the second phase.

This simple modification has deep consequences: as a matter of fact, the standard implementation of TR techniques implies that each time that a new converging wavefront is to be generated, the diverging version of the same wavefront needs to be generated by an actual source during the first phase. Furthermore, as the characteristics of the wavefront change, e.g., the direction of arrival or the polarization, the first phase is to be carried out again. This is clearly a strong limitation when proposing TR for testing applications, since as soon as a wide range of configurations is to be tested, the repetition of the two phases would be too costly. Moreover, the question of how to generate the diverging wavefront in the first place is far from trivial. The paradigm shift we propose solves all of these problems in a elegant and simple way. In fact, a preliminary characterization or *learning* phase can be considered during which the propagation medium is explored, proceeding to a direct measurement of $\boldsymbol{N}_{\mathrm{eq},i}(\boldsymbol{r},\omega)$ without any need to formulate any hypothesis on its nature. At this point, the signals that would have been received for any wavefront can be directly computed by means of (17).

The use of (17) implies that once a physical target wavefront is defined, the excitation signals needed to apply to the TRM antennas are readily available, even though the generation of this same wavefront could prove to be difficult when using real-life sources. It is therefore appropriate to refer to the time-reversed wavefronts provided by (17) as generated by synthetic sources. The approach here proposed is somewhat reminiscent of synthetic aperture radar techniques, where post-processing techniques allow to emulate the availability of a source that would be practically unfeasible, while its emulation is actually quite straightforward. The difference is that although the synthetic source does not radiate in the first place, its TR wavefront is actually generated, not only computed in a post-processing fashion.

The advantages of this approach are clear: passing from one wavefront to another just involves the synthesis of new excitation signals, without any need for further measurements, as long as the propagation medium has not undergone any modification, e.g., due to mechanical displacements of the EUT. Moreover, the linearity of the propagation of waves within the medium implies that superposition of effects holds: as a consequence, it is possible to conceive complex test scenarios where multiple wavefronts can be generated to impinge onto the EUT from different directions, with any type of time-dependence associated to each individual wavefront. The generation of similar scenarios by means of state-of-the-art facilities would involve a sophisticated system to feed the antennas associated to each direction of arrival and control their orientations [1]. As opposed to this need, the TREC is theoretically capable of generating arbitrary wavefronts with a reduced number of antennas, typically just one, by exploiting the weak spatial correlation of the wave-diffusive media [30].

From a practical point of view, this approach allows dramatically reducing the time needed for generating a new converging wavefront, as the only steps needed are the computation of the excitation signals and their direct digital synthesis. A flow-chart representation of the sequence of operations needed when testing with a standard anechoic chamber or a TREC based on an overmoded cavity is proposed in Fig. 4, where it is made clear that the modification of the testing wavefront does not require any physical modification of the test environment, but only changing excitation signals. Rather than repeating mechanical displacements each time that a new test configuration is required, these are relegated to the learning phase, before starting a cycle of uninterrupted tests.

The entire procedure here suggested relies on previous knowledge of the $\boldsymbol{N}_{\mathrm{eq,i}}(\boldsymbol{r},\omega)$ functions. A detailed discussion of this issue is out of the scope of this paper, and it was partially considered in [8].

VI. The case of a wave-diffusive medium

In this section we address the special case of an ideal wave-diffusive medium. By this term we consider any medium, not necessarily homogeneous, whose Green's functions can be approximated by means of a superposition of a large number of random plane waves propagating with equal probability along any direction [31], ensuring very simple statistical properties for the field: a Gaussian-distributed field with spatial-invariant moments and a perfect depolarization. Among the several configurations where this property can be invoked, large cavities such as reverberation chambers are perhaps the simplest way of implementing it, as soon as an overmoded condition is satisfied [32], [33].

The hypothesis of perfect diffusion and thus a random plane-wave spectrum are actually the basis for the asymptotic analysis of reverberation chambers, as proposed, e.g., in [4]. As a direct consequence of spatial stationarity, $\tilde{\boldsymbol{T}}_{\rm i}(\boldsymbol{r},\boldsymbol{r}',\omega)$ are independent from the position of the TRM antennas and their orientation, so that it is possible to drop the i index and consider the average response $\tilde{\boldsymbol{T}}(\boldsymbol{r},\boldsymbol{r}',\omega)$ of the TREC.

In order to derive a closed-form expression for the dyadic operator $\tilde{\boldsymbol{T}}(\boldsymbol{r},\boldsymbol{r}',\omega)$, we expand the vector transfer functions (11) over the local reference system depicted in Fig. 5, defined by of a longitudinal unit vector $\hat{\boldsymbol{\rho}}=\boldsymbol{d}/\|\boldsymbol{d}\|$, where $\boldsymbol{d}=\boldsymbol{r}'-\boldsymbol{r}$, a transversal unit vector $\hat{\boldsymbol{\nu}}$ lying on the plane defined by the vectors $\boldsymbol{r}$ and $\boldsymbol{r}'$ and a third unit vector $\hat{\boldsymbol{\eta}}=\hat{\boldsymbol{\rho}}\times\hat{\boldsymbol{\nu}}$.

The dyadic operators introduced in (15), e.g., for the case of the $\tilde{\boldsymbol{T}}_{\rm ee}(\boldsymbol{r},\boldsymbol{r}',\omega)$ dyadic function, can thus be expressed into this new basis, yielding scalar components

$$\left(\tilde{\boldsymbol{T}}_{\rm ee}\right)_{\hat{\boldsymbol{u}}_m\hat{\boldsymbol{u}}_n}(\boldsymbol{r},\boldsymbol{r}',\omega)= \mathsf{E}\left[\hat{\boldsymbol{u}}_m\cdot\boldsymbol{N}_{\rm e}(\boldsymbol{r},\omega)\;\hat{\boldsymbol{u}}_n\cdot\bar{\boldsymbol{N}}_{\rm e}(\boldsymbol{r}',\omega)\right], \tag{19}$$

where $\hat{\boldsymbol{u}}_m$ is any of the basis unit vectors $\hat{\boldsymbol{\rho}}$, $\hat{\boldsymbol{\eta}}$ and $\hat{\boldsymbol{\nu}}$. Recalling that the vector functions $\boldsymbol{N}(\boldsymbol{r},\omega)$ are generic transfer functions observed within a diffusive medium, the scalar terms (19) actually represent the covariances between the scalar components of two transfer functions evaluated at two positions within the medium. Hence, the results presented in [34] apply, leading to

$$\left(\tilde{\boldsymbol{T}}_{\rm ee}\right)_{\hat{\boldsymbol{\rho}}\hat{\boldsymbol{\rho}}}(\boldsymbol{r},\boldsymbol{r}',\omega) = \frac{N^2_{\rm e,av}(\omega)}{3}\rho_l(d,\omega) \tag{20a}$$

$$\left(\tilde{\boldsymbol{T}}_{\rm ee}\right)_{\hat{\boldsymbol{\nu}}\hat{\boldsymbol{\nu}}}(\boldsymbol{r},\boldsymbol{r}',\omega) = \frac{N^2_{\rm e,av}(\omega)}{3}\rho_t(d,\omega) \tag{20b}$$

$$\left(\tilde{\boldsymbol{T}}_{\rm ee}\right)_{\hat{\boldsymbol{\eta}}\hat{\boldsymbol{\eta}}}(\boldsymbol{r},\boldsymbol{r}',\omega) = \left(\tilde{\boldsymbol{T}}_{\rm ee}\right)_{\hat{\boldsymbol{\nu}}\hat{\boldsymbol{\nu}}}(\boldsymbol{r},\boldsymbol{r}',\omega), \tag{20c}$$

results that hold for any wave-diffusive medium.

In (20), $N_{\rm e,av}(\omega)/\sqrt{3}$ is the rms amplitude of the electric field observed along any of its scalar components within the region of space where the ideal diffused-field conditions hold [35]; this quantity is derived in Appendix A. The functions $\rho_t(d,\omega)$ and $\rho_l(d,\omega)$ are spatial correlation functions, so they only depend on the distance $d=|\boldsymbol{r}-\boldsymbol{r}'|$.

Apart for the three scalar components shown in (20), the remaining ones are identically null, as demonstrated in [34]. The two spatial-correlation functions $\rho_l(d,\omega)$ and $\rho_t(d,\omega)$ refer to the longitudinal the transversal components of the electric field, respectively. These functions are [34]

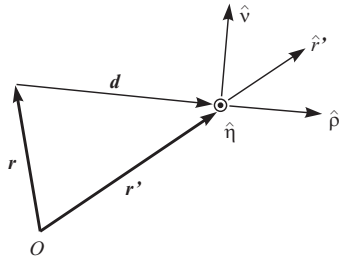

Fig. 5: The local reference system based on the orientation of the $\boldsymbol{r}$ and $\boldsymbol{r}'$ vectors, defined by the right-hand set of unit vectors $\hat{\boldsymbol{\nu}}$, $\hat{\boldsymbol{\eta}}$ and $\hat{\boldsymbol{\rho}}$. This choice is at the basis of the results derived for the case of a wave-diffusive medium, e.g., an overmoded reverberation chamber.

$$\rho_l(d,\omega) = \frac{3}{(kd)^2}\left[\mathrm{sinc}(kd)-\cos(kd)\right] \tag{21a}$$

$$\rho_t(d,\omega) = \frac{3}{2}\mathrm{sinc}(kd)-\frac{1}{2}\rho_l(d,\omega), \tag{21b}$$

with $k=\omega/c_0$ the wave-number and c_0 the speed of light in the homogeneous medium filling the cavity.

In dyadic formalism, $\tilde{\boldsymbol{T}}_{\rm ee}(\boldsymbol{r},\boldsymbol{r}',\omega)$ can be expressed as

$$\tilde{\boldsymbol{T}}_{\rm ee}(\boldsymbol{r},\boldsymbol{r}',\omega)= \frac{N^2_{\rm e,av}(\omega)}{3}\left[\hat{\boldsymbol{\rho}}\hat{\boldsymbol{\rho}}\rho_l(d,\omega)+(\hat{\boldsymbol{\nu}}\hat{\boldsymbol{\nu}}+\hat{\boldsymbol{\eta}}\hat{\boldsymbol{\eta}})\rho_t(d,\omega)\right]. \tag{22}$$

Following the same procedure for the $\tilde{\boldsymbol{T}}_{\rm em}(\boldsymbol{r},\boldsymbol{r}',\omega)$ dyadic function, recalling that only the cross-transversal components (defined with respect to $\hat{\boldsymbol{\rho}}$) of the electric and magnetic fields are correlated [34], we can state that the only non-zero components are

$$\left(\tilde{\boldsymbol{T}}_{\rm em}\right)_{\hat{\boldsymbol{\nu}}\hat{\boldsymbol{\rho}}}(\boldsymbol{r},\boldsymbol{r}',\omega) = \frac{N^2_{\rm e,av}(\omega)}{3\zeta_0}\rho_m(d,\omega)\hat{\boldsymbol{r}}'\times\hat{\boldsymbol{\nu}}\cdot\hat{\boldsymbol{\eta}} \tag{23a}$$

$$\left(\tilde{\boldsymbol{T}}_{\rm em}\right)_{\hat{\boldsymbol{\nu}}\hat{\boldsymbol{\rho}}}(\boldsymbol{r},\boldsymbol{r}',\omega) = \frac{N^2_{\rm e,av}(\omega)}{3\zeta_0}\rho_m(d,\omega)\hat{\boldsymbol{r}}'\times\hat{\boldsymbol{\eta}}\cdot\hat{\boldsymbol{\rho}} \tag{23b}$$

$$\left(\tilde{\boldsymbol{T}}_{\rm em}\right)_{\hat{\boldsymbol{\eta}}\hat{\boldsymbol{\eta}}}(\boldsymbol{r},\boldsymbol{r}',\omega) = \left(\tilde{\boldsymbol{T}}_{\rm em}\right)_{\hat{\boldsymbol{\nu}}\hat{\boldsymbol{\nu}}}(\boldsymbol{r},\boldsymbol{r}',\omega), \tag{23c}$$

where $\rho_m(d,\omega)$ is the mixed correlation function between the cross-transveral components of the electric and magnetic fields, given by [34]

$$\rho_m(d,\omega) = -\frac{1}{2}\mathrm{j}kd\rho_l(d,\omega). \tag{24}$$

Whence, the operator $\tilde{\boldsymbol{T}}(\boldsymbol{r},\boldsymbol{r}',\omega)$ reads, for the case of an ideally diffused field

$$\tilde{\boldsymbol{T}}(\boldsymbol{r},\boldsymbol{r}',\omega) = \frac{N^2_{\rm e,av}(\omega)}{3\zeta_0}\tilde{\boldsymbol{\rho}}(\boldsymbol{r},\boldsymbol{r}',\omega), \tag{25}$$

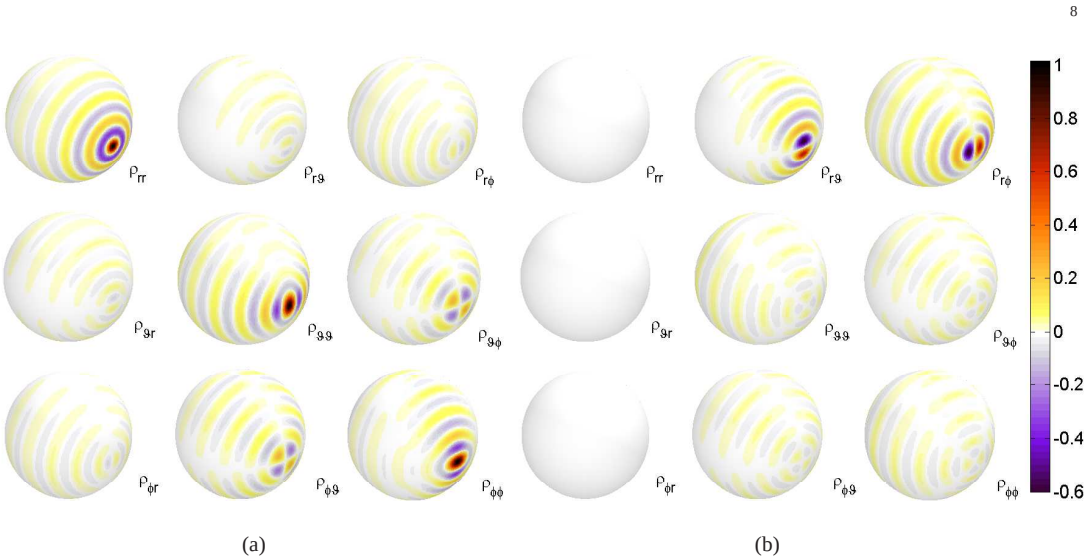

(a) (b)

Fig. 6: Normalized dyadic function $\tilde{\boldsymbol{\rho}}(\boldsymbol{r},\boldsymbol{r}',\omega)$ computed for $\boldsymbol{r}\in\Sigma$ and $\boldsymbol{r}'=r_\Sigma\hat{\boldsymbol{x}}$, with $r_\Sigma=3\lambda$: (a) real and (b) imaginary parts. The 9 terms of the dyadic response are shown, matrix-wise, considering standard spherical unit vectors, following the order $\hat{\boldsymbol{r}}$, $\hat{\boldsymbol{\vartheta}}$ and $\hat{\boldsymbol{\varphi}}$, defined with respect to a polar axis vertically oriented.

with

$$\begin{aligned}\tilde{\boldsymbol{\rho}}(\boldsymbol{r},\boldsymbol{r}',\omega)&=\hat{\boldsymbol{\rho}}\hat{\boldsymbol{\rho}}\rho_l(d,\omega)-\hat{\boldsymbol{\nu}}\hat{\boldsymbol{\rho}}\rho_m(d,\omega)\hat{\boldsymbol{r}}'\times\hat{\boldsymbol{\eta}}\cdot\hat{\boldsymbol{\rho}}+\\&+(\hat{\boldsymbol{\nu}}\hat{\boldsymbol{\nu}}+\hat{\boldsymbol{\eta}}\hat{\boldsymbol{\eta}})\left[\rho_t(d,\omega)-\rho_m(d,\omega)\hat{\boldsymbol{r}}'\times\hat{\boldsymbol{\nu}}\cdot\hat{\boldsymbol{\eta}}\right].\end{aligned}\tag{26}$$

introducing the normalized dyadic response $\tilde{\boldsymbol{\rho}}(\boldsymbol{d},\omega)$. As a result, the real and imaginary parts of the scalar components of this function are now bounded to one, since they correspond to the degree of coherence of the medium [36]. The operator $\tilde{\boldsymbol{\rho}}(\boldsymbol{r},\boldsymbol{r}',\omega)$ behaves as a point-spread function (PSF).

The PSF $\tilde{\boldsymbol{\rho}}(\boldsymbol{r},\boldsymbol{r}',\omega)$ will be used in two frameworks: 1) by setting $\boldsymbol{r},\boldsymbol{r}'\in\Sigma$, it allows assessing how a TREC-generated wavefront is distorted with respect to the target one in the far-field region; 2) with $\boldsymbol{r}'\in\Sigma$ and a generic $\boldsymbol{r}$, it provides a direct access to the spatial evolution of a wavefront generated by the proposed method.

VII. On the PSF of the TREC

Albeit the previous results hold for any diffusive medium, hereafter we will assume that this medium is an overmoded reverberation chamber, filled by a reciprocal and homogeneous medium surrounding the EUT. The target wavefront can be expressed, in the frequency domain, as

$$\boldsymbol{E}_{\mathrm{wf}}(\boldsymbol{r},\omega)=X(\omega)G(r,\omega)\boldsymbol{F}(\hat{\boldsymbol{r}},\omega),\tag{27}$$

where $\boldsymbol{F}(\hat{\boldsymbol{r}},\omega)$ is the radiation pattern of the synthetic source, $G(r,\omega)$ is the far-field Green's scalar function of the medium

$$G(r,\omega)=\frac{\mathrm{e}^{-\mathrm{j}k_0r}}{4\pi r}\tag{28}$$

and $X(\omega)$ is related to the excitation signal that would be used to drive the synthetic source. Such a factorized representation is made possible by the assumption of Σ being in the far-field region of the synthetic source. Again we stress the fact that this choice is not a limitation, but just a simplifying assumption. The time-domain representation of $\boldsymbol{\mathcal{E}}_{\mathrm{wf}}(\boldsymbol{r},t)$ can thus be expressed as

$$\boldsymbol{\mathcal{E}}_{\mathrm{wf}}(\boldsymbol{r},t)=\frac{x(t-r/c_0)}{4\pi r}*_t\mathcal{F}^{-1}\left\{\boldsymbol{F}(\hat{\boldsymbol{r}},\omega)\right\},\tag{29}$$

where $*_t$ stands for the convolution integral applied to the time variable; this result holds for any $\boldsymbol{r}=r\hat{\boldsymbol{r}}$ in the far-field region of the synthetic source.

Introducing (27) into (16) while using (25) yields

$$\mathsf{E}\left[\boldsymbol{\mathcal{E}}_{\mathrm{TR}}(\boldsymbol{r},t)\right]\propto x(-t)*_t\mathcal{F}^{-1}\left\{\tilde{\boldsymbol{\rho}}(\boldsymbol{r},\boldsymbol{r}',\omega)*_{\boldsymbol{r}'}\bar{\boldsymbol{F}}(\hat{\boldsymbol{r}}',\omega)\right\},\tag{30}$$

where $*_{\boldsymbol{r}'}$ is the pseudo-convolution integral required in (16) and carried out over Σ. Comparing (30) with (29) it appears that in order to have a converging version of the target wavefront, $\tilde{\boldsymbol{\rho}}(\boldsymbol{r},\boldsymbol{r}',\omega)$ should comply with the three following points: 1) it should provide a delay going like r/c_0; 2) a radial dependence like $1/r$ in the far-field region and 3) should not distort the angular dependence $\boldsymbol{F}(\hat{\boldsymbol{r}},\omega)$. The first two points are easily verified since the functions (21) appearing in the PSF (26) are dominated by terms going like $\exp(\pm\mathrm{j}k_0r)/r$. As shown in the examples in section VIII, the coexistence within the PSF of the incoming and outgoing versions of the free-space propagator has a simple physical meaning: if a focusing wavefront is generated, after focusing onto the phase-center of the synthetic source, it will inevitably diverge along the opposite direction. The only point requiring a closer investigation is the third one, i.e., the eventual distortion of the angular dependence, which is not easily assessable from (16).

To this effect, it is convenient to study the average wavefront $\mathsf{E}[\boldsymbol{E}_{\mathrm{TR}}(\boldsymbol{r},\omega)]$ over the equivalent-source surface Σ. The fact that the PSF $\tilde{\boldsymbol{\rho}}(\boldsymbol{r},\boldsymbol{r}',\omega)$ is dependent on the distance r_Σ/λ is not due to limitations in the equivalent-source approach, but rather because as r_Σ becomes smaller, while the wavefront in the far-field region shall not be modified, its progression towards the focal spot will indeed lead to a modification of the wavefront features, due to diffraction phenomena in the focal region [29].

Therefore, the properties of the PSF $\tilde{\boldsymbol{\rho}}(\boldsymbol{r},\boldsymbol{r}',\omega)$ can be evaluated in a general manner by setting the dominant parameter r_Σ/λ, i.e., deciding how close the observer will be to the focal spot. The choice of having the equivalent-source surface coinciding with that of the observer allows a simpler comparison of how the radiation pattern (considered independent of the distance) will eventually be affected by the PSF. An example is given in Fig. 6, where the nine components of the PSF $\tilde{\boldsymbol{\rho}}(\boldsymbol{r},\boldsymbol{r}',\omega)$ are shown for the case of vectors $\boldsymbol{r}$ and $\boldsymbol{r}'$ belonging to the same surface Σ, where the choice $r_\Sigma = 3\lambda$ was made. The PSF is expressed with respect to a spherical reference system, for a point-source positioned at an $\boldsymbol{r}'$ chosen to be along $\hat{\boldsymbol{x}}$.

Fig. 6 shows that the PSF is not perfectly isotropic, with diagonal terms depending on the field component, and off-diagonal terms (cross-polarization coupling) not identically equal to zero. The weak oscillations outside the peak regions present a zero mean-value and can be expected to lead to a very low result after the pseudo-convolution (16), as their overall contribution to the integral will be negligible as long as the target pattern undergoes angular variations slower than the pseudo-period of these oscillations. This point will be given more room in the rest of this section and in the next one.

The six off-diagonal terms share the absence of an even-symmetry positive-valued dominant peak, substituted by odd-symmetry responses. The low-level oscillations present patterns similar to those found in the three direct terms. Of particular interest is the fact that the coupling terms are stronger between the two tangential components ϑ and φ, which could be a source of inaccuracy in the reproduction of the target wavefront. Still, the $\hat{\boldsymbol{\vartheta}}\hat{\boldsymbol{\varphi}}$ and $\hat{\boldsymbol{\varphi}}\hat{\boldsymbol{\vartheta}}$ terms are characterized by a double odd-symmetry, implying that convolution with a even-symmetric radiation pattern would result in a zero at $\boldsymbol{r}'$, i.e., no coupling between the ϑ and φ components. In other words, the original polarization should be expected to be preserved. Examples are shown in section VIII for the radiation pattern generated by an aperture source, where it is made clear how the coupling is indeed very weak and negligible in practical configurations. These results are consistent with those presented in [37], [38], extending them to the general case of a wavefront rather than a mere focal spot.

For the PSF $\tilde{\boldsymbol{\rho}}(\boldsymbol{r},\boldsymbol{r}',\omega)$ to be expected not to modify the original radiation pattern, it should be real-valued: in any other case, it would at least imply a phase distortion of the wavefront. In practice the imaginary part of the PSF is much weaker than the real part, but for two components: $\hat{\boldsymbol{r}}\hat{\boldsymbol{\vartheta}}$ and $\hat{\boldsymbol{r}}\hat{\boldsymbol{\varphi}}$. As it will be shown in the examples presented in section VIII, the role of these two functions is to reproduce the natural distortion of the wavefront passing from essentially spherical (in the far-field region) to the one corresponding to the near-field region of the synthetic source. This remark does not involve the idea of reproducing the reactive components of the field, as the focal region of the wavefront is usually found in the far-field region of the TRM antennas, the actual sources of the converging wavefront [29]. These considerations should be clearer when compared with the numerical results presented in section VIII.

The impact of the PSF on the angular dependence of $\boldsymbol{E}_{\mathrm{TR}}(\boldsymbol{r},\omega)$ can be assessed by studying the zone of maximum correlation in the diagonal terms of the PSF. The null-to-null width of this main lobe can be computed from (21) and (24) and intercepts an angular resolution angle ψ_ρ that can be expressed (in radians) in a general way as

$$\psi_\rho = \alpha_\rho \frac{\lambda}{r_\Sigma}, \tag{31}$$

where α_ρ can take the values 0.89 or 1.45 depending on the direction along which the angle ψ_ρ is measured, since the examples in Fig. 6 show that the PSF does not present a cylindrical symmetry. It is common practice in optics to approximate the size of the PSF to about a wavelength for the diffraction of waves propagating in free-space: we will adopt this approximation by taking $\alpha_\rho \simeq 1$, for the sake of simplicity. We can expect the TREC to be capable of reliably reproducing the target wavefront as long as the angular rate of variation of the radiation pattern of the wavefront is not faster than that allowed by its PSFs.

With reference to Fig. 2, the assumption of an observation surface Σ in the far-field region of the synthetic source requires

$$\frac{r_\Sigma}{\lambda} > 8\left(\frac{r_\Xi}{\lambda}\right)^2, \tag{32}$$

implying that given the radius r_Σ of the equivalent-source surface, the maximum dimensions of the volume V_Ξ containing the synthetic source is given an upper bound, as well as its maximum gain [25]. A simple estimate can be derived by recalling that for a directive source, e.g., an aperture of maximum width $2r_\Xi$, the -3 dB angle ψ_F of its main lobe can be approximated by

$$\psi_F \simeq \frac{\lambda}{2r_\Xi}. \tag{33}$$

From (32), the maximum directivity of the synthetic source, or the minimum width of its main lobe, is

$$\psi_F > \sqrt{\frac{2\lambda}{r_\Sigma}}. \tag{34}$$

We can now consider that the PSF will lead to a minor modification of the radiation pattern as long as ψ_ρ is small enough with respect to the angular variation in $\boldsymbol{F}(\hat{\boldsymbol{r}},\omega)$, as measured by its main lobe ψ_F. To this end, we introduce the quantity R

$$R = \frac{\psi_F}{\psi_\rho}, \tag{35}$$

representing the angular resolution power of the TREC. A numerical analysis is proposed in section VIII, where the quality of the angular dependence of the wavefront produced by the TREC is assessed as a function of R.

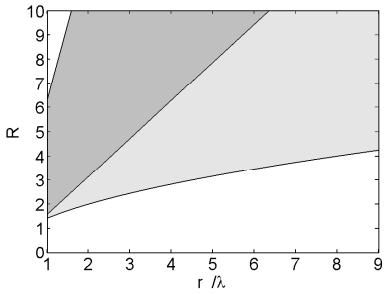

Fig. 7: Ranges of values taken by the ratio $R = \psi_F/\psi_\rho$, indicating the resolution power of the TREC. This quantity is plotted against the radius of r_Σ of the equivalent-source surface for two cases: (a) the lightly shaded area corresponds to a cut along the E plane of the synthetic source, i.e., for a main lobe that is physically lower-bounded by that of a Hertzian dipole; (b) the domain of existence of the resolution power is extended to the more deeply-shaded area when dealing with the H plane of a linearly polarized source, i.e., its azimuthal plane, where its main lobe can present any value up to 2π radian.

The range of values taken by R can be estimated by recalling that ψ_F is bounded as

$$\psi_{\max} > \psi_F > \sqrt{\frac{2\lambda}{r_\Sigma}}. \tag{36}$$

The lower bound is actually due to the far-field assumption at the base of the proposed analysis, leading to (34), whereas the upper-bound comes from the fact that for a linearly polarized source the main-lobe -3 dB angle is actually limited by a finite value. Considering the E plane of the synthetic source, the upper limit is given by $\psi_{\max} = \pi/2$ radians for an Hertzian dipole, whereas for the H plane it can reach up $\psi_{\max} = 2\pi$ radians. Accounting for these bounds, the range of variation of R is shown in Fig. 7, as a function of the electrical size of the equivalent-source surface Σ. It appears that $R > 1.5$ as long as Σ is at least one wavelength in radius. This lower limit is actually meaningful and even conservative, since any smaller choice would not allow the observer to be in the far-field of even the simplest source: indeed, the basic condition $k_0 r_\Sigma \gg 1$ for the far-field region must also apply, hence requiring $r_\Sigma/\lambda \gtrsim 1.58$.

The results in Fig. 7 prove that for any far-field configuration, R will always be higher than 1.5, typically closer to 2, i.e., radiation patterns will be at least twice larger than the PSFs main lobes.

VIII. Numerical results

Numerical results are here presented in order to support our conclusions about the ability of the TREC to reproduce arbitrary wavefronts within a wave-diffusive medium. These have been obtained by numerically solving the convolution integral in (16), as applied to a reference radiation pattern.

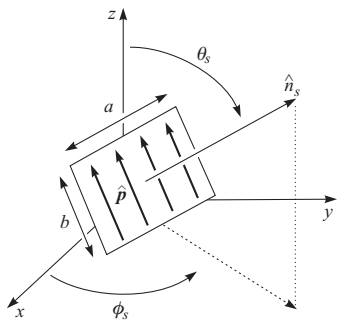

Fig. 8: The synthetic source considered in the validation presented in section VIII. It consists of an ideal rectangular aperture of dimensions a and b, with a uniform field distribution linearly polarized along the direction $\hat{\boldsymbol{p}}$.

Our choice was for a rectangular aperture, as the one shown in Fig. 8, with sides a and b, characterized by a uniform electric field linearly polarized along the generic direction $\hat{\boldsymbol{p}}$ lying on the aperture, radiating towards the half-space identified by $\hat{\boldsymbol{r}} \cdot \hat{\boldsymbol{n}}_s \geqslant 0$.

Assuming an aperture initially lying on the xy plane and its main-lobe radiating along $\hat{\boldsymbol{z}}$, its radiation pattern can be approximated in closed-form as [26]

$$\begin{aligned}\boldsymbol{F}_{\mathrm{wf}}(\hat{\boldsymbol{r}},\omega) = (1+\cos\vartheta)(\hat{\boldsymbol{\vartheta}}\hat{\boldsymbol{\vartheta}} + \hat{\boldsymbol{\varphi}}\hat{\boldsymbol{\varphi}})\cdot\hat{\boldsymbol{p}} \\ \operatorname{sinc}\left(\pi\frac{a}{\lambda}\hat{\boldsymbol{x}}\cdot\hat{\boldsymbol{r}}\right)\operatorname{sinc}\left(\pi\frac{b}{\lambda}\hat{\boldsymbol{y}}\cdot\hat{\boldsymbol{r}}\right),\end{aligned} \tag{37}$$

while a generic orientation along the angles ϑ_s and φ_s can be analyzed by applying standard rotation transformations.

We first proceed by assessing how accurately the radiation pattern is reproduced for a varying electrical distance from the synthetic-source volume, in the frequency domain, in section VIII-A. The existence of a focusing phenomenon is proven, while showing up to what distance the angular dependence dictated by target radiation pattern holds. We are particularly interested in assessing whether distortions of the wavefront intervene before its reaching the focal spot, which would imply a limitation in the accuracy of the TREC even during the far-field propagation of the wavefront. In a second time, section VIII-B elucidates the existence of a back-lobe contribution, by considering the time-domain evolution of the converging wavefront for a non-harmonic excitation.

A. Frequency domain : focusing

Thanks to (16) and (26), we computed the average field distribution that would be observed over concentric surfaces of radius $0.7, 1, 3$ and $5\ \lambda$, for an aperture of sides $a = b = 1\ \lambda$ pointing towards $\vartheta_s = \pi/2, \varphi_s = 0$ with a $\hat{\boldsymbol{y}}$-polarized electric field (see Fig. 8). The results are shown in Fig. 9, together with the target radiation pattern, as a reference. The results are expanded into the three spherical coordinate components, with the target radiation pattern having no radial component (far-field radiation). It appears that the TREC approach is indeed

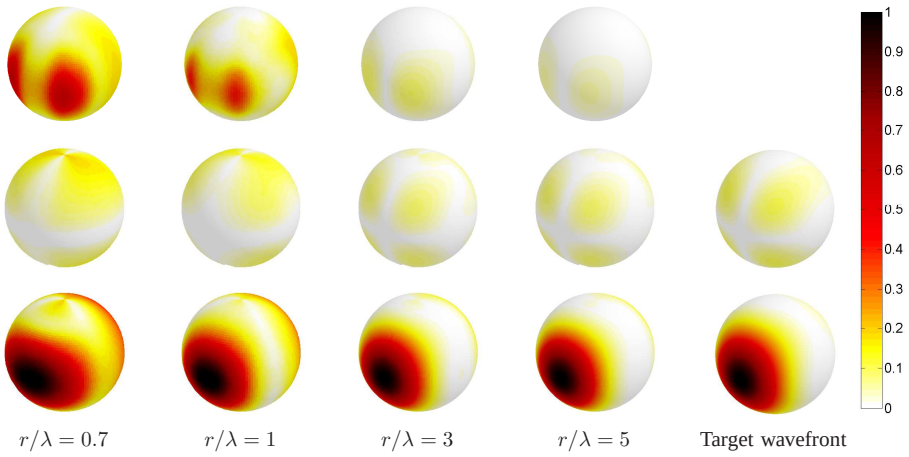

Fig. 9: The electric field distribution of the wavefront generated by a TREC as it would be observed at several distances. The side of incidence of the wavefront is shown, where the absolute value of the field is considered for the three spherical components of the field, in the order E_r, E_ϑ and E_φ respectively, from the top to the bottom. The target wavefront distribution is given as a reference in the last column. All results are normalized to the peak-amplitude of the E_φ component, for each distance.

capable of very accurately reproducing the target radiation pattern even at very close distance, with non-negligible distortions occurring only within a one-wavelength distance from the phase-center of the synthetic source. The polarization is also preserved, not only the dominant component along $\hat{\boldsymbol{\varphi}}$, but also the cross-polarization $\hat{\boldsymbol{\vartheta}}$. A substantial deformation of the radiation pattern is observed at $0.7\ \lambda$, where the PSF component for the $\hat{\boldsymbol{\varphi}}\hat{\boldsymbol{\varphi}}$ contribution is clearly recognizable, with a more elongated distribution along the $\hat{\boldsymbol{\varphi}}$.

The back-lobe contribution appearing in Fig. 9 will be shown in section VIII-B to result from the impinging wave focusing through the phase-center of the synthetic-source and subsequently diverging along the opposite direction.

The same type of computation was carried out over a continuous range of distances from $\lambda/10$ up to $3\ \lambda$, limited to a horizontal cut, along the xy plane, starting from an equivalent-source surface at $r_\Sigma = 3\lambda$. These results are shown in Fig. 10, where the two spherical components $E_\varphi(\boldsymbol{r},\omega)$ and $E_r(\boldsymbol{r},\omega)$ of the electric field are shown, $E_\vartheta(\boldsymbol{r})$ being identically null by virtue of symmetry. We therefore conclude that a focusing of the propagating energy is indeed occurring, as the electric field builds up converging towards the phase-center of the synthetic source.

Two notable distances are marked in Fig. 10: $r_\Sigma = 2\lambda$ and $r_\Xi = \lambda/2$. The target wavefront (far field) should only present a $\hat{\boldsymbol{\varphi}}$-oriented field, which is indeed found in the TREC-generated wavefront, as shown in Fig. 10(a)-(b); the purity of the polarization appears to start degrading as the wavefront crossed r_Ξ, when the focusing wavefront approximate the original field distribution found in the reactive part of the synthetic source, i.e., $\hat{\boldsymbol{y}}$-oriented, as clearly visible in the vector representation in Fig. 11. Since the TREC, as any other anechoic environment, can only produce propagative waves by means of distant sources (i.e., the TRM antennas), the diffraction limit ensues, leading to a focal spot about one wavelength wide. The appearance of a radial component in Fig. 10(b) is due to this phenomenon of approximation of the original source distribution, and it becomes more evident when looking at the total field in Fig. 10(c): the wavefront focuses back onto the source region, with an almost uniform intensity.

The accuracy of the angular distribution of the focusing wavefront is more easily observed in Fig. 10(d), where the wavefront is normalized to Green's scalar function, yielding the radiation pattern to be compared to that shown in Fig. 10(e). The comparison is very good, with the converging wavefront accurately reproducing a constant radiation pattern over its far-field region within a ± 0.2 dB range over the main lobe. Fig. 10(d) also provides a clear picture of the focal spot due to diffraction limit: directivity is lost, with energy almost equally spread over all directions, and particularly with a reduction in its increase with respect to an ideal spherical convergence.

These results imply that the loss of directivity is not due to an intrinsic limitation of the method, as could have been expected from the PSF shown in the previous section. It actually appears that the PSF is effectively capable of reproducing all the phenomena leading to wave focusing under physical conditions, including the diffraction limitation over the near-field region of the synthetic source. Practically, no significant distortion occurs over the main-lobe outside the surface Ξ, thus implying that there is no need to require $R \gg 1$ to avoid distortions of the far-field distribution of the wavefront.

The generated wavefront deviates from the target one outside the main lobe, even in the far-field region, within a range

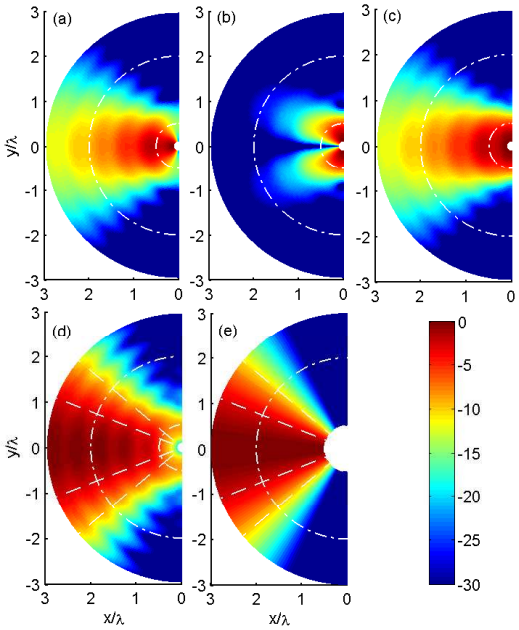

Fig. 10: Numerical solution of (16) for the case of the radiation pattern of the wideband aperture antenna described in the body of the text and shown in Fig. 8. The evolution of the electric field is studied over the half-plane of the xy cut along which the time-reversed wavefront is expected to focus, for radial distances going from $\lambda/10$ up to 3λ: (a) $E_\varphi(\boldsymbol{r})$; (b) $E_r(\boldsymbol{r})$; (c) $\|\boldsymbol{E}(\boldsymbol{r})\|$; (d) $\|\boldsymbol{E}(\boldsymbol{r})/G(r)\|$; (e) angular dependence $\|\boldsymbol{F}(\boldsymbol{r})\|$, proportional to $\|\boldsymbol{E}_{\rm wf}(\boldsymbol{r})/G(r)\|$. The outer dashed line represents the Fraunhofer distance for the synthetic source, whose volume is marked by the inner dashed line. All results are normalized to the peak-value of E_φ and expressed in dB. Radial dashed lines represent the -3 dB and the -10 dB angles.

of values inversely related to the intensity of the field. The reason for this phenomenon is not clear and deserves further investigations. It could indeed be caused by the approximate radiation pattern (37) used as target, or to intrinsical limitations in the TREC.

B. Time domain : causality and back-lobe radiation

The results in Fig. 9 present a back-lobe radiation related to the long-range correlation of the PSF. Its physical meaning becomes clear when studying the PSF in the time domain. We have considered the same case as in the previous section, with an equivalent-source surface of radius $r_\Sigma = 3\lambda$, imposing an unchanged radiation pattern over a relative bandwidth $B_T/f_c = 10\ \%$ around the central frequency f_c of the wavefront excitation. All results are normalized to the central frequency.

Following these choices, the field distribution over the xy-cut of Σ was computed in the time domain, yielding the results

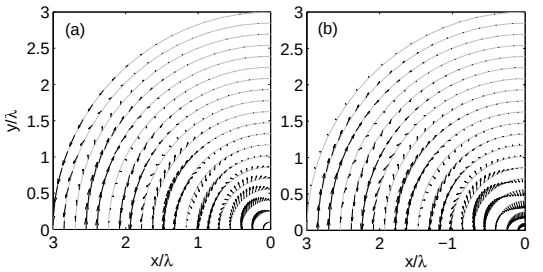

Fig. 11: Vector representation of the normalized electric field $\mathsf{E}\left[\boldsymbol{E}_{\rm TR}(\boldsymbol{r},\omega)\right]/G(r,\omega)$ shown in Fig. 10: (a) real and (b) imaginary part. As the wavefront closes onto the focal region, the electric field passes from the TEM configuration typical of far-field radiation to a $\hat{\boldsymbol{y}}$-oriented configuration, reminiscent of the original field distribution of the synthetic aperture.

shown in Fig. 12. Here, the field over the xy-cut of Σ is shown as an angular distribution function of the time, proving that the back lobe is actually the time-delayed replica of the impinging wavefront. The delay τ is equal to a normalized delay $f_c\tau = 6$, which coincides with a free-space propagation across a sphere of radius 3λ, since $f_c\tau = 2r_\Sigma/\lambda = 6$. Causality is thus preserved, indicating that the proposed model is capable of correctly assessing time-domain phenomena. In particular, the previous results dealing with the focusing of energy can be rightly interpreted as due to a convergent wavefront, while the presence of the back-lobe is necessary for the causality of the solution yielded by (16).

A non-ideality of the TREC method is apparent in Fig. 12(b): the wavefront emerging from the focal region is slightly distorted for the directions away from the main lobe. This fact corresponds to the an error in the position of the focusing spot of about $\lambda/8$, a fact that leaves room to the interpretation of these errors as due to the use of the approximate model (37). This notwithstanding, these errors do not affect the conclusions of our work, as the proposed method is clearly capable of a remarkably accurate reproduction of free-space propagation within a wave-diffusive medium.

IX. Summary and discussions

We reckon that at this point it is important to summarize the main results and ideas introduced in this paper. The concept of time-reversed wavefronts has been revisited in a novel manner, by looking at an originally diverging wavefront as being radiated by equivalent currents, as opposed to the standard approach based on a physical (and often point-like) source. This different approach allows the introduction of synthetic sources, which can be characterized by ideal features not easily found in real-life sources. Moreover, these features can be changed in real-time through a simple post-processing procedure, yielding new excitation signals to be applied to the ports of the TRM antennas. As a result, a wave-diffusive medium can be “converted” into an anechoic one where deterministic wavefronts propagate as in a free-space

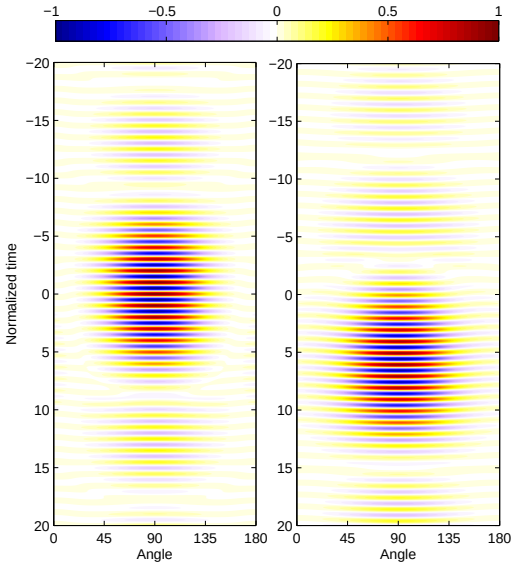

Fig. 12: Time-domain results for the $\hat{\boldsymbol{\varphi}}$ component of the average field generated by a TREC, as computed over a spherical surface of radius $r_\Sigma = 3\lambda$, for a relative bandwidth $B_T/f_c = 10\ \%$. The signal was chosen to have a constant spectrum over B_T, i.e., to have a sine cardinal profile in the time domain. The results refer to the xy-cut of : (a) the converging wavefront impinging over Σ, along the negative part of the x-axis; (b) the diverging wavefront observed on the opposed direction.

environment; interestingly, no hypothesis is needed about an eventual link between the direction of arrival of the wavefront and the positions of the TRM antennas, thanks to the diffusive nature of the medium.

This surprising result entirely relies on the knowledge of Green's functions between the equivalent-source surface Σ and the TRM antennas. These data can be readily measured by means of low-scattering probes moved over Σ, as describe in [8]. Previous experimental validations of the TREC approach are indeed already available in the literature. In this paper we rather aimed at providing a deeper insight into the physics of the TREC, from a theoretical point of view, in order to have a better understanding of its intrinsical limitations, whence our emphasizing theoretical and numerical results.

What is most surprising is that the coupling of time-reversed excitations to a diffusive cavity through the use of synthetic sources allows generating any kind of wavefront, on average. The question of how far the generated wavefront is from the average one can be directly assessed by recalling the concept of intrinsical SNR due to the inevitable finite number of degrees of freedom available within the cavity. This issue was studied in [11] and the main results are recalled in Appendix B, where it is shown that the actual response of a TREC is very close to its ensemble average.

The potential use of the TREC as a new kind of testing facility clearly implies the inclusion of an EUT into the test-volume defined by Σ. It goes without saying that the presence of the EUT can have a dramatic impact on the Green's functions that would be observed with and without the EUT. As a result, the EUT needs to be present during the characterization phase yielding the $\boldsymbol{N}_{\mathrm{eq},i}(\boldsymbol{r},\boldsymbol{r}',\omega)$ functions. Without entering into details, the presence of an EUT could impact the resulting wavefront at two levels: 1) by modifying the wavefront radiated by the equivalent currents; 2) by modifying the Green's functions within the cavity. The first point is actually not a real issue, since the equivalence theorem ensures that the use of electric and magnetic currents implies that only an outwards radiation (first phase) would take place, thus not interacting with the EUT found within Σ. As a result, the average wavefront generated by the TREC should be expected to be the same with and without an EUT, as long as the diffuse-field assumption holds, thanks to the self-averaging property of time reversal [27]. This point is fundamental if the TREC is to be used as a testing facility, since a reproducible wavefront independent of the EUT position, orientation and nature is a necessary condition for any metrology application.

A crucial issue is the question of the energy efficiency of the proposed procedure. We have not considered this point in the context of this paper, but it had already received attention in a previous work [39], where it was shown that the TREC also improves the ability to generate high-intensity peaks of electromagnetic power by a factor easily exceeding one hundred, with respect to standard harmonic excitations in an RC.

From a practical point of view, the simplifying assumptions used throughout the paper should be taken for what they are, i.e., not requirements, but just simplifications. For example, whenever the equivalent-current surface is not in the far-field region of the synthetic source, the TREC will reproduce the propagative part of the radiation pattern, filtering out the reactive part; the often dispersive response of electronic devices and antennas can be compensated when synthesizing the excitation signals; the average coupling between the TRM antennas can be kept as low as needed since they are operated in a wave-diffusive medium, i.e., with a weak spatial correlation.

X. Conclusions

In this paper we have investigated the potential advantages of applying TR techniques to tests based on the use of predefined wavefronts. Having found that these are not straightforwardly suitable for this purpose, an alternative approach, the TREC, has been introduced. A theoretical analysis has proved how the TREC enables a number of once held impossible features in a reverberation chamber, namely the generation of short-pulsed fields and a detailed control of the parameters of wavefronts. More specifically, the use of TR leads to an equivalent Green's function that appears to be very close to that of a free-space environment. The TREC is hence capable of recreating within a reverberation chamber the necessary conditions for the arbitrary generation of wavefronts.

As a result, it was shown that the TREC allows the definition of a testing environment sharing the advantages of anechoic and reverberation chambers, namely the possibility of knowing exactly the type of EM wavefront (polarization, direction of arrival, time-dependence) testing the EUT response, while maintaining the high energetic efficiency of reverberation chambers. Furthermore, it was shown that the test wavefront can be ideally steered in real-time, without requiring any mechanical displacement of the antennas. The use of fast-steered deterministic test wavefronts could lead to faster R&D cycles, giving a clearer information about the response of an EUT to impinging wavefronts.

Appendix A
RMS value of the $\boldsymbol{N}(\boldsymbol{r},\omega)$ transfer functions for a diffusive reverberation chamber

Following the conventions introduced in section VI, the field radiated by a TRM antenna is given by

$$\boldsymbol{E}(\boldsymbol{r},\omega) = \boldsymbol{N}_{\mathrm{e}}(\boldsymbol{r},\omega)\frac{V_{\mathrm{ex}}(\omega)}{Z_{\mathrm{ant}}(\omega)}h_e(\omega). \tag{38}$$

Assuming a purely resistive input impedance for the antennas and a perfectly matched generator leads to

$$\frac{\|\boldsymbol{E}(\boldsymbol{r},\omega)\|^2}{P_{\mathrm{av}}(\omega)} = \frac{4|h_e(\omega)|^2}{Z_{\mathrm{ant}}(\omega)}\|\boldsymbol{N}_{\mathrm{e}}(\boldsymbol{r},\omega)\|^2, \tag{39}$$

with $P_{\mathrm{av}}(\omega)$ the available power of the generator. Computing the ensemble average of (39) and recalling the uniformity property for the electric field in a diffusive cavity yields

$$\begin{aligned} N^2_{\mathrm{e,av}}(\omega) &= \mathsf{E}\left[\|\boldsymbol{N}_{\mathrm{e}}(\boldsymbol{r},\omega)\|^2\right] \\ &= \frac{Z_{\mathrm{ant}}(\omega)}{4|h_e(\omega)|^2}\mathsf{E}\left[\frac{\|\boldsymbol{E}(\boldsymbol{r},\omega)\|^2}{P_{\mathrm{av}}(\omega)}\right], \end{aligned} \tag{40}$$

thus showing how $N^2_{\mathrm{e,av}}(\omega)$ is related to the average energy efficiency of the cavity $\mathsf{E}\left[\|\boldsymbol{E}(\boldsymbol{r},\omega)\|^2/P_{\mathrm{av}}(\omega)\right]$ through the electrical parameters of the TRM antenna. For the special case of a reverberation chamber, the energy efficiency can be estimated in a straightforward manner as [35]

$$\mathsf{E}\left[\frac{\|\boldsymbol{E}(\boldsymbol{r},\omega)\|^2}{P_{\mathrm{av}}(\omega)}\right] = \frac{4\zeta_0}{\pi}\frac{Q(\omega)\lambda}{V}. \tag{41}$$

where $Q(\omega)$ is the average composite quality factor of the cavity, V is the volume of the medium filling it and λ the average wavelength corresponding to the frequency of excitation of the cavity. This result is straightforwardly linked to the variance of any Cartesian component of the electric field and the covariance of orthogonal components of the electric and magnetic field as

$$\mathsf{E}\left[|\hat{\boldsymbol{u}}_m \cdot \boldsymbol{N}_{\mathrm{e}}(\boldsymbol{r},\omega)|^2\right] = \frac{N^2_{\mathrm{e,av}}(\omega)}{3} \tag{42a}$$

$$\mathsf{E}\left[\hat{\boldsymbol{u}}_m \cdot \boldsymbol{N}_{\mathrm{e}}(\boldsymbol{r},\omega)\ \hat{\boldsymbol{u}}_n \cdot \bar{\boldsymbol{N}}_{\mathrm{m}}(\boldsymbol{r},\omega)\right] = \frac{N^2_{\mathrm{e,av}}(\omega)}{3\zeta_0} \tag{42b}$$

with $\hat{\boldsymbol{u}}_m \cdot \hat{\boldsymbol{u}}_n = 0$. The above result relies on the average isotropy of the electric and magnetic fields in a diffusive cavity.

Appendix B
Fluctuations in time-reversed wavefronts

The reason why the results presented in this paper always deal with ensemble averages is the self-averaging property typical of non-harmonic TR applications [27], [28]. This property is inherited by the fact that for a finite bandwidth B_T of excitation, the coherent excitation of a complex medium implies an average over B_T, that can be shown to approximate an ensemble average.

For the special case of bounded media with low losses, it has been shown that time-reversed signals are affected by a residual error in the transmission through the medium, due to the physical impossibility of efficiently transmitting certain spectral components in a steady-state configuration. As soon as frequency-selective media are considered, this residual error, intrinsical to the very procedure of time-reversal transmissions, can be assimilated to a background noise, or intrinsical noise. Its rms intensity can be straightforwardly linked to a few parameters, such as the average composite quality factor $Q(f_c)$ evaluated at the central frequency and the fractional bandwidth B_T/f_c [11]. By defining the intrinsical SNR Λ_p as the ratio between the peak instantaneous power of the coherent part of the time-reversed signal and the rms power of the residual noise, it can be proven that

$$\Lambda_p = \Lambda\frac{Q(f_c)\kappa^2}{\pi}\frac{B_T}{f_c}, \tag{43}$$

where Λ is the energy SNR, which can be shown to be close to one for a diffusive medium [11], while κ is the ratio of the real part of the average of $X(\omega)$ over its rms value, both defined over the bandwidth B_T.

Assuming the residual error to behave as a normally-distributed random variable, its rms amplitude coincides with its standard deviation σ_n. The confidence interval within which the fluctuations are expected to be found with a probability of, e.g., 95 %, is thus simply given by the interval $\pm 2\sigma_n$, resulting in a relative confidence margin around the peak value of the transmitted signal

$$\frac{\Delta E}{E} = \frac{2}{\sqrt{\Lambda_p}} = \frac{2}{\kappa}\sqrt{\frac{\pi f_c}{Q(f_c)B_T}}. \tag{44}$$

As a practical example, let us consider a moderately resonant cavity with $Q = 5\cdot 10^4$, $B_T/f_c = 5$ % and a sine cardinal signal excitation, i.e., $\kappa = 1$, yielding a range of fluctuations of about ± 7 %, with a confidence of 95 %. Such a low level of deviations is the reason why having access to a model of the average response is indeed representative of the actual response observed for a specific configuration.

References

[1] J. Toivanen, T. Laitinen, V. Kolmonen, and P. Vainikainen, "Reproduction of arbitrary multipath environments in laboratory conditions," *Instrumentation and Measurement, IEEE Transactions on*, vol. 60, no. 1, pp. 275 –281, jan. 2011.

[2] D. Ward and T. Abhayapala, "Reproduction of a plane-wave sound field using an array of loudspeakers," *Speech and Audio Processing, IEEE Transactions on*, vol. 9, no. 6, pp. 697 –707, sep 2001.

[3] P. Kildal, "Overview of 6 years R&D on characterizing wireless devices in Rayleigh fading using reverberation chambers," in *International Workshop on Antenna Technology: Small and Smart Antennas Metamaterials and Applications, 2007. IWAT'07.* IEEE, 2007, pp. 162–165.
[4] D. Hill, "Plane wave integral representation for fields in reverberation chambers," *IEEE Transactions on Electromagnetic Compatibility*, vol. 40, no. 3, pp. 209–217, 1998.
[5] P. Corona, G. Ferrara, and M. Migliaccio, "Reverberating chambers as sources of stochastic electromagnetic fields," *IEEE Transactions on Electromagnetic Compatibility*, vol. 38, no. 3, pp. 348 –356, Aug 1996.
[6] P.-S. K. M. Bäckström, O. Lundén, "Reverberation chambers for emc susceptibility and emission analyses," in *Review of Radio Science 1999-2002*, 2002, pp. 429–452.
[7] J. de Rosny, G. Lerosey, and M. Fink, "Theory of electromagnetic time-reversal mirrors," *IEEE Transactions on Antennas and Propagation*, vol. 58, no. 10, pp. 3139–3149, 2010.
[8] H. Moussa, A. Cozza, and M. Cauterman, "Experimental demonstration of directive pulsed wavefront generation in reverberation chambers," *Electronics Letters*, vol. 46, no. 9, pp. 623–624, 2010.
[9] C. Oestges, A. Kim, G. Papanicolaou, and A. Paulraj, "Characterization of space-time focusing in time-reversed random fields," *IEEE Transactions on Antennas and Propagation*, vol. 53, no. 1, pp. 283 – 293, jan. 2005.
[10] H. Moussa, A. Cozza, and M. Cauterman, "Directive wavefronts inside a time reversal electromagnetic chamber," in *IEEE EMC Symposium, Austin, Texas, 2009.*, 2009.
[11] A. Cozza, "Statistics of the performance of time reversal in a lossy reverberating medium," *Physical Review E*, vol. 80, no. 5, p. 56604, 2009.
[12] A. Yariv, "Phase conjugate optics and real-time holography," *IEEE Journal of Quantum Electronics*, vol. 14, no. 9, pp. 650–660, 1978.
[13] D. Cassereau and M. Fink, "Time-reversal of ultrasonic fields. III. Theory of the closed time-reversal cavity," *IEEE Transactions on Ultrasonics, Ferroelectrics and Frequency Control*, vol. 39, no. 5, pp. 579–592, 2002.
[14] C. Draeger and M. Fink, "One-channel time-reversal in chaotic cavities: Theoretical limits," *The Journal of the Acoustical Society of America*, vol. 105, p. 611, 1999.
[15] G. Lerosey, J. de Rosny, A. Tourin, A. Derode, G. Montaldo, and M. Fink, "Time reversal of electromagnetic waves," *Physical Review Letters*, vol. 92, no. 19, p. 193904, 2004.
[16] P. Roux, B. Roman, and M. Fink, "Time-reversal in an ultrasonic waveguide," *Applied Physics Letters*, vol. 70, p. 1811, 1997.
[17] E. Joy and D. Paris, "Spatial sampling and filtering in near-field measurements," *IEEE Transactions on Antennas and Propagation*, vol. 20, no. 3, pp. 253–261, 1972.
[18] *Environmental Conditions and Test Procedures for Airborne Equipment*, Radio Technical Commission for Aeronautics (RTCA) Std. DO-160E, 2005.
[19] C. Prada and M. Fink, "Eigenmodes of the time reversal operator: A solution to selective focusing in multiple-target media," *Wave Motion*, vol. 20, no. 2, pp. 151–163, 1994.
[20] F. Gruber, E. Marengo, and A. Devaney, "Time-reversal imaging with multiple signal classification considering multiple scattering between the targets," *The Journal of the Acoustical Society of America*, vol. 115, p. 3042, 2004.
[21] W. Kuperman, W. Hodgkiss, H. Song, T. Akal, C. Ferla, and D. Jackson, "Phase conjugation in the ocean: Experimental demonstration of an acoustic time-reversal mirror," *The Journal of the Acoustical Society of America*, vol. 103, p. 25, 1998.
[22] G. Lerosey, J. De Rosny, A. Tourin, A. Derode, G. Montaldo, and M. Fink, "Time reversal of electromagnetic waves and telecommunication," *Radio Science*, vol. 40, no. 6, 2005.
[23] M. Yavuz and F. Teixeira, "Full time-domain dort for ultrawideband electromagnetic fields in dispersive, random inhomogeneous media," *IEEE Transactions on Antennas and Propagation*, vol. 54, no. 8, pp. 2305–2315, 2006.
[24] R. Sullivan, *Microwave radar: Imaging and advanced concepts*. Artech House, Inc. Norwood, MA., 2000.
[25] R. Harrington, "On the gain and beamwidth of directional antennas," *IRE Transactions on Antennas and Propagation*, vol. 6, no. 3, pp. 219–225, 1958.
[26] ——, *Time-Harmonic Electromagnetic Fields*. McGraw-Hill, New York, NY, 1961.
[27] A. Derode, A. Tourin, and M. Fink, "Random multiple scattering of ultrasound. II. Is time reversal a self-averaging process?" *Physical Review E*, vol. 64, no. 3, p. 36606, 2001.
[28] J. Fouque and G. Papanicolaou, *Wave Propagation and Time Reversal in Randomly Layered Media*. Springer Verlag, 2007.
[29] J. Stamnes, *Waves in focal regions: propagation, diffraction, and focusing of light, sound, and water waves*. Taylor & Francis, 1986.
[30] C. Draeger, J. Aime, and M. Fink, "One-channel time-reversal in chaotic cavities: Experimental results," *The Journal of the Acoustical Society of America*, vol. 105, p. 618, 1999.
[31] A. Ishimaru, *Wave propagation and scattering in random media*. Wiley-IEEE Press, 1999, vol. 12.
[32] J. Davy, "The relative variance of the transmission function of a reverberation room," *Journal of Sound and Vibration*, vol. 77, no. 4, pp. 455–479, 1981.
[33] A. Cozza, "The Role of Losses in the Definition of the Overmoded Condition for Reverberation Chambers and Their Statistics," *IEEE Transactions on Electromagnetic Compatibility*, no. 53, pp. 296–307, 2010.
[34] D. Hill and J. Ladbury, "Spatial-correlation functions of fields and energy density in a reverberation chamber," *IEEE Transactions on Electromagnetic Compatibility*, vol. 44, no. 1, pp. 95–101, 2002.
[35] D. Hill, "Electromagnetic Theory of Reverberation Chambers," National Institute of Standards and Technology, Tech. Rep., 1998.
[36] E. Wolf, *Introduction to the Theory of Coherence and Polarization of Light*. Cambridge University Press, 2007.
[37] A. Cozza and H. Moussa, "Enforcing deterministic polarisation in a reverberating environment," *Electronics Letters*, vol. 45, no. 25, pp. 1299–1301, 2009.
[38] ——, "Polarization selectivity for pulsed fields in a reverberation chamber," in *2010 Asia-Pacific Symposium on Electromagnetic Compatibility (APEMC)*. IEEE, 2010, pp. 574–577.
[39] A. Cozza, "Increasing peak-field generation efficiency of reverberation chamber," *Electronics Letters*, vol. 46, no. 1, pp. 38–39, 2010.

Appendix C

Complete list of publications

Peer-reviewed journals

[J1] L. Abboud, A. Cozza, and L. Pichon, *A Matched-Pulse Approach for Soft-Fault Detection in Complex Wire Networks*, IEEE Transactions on Instrumentation and Measurement, 61 (2012), pp. 1719–1732.

[J2] A. Cozza, *Statistics of the performance of time reversal in a lossy reverberating medium*, Physical Review E: Statistical, Nonlinear, and Soft Matter Physics, 80 (2009), pp. 056604–056614.

[J3] ——, *Increasing peak-field generation efficiency of reverberation chamber*, IET Electronics Letters, 46 (2010), pp. 38–39.

[J4] ——, *The Role of Losses in the Definition of the Overmoded Condition for Reverberation Chambers and Their Statistics*, IEEE Transactions on Electromagnetic Compatibility, 53 (2011), pp. 296–307.

[J5] ——, *Emulating an Anechoic Environment in a Wave-Diffusive Medium through an Extended Time-Reversal Approach*, IEEE Transactions on Antennas and Propagation, (2012). Accepted for publication.

[J6] ——, *Linking the Energy Efficiency of Time-Reversal Transmissions through Severe Indoor Channels to the Degree of Field Diffusion*, IEEE Transactions on Antennas and Propagation, (2012). Under review.

[J7] ——, *Probability Distributions of Local Modal-Density Fluctuations in an Electromagnetic Cavity*, IEEE Transactions on Electromagnetic Compatibility, (2012). Accepted for publication.

[J8] ——, *Source Correlation in Randomly Excited Complex Media*, IEEE Antennas and Wireless Propagation Letters, 11 (2012), pp. 105–108.

[J9] A. COZZA AND A. ABOU-EL-AILEH, *Accurate Radiation-Pattern Measurements in a Time-Reversal Electromagnetic Chamber*, IEEE Antennas and Propagation Magazine, 52 (2010), pp. 186–193.

[J10] A. COZZA AND B. DEMOULIN, *On the modeling of electric railway lines for the assessment of infrastructure impact in radiated emission tests of rolling stock*, IEEE Transactions on Electromagnetic Compatibility, 50 (2008), pp. 566–576.

[J11] ——, *Closed-form expressions for the total power radiated by an electrically long multiconductor line*, IEEE Transactions on Electromagnetic Compatibility, 51 (2009), pp. 119 – 130.

[J12] A. COZZA AND B. DERAT, *On the dispersive nature of the power dissipated into a lossy half-space close to a radiating source*, IEEE Transactions on Antennas and Propagation, 57 (2009), pp. 2572–2582.

[J13] A. COZZA AND H. MOUSSA, *Enforcing a deterministic polarization in a reverberating environment*, IET Electronics Letters, 45 (2009), pp. 1299–1301.

[J14] F. MONSEF AND A. COZZA, *Limitations of the equivalence between spatial and ensemble estimators in the case of a single-tone excitation*, Journal of the Acoustical Society of America, 130 (2011), pp. 1943–1953.

[J15] H. MOUSSA, A. COZZA, AND M. CAUTERMAN, *Experimental demonstration of directive pulsed wavefront generation in reverberation chambers*, IET Electronics Letters, 46 (2010), pp. 623–624.

Peer-reviewed conferences

[C1] L. ABBOUD, A. COZZA, AND L. PICHON, *Utilization of matched pulses to improve fault detection in wire networks*, in 2009 International Conference on ITS Telecommunications, Aug. 2009.

[C2] ——, *Impact of network topology on matched-pulse-based fault detection*, in Progress in Electromagnetic Research Symposium (PIERS'10), Mar. 2010.

[C3] ——, *Performance analysis of the matched-pulse-based fault detection*, in Complex Systems Design & Management (CSDM 2010), Oct. 2010.

[C4] ——, *A Distributed Non-Iterative Approach for Soft-Fault Location in Complex Wire Networks*, in ISEM 2011, Sept. 2011.

[C5] A. COZZA, *An Experimental Method for Assessing the Modal Density in a Reverberation Chamber*, in 2010 Asia-Pacific Symposium on Electromagnetic Compatibility (APEMC), Apr. 2010.

[C6] ——, *Estimating the Expected Power Density in a Reverberating Cavity Through Space Averaging*, in 20th URSI International Symposium on Electromagnetic Theory, Aug. 2010.

[C7] ——, *A Skeptic's View of Unstirred Components*, in EMC Europe 2011, Sept. 2011.

[C8] ——, *Coherent wavefront synthesis in a wave-diffusive medium*, in 2012 IEEE International Symposium on Antennas and Propagation and USNC-URSI National Radio Science Meeting, July 2012.

[C9] A. COZZA AND A. ABOU-EL-AILEH, *Accurate radiation pattern measurements in a time-reversal electromagnetic chamber*, in 31st Annual Symposium of the Antenna Measurement Techniques Association (AMTA 2009), Nov. 2009.

[C10] A. COZZA, F. CANAVERO, AND B. DÉMOULIN, *High-frequency extension of the transmission-line theory for an open line*, in 12ème Colloque International et Exposition sur la Compatibilité Electromagnétique, CEM'04, 2004.

[C11] ——, *A Closed-Form Formulation for the Total Power Radiated by a Single-Wire Overhead Line*, in 16th International Symposium on Electromagnetic Compatibility, EMC Zurich, Feb. 2005.

[C12] A. COZZA, F. CANAVERO, B. DÉMOULIN, J.-M. BODSON, V. SABATE, AND J.-M. VANZEMBERG, *Experimental analysis of a multi-conductor uniform line above soil for modelling a railway line*, in 12ème Colloque International et Exposition sur la Compatibilité Electromagnétique, CEM'04, 2004.

[C13] A. COZZA, B. DERAT, AND N. RIBIÈRE-THARAUD, *A new SAR assessment procedure for homogeneous and heterogeneous flat-phantoms based on near-field free-space measurements*, in 29th Annual Symposium of the Antenna Measurement Techniques Association (AMTA 2007), Nov. 2007.

[C14] A. COZZA, C. GALLE, J.-P. BRASILE, AND C. CARREL, *Sensing Coupling Paths in an Equipment*, in 2012 Asia-Pacific International Symposium on Electromagnetic Compatibility, May 2012.

[C15] A. COZZA, W.J. KOH, Y.S. NG, AND Y.Y. TAN, *Controlling the State of a Reverberation Chamber by means of a Random Multiple-Antenna Stirring*, in 2012 Asia-Pacific International Symposium on Electromagnetic Compatibility, May 2012.

[C16] A. COZZA, O. MERCKEL, AND J.-C. BOLOMEY, *A probe-array approach for near-field measurements and field reconstruction in a lossy medium*, in 3rd International Conference on Electromagnetic Near-Field Characterization and Imaging (ICONIC 2007), June 2007.

[C17] A. COZZA AND F. MONSEF, *How a Physical Definition of Overmodedness Can Explain Local Statistical Non-Compliancy*, in EMC Europe 2011, Sept. 2011.

[C18] A. COZZA AND H. MOUSSA, *Polarization selectivity for pulsed fields in a reverberation chamber*, in 2010 Asia-Pacific Symposium on Electromagnetic Compatibility (APEMC), Apr. 2010.

[C19] B. DERAT, A. COZZA, AND J.-C. BOLOMEY, *Influence of source - phantom multiple interactions on the field transmitted in a flat phantom*, in 18th International Zurich Symposium on Electromagnetic Compatibility (EMC Zürich 07), Sept. 2007.

[C20] B. DERAT, A. COZZA, O. MERCKEL, AND J.-C. BOLOMEY, *Numerical analysis of a printed E-field RF probe-array used for rapid SAR assessment*, in 23rd Annual Review of Progress in Applied Computational Electromagnetics (ACES 2007), June 2007.

[C21] F. MONSEF AND A. COZZA, *Analysis of Time-Reversal-Based Propagation for Spatial focusing and Multiplexing*, in IEEE-APS Topical Conference on Antennas and Propagation in Wireless Communications, Sept. 2011.

[C22] ——, *Goodness-of-Fit Tests in Radiated Susceptibility Tests*, in 2012 ESA Workshop on Aerospace EMC, May 2012.

[C23] F. MONSEF, A. COZZA, AND L. ABBOUD, *Effectiveness of Time-Reversal technique for UWB wireless communications in standard indoor environments*, in 20th International Conference on Applied Electromagnetics and Communications, Sept. 2010.

[C24] H. MOUSSA, A. COZZA, AND M. CAUTERMAN, *A novel way of using reverberation chambers through time reversal*, in ESA Workshop on Aerospace EMC (ESA'09), Mar. 2009.

[C25] ——, *Directive Wavefronts Inside a Time Reversal Electromagnetic Chamber*, in IEEE EMC Society Symposium on Electromagnetic Compatibility (IEEE EMC Symposium 2009), Aug. 2009.

[C26] ——, *Experimental analysis of the performance of a time-reversal electromagnetic chamber*, in 2010 Asia-Pacific Symposium on Electromagnetic Compatibility (APEMC), Apr. 2010.

[C27] ——, *Vérification expérimentale des performances d'une chambre électromagnétique à retournement temporel*, in Colloque International et Exposition sur la Compatibilité Electromagnétique (CEM 2010), Apr. 2010.

Patents

[P1] A. Cozza, B. Derat, and S. Pannetrat, *Système pour mesurer un champ électromagnétique*, July 2011.

[P2] A. Cozza and H. Moussa, *Procédé de contrôle de la directivité et la polarisation de distributions cohérentes de champ dans un milieu réverbérant*, April 2011.

References

[R1] *Environmental conditions and test procedures for airborne equipment*, Tech. Report DO-160E, Washington DC, USA, 2005.

[R2] *IEC standard 61000 : Electromagnetic compatibility (EMC) - part 4-21: Testing and measurement techniques - reverberation chamber test methods*, 2011.

[R3] L.R. ARNAUT, *Statistics of the quality factor of a rectangular reverberation chamber*, IEEE Transactions on Electromagnetic Compatibility, 45 (2003), pp. 61 – 76.

[R4] ——, *Effect of size, orientation, and eccentricity of mode stirrers on their performance in reverberation chambers*, IEEE Transactions on Electromagnetic Compatibility, 48 (2006), pp. 600–602.

[R5] M.V. BERRY AND M. TABOR, *Level clustering in the regular spectrum*, Proceedings of the Royal Society of London A: Mathematical and Physical Sciences, 356 (1977), pp. 375–394.

[R6] O. BOHIGAS, M.J. GIANNONI, AND C. SCHMIT, *Characterization of chaotic quantum spectra and universality of level fluctuation laws*, Physical Review Letters, 52 (1984), pp. 1–4.

[R7] L. BORCEA, G. PAPANICOLAOU, C. TSOGKA, AND J. BERRYMAN, *Imaging and time reversal in random media*, Inverse Problems, 18 (2002), p. 1247.

[R8] L. BRILLOUIN, *Wave propagation in periodic structures: electric filters and crystal lattices*, Dover Publications, 1953.

[R9] D. CASSEREAU AND M. FINK, *Time-reversal of ultrasonic fields. III. Theory of the closed time-reversal cavity*, IEEE Transactions on Ultrasonics, Ferroelectrics and Frequency Control, 39 (2002), pp. 579–592.

[R10] S. CHANDRASEKHAR, *Radiative transfer*, Dover Publications, 1960.

[R11] N. CHERNOV AND R. MARKARIAN, *Chaotic billiards*, vol. 127, American Mathematical Society, 2006.

[R12] P.C. CLEMMOW, *The Plane wave spectrum representation of electromagnetic fields*, Pergamon Press, 1966.

[R13] P. CORONA, G. FERRARA, AND M. MIGLIACCIO, *A spectral approach for the determination of the reverberating chamber quality factor*, IEEE Transactions on Electromagnetic Compatibility, 40 (1998), pp. 145 –153.

[R14] T.J. COX AND P. D'ANTONIO, *Acoustic absorbers and diffusers: theory, design and application*, Taylor & Francis Group, 2009.

[R15] R.B. D'AGOSTINO AND M.A. STEPHENS, *Goodness-of-fit techniques*, CRC, 1986.

[R16] A. DERODE, A. TOURIN, AND M. FINK, *Random multiple scattering of ultrasound. II. Is time reversal a self-averaging process?*, Physical Review E, 64 (2001), p. 36606.

[R17] C. DRAEGER, J.C. AIME, AND M. FINK, *One-channel time-reversal in chaotic cavities: Experimental results*, The Journal of the Acoustical Society of America, 105 (1999), p. 618.

[R18] C. DRAEGER AND M. FINK, *One-channel time reversal of elastic waves in a chaotic 2D-silicon cavity*, Physical Review Letters, 79 (1997), pp. 407–410.

[R19] ——, *One-channel time-reversal in chaotic cavities: Theoretical limits*, The Journal of the Acoustical Society of America, 105 (1999), p. 611.

[R20] A. EINSTEIN, *Investigations on the Theory of the Brownian Movement*, Dover Publications, 1956.

[R21] L.B. FELSEN AND N. MARCUVITZ, *Radiation and scattering of waves*, vol. 31, Wiley-IEEE press, 1994.

[R22] M. FINK AND C. PRADA, *Acoustic time-reversal mirrors*, Inverse Problems, 17 (2001), p. R1.

[R23] J.P. FOUQUE, J. GARNIER, G. PAPANICOLAOU, AND K. SØLNA, *Wave Propagation and Time Reversal in Randomly Layered Media*, Springer Verlag, 2007.

[R24] I. FREUND, M. ROSENBLUH, AND S. FENG, *Memory effects in propagation of optical waves through disordered media*, Physical review letters, 61 (1988), pp. 2328–2331.

[R25] G.J. FREYER, M.O. HATFIELD, D.M. JOHNSON, AND M.B. SLOCUM, *Comparison of measured and theoretical statistical parameters of complex cavities*, in IEEE International Symposium on Electromagnetic Compatibility, aug 1996, pp. 250 –253.

[R26] J.W. GOODMAN, *Speckle phenomena in optics: theory and applications*, Roberts & Co., 2007.

[R27] F.K. GRUBER, E.A. MARENGO, AND A.J. DEVANEY, *Time-reversal imaging with multiple signal classification considering multiple scattering between the targets*, The Journal of the Acoustical Society of America, 115 (2004), p. 3042.

[R28] A. GUINIER, *X-ray diffraction in crystals, imperfect crystals, and amorphous bodies*, Dover Publications, 1994.

[R29] F. HAAKE, G. LENZ, P. SEBA, J. STEIN, H.J. STÖCKMANN, AND K. ŻYCZKOWSKI, *Manifestation of wave chaos in pseudointegrable microwave resonators*, Physical Review A, 44 (1991), pp. 6161–6164.

[R30] R.F. HARRINGTON, *Time-Harmonic Electromagnetic Fields*, McGraw-Hill, New York, NY, 1961.

[R31] D.A. HILL, *Electronic mode stirring for reverberation chambers*, IEEE Transactions on Electromagnetic Compatibility, 36 (1994), pp. 294 –299.

[R32] ——, *Spatial correlation function for fields in a reverberation chamber*, IEEE Transactions on Electromagnetic Compatibility, 37 (1995).

[R33] ——, *Electromagnetic Theory of Reverberation Chambers*, tech. report, National Institute of Standards and Technology, 1998.

[R34] ——, *Plane wave integral representation for fields in reverberation chambers*, IEEE Transactions on Electromagnetic Compatibility, 40 (1998), pp. 209–217.

[R35] D.A. HILL AND J.M. LADBURY, *Spatial-correlation functions of fields and energy density in a reverberation chamber*, IEEE Transactions on Electromagnetic Compatibility, 44 (2002), pp. 95–101.

[R36] C.L. HOLLOWAY, D.A. HILL, J.M. LADBURY, AND G. KOEPKE, *Requirements for an effective reverberation chamber: unloaded or loaded*, IEEE Transactions on Electromagnetic Compatibility, 48 (2006), pp. 187–194.

[R37] Y. HUANG, N. ABUMUSTAFA, Q.G. WANG, AND X. ZHU, *Comparison of two stirrer designs for a new reverberation chamber*, in Environmental Electromagnetics, The 2006 4th Asia-Pacific Conference on, aug. 2006, pp. 450–453.

[R38] A. ISHIMARU, *Wave propagation and scattering in random media*, vol. 12, Wiley-IEEE Press, 1999.

[R39] F. JACOBSEN AND A.R. MOLARES, *Sound power emitted by a pure-tone source in a reverberation room*, Journal of the Acoustical Society of America, 126 (2009), p. 676.

[R40] F. JAMES, *Statistical methods in experimental physics*, World Scientific, 2006.

[R41] S. KIM, W.A. KUPERMAN, W.S. HODGKISS, H.C. SONG, G. EDELMANN, AND T. AKAL, *Echo-to-reverberation enhancement using a time reversal mirror*, The Journal of the Acoustical Society of America, 115 (2004), p. 1525.

[R42] J.G. KOSTAS AND B. BOVERIE, *Statistical model for a mode-stirred chamber*, IEEE Transactions on Electromagnetic Compatibility, 33 (1991), pp. 366 –370.

[R43] WA KUPERMAN, W.S. HODGKISS, H.C. SONG, T. AKAL, C. FERLA, AND D.R. JACKSON, *Phase conjugation in the ocean: Experimental demonstration of an acoustic time-reversal mirror*, The Journal of the Acoustical Society of America, 103 (1998), p. 25.

[R44] K.H. KUTTRUFF, *Room acoustics*, Taylor & Francis, 2000.

[R45] T.H. LEHMAN, *A statistical theory of electromagnetic fields in complex cavities*, Interaction Notes, Note 494, (1993).

[R46] C. LEMOINE, P. BESNIER, AND M. DRISSI, *Investigation of reverberation chamber measurements through high-power goodness-of-fit tests*, IEEE Transactions on Electromagnetic Compatibility, 49 (2007), pp. 745 –755.

[R47] G. LEROSEY, J. DE ROSNY, A. TOURIN, A. DERODE, AND M. FINK, *Time reversal of wideband microwaves*, Applied Physics Letters, 88 (2006), p. 154101.

[R48] G. LEROSEY, J. DE ROSNY, A. TOURIN, A. DERODE, G. MONTALDO, AND M. FINK, *Time reversal of electromagnetic waves*, Physical Review Letters, 92 (2004), p. 193904.

[R49] G. LEROSEY, J. DE ROSNY, A. TOURIN, A. DERODE, G. MONTALDO, AND M. FINK, *Time reversal of electromagnetic waves and telecommunication*, Radio Science, 40 (2005).

[R50] B.H. LIU, D.C. CHANG, AND M.T. MA, *Eigenmodes and the Composite Quality Factor of a Reverberation Chamber*, Tech. Report 1066, National Bureau of Standards, 1983.

[R51] D. LUBMAN, *Spatial averaging in a diffuse sound field*, Journal of the Acoustical Society of America, 46 (1969), p. 532.

[R52] ——, *Spatial averaging in sound-power measurements*, Journal of the Acoustical Society of America, 45 (1969), p. 337.

[R53] D. LUBMAN, R.V. WATERHOUSE, AND C.S. CHIEN, *Effectiveness of continuous spatial averaging in a diffuse sound field*, Journal of the Acoustical Society of America, 53 (1973), p. 650.

[R54] O. LUNDÉN AND M. BÄCKSTRÖM, *How to avoid unstirred high frequency components in mode stirred reverberation chambers*, in IEEE International Symposium on Electromagnetic Compatibility, July 2007, pp. 1–4.

[R55] F. MOGLIE AND V.M. PRIMIANI, *Numerical analysis of a new location for the working volume inside a reverberation chamber*, IEEE Transactions on Electromagnetic Compatibility, 54 (2012), pp. 238–245.

[R56] P.M. MORSE AND H. FESHBACH, *Methods of Theoretical Physics*, Feshback Publishing, 1981.

[R57] M. NIETO-VESPERINAS, *Scattering and diffraction in physical optics*, New York, 1991.

[R58] C. OESTGES, A.D. KIM, G. PAPANICOLAOU, AND A.J. PAULRAJ, *Characterization of space-time focusing in time-reversed random fields*, IEEE Transactions on Antennas and Propagation, 53 (2005), pp. 283 – 293.

[R59] R.E. PALEY AND N. WIENER, *Fourier transforms in the complex domain*, vol. 19, American Mathematical Society, 1934.

[R60] G. PAPANICOLAOU, L. RYZHIK, AND K. SØLNA, *Statistical stability in time reversal*, SIAM Journal on Applied Mathematics, (2004), pp. 1133–1155.

[R61] A. PAPOULIS, *The Fourier Integral and Its Applications*, McGraw-Hill, 1962.

[R62] W. PETIRSCH AND A.J. SCHWAB, *Investigation of the field uniformity of a mode-stirred chamber using diffusers based on acoustic theory*, IEEE Transactions on Electromagnetic Compatibility, 41 (1999), pp. 446–451.

[R63] M. PETIRSH AND A. SCHWAB, *Improving a mode-stirred chamber utilizing acoustic diffusers*, in IEEE International Symposium on Electromagnetic Compatibility, vol. 1, IEEE, 1998, pp. 39–43.

[R64] C. PRADA AND M. FINK, *Eigenmodes of the time reversal operator: A solution to selective focusing in multiple-target media*, Wave Motion, 20 (1994), pp. 151–163.

[R65] V.M. PRIMIANI, F. MOGLIE, AND V. PAOLELLA, *Numerical and experimental investigation of unstirred frequencies in reverberation chambers*, in IEEE International Symposium on Electromagnetic Compatibility, August 2009, pp. 177–181.

[R66] J.G. PROAKIS AND M. SALEHI, *Digital communications*, McGraw-Hill New York, 2001.

[R67] P. ROUX, B. ROMAN, AND M. FINK, *Time-reversal in an ultrasonic waveguide*, Applied Physics Letters, 70 (1997), p. 1811.

[R68] R. ROY AND T. KAILATH, *Esprit-estimation of signal parameters via rotational invariance techniques*, IEEE Transactions on Acoustics, Speech and Signal Processing, 37 (1989), pp. 984–995.

[R69] P.E. SABINE, *Acoustics and architecture*, Sabine Press, 2008.

[R70] A. SALEH AND R. VALENZUELA, *A statistical model for indoor multipath propagation*, IEEE Journal on Selected Areas in Communications, 5 (1987), pp. 128–137.

[R71] R. SCHMIDT, *Multiple emitter location and signal parameter estimation*, IEEE Transactions on Antennas and Propagation, 34 (1986), pp. 276–280.

[R72] M.R. SCHROEDER, *Die statistischen parameter der frequenzkurven von grossen räumen*, Acustica, 4 (1954), pp. 594–600.

[R73] ——, *Measurement of sound diffusion in reverberation chambers*, The Journal of the Acoustical Society of America, 31 (1959), p. 1407.

[R74] ——, *Spatial averaging in a diffuse sound field and the equivalent number of independent measurements*, Journal of the Acoustical Society of America, 46 (1969), p. 534.

[R75] ——, *Statistical parameters of the frequency response curves of large rooms*, Journal of Audio Engineers Society, 35 (1987), pp. 299–305.

[R76] ——, *Phase gratings with suppressed specular reflection*, Acta Acustica united with Acustica, 81 (1995), pp. 364–369.

[R77] M.R. SCHROEDER AND K.H. KUTTRUFF, *On frequency response curves in rooms. Comparison of experimental, theoretical, and Monte Carlo results for the average frequency spacing between maxima*, Journal of the Acoustical Society of America, 34 (1962), p. 76.

[R78] P. SHENG, *Introduction to wave scattering, localization and mesoscopic phenomena*, vol. 88, Springer Verlag, 2006.

[R79] J.J. STAMNES, *Waves in focal regions: propagation, diffraction, and focusing of light, sound, and water waves*, Taylor & Francis, 1986.

[R80] I.S. STIEVANO, I.A. MAIO, AND F. CANAVERO, *Behavioral models of i/o ports from measured transient waveforms*, IEEE Transactions on Instrumentation and Measurement, 51 (2002), pp. 1266–1270.

[R81] H.J. STÖCKMANN, *Quantum chaos: an introduction*, vol. 3, Cambridge Univ Press, 1999.

[R82] H.-J. STÖCKMANN AND J. STEIN, *Quantum chaos in billiards studied by microwave absorption*, Physical Review Letters, 64 (1990), pp. 2215–2218.

[R83] K.S. STOWE, *An Introduction to Thermodynamics And Statistical Mechanics*, Cambridge University Press, 2007.

[R84] G.L. TURIN, F.D. CLAPP, T.L. JOHNSTON, S.B. FINE, AND D. LAVRY, *A statistical model of urban multipath propagation*, IEEE Transactions on Vehicular Technology, 21 (1972), pp. 1–9.

[R85] T.R. TURLINGTON, *Behavioral modeling of nonlinear RF and microwave devices*, Artech House, 2000.

[R86] C. VAA, P. M. KOCH, AND R. BLÜMEL, *Weyl formula: Experimental test of ray splitting and corner corrections*, Physical Review E, 72 (2005), p. 056211.

[R87] J. VAN BLADEL, *Electromagnetic fields*, IEEE Press, 2nd ed., 2007.

[R88] H.C. VAN DE HULST, *Light scattering by small particles*, Dover Publications, 1957.

[R89] R. WATERHOUSE AND D. LUBMAN, *Discrete versus continuous space averaging in a reverberant sound field*, Journal of the Acoustical Society of America, 48 (1970), p. 1.

[R90] R.L. WEAVER, *On the ensemble variance of reverberation room transmission functions, the effect of spectral rigidity*, Journal of Sound and Vibration, 130 (1989), pp. 487–491.

[R91] N. WELLANDER, O. LUNDÉN, AND M. BÄCKSTRÖM, *Experimental investigation and mathematical modeling of design parameters for efficient stirrers in mode-stirred reverberation chambers*, IEEE Transactions on Electromagnetic Compatibility, 49 (2007), pp. 94 –103.

[R92] E.P. WIGNER, *Random matrices in physics*, Siam Review, 9 (1967), pp. 1–23.

[R93] E. WOLF, *Introduction to the Theory of Coherence and Polarization of Light*, Cambridge University Press, 2007.

[R94] F. WU, J.L. THOMAS, AND M. FINK, *Time reversal of ultrasonic fields. il. experimental results*, IEEE Transactions on Ultrasonics, Ferroelectrics and Frequency Control, 39 (1992), pp. 567–578.

[R95] A. YARIV, *Phase conjugate optics and real-time holography*, IEEE Journal of Quantum Electronics, 14 (1978), pp. 650–660.

[R96] M.E. YAVUZ AND F.L. TEIXEIRA, *Full time-domain DORT for ultrawideband electromagnetic fields in dispersive, random inhomogeneous media*, IEEE Transactions on Antennas and Propagation, 54 (2006), pp. 2305–2315.

[R97] Z.Y. YUAN, J.L. HE, S.M. CHEN, R. ZENG, AND T. LI, *Evaluation of the split stirrer in reverberation chamber*, in Environmental Electromagnetics, The 2006 4th Asia-Pacific Conference on, aug. 2006, pp. 454–457.